

University of Alberta

**Synthesis of Millimeter-Scale Carbon Nanotube Arrays
and Their Applications on Electrochemical
Supercapacitors**

by

Xinwei Cui

A thesis submitted to the Faculty of Graduate Studies and Research
in partial fulfillment of the requirements for the degree of

Doctor of Philosophy

in

Materials Engineering

Department of Chemical and Materials Engineering

©Xinwei Cui

Fall 2010

Edmonton, Alberta

Permission is hereby granted to the University of Alberta Libraries to reproduce single copies of this thesis and to lend or sell such copies for private, scholarly or scientific research purposes only. Where the thesis is converted to, or otherwise made available in digital form, the University of Alberta will advise potential users of the thesis of these terms.

The author reserves all other publication and other rights in association with the copyright in the thesis and, except as herein before provided, neither the thesis nor any substantial portion thereof may be printed or otherwise reproduced in any material form whatsoever without the author's prior written permission.

Examining Committee

Weixing Chen, Department of Chemical and Materials Engineering

Dongyang Li, Department of Chemical and Materials Engineering

Douglas Ivey, Department of Chemical and Materials Engineering

Dave Mitlin, Department of Chemical and Materials Engineering

Xiaodong Wang, Department of Mechanical Engineering

Qiaoqin Yang, Department of Mechanical Engineering,
University of Saskatchewan

Dedication

To my fiancée

Qian (Jane) Zhang

Abstract

This research is aimed at synthesizing millimeter-scale carbon nanotube arrays (CNTA) by conventional chemical vapor deposition (CCVD) and water-assisted chemical vapor deposition (WACVD) methods, and exploring their application as catalyst supports for electrochemical supercapacitors.

The growth mechanism and growth kinetics of CNTA under different conditions were systematically investigated to understand the relationship among physical characteristics of catalyst particles, growth parameters, and carbon nanotube (CNT) structures within CNTAs. Multiwalled CNT (MWCNT) array growth demonstrates lengthening and thickening stages in CCVD and WACVD. In CCVD, the lengthening and thickening were found to be competitive. By investigating catalyst particles after different pretreatment conditions, it has been found that inter-particle spacing plays a significant role in influencing CNTA height, CNT diameter and wall number. In WACVD, a long linear lengthening stage has been found. CNT wall number remains constant and catalysts preserve the activity in this stage, while MWCNTs thicken substantially and catalysts deactivate following the previously proposed radioactive decay model in the thickening stage of WACVD. Water was also shown to preserve the catalyst

activity by significantly inhibiting catalyst-induced and gas phase-induced thickening processes in WACVD.

Mn₃O₄ nanoparticles were successfully deposited and uniformly distributed within millimeter-long CNTAs by dip-casting method from non-aqueous solutions. After modification with Mn₃O₄ nanoparticles, CNTAs have been changed from hydrophobic to hydrophilic without their alignment and integrity being destroyed. The hydrophilic Mn₃O₄/CNTA composite electrodes present ideal capacitive behavior with high reversibility. This opens up a new route of utilizing ultra-long CNTAs, based on which a scalable and cost-effective method was developed to fabricate composite electrodes using millimeter-long CNTAs. To improve the performance of the composites, ε-MnO₂ nanorods were anodically pulse-electrodeposited within hydrophilic 0.5 mm-thick Mn₃O₄ decorated CNTAs. The maximum gravimetric capacitance for the MnO₂ nanorods/CNTA composite electrode was found to be 185 F/g, and that for ε-MnO₂ nanorods was determined to be 221 F/g. After electrodeposition, the area-normalized capacitance and volumetric capacitance values were increased by a factor of 3, and an extremely high area-normalized capacitance of 1.80 F/cm² was also achieved for the MnO₂ nanorods/CNTA composite.

Acknowledgements

First and foremost, I would like to acknowledge my advisor, Prof. Weixing Chen, for his superior supervision during my Ph. D. research program. He led me to the research field of materials engineering and electrochemistry, gave me continuous support and encouragement during my persistent pursuit of research goals. I will not forget how he showed his faith in me when I doubted myself. More importantly, he taught me how to open my mind and gave me a lot of freedom in doing research. Without his profound knowledge, wonderful advice and wise guidance, I would not be able to complete this thesis work.

I would like to thank a graduated group member, Dr. Weifeng Wei, for his generous help and research discussion from the start of my project. He showed me different ways to approach a research problem, and introduced me hands-on instruction on materials characterization techniques. Thanks are also due to other group members, Dr. Haifeng Liu, Dr. Fengping Hu, Dr. Yingcai Liu, Dr. Yongwang Kang, and Dr. Tingyong Xing. Special thanks would be given to Prof. Dave Mitlin and his research group, Chris Harrower, Brian Olsen, Chris Holt, Dr. Li Zhang, for allowing me use their sputtering facility and having wonderful research discussion with me.

I would also like to thank many technical contributions from Shiraz Merali (XRD), Tina Barker (SEM/EDS), Dr. Rajeev Nair, Geroge Braybrook, De-ann Rollings (FESEM), Dr. Anqiang He (XPS), Dr. Adam Johan Bergren (Raman). Special thanks would be given to Dr. Shihong Xu (SEM/AES/XPS/Contact angle measurments), Dr. Jian Chen (TEM), and Luning Wang (Electrochemical charge-discharge tests).

Finally, I would like to acknowledge the research funding from the Natural Sciences and Engineering Research Council (NSERC) of Canada and Nova Chemicals Limited.

Table of Contents

1. Introduction and Literature Review	1
1.1. Introduction.....	2
1.2. Carbon Nanotubes: Structure and Properties	6
1.3. Synthesis Methods	12
1.3.1. Arc Discharge.....	12
1.3.2. Laser Ablation.....	14
1.3.3. Thermal Synthesis.....	15
1.4. Growth Mechanism of Carbon Nanotubes.....	20
1.4.1. Carbon Nanotube Growth from Catalyst	20
1.4.2. Deactivation Mechanism of Carbon Nanotube Growth.....	24
1.5. Carbon Nanotube Arrays.....	25
1.5.1. Development of Carbon Nanotube Arrays.....	25
1.5.2. Growth Mechanism and Growth Kinetics of Carbon Nanotube Arrays	28
1.5.3. Barriers to Application.....	30
1.6. Electrochemical Supercapacitors	31
1.6.1. Electrochemical Double Layer Capacitors	32
1.6.2. Pseudo-capacitors	33
1.7. Motivation.....	36
1.8. Overview of Thesis	38
1.9. References.....	41
2. Experimental Methods and Procedures.....	57
2.1. Introduction.....	58
2.2. Carbon Nanotube Array Growth Procedure.....	59
2.2.1. Piranha Cleaning of Si Wafers	59
2.2.2. Sputtering.....	59

2.2.3. Carbon Nanotube Array Growth by CVD Method	62
2.3. Electrochemical Deposition and Measurements	63
2.3.1. Electrodeposition	64
2.3.2. Cyclic Voltammetry Curves	65
2.3.3. Charge-discharge Curves	66
2.3.4. EIS Measurements	67
2.4. Material Characterization Methods	68
2.4.1. X-ray Diffraction	69
2.4.2. Transmission Electron Microscopy	70
2.4.3. Scanning Electron Microscopy	72
2.4.4 Energy-dispersive X-ray Spectroscopy	73
2.4.5 X-ray Photoelectron Spectroscopy	73
2.4.6 Auger Electron Spectroscopy	74
2.4.7 Raman Spectroscopy	74
2.4.8 Contact Angle Measurement	75
2.4.9 Image-Pro [®] Plus Software	76
2.5. References	77
3. Growth of Millimeter-Scale Carbon Nanotube Arrays by Conventional Chemical Vapor Deposition: Effect of Catalyst Particle Interspacing	78
3.1. Introduction	79
3.2. Experimental Procedure	81
3.3. Results and Discussion	83
3.3.1. Morphology and Growth Kinetics of Vertically Aligned MWCNT Arrays ...	83
3.3.2. Characterization of Catalyst Particles after Different Pretreatments	86
3.3.3. Dependence of CNTA Growth on Catalyst Particle Interspacing	90
3.3.4. CNTA Growth Mechanism Affected by Catalyst Particle Interspacing	94
3.4. Conclusions	103
3.5. References	104
4. Growth Kinetics of Millimeter-Scale Carbon Nanotube Arrays by Chemical Vapor Deposition in the Presence and Absence of Water: Mechanism in Lengthening and Thickening Stages	108

4.1. Introduction.....	109
4.2. Experimental Procedure.....	111
4.3. Results and Discussion.....	112
4.3.1. Lengthening and Thickening Process in WACVD	112
4.3.2. Lengthening and Thickening Process in CCVD.....	120
4.3.3. Raman Spectroscopy and Thickening Behavior in the Lengthening Stage of CCVD	127
4.3.4. The Effect of Water.....	131
4.3.5. The Effects of Ethylene and Hydrogen for MWCNT Array Growth in WACVD.....	133
4.4. Conclusions.....	138
4.5. References.....	140
5. A Novel Hydrophilic Mn₃O₄/Millimeter-Long Carbon Nanotube Array Composite Electrode for Electrochemical Supercapacitors	144
5.1. Introduction.....	145
5.2. Experimental Procedure.....	147
5.2.1. Millimeter-long Carbon Nanotube Array (CNTA) Growth	147
5.2.2. Composite Electrode Production	148
5.2.3. Materials Characterization.....	149
5.2.4. Electrochemical Capacitive Behavior.....	150
5.3. Results and Discussion.....	151
5.3.1. Characterization of CNTA	151
5.3.2. Structural Characterization of Mn ₃ O ₄ /CNTA Composite Arrays.....	152
5.3.3. Hydrophilicity of Mn ₃ O ₄ /CNTA Composite Arrays	158
5.3.4. Electrochemical Properties of Mn ₃ O ₄ /CNTA Composite Electrodes	160
5.4. Conclusions.....	168
5.5. References.....	169
6. Anodic Pulse-Electrodeposition of MnO₂ Nanorods within Hydrophilic Vertically Aligned Carbon Nanotube Arrays for Supercapacitors.....	172
6.1. Introduction.....	173
6.2. Experimental Procedure.....	174

6.2.1. Millimeter-long Carbon Nanotube Array Growth	174
6.2.2 Composite Electrode Production	175
6.2.3. Materials Characterization and Electrochemical Measurements	176
6.3. Results and Discussion.....	177
6.3.1. Structural Characterization	177
6.3.2. Electrochemical Properties	177
6.4. Conclusions.....	186
6.5. References.....	187
7. General Conclusions, Contributions, and Future Work Recommendations	189
7.1. Growth of Ultra-long CNTAs by CCVD and WACVD	190
7.2. Application of Ultra-long CNTAs to Supercapacitors	192
7.3. Contributions.....	193
7.4. Future Work Recommendations.....	194
AI. Saccharin Effects on Direct-Current Electroplating Nanocrystalline Ni-Cu Alloys.....	196
AI.1. Introduction.....	197
AI.2. Experimental Procedure.....	199
AI.3. Results and Discussion	202
AI.3.1. Composition of Electroplated Ni-Cu Nanocrystalline Coatings	202
AI.3.2. Characterization of Electroplated Ni-Cu Nanocrystalline Coatings.....	203
AI.3.3. Steady-state Polarization and Electrochemical Impedance Investigation .	210
AI.3.4. Mechanism of Ni-Cu Plating as Affected by Saccharin Addition	213
AI.4. Conclusions.....	216
AI.5. References.....	218
AII. Electrochemical Study of Codeposition of Al particle – Nanocrystalline Ni/Cu composite coatings	220
AII.1. Introduction.....	221
AII.2. Experimental Procedure.....	223

AII.3. Results and Discussion.....	224
AII.3.1. Morphology and Microstructural Studies of Ni/Cu-Al Composite Coatings	224
AII.3.2. Potentiodynamic Polarization.....	227
AII.3.3. Effect of Particle Loading on Embedded Particle Content at Different Current Densities	230
AII.3.4. Codeposition Mechanism.....	231
AII.4. Conclusions.....	237
AII.5. References.....	238

List of Tables

Table 3-1. Summary of catalyst particle data and the dimensions of CNTs grown from the corresponding catalyst particles for 30 min.....	91
Table 5-1. Capacitance values for $\text{Mn}_3\text{O}_4/\text{CNTA}(0.84)$, $\text{Mn}_3\text{O}_4/\text{CNTA}(0.33)$ composite electrodes and as-grown CNTA electrode derived from cyclic voltammetry.	164
Table 6-1. Improvement of the capacitance by anodic pulse-electrodeposition.	184
Table AI-1. Composition and operating conditions for Ni/Cu and Ni/Cu-Al plating	201

List of Figures

Figure 1-1. Schematic diagram showing how a graphene sheet is rolled up to form (5, 3) nanotube. 7

Figure 1-2. Illustrations of atomic structures of (a) an armchair, (b) a zigzag, and (c) a chiral (5, 3) nanotubes. 8

Figure 1-3. High-resolution transmission electron micrographs (HRTEMs) of the first observed (a) SWCNT and (b-d) MWCNTs. 10

Figure 1-4. Relaxed structures of different joints connecting two zigzag nanotubes: (12,0), and (I: single 5/7 defect) (11,0), (II: double 5/7 defects) (10,0), (III: triple 5/7 defects) (9,0), respectively. The 5/7 pair defects are (a) either distributed around the circumference of the tube, (b) aligned along the cylindrical axis, (IIc) or transformed into another defect: as 5/6/7 defect. The pentagon and heptagon rings, responsible for the change in nanotube diameter, are visualized in white, while the rest of the joint is in grey. The lefthand side of the figure shows the top of the structure which includes the 5/7 pair defects. The right-hand side is a projection of the structure, elongated by a few belts of hexagons, on a symmetry

plane passing through the 5/7 defect(s).....	11
Figure 1-5. Arc discharge setup.	14
Figure 1-6. Laser ablation apparatus.....	15
Figure 1-7. Schematic of a conventional CVD furnace.....	17
Figure 1-8. Schematic of a HiPco furnace.....	19
Figure 1-9. Schematic of CNT growth process.....	21
Figure 1-10. Schematics of root and tip growth modes for CNTs	23
Figure 1-11. A SEM image and a schematic illustration of vertically-aligned CNTA.....	27
Figure 1-12. The detailed growth procedure for CNTAs by conventional CVD and water-assisted CVD methods.....	29
Figure 2-1. Schematic diagram of a sputtering system with DC, pulsed-DC and RF power supplies.....	60

Figure 2-2. Configuration of sputtered wafers.....	61
Figure 2-3. Setup for CCVD and WACVD.....	62
Figure 2-4. Typical (a) cyclic voltammetry curve; (b) galvanic charge-discharge curves; (c) EIS curves.	68
Figure 3-1. FESEM cross section images of vertically aligned CNTAs after 1 hr CNT test: (a) 1.1 mm long CNTA grown on 60 min-pretreated Fe(3nm) catalyst film; (b) 0.9 mm long CNTA grown on 4 min-pretreated Fe(1nm) catalyst film.	83
Figure 3-2. (a) Growth kinetic curves of CNTAs grown on 60 min-pretreated Fe(3nm) and 4 min-pretreated Fe(1nm) catalyst films. The inset is the corresponding growth rate vs. growth time curves for the two catalyst films. (b) The histograms of the diameter of CNTs grown on the catalyst films in (a); (c) The histograms of the wall number of CNTs grown on the catalyst films in (a)..	84
Figure 3-3. FESEM images of the Fe(1nm) catalyst film (a) after pretreatment for 4 min; (b) Auger profiles detected from the particles and substrate in (a); (c) after pretreatment for 6 min; (d) Auger mapping of the catalyst film in (c).....	87
Figure 3-4. FESEM images of the Fe(3nm) catalyst film after (a) pretreatment for 60 min; (b) pretreatment for 70 min.....	88

Figure 3-5. CNTA height vs. inter-particle spacing, particle size (inset (a)) and particle density (inset (b)). 93

Figure 3-6. (a) TEM image of CNTs deposited for 30 min on the Fe(3nm) catalyst film after pretreatment for 60 min; the inset is a HRTEM image showing the catalyst particle at the tip of the CNT (scale bar: 5 nm); (b) FESEM image of 60 min-pretreated Fe(3nm) catalyst film after removal of the grown CNTA; (c) XPS spectra of the as-pretreated catalyst film and the substrate after removal of the grown CNTA. 96

Figure 3-7. High resolution surface morphology and cross section FESEM images of CNTAs deposited for 30 min on the Fe(1nm) catalyst film after (a), (b) pretreatment for 4 min; (c), (d) pretreatment for 6 min. The insets are low magnification FESEM images of the CNTAs from the corresponding pretreated catalyst films. 98

Figure 3-8. Wall number of CNTs grown on 60 min-pretreated Fe(3nm) and 4 min-pretreated Fe(1nm) catalyst films vs. CNT growth time, and HRTEM images of the corresponding CNTs (scale bar: 5 nm). 100

Figure 3-9. Growth kinetic curves of CNTAs grown on 4 min-pretreated and 6 min-pretreated Fe(1nm) catalyst films, and HRTEM images of the corresponding CNTs (scale bar: 5 nm). 102

Figure 4-1. (a) The growth kinetic curve of MWCNT arrays grown by WACVD; the insets are photographs of millimeter-long MWCNT arrays in two stages (Si wafer is 500 μm thick). (b)-(e) are typical HRTEM images of MWCNTs grown by WACVD for (b) 5 min; (c) 30 min; (d) 60 min; (e) 120 min, respectively. (Scale bar in HRTEM images: 10 nm)..... 113

Figure 4-2. (a) A family of histograms of the wall number of MWCNTs grown for different periods, from 5 min to 45 min, by WACVD. (b) TEM image of MWCNTs grown by WACVD for 120 min showing the final stage of gas phased-induced thickening. (c) HRTEM image of a DWCNT grown by WACVD for 60 min showing the nucleation stage (conical structure) of gas phased-induced thickening..... 114

Figure 4-3. Plot of CNT wall number as a function of growth time in the initial 45 min of WACVD. The solid line is the linear fitting line with very small slope showing that the CNT wall number remained constant in the initial 45 min of WACVD..... 116

Figure 4-4. (a) The fitting of the growth kinetic data (dots) of MWCNT arrays grown after 45 min by WACVD to the radioactive decay model (solid line). (b) The defined parameters for the dimension of a MWCNT..... 119

Figure 4-5. (a) The growth kinetic curve of MWCNT arrays grown by CCVD; the

insets are HRTEM images of MWCNTs grown for 10 min and 60 min in CCVD. (b) and (c) are TEM images of MWCNTs grown in CCVD for 5 min, 15 min and 30 min, respectively. (Scale bar in HRTEM images: 10 nm)..... 121

Figure 4-6. A family of histograms of the wall number of MWCNTs grown for different periods, from 5 min to 30 min, by CCVD. The thickening process in the lengthening stage of CCVD is confidently proved by this diagram. 122

Figure 4-7. HRTEM image of a MWCNT grown for 30 min by CCVD showing the nucleation sites (conical structure) for the gas phase-induced thickening. (Scale bar in the HRTEM image: 10 nm)..... 123

Figure 4-8. Plots of (a) MWCNT array height vs. CNT wall number; (b) MWCNT thickening rate vs. growth time, in CCVD..... 124

Figure 4-9. Plot of CNT wall number as a function of growth time in CCVD; the inset is the enlarged view of the fitting curve in the initial 30 min..... 126

Figure 4-10. Raman spectra for MWCNT arrays grown for 5 min, 30 min and 120 min by (a) WACVD and (b) CCVD. (c) The growth time dependence of G/D ratio. 128

Figure 4-11. Schematic diagram of catalyst-induced and gas phase-induced

thickening for both tip and root growth modes..... 131

Figure 4-12. (a) MWCNT array height vs. ethylene flow rate. (b) A family of histograms of the wall number of MWCNTs grown for different ethylene flow rates, from 25 sccm to 400 sccm, by WACVD. 134

Figure 4-13. (a) MWCNT array height vs. hydrogen flow rate. (b) A family of histograms of the wall number of MWCNTs grown for different hydrogen flow rates, from 250 sccm to 550 sccm, by WACVD. 135

Figure 4-14. (a) The growth kinetic curve of MWCNT arrays grown by WACVD at 100 sccm C₂H₄; the insets are photographs of millimeter-long MWCNT arrays in two stages (Si wafer is 500 μm thick). (b) A family of histograms of the wall number of MWCNTs grown for different periods, from 5 min to 60 min, by WACVD at 100 sccm C₂H₄..... 136

Figure 5-1. Schematic diagram of making Mn₃O₄/CNTA composite electrode. The inset image is the photograph of the composite electrode before sealed with green Mask-it. 151

Figure 5-2. Surface wettability of as-grown CNTA with a contact angle of 138°. 152

Figure 5-3. (a) TEM image of $\text{Mn}_3\text{O}_4/\text{CNTA}(0.33)$ and its inset HRTEM image of the Mn_3O_4 nanoparticle. (b) EDS and (c) SAD patterns detected from $\text{Mn}_3\text{O}_4/\text{CNTA}(0.33)$ in (a). (d) Statistical distribution of Mn_3O_4 nanoparticle size deposited within CNTA in $\text{Mn}_3\text{O}_4/\text{CNTA}(0.33)$. (e) TEM image of $\text{Mn}_3\text{O}_4/\text{CNTA}(0.84)$. (f) Statistical distribution of Mn_3O_4 nanoparticle size deposited within CNTA in $\text{Mn}_3\text{O}_4/\text{CNTA}(0.84)$ 154

Figure 5-4. (a) Bright-field and (b) dark-field TEM images of $\text{Mn}_3\text{O}_4/\text{CNTA}(0.33)$. (c) Bright-field and (d) dark-field TEM images of $\text{Mn}_3\text{O}_4/\text{CNTA}(0.84)$ 155

Figure 5-5. XPS Mn 3s spectrum from $\text{Mn}_3\text{O}_4/\text{CNTA}$ composite. The splitting width of the doublet peaks is indicated. 156

Figure 5-6. (a,b) Surface morphology and (c,d) cross section FESEM images of $\text{Mn}_3\text{O}_4/\text{CNTA}$ composites at different magnifications. (e) Cross-section SEM image of $\text{Mn}_3\text{O}_4/\text{CNTA}$ composite and its corresponding EDS mapping patterns for C, Mn and O. 157

Figure 5-7. (a) Time sequence images of a water droplet dropped to the surface of $\text{Mn}_3\text{O}_4/\text{CNTA}$ composite. (b) Schematic diagram of the inner structure of $\text{Mn}_3\text{O}_4/\text{CNTA}$ composite showing how the composite works in ESs. 160

Figure 5-8. CV curves of (a) $\text{Mn}_3\text{O}_4/\text{CNTA}(0.84)$ composite electrode and (b)

Mn₃O₄/CNTA(0.84) composite electrode detected in 0.5 M Na₂SO₄ electrolyte at various scan rates spanning from 2 mV/s to 200 mV/s. (c) Specific capacitance for Mn₃O₄/CNTA composite electrodes at two different loadings and as-grown CNTA electrode calculated from galvanostatic charge-discharge curves at various current densities. (d) Nyquist plot for the as grown CNTA electrode. 161

Figure 5-9. (a) CV curves of Mn₃O₄/CNTA composite electrodes at two different loadings and as-grown CNTA electrode at 50 mV/s. (b) Galvanostatic charge-discharge curves of the three electrodes at 1 A/g. (c) Specific capacitance for the three electrodes calculated from CV curves at various scan rates. (d) Specific capacitance for the deposited Mn₃O₄ nanoparticles for the composite electrodes with two loadings at various scan rates..... 163

Figure 5-10. (a) Nyquist plots for Mn₃O₄/CNTA(0.84) and Mn₃O₄/CNTA(0.33) composite electrodes. (b) Variation of capacitance with respect to CV cycle number for Mn₃O₄/CNTA(0.84) and Mn₃O₄/CNTA(0.33) composite electrodes and also for the deposit Mn₃O₄ nanoparticles. 167

Figure 6-1. Schematic diagram of making composite electrode based on millimeter-long carbon nanotube arrays. 176

Figure 6-2. Cross-sectional SEM images taken at the top (a), middle (b), and bottom (c) part of the MnO₂ nanorods/CNTA composite; (d) a high-magnification

cross-sectional SEM image. The inset image in (a) is a low-magnification SEM image showing the whole cross section of the composite..... 179

Figure 6-3. (a) Bright-field and (b) dark-field TEM images; (c) SAD pattern; (d) high-magnification TEM image with nanorod's lattice fringes in the inset image, of the MnO₂ nanorods/CNTA composite. 180

Figure 6-4. (a) CV curves and (b) EIS Nyquist plots, of three composite electrodes, a Mn₃O₄/CNTA composite electrode before electrodeposition (denoted as 0 min) and two MnO₂/CNTA composite electrodes after 10 min and 20 min's electrodeposition (denoted as 10 min and 20 min, respectively). 183

Figure 6-5. TEM images of Mn₃O₄ nanoparticles dip-casted on (a) large wall-number CNTs grown by CCVD (b) small wall-number CNTs grown by WACVD..... 185

Figure AI-1. Composition of as-plated Ni-Cu alloy coatings from Green baths and GSS baths as a function of current density..... 202

Figure AI-2. Plan-view of SEM images of as-plated Ni-Cu alloy coatings prepared from (a) Green baths, $i=10 \text{ mA/cm}^2$ (Ni-55.4 wt % Cu), (b) Green baths, $i=20 \text{ mA/cm}^2$ (Ni-24.6 wt % Cu), (c) GSS baths, $i=10 \text{ mA/cm}^2$ (Ni-52.2 wt % Cu), (d) GSS baths, $i=20 \text{ mA/cm}^2$ (Ni-20.2 wt % Cu), and (e) GSS baths, $i=40 \text{ mA/cm}^2$

(Ni-9.5 wt % Cu)..... 204

Figure AI-3. Cross-section SEM images of as-plated Ni-Cu alloy coatings prepared from (a) Green baths, $i=10 \text{ mA/cm}^2$ (Ni-55.4 wt % Cu), and (b) GSS baths, $i=10 \text{ mA/cm}^2$ (Ni-52.2 wt % Cu). 205

Figure AI-4. XRD patterns of as-plated Ni-Cu alloy coatings prepared at $i=20 \text{ mA/cm}^2$, from (a) Green baths (Ni-24.6 wt % Cu), and (b) GSS baths (Ni-20.2 wt % Cu). 206

Figure AI-5. TEM images of as-plated Ni-24.6 wt % Cu coating prepared from Green baths at $i=20 \text{ mA/cm}^2$, (a) BF image, (b) DF image, and (c) distribution of grain size. 207

Figure AI-6. TEM images of as-plated Ni-20.2 wt % Cu coating prepared from GSS baths at $i=20 \text{ mA/cm}^2$, (a) BF image, (b) DF image, and (c) distribution of grain size. 208

Figure AI-7. Diffraction patterns of as-plated Ni-Cu alloy coatings prepared at $i=20 \text{ mA/cm}^2$ from (a) Green baths (Ni-24.6 wt % Cu) and (b) GSS baths (Ni-20.2 wt % Cu)..... 210

Figure AI-8. Partial steady-state polarization curves for Ni, corrected for ohmic

drop, recorded in the potential range for the Ni deposition from the plating baths without additive (■), with SDS (●), saccharin (▲), and both additives (▼). 211

Figure AI-9. Nyquist plots recorded at a current density of 20 mA/cm² in the plating baths without additive (■), with SDS (●), saccharin (▲), and both additives (▼)..... 212

Figure AII-1. Plan view SEM image (a) and backscattered cross-section image (b) of as-plated Ni/Cu-Al particle composite coating (Ni-17 wt % Cu-8 wt % Al). 225

Figure AII-2. Bright-field image with its inset electro-diffraction patterns (a), and dark-field image (b) of as-plated Ni-17 wt % Cu-8 wt % Al composite coating. (c) Dark-field image of as-plated Ni-20 wt % Cu coating. 226

Figure AII-3. Effect of particle loading on potentiodynamic polarization scans, (a) solid lines are polarization scans start at the beginning of plating, while dashed lines are those start after 30 min plating under $i=10 \text{ mA/cm}^2$, (b) solid lines are simulated polarization curves, while dashed lines are scans start after 30 min plating under $i=10 \text{ mA/cm}^2$ 228

Figure AII-4. Volume percentage of embedded Al particles as a function of (a) particle loading and (b) volume percentage of particles in suspension, under different current densities. Error bar: 95% confidence. 230

Figure AII-5. (a) $C(1-\alpha)^{1.55}/\alpha$ vs. C for Ni/Cu-Al coatings at three different current densities. Error bar: 95% confidence. (b) $\log(\tan\phi)$ vs. $\log i$ for the Ni/Cu-Al particle system.235

List of Abbreviations

Auger Electron Spectroscopy:	AES
Atomic Force Microscopy:	AFM
Backscattered Electron:	BSE
Bright Field:	BF
Conventional Chemical Vapor Deposition:	CCVD
Conventional Electrodeposition:	CED
Carbon Nanotube:	CNT
Carbon Nanotube Array:	CNTA
Chemical Vapor Deposition:	CVD
Cyclic Voltammetry:	CV
Dark Field:	DF
Double-walled Carbon Nanotube:	DWCNT
Direct Current:	DC
Electrochemical Double Layer Capacitor:	EDLC
Energy Dispersive Spectroscopy:	EDS
Electrochemical Impedance Spectroscopy:	EIS
Electrochemical Supercapacitors:	ES
Field-emission Scanning Electron Microscopy:	FESEM

High-resolution Transmission Electron Microscopy:	HRTEM
Multiwalled Carbon Nanotube:	MWCNT
Pulse Current:	PC
Selected Area Diffraction:	SAD
Sediment Codeposition:	SCD
Saturated Calomel Electrode:	SCE
Single-walled Carbon Nanotube:	SWCNT
Scanning Electron Microscopy:	SEM
Specific Surface Area:	SSA
Transmission Electron Microscopy:	TEM
X-ray Diffraction:	XRD
X-ray Photoelectron Spectroscopy:	XPS
Water-assisted Chemical Vapor Deposition:	WACVD

Chapter 1

Introduction and Literature Review

1.1. Introduction

A renewable and clean energy supply that can support the sustainable development of the global economy and society becomes more important than ever before because of the rapid depletion of fossil fuels and increasingly worsened global environment, such as the greenhouse effect, acid rain, and air pollution, caused by vast fossil-fuel consumption. Energy storage is usually required as an intermediate step to the versatile, clean, and efficient use of energy. This is because the production of renewable energy, such as wind and solar energy, significantly relies on natural conditions (day time, night time, wind, etc.) and is often disruptive and fluctuating. High performance electrochemical energy storage systems that can match the production of renewable energy, in addition to match the fast development of portable electronics and hybrid electric vehicles with low CO₂ emissions, are needed. Many forms of carbon, such as carbide-derived carbons [1], activated carbon [2, 3], carbon onions and nanohorns [4, 5], have been utilized experimentally, and some commercially, in electrochemical energy storage systems. To further improve the performance of these devices and to meet the higher requirement of future systems, carbon nanotubes (CNTs) and CNT arrays (CNTAs) are considered as promising candidates.

Since CNTs were discovered in 1991 by Sumio Iijima [6], CNTs have captured

the interest of the world. CNTs are members of the fullerene family; and their morphology is considered to be graphene sheets rolled up into a seamless tube and capped with half of a carbon cage (C_{60} , C_{70} , etc.) on both ends. According to the number of graphene walls, CNTs can be classified into single-walled CNT (SWCNT) and multiwalled CNT (MWCNT). This new form of carbon has been shown to exhibit remarkable mechanical, electronic and thermal properties depending on its symmetric structure, including length, diameter, chirality and wall number [7]. The predicted Young's modulus, shear modulus and bulk modulus for SWCNTs are ~ 1 TPa, 0.45 TPa and 0.74 TPa, respectively, which are comparable to those of diamond [8, 9]; and the reported strengths are 10-100 times higher than the strongest steel at a fraction of the weight [10]. In addition, CNTs are thermally stable up to 2800°C in vacuum, have a thermal conductivity about twice as high as diamond, and have electric-current-carrying capacity 3 orders higher than copper wires [11]. As such, CNTs have been investigated for many applications; for example, nanocomposites [12], field-emission displays [13], field-effect transistors [14], scanning probe microscopy tips [15], micro-electronic devices [16], solar cells [17], supercapacitors [18], Li-ion batteries [19], hydrogen storage [20], sensors [21], biomedical [22], etc. However, a fundamental problem that hinders the use of CNTs for applications is the availability of ensembles of CNTs with uniform length, diameter, and electronic properties. The most controllable method to produce CNTs with consistent

structures is chemical vapor deposition (CVD), especially for one particular product form, vertically aligned CNTAs.

CNTA, also termed as CNT forest or CNT carpet, is one of the most important macroscopic forms of CNTs, which is composed of millions of individual CNTs well organized and vertically aligned to the substrate. Combined with the excellent properties provided by individual CNTs including high conductivity and good chemical stability, CNTA as a whole also possesses its own unique characteristics, such as one of the lightest synthetic materials [23], high surface area [24], high aspect ratio, high purity [25], highly ordered structure, ease of patterning [13], etc. Many efforts have been undertaken to grow CNTA with controlled height (CNT length) [25, 26], CNT diameters [23, 27], wall numbers [28, 29] and even chiralities [30, 31] using CVD methods. The milestone of CNTA synthesis is the successful growth of 2.5 mm long SWCNT array by Hata et al. in 2004 using water-assisted CVD [25]. However, the growth of millimeter-long CNTA requires fine tuning of catalyst particle size, particle interspacing (within nanometer size) and catalyst surface modification (within ppm change of reaction gases). Hence, growing millimeter-long CNTA with good reproducibility is a major challenge; and the growth mechanism and growth kinetics of millimeter-long CNTAs are not well understood. The first aim of this thesis work is to develop reliable and repeatable processes to fabricate

millimeter-long CNTAs with consistent and controllable CNT structures. This goal will be achieved through a careful study of the growth kinetics of CNTA under different conditions including those related to reactive gases for the direct deposition of CNTAs and those affecting characteristics of catalyst films prior to the deposition of CNTAs.

Although CNTAs have many potential applications in field-emission devices [13, 32], and electrochemical and biosensors [33, 34], their applications for electrochemical energy storage devices are an emerging area and require considerable efforts. The second goal of this thesis work is to explore the usage of millimeter-long CNTA for electrochemical supercapacitors (ESs), one type of electrochemical energy storage devices characterized with high power density, excellent reversibility and long cycle life. In the application of supercapacitors, manganese oxides have been extensively evaluated as active materials, due to their reasonably high capacitance, low cost, abundance and environmental-friendliness. In this thesis, millimeter-long CNTAs were successfully used as a supporting material for nano-manganese oxides, forming a novel high-performance composite electrode. The nano-manganese oxides can be uniformly dispersed within millimeter-long CNTAs by dip-casting and anodic-pulse electrodeposition methods. Their electrochemical capacitive performance was also extensively investigated.

1.2. Carbon Nanotubes: Structure and Properties

A SWCNT is a rolled graphene sheet, but the way the graphene sheet is rolled determines the fundamental properties of the nanotube. The atomic structure of the nanotube is usually characterized by two vectors, \vec{C}_h and \vec{T} , whose rectangle defines the unit cell, as shown in Figure 1-1. \vec{C}_h is the chiral vector that defines the circumference on the surface of the tube connecting two equivalent carbon atoms, i.e. the way the graphene sheet is rolled. The chiral vector can be described using the following equation:

$$\vec{C}_h = n\vec{a}_1 + m\vec{a}_2 \quad (1-1)$$

where \vec{a}_1 and \vec{a}_2 are two unit vectors; the integers (n, m) are the number of steps along the two unit vectors on the zig-zag carbon bonds of the hexagonal honeycomb lattice; and n and m also give the chiral angle θ shown in Figure 1-1 as:

$$\theta = \tan^{-1}[\sqrt{3}(m/(2m+n))] \quad (1-2)$$

The chiral angle determines the amount of “twist” in the tube. As a result, the diameter of the nanotube can also be expressed in terms of (m, n) or \vec{C}_h :

$$d_t = \sqrt{3}[a_{c-c}(m^2 + mn + n^2)^{1/2} / \pi] = |\vec{C}_h| / \pi \quad (1-3)$$

where d_t is the diameter of the rolled nanotube; a_{c-c} is the length of carbon bonds.

In addition, \vec{T} is a vector that is perpendicular to \vec{C}_h and designates the direction of the nanotube. Figure 1-1 provides an example of the way to roll up (5, 3) nanotube with all the vectors presented. The atomic arrangement of SWCNT is,

therefore, determined by its chirality, or helicity.

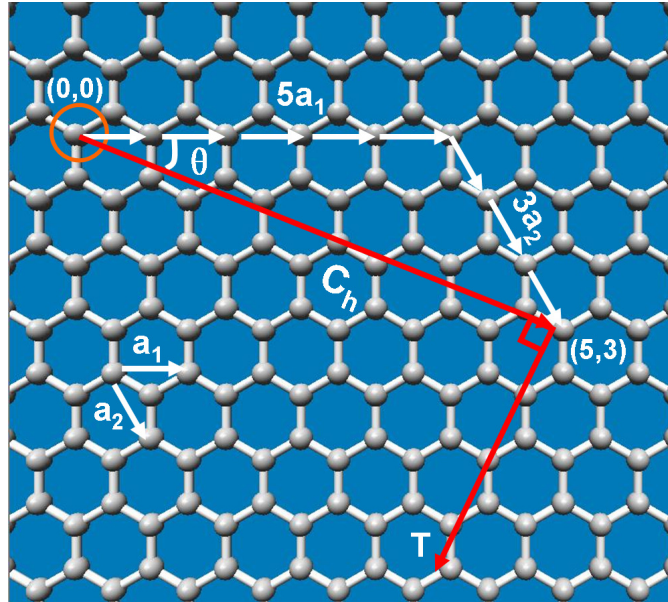


Figure 1-1. Schematic diagram showing how a graphene sheet is rolled up to form (5, 3) nanotube.

The chirality of the SWCNT has significant implications on its properties. In particular, tube chirality is known to have a strong impact on the electronic properties of the nanotube. The chiral angle is used to differentiate electronic properties of carbon nanotubes, which are divided into three classes: armchair ($n = m$, $\theta = 30^\circ$), zig-zag ($m = 0$, $n > 0$, $\theta = 0^\circ$), and chiral ($0 < |m| < n$, $0 < \theta < 30^\circ$). Their atomic structures are shown in Figure 1-2. Armchair carbon nanotubes are metallic; zig-zag and chiral carbon nanotubes can be semimetals with a finite

band gap if $n - m/3 = i$ (i being an integer and $m \neq n$) or semiconductors in all other cases [7]. The band gap for the semimetallic and semiconductive carbon nanotubes also approximately increases with the inverse of the tube diameter [35, 36]. A Combination of different diameters and chiralities results in a large scope of individual nanotubes, each with its own distinct mechanical, electrical, and optical properties [7].

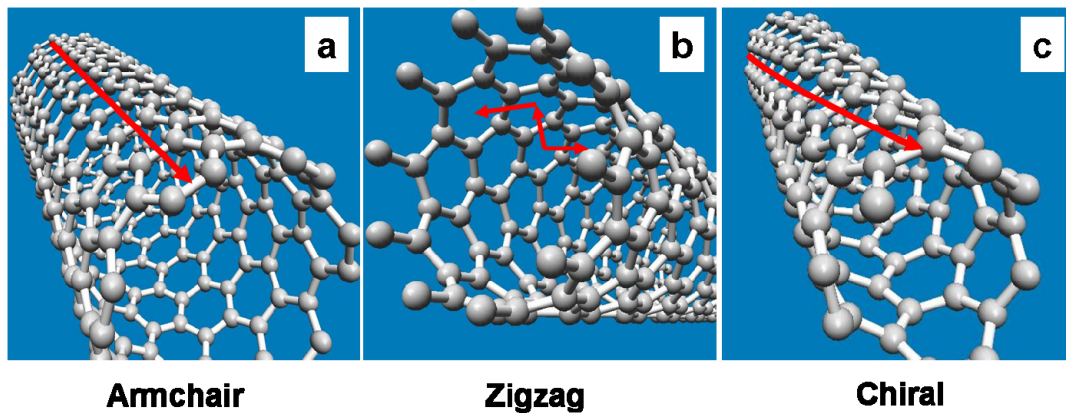


Figure 1-2. Illustrations of atomic structures of (a) an armchair, (b) a zigzag, and (c) a chiral (5, 3) nanotubes.

MWCNTs are essentially composed of two or more concentric single-walled nanotubes, where in most cases each nanotube has different chiralities. These concentric nanotubes are held together by van der Waals bonding. The nanostructure of SWCNT and MWCNTs is clearly demonstrated by the high-resolution transmission electron microscopy (HRTEM) images in Figure 1-3

[6, 37, 38]. In addition to CNT diameter, the properties of MWCNTs also strongly depend on their wall numbers. Take the application in field-emission display (FED) as an example. SWCNTs have the advantage of a low threshold voltage but not a satisfactory emission lifetime for real applications. In contrast, MWCNT emitters possess the durability for real applications, but their threshold voltage is high [27]. Therefore, double-walled CNTs (DWCNT) are considered to be the best choice for real FED applications [39, 40] because they benefit from a synergetic blend of both SWCNT and MWCNT (with large wall number). It is believed that MWCNTs may possess unique properties, transient from flexibility of SWCNT to thermal and electrical stability of MWCNT, as wall number changes. Another example is the mechanical properties of SWCNTs and MWCNTs. Yu and co-workers [41, 42] have investigated the tensile behavior of SWCNT ropes and MWCNT ropes by using two opposing atomic force microscopy (AFM) tips and loading under tension. A tensile strength of 13 to 52 GPa and average elastic moduli of 320 to 1470 GPa were found for SWCNTs; while a tensile strength of 11 to 63 GPa and average elastic moduli of 270 to 950 GPa were found for MWCNTs. The difference can be related to the change of wall number. Although many researchers attempted to fabricate MWCNTs with similar wall number during CNT growth [27-29, 43], the challenge still exists. This prevents our understanding of the effect of CNT wall number on the properties of MWCNTs.

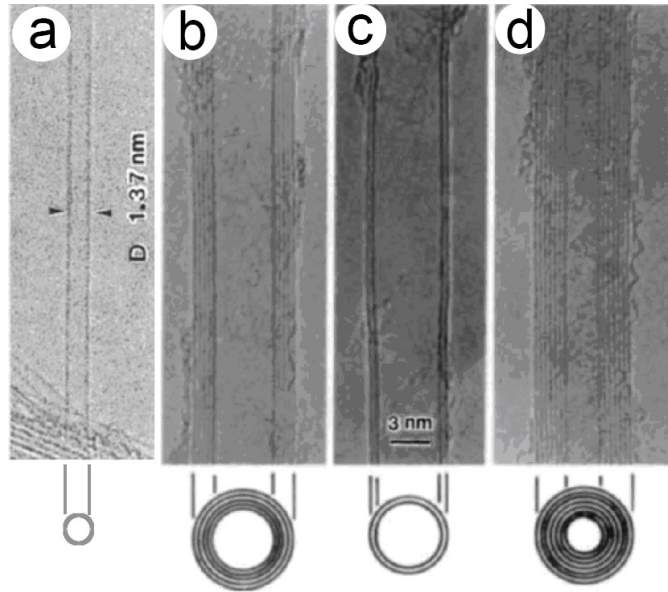


Figure 1-3. High-resolution transmission electron micrographs (HRTEMs) of the first observed (a) SWCNT [37] and (b-d) MWCNTs [6].

CNTs are rarely as perfect as they were once thought to be [44, 45]. As metals and alloys, CNTs can be defective and the defects in CNTs also affect their morphology, properties and possible applications. The possible defects in CNT structures can be classified into three general groups [44]: topological (introduction of ring sizes other than hexagons, such as pentagons and heptagons), rehybridization (introduction of hybridization between sp^2 and sp^3 depending on the degree of the curvature of the graphene sheet bending), and incomplete bonding defects (vacancies, dislocations, etc.). Charlier et al. [46] investigated heptagon/heptagon (5/7) pairs within the cylindrical hexagonal network of the carbon nanotube (first group defect). They attributed the observations of increased

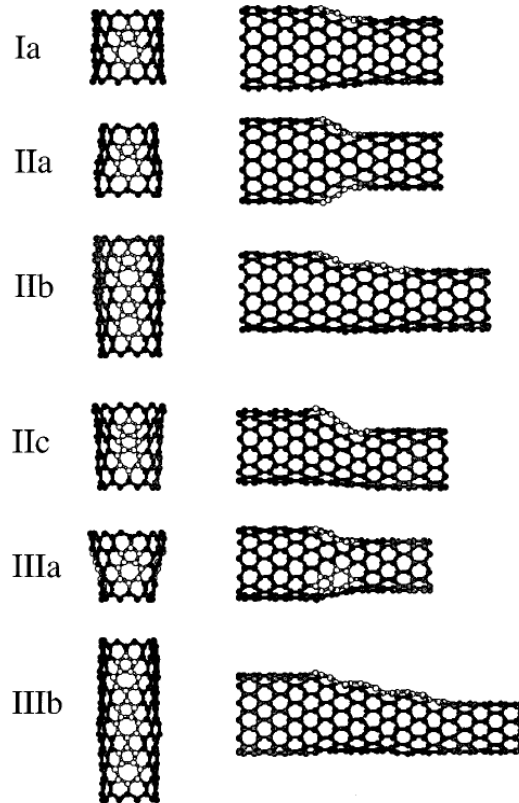


Figure 1-4. Relaxed structures of different joints connecting two zigzag nanotubes [46]: (12,0), and (I: single 5/7 defect) (11,0), (II: double 5/7 defects) (10,0), (III: triple 5/7 defects) (9,0), respectively. The 5/7 pair defects are (a) either distributed around the circumference of the tube, (b) aligned along the cylindrical axis, (IIc) or transformed into another defect: as 5/6/7 defect. The pentagon and heptagon rings, responsible for the change in nanotube diameter, are visualized in white, while the rest of the joint is in grey. The lefthand side of the figure shows the top of the structure which includes the 5/7 pair defects. The right-hand side is a projection of the structure, elongated by a few belts of hexagons, on a symmetry plane passing through the 5/7 defect(s).

tube diameters to a very large number of 5/7 pairs defects accidentally aligned, as shown in Figure 1-4. In this case, the change in the tube diameter, and possible chirality, by these defects perturbs the electronic properties of the hexagonal network leading to the possible design of metal-metal, metal-semiconductor, and semiconductor-semiconductor hybrid devices. The influence of the defects on the structure and properties has been substantially investigated recently [47-49].

1.3. Synthesis Methods

The mass production of random SWCNTs and MWCNTs has been achieved and their prices keep decreasing over the last 10 years, thanks to efficient synthesis methods developed. CNT synthesis has been shown to occur in a wide range of environments, but the basic prerequisites for the growth of CNTs are the same, which mainly consist of a source of carbon, an active catalyst, and adequate energy.

1.3.1. Arc Discharge

Arc discharge was the first recognized method by Iijima [6, 37] and Bethune [38] for producing MWCNTs and SWCNTs. The scheme of this technique is shown in Figure 1-5. Two graphite electrodes, an anode and a cathode with the anode having a smaller diameter, are water-cooled and placed close to each other, less

than 1 mm apart. An inert gas, He or Ar, is used as the atmosphere for the reactions, at a pressure of 100 to 1000 Torr (13.3 to 133 kPa). A low voltage (~12 to 25 V) and high current (~50 to 120 A) power is then applied across the gap generating a plasma arc across the gap. The temperature of this plasma typically reaches 4000 K, at which carbon on the anode is vaporized and deposits onto the cathode. Only when adding metal catalyst to the anode, do SWCNTs form on the cathode. Several parameters that affect the quality and quantity of SWCNTs can be tailored in the arc discharge process. By manipulating the Ar:He gas ratio, the diameter of the SWCNTs formed can be controlled, yielding smaller diameters at higher Ar concentration [50]. The overall inert gas pressure has been shown to affect the weight percent of SWCNTs produced [51]. Different kinds of metal catalysts and their concentrations give different yields of SWCNTs. A widely used metal catalyst is a Y:Ni mixture that has been shown to yield up to 90% SWCNTs, with an average diameter of 1.2 to 1.4 nm [52]. Discharge current and system geometry also influence the quality of the final products [53]. This technique is the simplest and most commonly used method; and SWCNTs and MWCNTs made from this technique were commercially available several years ago. However, the CNTs produced by this method contain many un-wanted by-products, such as fullerenes, amorphous carbon, and graphite sheets, which requires extensive purification before use.

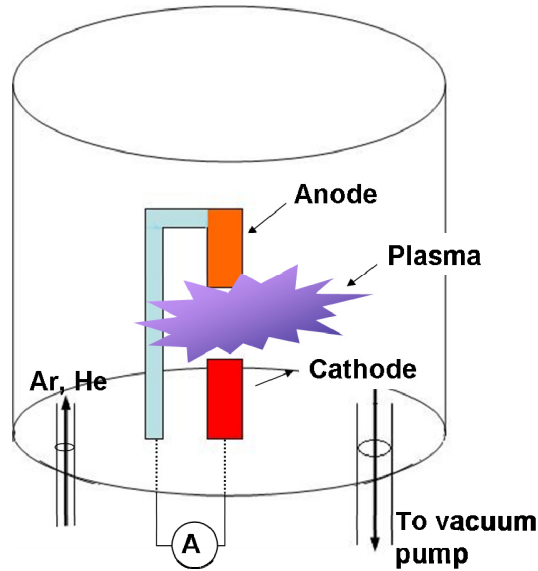


Figure 1-5. Arc discharge setup.

1.3.2. Laser Ablation

Laser ablation method was first used to synthesize CNTs by Guo et al. [54] in 1995. As illustrated in Figure 1-6, in a furnace with high temperatures (500 to 1200 °C), a pulsed [55] or a continuous [56] laser is used to vaporize a target composed of a mixture graphite and transition metal catalysts, such as cobalt or nickel, in the presence of 500 Torr (66.7 kPa) Ar or He gas. CNTs are then formed following the mechanism proposed by Scott et al. [57]: under the irradiation of the laser beam and high temperature, the target is rapidly vaporized forming a cloud of C_3 , C_2 , C and catalyst vapors. As the cloud cools, nanometer size metal catalyst particles are formed in the plume of vaporized graphite and catalyze the growth of

SWCNTs. Simultaneously, the condensation of the carbon species forms many side products. SWCNTs, together with the by-products, are collected at a cold-finger downstream from the target. The nature of the laser, laser power and gas pressure can affect the yield of SWCNTs [58-60] which normally varies from 20% to 80% of SWCNTs by weight. Similar to the arc discharge method, the CNTs obtained from laser ablation method are tangled and have low purity, thus post-purification is needed [61].

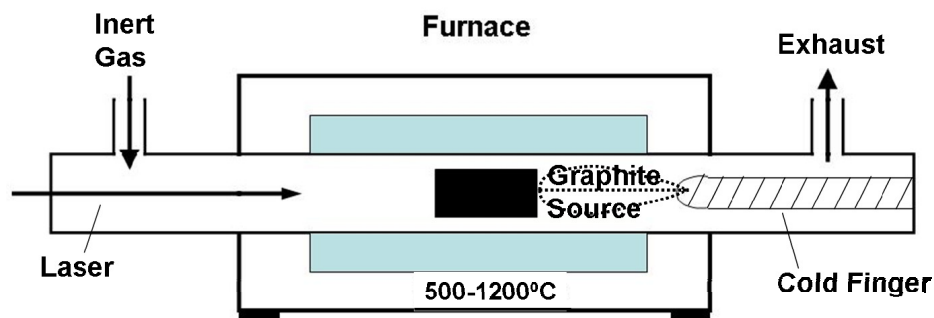


Figure 1-6. Laser ablation apparatus.

1.3.3. Thermal Synthesis

Thermal synthesis relies only on thermal energy, rather than plasma or laser energy, and is achieved by catalytic breakage of carbon sources and deposition of CNTs on catalyst species such as Fe, Ni, and Co. The temperature of the reaction is rarely over 1200 °C, normally between 600 °C and 1100 °C. CVD, high-pressure carbon monoxide (HiPco) and flame synthesis are considered as

thermal CNT synthesis methods [7]. Thermal synthesis methods are simple, efficient and highly controllable, which has attracted great attention during the last two decades.

1.3.3.1. Chemical vapor deposition

The concept of decomposing hydrocarbons over catalyst, referred to as CVD, is not a new idea. It has been used for many years to produce carbon fibers [62] before it was firstly used to produce MWCNTs by Endo et al. in 1993 [63], and to produce SWCNTs by Dai et al. in 1996 [64]. Since then, the growth of CNTs by CVD has been extensively investigated and has progressed at an amazing rate. The setup of CVD is very simple as shown in Figure 1-7. Carbon precursors, such as hydrocarbon gases, CO, and ferrocene ($\text{Fe}(\text{C}_5\text{H}_5)_2$), flow over the pre-patterned transitional-metal catalyst nanoparticles which sit on the substrate at a medium temperature (600 °C to 900 °C), and react with the nanoparticles to produce CNTs. However, technically and theoretically, CVD is not a simple process to grow CNTs because it involves many variables that are needed to be carefully controlled simultaneously, such as heat rate, pretreatment conditions, reaction gas ratios, etc. A slight change in any one of them would induce substantial variation of the final product of CNTs. Over a decade of efforts, CVD for CNT growth has evolved into various forms, including thermal CVD (or conventional CVD) [13, 65], water-assisted CVD [25, 66], floating catalyst CVD [67, 68], alcohol CVD

[69]; and some generalized CVD methods with the combination of other forms of energy, such as plasma-enhanced CVD [70, 71], microwave plasma CVD [72], etc.

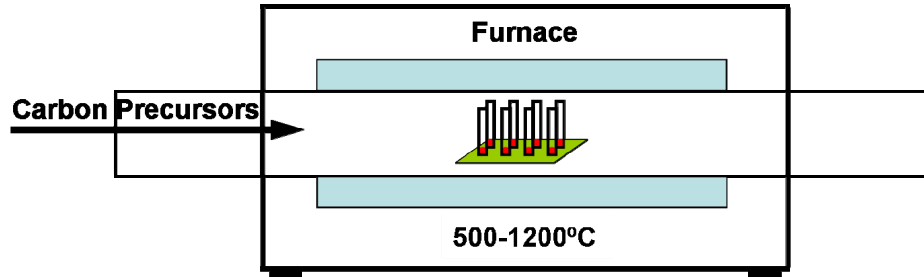


Figure 1-7. Schematic of a conventional CVD furnace.

CVD for CNT growth exhibits great advantages, including low temperatures, possibility of mass production, selective and large-area deposition, and flexibility of process control. The pioneer work of growing long CNTs was reported by Kim et al. [73] in 2002, where up to 400 μm long CNTs were obtained from CVD growth using ferritin-derived Fe catalyst particles under the environment of $\text{CH}_4/\text{C}_2\text{H}_4/\text{H}_2$ mixed gases at 900 $^\circ\text{C}$. In 2003, Huang et al. [74] reported millimeter-long, horizontally aligned growth of SWCNTs on large areas of silicon oxide surfaces by the CVD method. This method involves rapidly inserting a pre-patterned sample of catalyst (monodispersed Fe/Mo nanoparticles) from room temperature to a hot furnace at 900 $^\circ\text{C}$. The catalyst particles lift off the substrate surface and grow along the gas flow direction. 2D nanotube network with

controlled geometry were easily fabricated in their work. This is a major step toward controlling the arrangement of SWCNTs for the fabrication of nanotube devices. Later in 2004, a record length of 4 cm long SWCNTs was produced by Zheng et al. at Los Alamos National Laboratory using ethanol CVD method [75]. The length was actually limited by the substrate size. Thus, by optimizing the reaction gases, catalyst, and temperature, CNTs may potentially to grow to any desired length.

The advantages rendered by CVD are specially manifested in one of its product forms, CNT arrays. In addition, vertically-aligned CNTAs grown on flat substrates offer an ideal platform for studying the mechanisms and kinetics of CNT growth. The growth mechanism of CNTs from the catalyst particles by CVD will be reviewed in Section 1.4 and the growth kinetics of CNTA growth will be reviewed in Section 1.5.

1.3.3.2. High-pressure carbon monoxide synthesis (HiPco)

HiPco process became one of the most important methods to produce SWCNTs in late 1990s, because of its capability of synthesizing high-quality, narrow-diameter distribution SWCNTs in gram to kilogram quantities [76, 77]. The setup of the equipment is based on that of traditional CVD but a metal catalyst is added by the injection of metal-organic compounds, e.g., $\text{Fe}(\text{C}_5\text{H}_5)_2$, $\text{Fe}(\text{CO})_5$, or $\text{Ni}(\text{CO})_5$, and

formation of the catalyst particles in the vapor phase, as shown in Figure 1-8. CO gas flows together with metal-organic compounds into the reactor and SWCNTs are deposited by the disproportionation of CO by the nanometer-size catalyst particles. SWCNTs made by this technique also need post-purification treatment. However, the well-developed purification steps can produce the cleaned SWCNTs with little sidewall damage, as well as around 1% Fe content and 70% yield of SWCNTs [78]. The HiPco SWCNTs have been widely investigated in the last decade because the post-growth treatments (functionalization, microwave irradiation, etc.) of HiPco SWCNTs have been found to be possible to tune SWCNTs diameter [79], chirality [30], and to realize the enrichment of semiconducting SWCNTs [80].

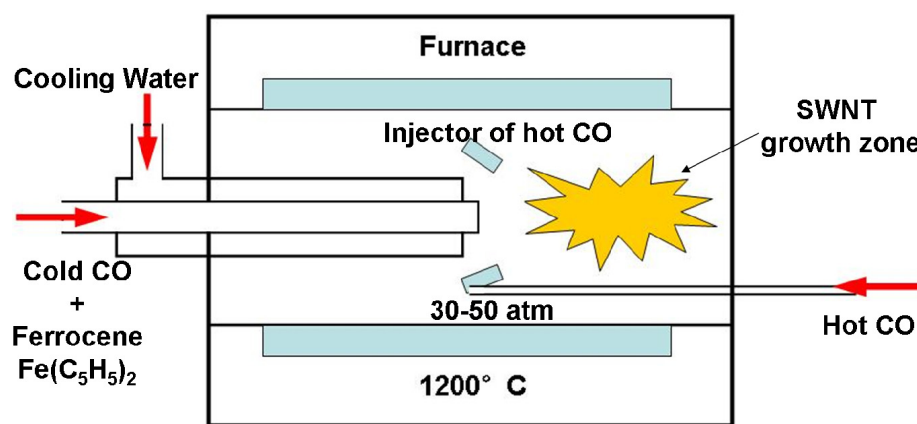


Figure 1-8. Schematic of a HiPco furnace.

1.3.3.3 Flame synthesis

Flames have been shown to produce MWCNTs [81] and SWCNTs [82]. Although

the current yield of this technique is low, it is attractive as it is extremely cheap and simple to produce CNTs.

1.4. Growth Mechanism of Carbon Nanotubes

1.4.1. Carbon Nanotube Growth from Catalyst

The growth of CNTs by CVD methods can be briefly described using the following three steps including: 1) decomposition of carbon sources on the catalyst; 2) diffusion of C atoms to the precipitation sites; 3) extrusion of graphene walls, as shown in Figure 1-9 [83]. However, the detailed process is not as simple as the steps listed above, which encompasses a series of phenomena that are unclear till now. The complexity of investigating the CNT growth mechanism arises from the nanometer size of catalyst particles and CNTs, the fast kinetics of CNT nucleation and growth from catalyst particles, as well as a considerable number of variables that can affect CNT growth. To simplify the discussion of CNT growth from a catalyst, almost all the studies assume that one particle leads to only one nanotube during a single growth step. An alternative situation is the formation of bundles of CNTs from a large catalyst particle [84], which rarely occurs and can be avoided in most synthesis methods. This section will review only the growth mechanism of individual CNTs from catalyst. The CNTA growth mechanism and kinetics will be dealt with in the next section.

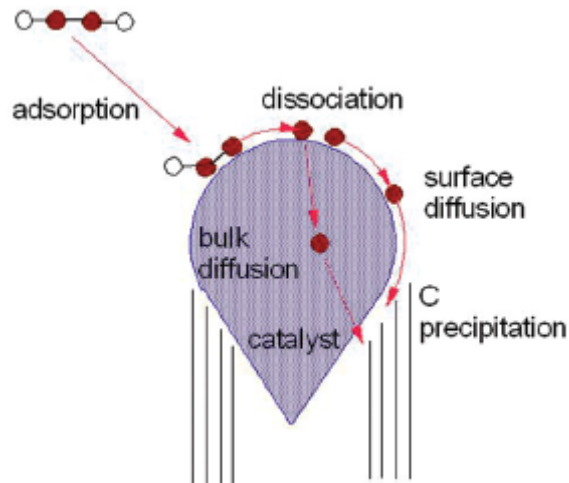


Figure 1-9. Schematic of CNT growth process [83].

CNT growth can be classified into two basic types, the gas phase growth and the substrate growth, depending on the location of the catalyst. In gas phase growth, the catalyst forms and the nanotube grows in the mid-air, as the case in arc discharge, laser ablation, HiPco, and floating catalyst CVD methods. In substrate growth, however, catalyst particles are deposited either on a flat substrate, or on a high surface area porous substrate (e.g., silica [85] or alumina [86]). In both growth pathways, the underlying chemistry for the formation of nanotubes from nanoparticles is similar. In addition, depending on the carbon atom diffusion route, CNT growth from catalysts can be further classified into surface carbon diffusion and bulk carbon diffusion, as shown in Figure 1-9. In surface carbon diffusion, the “cracked” carbon diffuses around the catalyst surface, and CNT graphene walls nucleate on the side of the catalyst particle. In bulk carbon diffusion, the carbon

source is “cracked” on the surface of the catalyst particles, similar to surface carbon diffusion; however, the catalyst particle dissolves the carbon atoms until it reaches the saturation state. For example, Fe carbide forms from Fe catalyst particles before CNT nucleation. Further C deposition from the gas phase makes catalyst particles over-saturated with C, and thus C atoms precipitate in the form of graphene walls from the outer surface [7, 83].

In substrate growth, once the nanotube starts to grow by either surface or bulk carbon diffusion, further growth will proceed by one of the two growth modes: tip (or top) growth mode and root (or base, bottom) growth mode. These two CNT growth modes were first proposed by Sinnott et al. [87], as schematically shown in Figure 1-10. In root growth mode, the catalyst particles attach to the surface of the substrate during CNT growth. In tip growth mode, the catalyst particles detach from the substrate and move at the head of growing CNTs. Whether CNTs will undergo tip or root growth mode largely depend on the adhesion between the nanoparticles and the substrate [88]. Strong adhesion favors root growth mode, while weak adhesion promotes tip growth mode. The strength of the adhesion can be adjusted by using different buffer layers (Al_2O_3 or SiO_2 , etc.) between catalyst particles and the substrate [89]. This adhesion strength is also related to the growth conditions and catalyst particle size. Recently, Gohier et al. [90] reported a switch of growth modes from tip to root growth with decreasing catalyst particle

size. Furthermore, for SWCNT growth, root growth mode is considered as the dominant mode. For MWCNT growth, both growth modes could be dominant depending on the growth conditions. Recent studies, including our study introduced in Chapter 3, confirm that both mechanisms coexist in the MWCNT array growth by CVD methods [91, 92] but only one mode is predominant. Further investigation into how to manipulate growth conditions and catalysts to favor one or the other growth mode continues to be an important topic of research [7].

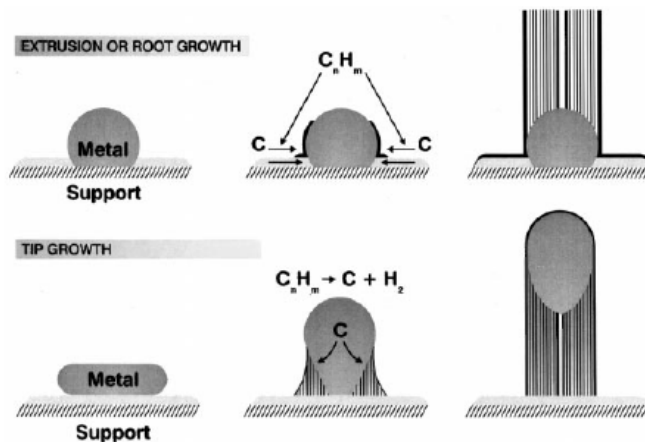


Figure 1-10. Schematics of root and tip growth modes for CNTs [87].

Whether catalyst particles maintain the metallic state or transform to the carbide phase has long been controversial, but the latest investigations suggest that the latter case is more plausible, especially for Fe catalyst particles [93, 94]. In particular, Yoshida et al. [93] investigated the state of Fe catalyst particles for both

SWCNT and MWCNT growth with root growth mode by environmental TEM. It was clearly shown that Fe particles are neither pure iron α (bcc) nor γ (fcc) structures but the iron carbide structure, that is, cementite phase, Fe_3C . As such, bulk carbon diffusion was suggested. Moreover, in their study, it was also found by *in-situ* HRTEM that iron carbide nanoparticles fluctuate structurally during CNT nucleation and growth. The structural fluctuation of catalyst particles could give the optimized atomistic structure that leads to the nucleation of CNTs. However, the reason for the structural fluctuation of catalyst particles during CNT growth is still unknown.

Recent studies also confirm that Fe and Ni catalyst particles act as “liquid-like” nanoparticles during CNT nucleation and growth. The deformation of Fe or Ni catalyst particles during MWCNT nucleation has been observed by many researchers using *in-situ* characterization techniques [95, 96]. Hence, vapor-liquid-solid (VLS) growth mechanism has been elucidated for CNT growth by CVD methods, with catalyst particles being in the quasi-liquid state, not exactly liquid state.

1.4.2. Deactivation Mechanism of Carbon Nanotube Growth

Understanding the deactivation mechanism of CNT growth could provide

experimental solutions to control the length and purity of CNTs. Theoretically, CNTs should grow continuously as long as catalyst particles are exposed to carbon sources. However, there are competing reactions at the catalyst sites, such as precipitation of the graphene wall for CNT growth, formation of graphitic caps around the catalyst, and deposition of amorphous carbon on the catalyst. The latter two could cut off the catalyst particles from carbon sources and deactivate the catalyst. This understanding is very useful, because it has inspired researchers to add oxidation agents into the growth environment to increase the catalyst activity and to extend the catalyst lifetime. Previous studies considered amorphous carbon as the major by-product to deactivate catalyst particles [25]. Recently, more and more indirect evidence, including our results introduced in Chapter 3 and 4, show that graphitic carbon is a primary reason to deactivate catalyst particles [97]. Additionally, in the case of root growth mode, the diffusion of carbon sources through the CNT arrays to catalyst particle sites at the bottom could be another limiting factor that inhibits the CNT growth [98, 99].

1.5. Carbon Nanotube Arrays

1.5.1. Development of Carbon Nanotube Arrays

A vertically-aligned CNTA is a highly ordered macroscopic form of CNTs, the structure of which can be clearly shown by a scanning electron microscopy (SEM)

image and a schematic illustration in Figure 1-11. The growth of CNTAs using the CVD method was first achieved by Li et al. [100] in 1996. Since then, CNTAs have attracted great attention, because, as mentioned previously, they inherit high conductivity and good chemical stability of CNTs, and also possess their own characteristics owing to their well-organized structure and ability to pattern. Fan et al. [13] reported good electron emission property for a patterned CNTA making it a promising candidate for scaled-up functional devices. In 2004, the excellent characteristics of CNTAs were entirely unveiled by Hata et al. who reported the super-growth of millimeter-long SWCNT arrays by water-assisted CVD method [25]. In their study, a SWCNT array could grow over millimeter scale at a fast growth rate, 2.5 mm in 10 min, indicating the possibility of mass and cost effective production of SWCNTs. The SWCNTs produced by this method also have high purity, high aspect ratio, and high surface area. The SWCNT/catalyst weight ratio is over 50,000% and carbon purity 99.98%, which saves the cost of post-growth purification. The surface area is 1000 m²/g for closed-end SWCNT arrays [24] and 2240 m²/g for open-end SWCNT arrays [101], which is much higher than that measured for closed HiPco samples (520 m²/g) [102]. Moreover, it is a simple CVD setup, only adding a small amount of water in the conventional CVD system. Since then, the growth of millimeter-long CNTA by water-assisted CVD has been the focus of research. Large-diameter DWCNT arrays were synthesized by this method as one of the lightest man-made solids (0.015±0.002

g/cm^3) that have been reported [23]. 4-mm long MWCNT arrays were produced by this method to increase the adjustable range of CNT array height. Controllable CNT diameters [23, 27] and wall numbers [28, 29] have also been realized to some extent using water-assisted CVD. Recently, Yasuda et al. reported centimeter-scale SWCNT array growth using this method by changing the gas flow direction [103]. Despite this amazing progress for water-assisted CVD method, the role of water has not been fully understood.

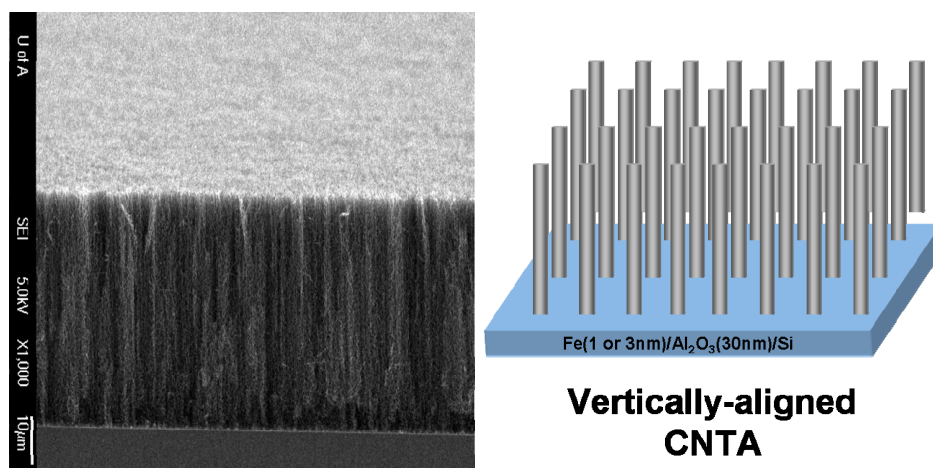


Figure 1-11. A SEM image and a schematic illustration of vertically-aligned CNTA.

Conventional CVD, as well as alcohol CVD [104] and floating catalyst [67, 68, 91] CVD, were also used to grow millimeter-long CNTAs [65, 105] on substrates with finely tuned catalyst particles,. Alcohol CVD has the same mechanism as water-assisted CVD method, and floating catalyst CVD needs substantial

modification of the CVD setup. Therefore, in this thesis, CNTA growth by conventional CVD and water-assisted CVD methods were explored only.

1.5.2. Growth Mechanism and Growth Kinetics of Carbon Nanotube Arrays

The mechanism of individual CNT growth is also applicable to that of CNTA growth, except that both catalyst particles and their patterns must be controlled in the latter. As shown in Figure 1-12, the growth process using conventional CVD can be divided into four steps, heating, pretreatment (activation), CNTA growth, and cooling. For water-assisted CVD, a small amount of water is added during the process. The heating and pretreatment steps are very important for CNTA growth, because these two steps determine the dimension of the catalyst particles and their distribution. During the heating and the subsequent pretreatment stages, the pre-deposited catalyst films (e.g., by sputtering or e-beam evaporation) break down to highly compact nanoparticles. However, over-pretreatment leads to the growth of nanoparticles due to Ostwald ripening effect [106, 107]. Heating rate, pretreatment time, H_2 and C_2H_4 gas flow rates, and water amount (for water-assisted CVD) are all important parameters. However, the understanding of their effects is still empirical. Higher heating rate is believed to induce smaller and denser particles. Zhang et al. stated that pretreatment time and H_2 flow rate greatly influence catalyst morphology and activity [106]. In the CNTA growth step, H_2

not only facilitates molecular transformation such as carbon ring closure and five- to six-member ring conversion, but also etches amorphous carbon and CNTs [108, 109]. C_2H_4 gas ratio determines carbon activity in the environment [110]. Water is considered as a weak oxidizer to burn amorphous and/or graphitic carbon that deactivates the catalyst particles [25, 97]. Recent investigation of the role of water shows that water inhibits Ostwald ripening due to the ability of oxygen and hydroxyl species to reduce diffusion rates of catalyst atoms [111]. Interestingly, it seems that any oxidation agent could have the same effect as water does, such as air [112] and oxygen-containing aromatics [113], etc. In this thesis, all these effects were systematically studied in order to improve the reproducibility of millimeter-long CNTA growth.

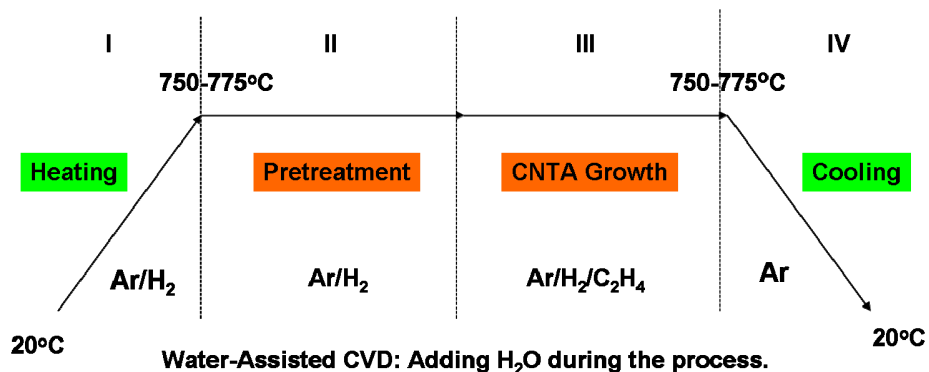


Figure 1-12. The detailed growth procedure for CNTAs by conventional CVD and water-assisted CVD methods.

The growth kinetics of SWCNT arrays under different ratios of reaction gases in water-assisted CVD has been investigated by Iijima's group [114]. It was found that the growth of SWCNT array is very fast in the initial 10 min but levels off quickly afterwards, which agrees well with the radioactive decay model. Recently, the accumulation process of carbonaceous impurities resulting from the pyrolytic deposition on the CNT arrays has also been exclusively studied [115]. The growth kinetics of MWCNT arrays has also been investigated. Meshot et al. investigated the effect of temperature on the growth kinetics of MWCNT array using conventional CVD method with decoupled thermal treatment of precursor and catalyst [116]. Zhu et al. invented a stacking-structure of CNTA growth to facilitate investigating CNTA growth kinetics [98, 117]. Xiang et al. studied the deactivation mechanism of MWCNT array growth by feedstock gas diffusion control [99]. However, the growth kinetics of MWCNT arrays has not been clearly elucidated either in conventional CVD or in water-assisted CVD. As a clear understanding of the growth mechanism and growth kinetics of CNT arrays would serve as a guide to the manipulation of CNT structures, detailed investigation is required for MWCNT array growth.

1.5.3. Barriers to Application

Despite the CNTA holds great potential for applications on field-emission emitters

[13, 32], electrochemical and biosensors [33, 34], supercapacitors [24], millimeter-long CNTA based applications are limited by two problems. Firstly, fabrication of CNTA based devices can either damage the tubes or destroy the aligned structures of CNTAs [24]. Secondly, CNTAs are hydrophobic [118], which prevents the insertion of aqueous solution into the inner porous CNTAs and the usage of the whole surface area of CNTAs, although this property has been used to separate oil and water [119]. Recently, Hata et al. developed a liquid-induced collapse method to prevent the cracking of millimeter-long SWCNT arrays [24]. The wet process in their study can be used to fabricate CNT arrays with versatile structures potentially to be used in many applications [120]. Nevertheless, the hydrophobic state of CNTAs is still a problem that requires enormous efforts.

1.6. Electrochemical Supercapacitors (ESs)

ESs are promising power sources that can be fully charged or discharged in seconds. As a result, high power density (10^3 to 10^4 W/kg) can be achieved for ESs, but their energy density (5-10 Wh/kg) is much lower than that for battery devices (25 to 50 Wh/kg) [121]. Hence, they play a significant role in complementing batteries in the energy storage field, such as portable devices, automotive applications, renewable energy production, and aerospace systems

[122-124]. Recently, the US Department of Energy assigned equal importance to supercapacitors and batteries for future energy storage systems [125]. Depending on the charge-storage mechanism, ESs are basically divided into two types: electrochemical double layer capacitors (EDLCs) and pseudo-capacitors.

1.6.1. Electrochemical Double Layer Capacitors

EDLCs electrostatically store the charge using reversible adsorption of ions of the electrolyte onto active materials; as a consequence, no Faradaic reaction occurs at EDLC electrodes. In EDLCs, charge separation occurs at the electrode-electrolyte interface with an inner layer (Helmholtz or Stern layer) and an outer diffusion layer. The double layer capacitance can be described by equation 1-4:

$$C = \frac{\epsilon_r \epsilon_0 A}{d} \quad (1-4)$$

where ϵ_r is the electrolyte dielectric constant, ϵ_0 is the dielectric constant of the vacuum, d is the effective thickness of the double layer, and A is electrode surface area. The active materials used in EDLCs should be electrochemically stable and have high accessible specific surface area (SSA). Hence, carbon materials (activated carbon [2, 3, 126], carbon onions and nanohorns [4, 5], CNTs and CNTAs [127], etc.) are perfect candidates for EDLCs. In fact, activated carbons have been widely used as electrode materials for ESs, and the detailed overview of carbon materials in supercapacitors is available in a recent paper

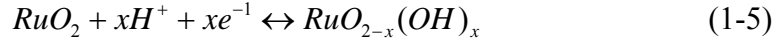
[128]. CNTs and CNTAs have also been attempted in supercapacitors. Untreated (as-grown) CNTs normally have lower capacitance, less than 50 F/g, than that for activated CNTs, between 50 and 100 F/g [129-132]. CNTAs have superior power capacitor performance [133]; however, their capacitance is as low as 10 to 25 F/g [134, 135] and very sensitive to their heights [136]. Recently, Futaba et al. made a SWCNT solid sheet from a millimeter-long SWCNT array, and found its capacitance to be 80 F/g in an ionic liquid electrolyte [24].

1.6.2. Pseudo-capacitors

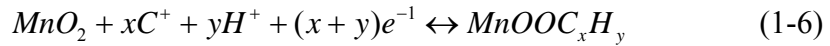
In contrast to EDLCs, pseudo-capacitors involve fast, reversible Faradiac reactions at the surface and in the bulk of active materials, which could be metal oxides, such as TiO_2 [137], SnO_2 [138], NiO [139], RuO_2 [140, 141], MnO_x [142, 143], etc, as well as conducting polymers [144, 145]. The specific pseudo-capacitance exceeds that of carbon materials, but suffers from a lack of stability during cycling, similar to batteries.

Ruthenium oxides have been widely investigated because they have high specific capacitance from 200 to 1000 F/g [146, 147]. This high specific capacitance originates from their relatively high conductivity and three distinct oxidation states accessible within 1.2 V. The pseudo-capacitive behaviour of RuO_2 in acid

solution follows the equation below [148]:



where $0 \leq x \leq 2$. However, Ru oxides are scarce and very expensive. Manganese oxides, on the other hand, are characterized by their low cost, abundance in nature, environmental friendliness [149, 150], and high capacitance. The theoretical capacitance of manganese oxides can reach 1100 C/g from Mn(IV) to Mn(III). The charge storage mechanisms are based on surface Faradaic reaction involving the surface adsorption of electrolyte cations ($C^+ = Li^+$, Na^+ and K^+) [151, 152] as well as proton incorporation [148] in the manganese oxides, and bulk Faradaic reactions involving electrolyte cations and proton intercalation and deintercalation in the bulk of manganese oxides [152, 153]. The combined Faradaic reaction can be described as [148]:



The specific capacitance of MnO_2 was reported to be as high as 600 F/g for nanometer thick thin films [154, 155] and 150 F/g for micro-powder and micrometer-thick films [156, 157] in neutral aqueous electrolyte. In our previous reports [158-160], an anodic electrodeposition method has been used to deposit micrometer-thick MnO_2 coatings with different crystal structures and different defect chemistry (cation distributions and oxidation states). Their specific capacitances were found to be in the range of 100 to 250 F/g. In order to increase

materials utilization, direct deposition of manganese oxides on a carbon host, such as active carbon and CNTs [161, 162], carbon nanofoams [163], and templated mesoporous carbon [164], has also been widely studied. Carbon-supported MnO₂ nanorods as a composite electrode gave a specific capacitance of 165 F/g while MnO₂ gave a higher value of 458 F/g [165]. Long et al. [163] successfully electroless deposited a 20 nm pseudo-capacitive layer of MnO₂ on a porous carbon nanofoam. As a result, exceptionally high area-normalized capacitance and volumetric capacitance were obtained, 1.5 F/cm² and 90 F/cm³, respectively. Although much research has been conducted to deposit manganese oxides on treated (activated) CNTs [129], no method has been reported to fabricate millimeter-long CNTA as an electrode with manganese oxides well dispersed in it. Zhang et al. [166] has reported a potentiodynamic electrodeposition method, but it was only able to deposit ~100 nm diameter manganese oxide nanoflowers within 35 μm thick CNTAs.

As a transition metal, manganese have many stable valences, such as +2, +3, +4; and thus, a variety of stable oxides can exist, e.g., MnO, Mn₃O₄, Mn₂O₃, MnO₂. In addition, MnO₂ itself also have many polymorphs, α, β, γ, δ, ε, and η-MnO₂. A detailed review of the crystal structure of different manganese oxides, and their electrochemical synthesis methods has been provided by Weifeng Wei in his Ph. D. thesis [167]. The stability of these manganese oxides is also quite different

[168]. At higher temperatures, other forms of manganese oxides transform to Mn_3O_4 , which is the most thermodynamically stable form of the manganese oxides. However, Mn_3O_4 is a low-specific capacitance material (40 to 200 F/g [169-171]) compared with MnO_2 [170].

1.7. Motivation

The initial project of my Ph.D. studies started from developing a high temperature corrosion resistant coating that can be used in industry, e.g., ethylene production industry, to prevent materials degradation, such as carburization, coke formation and metal dusting, which costs \$2 billion in losses per year alone for ethylene production [172]. A detailed review of the high temperature corrosion and protection has been presented by Haifeng Liu in his Ph. D. thesis [173]. A novel Ni/Cu-Al composite coating was developed by electrodeposition and tested in the carburization, coke formation and metal dusting environment. Electrodeposition was used because it offers high flexibility in controlling the morphology, chemistry, crystal structure, and defects, as well as it is a cost-effective method. The detailed information regarding the electrodeposition process for nanocrystalline Ni/Cu coatings and nanocrystalline Ni/Cu matrix with Al particle composite coatings, as well as their electrochemical deposition mechanisms also contribute to part of my Ph. D. work; and thus, has been included in the thesis as

Appendix I and II.

During the initial project, the substantial catalytic formation of CNTs for the element of Fe in the alloys were found during coke formation and metal dusting processes, which encouraged us to go in a different direction, that is, synthesizing CNTs based on the mechanism of coke formation. In this thesis, millimeter-long vertically-aligned CNTAs were controllably produced in our lab using Fe as a catalyst, and their growth mechanism and kinetics were also elucidated. Furthermore, electrochemical supercapacitors are considered as promising power sources that complement batteries in the energy storage field, as mentioned in the above sections. The previous work of anodic electrodeposition of MnO₂ coatings for their potential usage in ESs has also been extensively investigated in our group (collaboration with Dr. Douglas Ivey's group). Inspired by these two considerations, the application of millimeter-long CNTA on ESs were, for the first time, explored by decorating millimeter-long CNTA with manganese oxides nanoparticles using dip-casting and anodic-pulse electrodeposition methods. Their performance presented in this thesis makes the newly developed composite electrodes very promising to be used in future energy storage systems. The work made in this thesis also open up a new route of utilizing millimeter-long CNTA.

1.8. Overview of Thesis

The aim of this thesis work is to repeatedly synthesize millimeter-long CNTA, to systematically investigate the growth mechanism and growth kinetics of CNTA under different conditions, and to originally explore the usage of millimeter-long CNTA as catalyst support for electrochemical supercapacitors. The results obtained have been grouped and introduced in the chapters as listed below.

Chapter 2: Experimental methods and procedures. This chapter summarizes millimeter-scale CNTA growth techniques, electrochemical measurements for ESs, and materials characterization techniques applied in this thesis.

Chapter 3: Growth of millimeter-scale carbon nanotube arrays by conventional chemical vapor deposition: effect of catalyst particle interspacing. This chapter investigates the significant role of catalyst particle interspacing in influencing CNTA height, CNT diameter and wall number by CCVD method.

Chapter 4: Growth kinetics of millimeter-scale carbon nanotube arrays by chemical vapor deposition in the presence and absence of water: mechanisms in lengthening and thickening stages. In this chapter, the growth kinetics of MWCNT arrays by WACVD and CCVD methods has been systematically investigated, and the mechanisms in the lengthening and thickening stages have

been elucidated. The effects of reaction gases including water, ethylene, and hydrogen on the growth kinetics of CNTAs have also been discussed.

Chapter 5: A novel hydrophilic Mn_3O_4 /millimeter-long carbon nanotube array composite electrode for electrochemical supercapacitors. This chapter provides a new route of changing CNTAs from hydrophobic to hydrophilic while maintaining their alignment. The developed Mn_3O_4 /millimeter-long CNTA composite electrode also presents excellent electrochemical behavior in aqueous electrolyte.

Chapter 6: Anodic pulse-electrodeposition of MnO_2 nanorods within hydrophilic vertically aligned carbon nanotube arrays for supercapacitors. This chapter presents a scalable and cost-effective method to fabricate composite electrodes based on millimeter-long CNTAs. The electrochemical performance of the composite was improved by anodic pulse-electrodepositing $\epsilon\text{-MnO}_2$ nanorods within hydrophilic 0.5 mm-thick Mn_3O_4 decorated CNTAs.

Chapter 7: General conclusions and future recommendations.

Appendix I: Saccharin effects on direct-current electroplating nanocrystalline Ni-Cu alloys. In this appendix, mirror-surface finished nanocrystalline Ni-Cu

alloys have been electrodeposited with the addition of 0.5 g/L saccharin into the electrolyte. The chemistry and structure of the deposited Ni-Cu alloys have been discussed and a mechanism has been proposed to elucidate the saccharin effect.

Appendix II: Electrochemical study of codeposition of Al particle–nanocrystalline Ni/Cu composite coatings. In this appendix, Al metal particles have been codeposited with nanocrystalline Ni-Cu alloys to form composite alloy coatings. The effect of Al metal particles has been investigated by electrochemical tests and their behavior has been proved to be described by Guglielmi's model.

1.9. References

- [1] Korenblit, Y.; Rose, M.; Kockrick, E.; Borchardt, L.; Kvit, A.; Kaskel, S.; Yushin, G. *Acs Nano* **2010**, 4, 1337-1344.
- [2] Shi, H. *Electrochimica Acta* **1996**, 41, 1633-1639.
- [3] Barbieri, O.; Hahn, M.; Herzog, A.; Kotz, R. *Carbon* **2005**, 43, 1303-1310.
- [4] Yang, C. M.; Kim, Y. J.; Endo, M.; Kanoh, H.; Yudasaka, M.; Iijima, S.; Kaneko, K. *Journal of the American Chemical Society* **2007**, 129, 20-21.
- [5] Portet, C.; Chmiola, J.; Gogotsi, Y.; Park, S.; Lian, K. *Electrochimica Acta* **2008**, 53, 7675-7680.
- [6] Iijima, S. *Nature* **1991**, 354, 56-58.
- [7] O'Connell, M. J. in *Carbon nanotubes: properties and applications*, edited by O'Connell, M. J. (CRC Press, Boca Raton, 2006).
- [8] Hernandez, E.; Goze, C.; Bernier, P.; Rubio, A. *Physical Review Letters* **1998**, 80, 4502-4505.
- [9] Lu, J. P. *Physical Review Letters* **1997**, 79, 1297-1300.
- [10] Thostenson, E. T.; Ren, Z. F.; Chou, T. W. *Composites Science and Technology* **2001**, 61, 1899-1912.
- [11] Collins, P. G.; Avouris, P. *Scientific American* **2000**, 283, 62-69.
- [12] Bakshi, S. R.; Lahiri, D.; Agarwal, A. *International Materials Reviews* **2010**, 55, 41-64.
- [13] Fan, S. S.; Chapline, M. G.; Franklin, N. R.; Tomblor, T. W.; Cassell, A. M.;

- Dai, H. J. *Science* **1999**, 283, 512-514.
- [14] Alvi, P. A.; Lal, K. M.; Siddiqui, M. J.; Naqvi, S. A. H. *Indian Journal of Pure & Applied Physics* **2005**, 43, 899-904.
- [15] Wong, S. S.; Joselevich, E.; Woolley, A. T.; Cheung, C. L.; Lieber, C. M. *Nature* **1998**, 394, 52-55.
- [16] Yao, Z.; Postma, H. W. C.; Balents, L.; Dekker, C. *Nature* **1999**, 402, 273-276.
- [17] Pasquier, A. D.; Unalan, H. E.; Kanwal, A.; Miller, S.; Chhowalla, M. *Applied Physics Letters* **2005**, 87, 203511.
- [18] Kaempgen, M.; Chan, C. K.; Ma, J.; Cui, Y.; Gruner, G. *Nano Letters* **2009**, 9, 1872-1876.
- [19] Masarapu, C.; Subramanian, V.; Zhu, H. W.; Wei, B. Q. *Advanced Functional Materials* **2009**, 19, 1008-1014.
- [20] Darkrim, F. L.; Malbrunot, P.; Tartaglia, G. P. *International Journal of Hydrogen Energy* **2002**, 27, 193-202.
- [21] Mahar, B.; Laslau, C.; Yip, R.; Sun, Y. *Ieee Sensors Journal* **2007**, 7, 266-284.
- [22] Liang, F.; Chen, B. *Current Medicinal Chemistry* **2010**, 17, 10-24.
- [23] Ci, L.; Vajtai, R.; Ajayan, P. M. *Journal of Physical Chemistry C* **2007**, 111, 9077-9080.
- [24] Futaba, D. N.; Hata, K.; Yamada, T.; Hiraoka, T.; Hayamizu, Y.; Kakudate, Y.;

- Tanaike, O.; Hatori, H.; Yumura, M.; Iijima, S. *Nature Materials* **2006**, *5*, 987-994.
- [25] Hata, K.; Futaba, D. N.; Mizuno, K.; Namai, T.; Yumura, M.; Iijima, S. *Science* **2004**, *306*, 1362-1364.
- [26] Yun, Y. H.; Shanov, V.; Tu, Y.; Subramaniam, S.; Schulz, M. J. *Journal of Physical Chemistry B* **2006**, *110*, 23920-23925.
- [27] Yamada, T.; Namai, T.; Hata, K.; Futaba, D. N.; Mizuno, K.; Fan, J.; Yudasaka, M.; Yumura, M.; Iijima, S. *Nature Nanotechnology* **2006**, *1*, 131-136.
- [28] Xiong, G. Y.; Wang, D. Z.; Ren, Z. F. *Carbon* **2006**, *44*, 969-973.
- [29] Patole, S. P.; Alegaonkar, P. S.; Shin, H. C.; Yoo, J. B. *Journal of Physics D-Applied Physics* **2008**, *41*, 155311.
- [30] Smalley, R. E.; Li, Y. B.; Moore, V. C.; Price, B. K.; Colorado, R.; Schmidt, H. K.; Hauge, R. H.; Barron, A. R.; Tour, J. M. *Journal of the American Chemical Society* **2006**, *128*, 15824-15829.
- [31] Iwasaki, T.; Robertson, J.; Kawarada, H. *Nano Letters* **2008**, *8*, 886-890.
- [32] Zhu, L. B.; Sun, Y. Y.; Hess, D. W.; Wong, C. P. *Nano Letters* **2006**, *6*, 243-247.
- [33] Lin, Y. H.; Lu, F.; Tu, Y.; Ren, Z. F. *Nano Letters* **2004**, *4*, 191-195.
- [34] Yun, Y. H.; Shanov, V.; Schulz, M. J.; Dong, Z. Y.; Jazieh, A.; Heineman, W. R.; Halsall, H. B.; Wong, D. K. Y.; Bange, A.; Tu, Y.; Subramaniam, S. *Sensors and Actuators B-Chemical* **2006**, *120*, 298-304.

- [35] Kataura, H.; Kumazawa, Y.; Maniwa, Y.; Umezu, I.; Suzuki, S.; Ohtsuka, Y.; Achiba, Y. *Synthetic Metals* **1999**, 103, 2555-2558.
- [36] Rao, A. M.; Richter, E.; Bandow, S.; Chase, B.; Eklund, P. C.; Williams, K. A.; Fang, S.; Subbaswamy, K. R.; Menon, M.; Thess, A.; Smalley, R. E.; Dresselhaus, G.; Dresselhaus, M. S. *Science* **1997**, 275, 187-191.
- [37] Iijima, S.; Ichihashi, T. *Nature* **1993**, 364, 737-737.
- [38] Bethune, D. S.; Kiang, C. H.; Devries, M. S.; Gorman, G.; Savoy, R.; Vazquez, J.; Beyers, R. *Nature* **1993**, 363, 605-607.
- [39] Machida, H.; Honda, S.; Ohkura, S.; Oura, K.; Inakura, H.; Katayama, M. *Japanese Journal of Applied Physics Part 1-Regular Papers Brief Communications & Review Papers* **2006**, 45, 1044-1046.
- [40] Seko, K.; Kinoshita, J.; Saito, Y. *Japanese Journal of Applied Physics Part 2-Letters & Express Letters* **2005**, 44, L743-L745.
- [41] Yu, M. F.; Files, B. S.; Arepalli, S.; Ruoff, R. S. *Physical Review Letters* **2000**, 84, 5552-5555.
- [42] Yu, M. F.; Lourie, O.; Dyer, M. J.; Moloni, K.; Kelly, T. F.; Ruoff, R. S. *Science* **2000**, 287, 637-640.
- [43] Patole, S. P.; Park, J. H.; Lee, T. Y.; Lee, J. H.; Patole, A. S.; Yoo, J. B. *Applied Physics Letters* **2008**, 93, 114101.
- [44] Ebbesen, T. W.; Takada, T. *Carbon* **1995**, 33, 973-978.
- [45] Kosaka, M.; Ebbesen, T. W.; Hiura, H.; Tanigaki, K. *Chemical Physics*

Letters **1995**, 233, 47-51.

[46] Charlier, J. C.; Ebbesen, T. W.; Lambin, P. *Physical Review B* **1996**, 53, 11108-11113.

[47] Shtogun, Y. V.; Woods, L. M. *Journal of Applied Physics* **2010**, 107, 061803.

[48] Shimada, T.; Shirasaki, D.; Kitamura, T. *Physical Review B* **2010**, 81, 035401.

[49] Okada, S. *Chemical Physics Letters* **2007**, 447, 263-267.

[50] Farhat, S.; de La Chapelle, M. L.; Loiseau, A.; Scott, C. D.; Lefrant, S.; Journet, C.; Bernier, P. *Journal of Chemical Physics* **2001**, 115, 6752-6759.

[51] Waldorff, E. I.; Waas, A. M.; Friedmann, P. P.; Keidar, M. *Journal of Applied Physics* **2004**, 95, 2749-2754.

[52] Journet, C.; Maser, W. K.; Bernier, P.; Loiseau, A.; delaChapelle, M. L.; Lefrant, S.; Deniard, P.; Lee, R.; Fischer, J. E. *Nature* **1997**, 388, 756-758.

[53] Journet, C.; Bernier, P. *Applied Physics a-Materials Science & Processing* **1998**, 67, 1-9.

[54] Guo, T.; Nikolaev, P.; Thess, A.; Colbert, D. T.; Smalley, R. E. *Chemical Physics Letters* **1995**, 243, 49-54.

[55] Yudasaka, M.; Yamada, R.; Sensui, N.; Wilkins, T.; Ichihashi, T.; Iijima, S. *Journal of Physical Chemistry B* **1999**, 103, 6224-6229.

[56] Maser, W. K.; Munoz, E.; Benito, A. M.; Martinez, M. T.; de la Fuente, G. F.; Maniette, Y.; Anglaret, E.; Sauvajol, J. L. *Chemical Physics Letters* **1998**, 292,

587-593.

[57] Scott, C. D.; Arepalli, S.; Nikolaev, P.; Smalley, R. E. *Applied Physics a-Materials Science & Processing* **2001**, 72, 573-580.

[58] Qin, L. C.; Iijima, S. *Chemical Physics Letters* **1997**, 269, 65-71.

[59] Zhang, H.; Chen, K.; He, Y.; Zhu, Y.; Chen, Y.; Wu, C.; Wang, J.; Liao, J. H.; Liu, S. H. *Journal of Physics and Chemistry of Solids* **2001**, 62, 2007-2010.

[60] Munoz, E.; Maser, W. K.; Benito, A. M.; Martinez, M. T.; de la Fuente, G. F.; Maniette, Y.; Righi, A.; Anglaret, E.; Sauvajol, J. L. *Carbon* **2000**, 38, 1445-1451.

[61] Baddour, C.; Briens, C. *International Journal of Chemical Reactor Engineering* **2005**, 3, Review R3.

[62] Baker, R. T. K. *Carbon* **1989**, 27, 315-323.

[63] Endo, M.; Takeuchi, K.; Igarashi, S.; Kobori, K.; Shiraishi, M.; Kroto, H. W. *Journal of Physics and Chemistry of Solids* **1993**, 54, 1841-1848.

[64] Dal, H. J.; Rinzler, A. G.; Nikolaev, P.; Thess, A.; Colbert, D. T.; Smalley, R. E. *Chemical Physics Letters* **1996**, 260, 471-475.

[65] Hart, A. J.; Slocum, A. H. *Journal of Physical Chemistry B* **2006**, 110, 8250-8257.

[66] Li, X. S.; Cao, A. Y.; Jung, Y. J.; Vajtai, R.; Ajayan, P. M. *Nano Letters* **2005**, 5, 1997-2000.

[67] Rao, C. N. R.; Sen, R.; Satishkumar, B. C.; Govindaraj, A. *Chemical Communications* **1998**, 1525-1526.

- [68] Zhang, X. F.; Cao, A. Y.; Wei, B. Q.; Li, Y. H.; Wei, J. Q.; Xu, C. L.; Wu, D. H. *Chemical Physics Letters* **2002**, 362, 285-290.
- [69] Murakami, Y.; Chiashi, S.; Miyauchi, Y.; Hu, M. H.; Ogura, M.; Okubo, T.; Maruyama, S. *Chemical Physics Letters* **2004**, 385, 298-303.
- [70] Ren, Z. F.; Huang, Z. P.; Xu, J. W.; Wang, J. H.; Bush, P.; Siegal, M. P.; Provencio, P. N. *Science* **1998**, 282, 1105-1107.
- [71] Malesevic, A.; Vizireanu, S.; Kemps, R.; Vanhulsel, A.; Van Haesendonck, C.; Dinescu, G. *Carbon* **2007**, 45, 2932-2937.
- [72] Zhong, G. F.; Iwasaki, T.; Honda, K.; Furukawa, Y.; Ohdomari, I.; Kawarada, H. *Chemical Vapor Deposition* **2005**, 11, 127-130.
- [73] Kim, W.; Choi, H. C.; Shim, M.; Li, Y. M.; Wang, D. W.; Dai, H. J. *Nano Letters* **2002**, 2, 703-708.
- [74] Huang, S. M.; Cai, X. Y.; Liu, J. *Journal of the American Chemical Society* **2003**, 125, 5636-5637.
- [75] Zheng, L. X.; O'Connell, M. J.; Doorn, S. K.; Liao, X. Z.; Zhao, Y. H.; Akhadov, E. A.; Hoffbauer, M. A.; Roop, B. J.; Jia, Q. X.; Dye, R. C.; Peterson, D. E.; Huang, S. M.; Liu, J.; Zhu, Y. T. *Nature Materials* **2004**, 3, 673-676.
- [76] Bronikowski, M. J.; Willis, P. A.; Colbert, D. T.; Smith, K. A.; Smalley, R. E. *Journal of Vacuum Science & Technology a-Vacuum Surfaces and Films* **2001**, 19, 1800-1805.
- [77] Nikolaev, P.; Bronikowski, M. J.; Bradley, R. K.; Rohmund, F.; Colbert, D. T.;

- Smith, K. A.; Smalley, R. E. *Chemical Physics Letters* **1999**, 313, 91-97.
- [78] Xu, Y. Q.; Peng, H. Q.; Hauge, R. H.; Smalley, R. E. *Nano Letters* **2005**, 5, 163-168.
- [79] Fernando, K. A. S.; Lin, Y.; Wang, W.; Cao, L.; Mezziani, M. J.; Wang, X.; Veca, M. L.; Zhang, P. Y.; Quinn, R. A.; Allard, L. F.; Sun, Y. P. *Journal of Physical Chemistry C* **2007**, 111, 10254-10259.
- [80] Qiu, H. X.; Maeda, Y.; Akasaka, T. *Journal of the American Chemical Society* **2009**, 131, 16529-16533.
- [81] Richter, H.; Hernadi, K.; Caudano, R.; Fonseca, A.; Migeon, H. N.; Nagy, J. B.; Schneider, S.; Vandooren, J.; VanTiggelen, P. J. *Carbon* **1996**, 34, 427-429.
- [82] Diener, M. D.; Nicholson, N.; Alford, J. M. *Journal of Physical Chemistry B* **2000**, 104, 9615-9620.
- [83] Wirth, C. T.; Zhang, C.; Zhong, G. F.; Hofmann, S.; Robertson, J. *Acs Nano* **2009**, 3, 3560-3566.
- [84] Gavillet, J.; Loiseau, A.; Journet, C.; Willaime, F.; Ducastelle, F.; Charlier, J. *C. Physical Review Letters* **2001**, 87, 275504.
- [85] Kitiyanan, B.; Alvarez, W. E.; Harwell, J. H.; Resasco, D. E. *Chemical Physics Letters* **2000**, 317, 497-503.
- [86] Cassell, A. M.; Raymakers, J. A.; Kong, J.; Dai, H. J. *Journal of Physical Chemistry B* **1999**, 103, 6484-6492.
- [87] Sinnott, S. B.; Andrews, R.; Qian, D.; Rao, A. M.; Mao, Z.; Dickey, E. C.;

- Derbyshire, F. *Chemical Physics Letters* **1999**, 315, 25-30.
- [88] Huang, S. M.; Woodson, M.; Smalley, R.; Liu, J. *Nano Letters* **2004**, 4, 1025-1028.
- [89] Hongo, H.; Nihey, F.; Ichihashi, T.; Ochiai, Y.; Yudasaka, M.; Iijima, S. *Chemical Physics Letters* **2003**, 380, 158-164.
- [90] Gohier, A.; Ewels, C. P.; Minea, T. M.; Djouadi, M. A. *Carbon* **2008**, 46, 1331-1338.
- [91] Zhang, Q.; Zhou, W. P.; Qian, W. Z.; Xiang, R.; Huang, J. Q.; Wang, D. Z.; Wei, F. *Journal of Physical Chemistry C* **2007**, 111, 14638-14643.
- [92] Kunadian, I.; Andrews, R.; Qian, D. L.; Menguc, M. P. *Carbon* **2009**, 47, 384-395.
- [93] Yoshida, H.; Takeda, S.; Uchiyama, T.; Kohno, H.; Homma, Y. *Nano Letters* **2008**, 8, 2082-2086.
- [94] Heresanu, V.; Castro, C.; Cambedouzou, J.; Pinault, M.; Stephan, O.; Reynaud, C.; Mayne-L'Hermite, M.; Launois, P. *Journal of Physical Chemistry C* **2008**, 112, 7371-7378.
- [95] Hofmann, S.; Sharma, R.; Ducati, C.; Du, G.; Mattevi, C.; Cepek, C.; Cantoro, M.; Pisana, S.; Parvez, A.; Cervantes-Sodi, F.; Ferrari, A. C.; Dunin-Borkowski, R.; Lizzit, S.; Petaccia, L.; Goldoni, A.; Robertson, J. *Nano Letters* **2007**, 7, 602-608.
- [96] Helveg, S.; Lopez-Cartes, C.; Sehested, J.; Hansen, P. L.; Clausen, B. S.;

- Rostrup-Nielsen, J. R.; Abild-Pedersen, F.; Norskov, J. K. *Nature* **2004**, 427, 426-429.
- [97] Feng, X. F.; Liu, K.; Xie, X.; Zhou, R. F.; Zhang, L. N.; Li, Q. Q.; Fan, S. S.; Jiang, K. L. *Journal of Physical Chemistry C* **2009**, 113, 9623-9631.
- [98] Zhu, L. B.; Hess, D. W.; Wong, C. P. *Journal of Physical Chemistry B* **2006**, 110, 5445-5449.
- [99] Xiang, R.; Yang, Z.; Zhang, Q.; Luo, G. H.; Qian, W. Z.; Wei, F.; Kadowaki, M.; Einarsson, E.; Maruyama, S. *Journal of Physical Chemistry C* **2008**, 112, 4892-4896.
- [100] Li, W. Z.; Xie, S. S.; Qian, L. X.; Chang, B. H.; Zou, B. S.; Zhou, W. Y.; Zhao, R. A.; Wang, G. *Science* **1996**, 274, 1701-1703.
- [101] Hiraoka, T.; Izadi-Najafabadi, A.; Yamada, T.; Futaba, D. N.; Yasuda, S.; Tanaike, O.; Hatori, H.; Yumura, M.; Iijima, S.; Hata, K. *Advanced Functional Materials* **2010**, 20, 422-428.
- [102] Yang, C. M.; Kaneko, K.; Yudasaka, M.; Iijima, S. *Nano Letters* **2002**, 2, 385-388.
- [103] Yasuda, S.; Futaba, D. N.; Yamada, T.; Satou, J.; Shibuya, A.; Takai, H.; Arakawa, K.; Yumura, M.; Hata, K. *Acs Nano* **2009**, 3, 4164-4170.
- [104] Sugime, H.; Noda, S. *Carbon* **2010**, 48, 2203-2211.
- [105] Kayastha, V. K.; Wu, S.; Moscatello, J.; Yap, Y. K. *Journal of Physical Chemistry C* **2007**, 111, 10158-10161.

- [106] Zhang, H.; Cao, G. P.; Wang, Z. Y.; Yang, Y. S.; Shi, Z. J.; Gu, Z. N. *Journal of Physical Chemistry C* **2008**, 112, 4524-4530.
- [107] Nessim, G. D.; Hart, A. J.; Kim, J. S.; Acquaviva, D.; Oh, J. H.; Morgan, C. D.; Seita, M.; Leib, J. S.; Thompson, C. V. *Nano Letters* **2008**, 8, 3587-3593.
- [108] Frenklach, M.; Ping, J. *Carbon* **2004**, 42, 1209-1212.
- [109] Eres, G.; Kinkhabwala, A. A.; Cui, H. T.; Geohegan, D. B.; Poretzky, A. A.; Lowndes, D. H. *Journal of Physical Chemistry B* **2005**, 109, 16684-16694.
- [110] Zhang, H.; Cao, G. P.; Wang, Z. Y.; Yang, Y. S.; Shi, Z. J.; Gu, Z. N. *Journal of Physical Chemistry C* **2008**, 112, 12706-12709.
- [111] Amama, P. B.; Pint, C. L.; McJilton, L.; Kim, S. M.; Stach, E. A.; Murray, P. T.; Hauge, R. H.; Maruyama, B. *Nano Letters* **2009**, 9, 44-49.
- [112] Li, X. S.; Zhang, X. F.; Ci, L. J.; Shah, R.; Wolfe, C.; Kar, S.; Talapatra, S.; Ajayan, P. M. *Nanotechnology* **2008**, 19, 455609.
- [113] Futaba, D. N.; Goto, J.; Yasuda, S.; Yamada, T.; Yumura, M.; Hata, K. *Journal of the American Chemical Society* **2009**, 131, 15992-15993.
- [114] Futaba, D. N.; Hata, K.; Yamada, T.; Mizuno, K.; Yumura, M.; Iijima, S. *Physical Review Letters* **2005**, 95, 056104.
- [115] Yasuda, S.; Hiraoka, T.; Futaba, D. N.; Yamada, T.; Yumura, M.; Hata, K. *Nano Letters* **2009**, 9, 769-773.
- [116] Meshot, E. R.; Plata, D. L.; Tawfick, S.; Zhang, Y. Y.; Verploegen, E. A.; Hart, A. J. *Acs Nano* **2009**, 3, 2477-2486.

- [117] Zhu, L. B.; Xiu, Y. H.; Hess, D. W.; Wong, C. P. *Nano Letters* **2005**, 5, 2641-2645.
- [118] Lau, K. K. S.; Bico, J.; Teo, K. B. K.; Chhowalla, M.; Amaratunga, G. A. J.; Milne, W. I.; McKinley, G. H.; Gleason, K. K. *Nano Letters* **2003**, 3, 1701-1705.
- [119] Lee, C.; Baik, S. *Carbon* **2010**, 48, 2192-2197.
- [120] Futaba, D. N.; Miyake, K.; Murata, K.; Hayamizu, Y.; Yamada, T.; Sasaki, S.; Yumura, M.; Hata, K. *Nano Letters* **2009**, 9, 3302-3307.
- [121] Burke, A.; Arulepp, M. *Recent developments in carbon-based electrochemical capacitors: status of the technology and future prospects*. in *Electrochemical Society Proceedings*. **2001**, 2001-21, 576-591.
- [122] Kotz, R.; Carlen, M. *Electrochimica Acta* **2000**, 45, 2483-2498.
- [123] Frackowiak, E.; Beguin, F. *Carbon* **2001**, 39, 937-950.
- [124] Miller, J. R.; Burke, A. F. *The Electrochemical Society's Interface* **2008**, 17, 53-57.
- [125] US Department of Energy. *Basic Research Needs for Electrical Energy Storage*. **2007**, www.sc.doe.gov/bes/reports/abstracts.html#EES2007.
- [126] Centeno, T. A.; Stoeckli, F. *Journal of Power Sources* **2006**, 154, 314-320.
- [127] Pan, H.; Li, J. Y.; Feng, Y. P. *Nanoscale Research Letters* **2010**, 5, 654-668.
- [128] Obreja, V. V. N. *Physica E-Low-Dimensional Systems & Nanostructures* **2008**, 40, 2596-2605.
- [129] Ko, J. M.; Kim, K. M. *Materials Chemistry and Physics* **2009**, 114,

837-841.

[130] Frackowiak, E.; Metenier, K.; Bertagna, V.; Beguin, F. *Applied Physics Letters* **2000**, 77, 2421-2423.

[131] Kim, Y. T.; Ito, Y.; Tadai, K.; Mitani, T.; Kim, U. S.; Kim, H. S.; Cho, B. W. *Applied Physics Letters* **2005**, 87, 234106.

[132] Niu, C. M.; Sichel, E. K.; Hoch, R.; Moy, D.; Tennent, H. *Applied Physics Letters* **1997**, 70, 1480-1482.

[133] Honda, Y.; Haramoto, T.; Takeshige, M.; Shiozaki, H.; Kitamura, T.; Ishikawa, M. *Electrochemical and Solid State Letters* **2007**, 10, A106-A110.

[134] Zhang, H.; Cao, G. P.; Yang, Y. S. *Nanotechnology* **2007**, 18, 195607.

[135] Zhang, H.; Cao, G. P.; Yang, Y. S.; Gu, Z. N. *Journal of the Electrochemical Society* **2008**, 155, K19-K22.

[136] Shah, R.; Zhang, X. F.; Talapatra, S. *Nanotechnology* **2009**, 20, 395202.

[137] Brousse, T.; Marchand, R.; Taberna, P. L.; Simon, P. *Journal of Power Sources* **2006**, 158, 571-577.

[138] Selvan, R. K.; Perelshtein, I.; Perkas, N.; Gedanken, A. *Journal of Physical Chemistry C* **2008**, 112, 1825-1830.

[139] Xing, W.; Li, F.; Yan, Z. F.; Lu, G. Q. *Journal of Power Sources* **2004**, 134, 324-330.

[140] Liang, Y. Y.; Li, H. L.; Zhang, X. G. *Journal of Power Sources* **2007**, 173, 599-605.

- [141] Hu, C. C.; Liu, M. J.; Chang, K. H. *Electrochimica Acta* **2008**, 53, 2679-2687.
- [142] Toupin, M.; Brousse, T.; Belanger, D. *Chemistry of Materials* **2002**, 14, 3946-3952.
- [143] Hu, C. C.; Wu, Y. T.; Chang, K. H. *Chemistry of Materials* **2008**, 20, 2890-2894.
- [144] Rudge, A.; Davey, J.; Raistrick, I.; Gottesfeld, S.; Ferraris, J. P. *Journal of Power Sources* **1994**, 47, 89-107.
- [145] Naoi, K.; Suematsu, S.; Manago, A. *Journal of the Electrochemical Society* **2000**, 147, 420-426.
- [146] Sugimoto, W.; Iwata, H.; Yokoshima, K.; Murakami, Y.; Takasu, Y. *Journal of Physical Chemistry B* **2005**, 109, 7330-7338.
- [147] Liu, X. R.; Pickup, P. G. *Journal of Power Sources* **2008**, 176, 410-416.
- [148] Simon, P.; Gogotsi, Y. *Nature Materials* **2008**, 7, 845-854.
- [149] Hu, C. C.; Tsou, T. W. *Journal of Power Sources* **2003**, 115, 179-186.
- [150] Kim, H.; Popov, B. N. *Journal of the Electrochemical Society* **2003**, 150, D56-D62.
- [151] Lee, H. Y.; Goodenough, J. B. *Journal of Solid State Chemistry* **1999**, 144, 220-223.
- [152] Toupin, M.; Brousse, T.; Belanger, D. *Chemistry of Materials* **2004**, 16, 3184-3190.

- [153] Chigane, M.; Ishikawa, M. *Journal of the Electrochemical Society* **2000**, 147, 2246-2251.
- [154] Pang, S. C.; Anderson, M. A.; Chapman, T. W. *Journal of the Electrochemical Society* **2000**, 147, 444-450.
- [155] Chin, S. F.; Pang, S. C.; Anderson, M. A. *Journal of the Electrochemical Society* **2002**, 149, A379-A384.
- [156] Jeong, Y. U.; Manthiram, A. *Journal of the Electrochemical Society* **2002**, 149, A1419-A1422.
- [157] Prasad, K. R.; Miura, N. *Journal of Power Sources* **2004**, 135, 354-360.
- [158] Wei, W. F.; Cui, X. W.; Chen, W. X.; Ivey, D. G. *Journal of Physical Chemistry C* **2008**, 112, 15075-15083.
- [159] Wei, W. F.; Cui, X. W.; Chen, W. X.; Ivey, D. G. *Journal of Power Sources* **2009**, 186, 543-550.
- [160] Wei, W. F.; Cui, X. W.; Chen, W. X.; Ivey, D. G. *Electrochimica Acta* **2009**, 54, 2271-2275.
- [161] Kuo, S. L.; Wu, N. L. *Journal of Power Sources* **2006**, 162, 1437-1443.
- [162] Ma, S. B.; Nam, K. W.; Yoon, W. S.; Yang, X. Q.; Ahn, K. Y.; Oh, K. H.; Kim, K. B. *Journal of Power Sources* **2008**, 178, 483-489.
- [163] Fischer, A. E.; Pettigrew, K. A.; Rolison, D. R.; Stroud, R. M.; Long, J. W. *Nano Letters* **2007**, 7, 281-286.
- [164] Dong, X. P.; Shen, W. H.; Gu, J. L.; Xiong, L. M.; Zhu, Y. F.; Li, Z.; Shi, J.

- L. *Journal of Physical Chemistry B* **2006**, 110, 6015-6019.
- [165] Sharma, R. K.; Oh, H. S.; Shul, Y. G.; Kim, H. *Journal of Power Sources* **2007**, 173, 1024-1028.
- [166] Zhang, H.; Cao, G. P.; Wang, Z. Y.; Yang, Y. S.; Shi, Z. J.; Gu, Z. N. *Nano Letters* **2008**, 8, 2664-2668.
- [167] Wei, W., *Synthesis and properties of nanocrystalline manganese-cobalt oxide coatings prepared by anodic electrodeposition*, Ph.D. Thesis in University of Alberta (Canada), **2009**, 190 pages.
- [168] Malati, M. A. *Chemistry and Industry* **1971**, 17, 446-452.
- [169] Dai, Y.; Wang, K.; Xie, J. Y. *Applied Physics Letters* **2007**, 90, 104102.
- [170] Sharma, R. K.; Oh, H. S.; Shul, Y. G.; Kim, H. *Physica B-Condensed Matter* **2008**, 403, 1763-1769.
- [171] Dubal, D. P.; Dhawale, D. S.; Salunkhe, R. R.; Pawar, S. M.; Fulari, V. J.; Lokhande, C. D. *Journal of Alloys and Compounds* **2009**, 484, 218-221.
- [172] Crabb, C.; Armesto, C. *Chemical Engineering* **1999**, 106, 1-45.
- [173] Liu, H., *Electrodeposited nickel(3) aluminide base intermetallic coatings and their resistance to high temperature degradation in hydrocarbon cracking environments*, Ph.D. Thesis in University of Alberta (Canada), **2006**, 291 pages.

Chapter 2

Experimental Methods and Procedures

2.1. Introduction

The first part of the investigation focused on the growth of millimeter-long carbon nanotube arrays (CNTAs) using chemical vapor deposition (CVD) methods. CNTA growth involves the procedures including Si wafer cleaning, buffer layer and catalyst film deposition, and CNTA growth from the catalyst film by CVD methods. The second part of investigation was aimed at fabricating CNTA based composite electrodes for supercapacitor applications. This investigation involved various electrochemical measurements, e.g., cyclic voltammetry (CV), galvanostatic charge-discharge and potentiostatic electrochemical impedance spectroscopy (EIS). These tests were conducted using a Solartron SI1287 and a Gamry PC4/750 potentiostat/galvanostat under a three-electrode cell configuration. Furthermore, all the investigation required extensive materials characterization using X-ray diffraction (XRD), transmission electron microscopy (TEM), scanning electron microscopy (SEM), energy-dispersive spectroscopy (EDS), X-ray photoelectron spectroscopy (XPS), Auger electron spectroscopy (AES), Raman spectroscopy, contact angle measurement, and Image-Pro[®] Plus. All these experimental methods and the detailed experimental procedure will be briefly reviewed in this chapter, while CNTA-based electrode making will be illustrated in detail in Chapters 5 and 6.

2.2. Carbon Nanotube Array Growth Procedure

2.2.1. Piranha Cleaning of Si Wafers

P-type Si wafers (100) with 4-in. diameter and resistivity of 1-35 Ohm-cm were used as substrates for catalyst films. Before depositing catalyst films, Si wafers were piranha cleaned by dipping the wafers into sulfuric acid (H_2SO_4) and hydrogen peroxide (H_2O_2) solution (volume percentage 3:1) for 15 min. After cleaning, wafers were taken out the piranha solution and thoroughly rinsed in the dump rinser and dried in the spin rinse dryer. Piranha cleaning is aimed at removing organics and metallic contaminations from substrates.

2.2.2. Sputtering

Sputtering is a process where atoms are ejected from a solid material (target) surface by mechanical bombardment of ionized inert gas (plasma) and deposited as a thin film on a substrate, as schematically shown in Figure 2-1. As the most common form of sputtering, magnetron sputtering was used in this thesis work. Powerful magnets that are mounted behind the target generate a strong magnetic field. The electrons are trapped by the increased local density of the magnetic field, and accelerated plasma ions colliding onto the target surface. High deposition rates can be achieved through magnetron sputtering.

Depending on the power supply used, magnetron sputtering can be classified into direct current (DC), pulsed-DC and radiofrequency (RF) magnetron sputtering. In DC magnetron sputtering, a large negative potential is applied to the target to attract plasma ions to form collision cascades. DC magnetron is used to sputter highly conductive materials such as metals, in this case Fe. To deposit dielectric materials, pulsed-DC and RF magnetron sputtering must be used to avoid charge buildup and discontinuous deposition. RF magnetron sputtering can be used to deposit any material, but only at a very slow deposition rate; thus, pulsed-DC magnetron sputtering was applied to deposit the Al_2O_3 buffer layer.

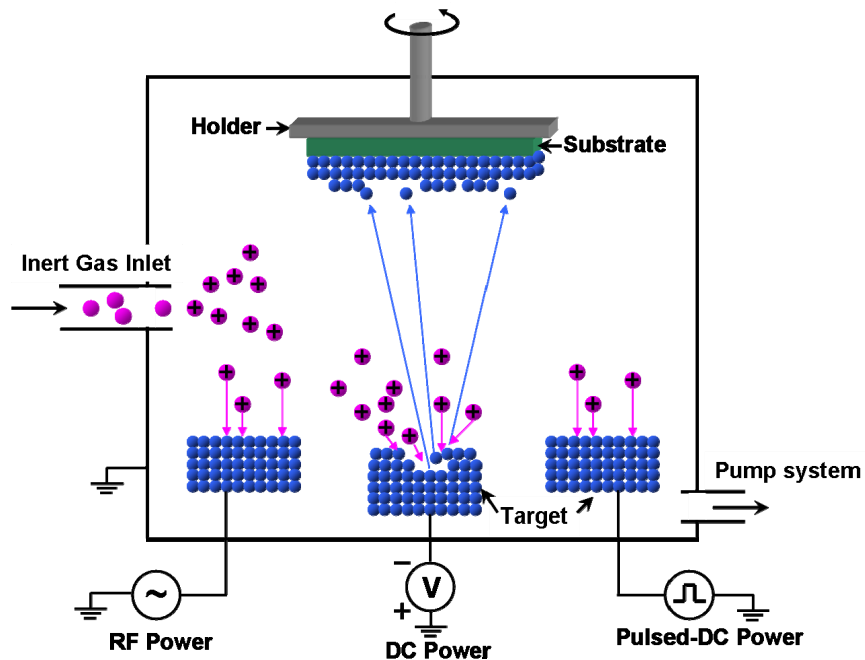


Figure 2-1. Schematic diagram of a sputtering system with DC, pulsed-DC and RF power supplies.

Two layers of thin films were sputtered on the piranha cleaned Si wafers, a 30 nm thick Al_2O_3 buffer layer and 1 or 3 nm thick Fe catalyst films, as shown in Figure 2-2. The deposition rate was calibrated by a quartz crystal monitor under real deposition conditions before any sputtering process. The base pressure was $<1.0 \times 10^{-7}$ Torr (1.33×10^{-5} Pa). Pulsed-DC magnetron sputtering was used to deposit the Al_2O_3 buffer layer at 300°C with a frequency of 20 kHz and a reverse time of 5 μs . During the deposition, the working pressure was controlled at 5 mTorr (0.667 Pa) with the gas flow rates of Ar (99.999%) and O_2 (99.999%) being 0.98 sccm and 0.14 sccm, respectively. The comprehensive investigation of sputtering Al_2O_3 films by pulsed-DC magnetron sputtering can be referred to the report by Sridharan et al. [1]. After cooling down to room temperature, Fe catalyst films with a thickness of 1 nm or 3 nm were then DC magnetron sputtered on top of the buffer layer at a working pressure of 4 mTorr (0.553 Pa). The power was kept at a very low value, 25 W, ensuring the uniform deposition of Fe catalyst films.

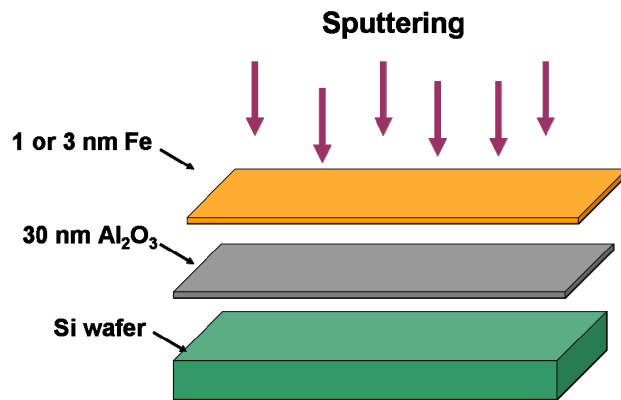


Figure 2-2. Configuration of sputtered wafers.

2.2.3. Carbon Nanotube Array Growth by CVD Method

A 1 m-long, single-zone quartz tube furnace with an inner diameter of 5 in. was used to grow multiwalled CNT (MWCNT) arrays. The setup for conventional CVD (CCVD) and water-assisted CVD (WACVD) is shown in Figure 2-3.

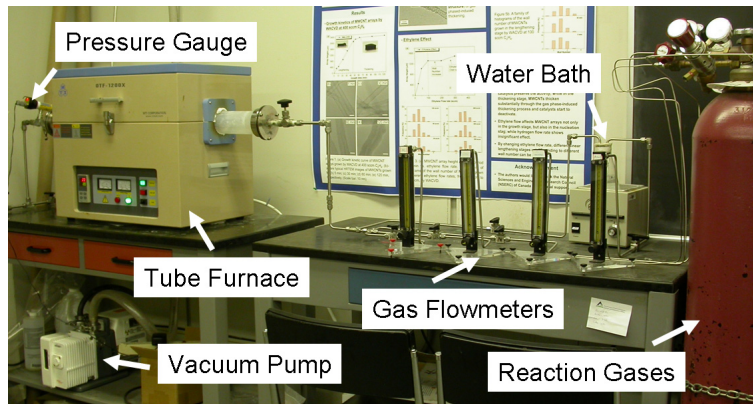


Figure 2-3. Setup for CCVD and WACVD.

MWCNT array growth is very sensitive to reaction conditions and the growth procedure. Only a correct combination of various variables can grow millimeter-long CNTAs. A typical CVD process is as follows: 1) The quartz chamber was evacuated to ≤ 0.1 Torr (13.3 Pa), and purged with Ar gas for at least 0.5 hr. This step purifies the gas components and eliminates the subtle effects that may be caused by gases other than the reaction gases. (2) After Ar purging, the furnace temperature was ramped up to 775°C in 20 min under 200 sccm Ar and 400 sccm H₂ gas flow. The heating rate is essential to grow millimeter-long CNTAs. It must be kept constant for all the tests. (3) The same gas flow in the

heating step was held for a certain period of time, termed as pretreatment time, to achieve the optimum catalyst patterns. (4) 400 sccm C_2H_4 was then flowed into the system for MWCNT array growth. (5) At the end of CNT array growth, the flow of H_2 and C_2H_4 was terminated and the system was purged again with Ar during furnace cooling to below $100^\circ C$. (6) For WACVD, another route of Ar gas bubbling through a water bottle (which was kept at $22^\circ C$) with a flow rate between 5 sccm to 100 sccm was added during catalyst film pretreatment and MWCNT array growth. Adding appropriate amounts of H_2 and H_2O are essential to grow millimeter-long CNTAs.

2.3. Electrochemical Deposition and Measurements

Electrochemical deposition is achieved by delivering an electric current between two electrodes separated by a conductive electrolyte. Both a two-electrode cell and a three-electrode cell can be employed for electrodeposition. The three-electrode cell consists of a working electrode, a counter electrode and a reference electrode. In this work, a platinum plate was used as the counter electrode and a saturated calomel electrode (SCE) was used as the reference electrode. All potentials quoted are with respect to SCE. Electrochemical measurements were investigated with a Solartron SI1287 potentiostat/galvanostat under cyclic voltammetry (CV) and galvanostatic charge-discharge modes, and

with a Gamry PC4/750 potentiostat/galvanostat under CV and potentiostatic electrochemical impedance spectroscopy (EIS) modes, in the aqueous electrolyte, 0.5 M Na₂SO₄. CV curves were recorded between -0.2 and 0.8V (vs. SCE) at various scan rates ranging from 1 mV/s to 200 mV/s. The galvanostatic charge-discharge was conducted in the voltage range of -0.2 and 0.8V (vs. SCE) at various specific currents spanning from 0.5 A/g to 75 A/g. EIS measurements were performed in constant voltage mode (0.4V vs. SCE) by sweeping frequencies from 100 kHz to 0.01 Hz at an amplitude of 5 mV.

2.3.1. Electrodeposition

Electrodeposition is one of the simplest and the most cost-effective film deposition techniques due to its low temperature, easy setup, and precise control of film thickness, composition and crystal structure, etc. A broad category of deposition techniques fall under electrodeposition, such as cathodic and anodic electrodeposition; DC, pulse-current (PC) and CV electrodeposition; electro-codeposition, etc. This variety allows electrodeposition techniques to deposit metals, alloys, oxides, conductive polymer and composite films.

Anodic pulse-electrodeposition was employed in a three-electrode cell to deposit MnO₂ crystals within CNTA scaffold, with CNTA scaffold being the working

electrode, in Chapter 6. Anodic electrodeposition has been attempted to deposit MnO₂ thin films on conductive substrates such as stainless steel [2]. However, in order to deposit crystals within porous materials, PC electrodeposition should be applied to allow the electrolyte diffusion into the inner part of the porous materials.

DC-electrodeposition of Ni-Cu alloy coatings was conducted in a two-electrode cell in Appendix I by carefully controlling the additives in the electrolyte, while Ni/Cu-Al composite coatings were DC-electrodeposited using sediment codeposition of Al particles with Ni-Cu alloys coatings in Appendix II.

2.3.2. Cyclic Voltammetry Curves

Cyclic voltammetry is the most common measurement used to evaluate capacitive behavior of electrodes or cells. As shown in Figure 2-4a, ideal capacitors have symmetric rectangular CV curves with no obvious redox peaks appearing in the tested voltage window. For a single electrode, the specific capacitance (C_{sp}) can be obtained from the CV curve according to the following equation:

$$C_{sp} = \frac{i}{sm} \quad (2-1)$$

where i is the average cathodic or anodic current, s is the potential scan rate, and m is the mass of the electrode. For a symmetric cell (same electrodes for

anode and cathode), the capacitance of the cell will be 1/2 of the single electrode. If counting for the mass of both electrodes, the specific capacitance of the cell will be 1/4 of the single electrode.

The area of the CV curves above and below the x-axis (0 mA) over the scan rate gives the total charge involved during charging and discharging processes, from which the volumetric capacitance (C_V) and area-normalized capacitance (C_A) can be determined based on the equations below:

$$C_V = \frac{q}{U\Delta V} \quad (2-2)$$

$$C_A = \frac{q}{A\Delta V} \quad (2-3)$$

where q is the charge, ΔV is the voltage window, U and A are the volume and apparent area of the electrode (area of current collect), respectively.

2.3.3. Charge-discharge Curves

Ideal capacitors show symmetrical linear galvanostatic charge-discharge curves, as shown in Figure 2-4b. For a single electrode, the specific capacitance (C_{sp}) can also be estimated from the galvanostatic discharge curve according to the following equation:

$$C_{sp} = \frac{I}{m(dV/dt)} \quad (2-4)$$

where I is the applied current, m is the mass of the electrode, and dV/dt is

the slope of the potential drop in the linear region. The sudden potential drop at the beginning of the discharge is normally used to calculate the equivalent series resistance (ESR) [3] including the resistance of electrode and electrolyte and the distributed resistance featured by electrochemical charging process [4].

2.3.4. EIS Measurements

The complex-plane electrochemical impedance spectra (Nyquist plots) for an ideal capacitor and a typical electrochemical capacitor are shown in Figure 2-4c. For an ideal capacitor, the impedance plot should be a vertical line, parallel to the imaginary axis (y axis); however, for an electrochemical capacitor, a semicircle loop at high frequencies is due to the charge-transfer resistance of the electrode, while the inclined line at low frequencies may result from a distribution in macroscopic path length (non-uniform active material thickness) or a distribution in microscopic charge transfer rates, adsorption processes, or surface roughness [4]. ESR can be obtained from the x-intercept of the impedance plot [5], while the capacitance can be calculated from the equation below:

$$Z'' = \frac{1}{2\pi f C} \quad (2-5)$$

where Z'' is the imaginary part of the impedance, f is the frequency, and C is the capacitance. According to Eq. (2-5), the maximum specific capacitance can be calculated from the low frequency data and the mass of the electrode. In addition,

Bode plot and phase frequency dependence plots, together with simulation method, were also used to interpret electrochemical process involved, which can be referred to the work reported by Wei et al. [6].

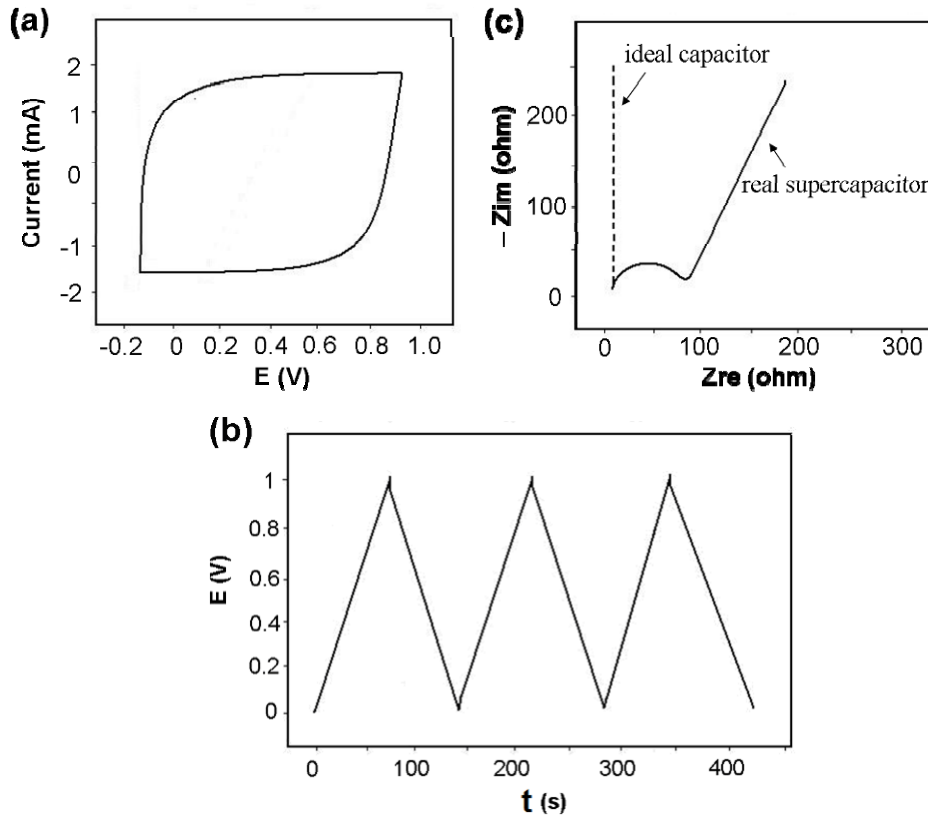


Figure 2-4. Typical (a) cyclic voltammetry curve; (b) galvanic charge-discharge curves; (c) EIS curves.

2.4. Material Characterization Methods

Numerous techniques exist to characterize the chemistry, morphology, micro- and nano-structure, and physical properties of materials. Each technique has its own

advantages and limitations. In this section, only those characterization techniques utilized in the current investigation are outlined.

2.4.1. X-ray Diffraction

XRD is a versatile, non-destructive technique that uses a monochromatic X-ray beam to project onto a crystalline material, which is diffracted or scattered by the material atom's electrons following Bragg's law or the Laue equations. The diffraction pattern provides a wealth of structural, physical and chemical information, such as type of phases, phase percentage, local stress and strain, crystal size, etc. In addition, XRD can be performed in air without the high vacuum as required in electron microscopy.

Powder diffraction and small angle diffraction are the two most commonly used modes in XRD. Powder diffraction mode is performed by varying the X-ray beam incident angle within a fairly large range (0° to 90°), while small angle diffraction mode is performed by fixing the incident beam at a small angle (normally between 1° and 4°) allowing the X-ray interaction depth on the scale of hundreds of nanometers to several microns. Hence, small angle diffraction mode is preferred to characterize thin films.

Detailed microstructures such as defects and physical discontinuities could not be clearly identified by XRD, which may be the limitation of XRD. However, the newly developed X-ray diffraction imaging technique may substantially expand the application of XRD in materials characterization [7].

2.4.2. Transmission Electron Microscopy

TEM is a microscopy technique whereby a beam of high energy (accelerating voltage normally over 200 kV) electrons is transmitted through an ultra thin specimen, and interact with the specimen to form an image on an imaging device.

TEM is capable of imaging at a significantly high magnification with high resolution owing to the short wavelength of high energy electron beam.

Depending on the focal positions, the image of either the local sample structure or a diffraction pattern characteristic of crystallographic structures from the same region on the sample, called selected area diffraction (SAD) pattern, can be formed. The central beam or the diffracted beam could be selected and used to form the structural images, called bright field (BF) and dark field (DF) images, respectively. It is the dual information channels, regular and inverse spatial information, that make TEM so powerful.

In nanomaterials characterization, several other TEM operating modes are

frequently applied, such as nano-beam diffraction mode, convergence beam diffraction mode, and especially, high-resolution TEM (HRTEM) mode. HRTEM image is a TEM image with phase contrast which arises due to the differences in the phase of the electron waves scattered through a thin specimen. HRTEM image is very important because it gives lattice fringes that can be exploited to image the atomic structure of thin specimens. In this thesis, HRTEM technique was frequently used to quantify the CNT wall number and to confirm the microstructures. Recently, z-contrast scanning TEM (STEM) images have become more and more popular, since they provide additional information of the chemistry of the thin specimen, together with structural information. As discussed above, TEM is a powerful technique to examine microstructures of materials.

The limitations of TEM technique are: (1) in TEM, only a small part of specimen can be examined. The higher the resolution, the worse the sampling abilities. (2) Sample preparation requires lots of effort, since the sample must be extremely thin. In addition, sample preparation process may also affect the structure and chemistry of the sample. Fortunately, preparing TEM samples of nanomaterials is much easier. (3) The micrograph interpretation is not as straightforward as other techniques. (4) High energy electron beam could damage the specimen during examination. More information about TEM theory and techniques can be found in an excellent book written by Williams and Carter [8].

2.4.3. Scanning Electron Microscopy

SEM is a microscopy technique that probe the sample surface by scanning it with a high-energy electron beam (the typical accelerating voltage is 5~20 kV) in a raster scan pattern. The interaction of the electron beam with the specimen produces different types of signals including secondary electrons, backscattered electrons, characteristic X-rays, and other photons of various energies. These signals emitted from microvolumes of the specimen can be used to examine the surface morphology, crystallography, composition, and many other characteristics of the specimen. Secondary and backscattered SEM modes are the most commonly used. Secondary SEM mode is primarily used to obtain the surface topography of the specimen, while backscattered SEM mode is mainly used together with EDS to determine the distribution of different elements within the specimen. One important advantage of SEM is that it has a large depth of field yielding a characteristic three-dimensional appearance of the sample surface. The technique of electron backscattering diffraction (EBSD) has been developed to determine the crystal structure and grain orientation of crystals on the surface of the specimen. However, the structural information is not preferable by SEM, when it compares with TEM. An excellent text book written by Goldstein et al. [9] can be referred for detailed information of SEM theory and techniques.

2.4.4 Energy-dispersive X-ray Spectroscopy

EDS is an analytical technique used to determine the chemistry of a specimen. It is normally coupled with SEM or TEM to expand the variety of those techniques. When a high-energy beam of electrons, or photons, or X-rays is focused onto a specimen, some electrons of the inner orbitals are excited into higher orbitals, or ejected (secondary electrons, or photoelectrons) forming holes at the inner orbitals. The electrons at higher energy levels drop into the holes, and emit characteristic X-rays depending on the elements. The energy of the characteristic X-rays can be used to identify the element(s) present, while the relative intensity of different elements can be employed to determine the percentage of the elements in the specimen.

2.4.5 X-ray Photoelectron Spectroscopy

XPS is a quantitative spectroscopic technique that measures the composition, chemical state, electronic state and empirical formula of the elements at the specimen surface (typically between 1 to 10 nm). When the specimen is irradiated by X-ray, photoelectrons escape from the sample surface. The ejected photoelectrons are detected and measured in terms of their kinetic energy and numbers, from which the intensity of the electron at a certain binding energy is converted in XPS spectrum. In this thesis, XPS was performed using a Kratos

AXIS Ultra X-ray photoelectron spectrometer to identify Fe catalyst particles as well as the valence of Mn. A monochromatic Al source, operating at 210 W with a pass energy of 20 eV and a step of 0.1 eV, was utilized. Curve fitting and background subtraction were accomplished using Casa XPS Version 2.3.13 software.

2.4.6 Auger Electron Spectroscopy

AES is another surface analytical spectroscopic technique using Auger electrons rather than photoelectrons by XPS. When the photoelectrons or secondary electrons are ejected, the electrons at higher orbitals drop to the inner orbitals resulting in a release of energy. This energy is sometimes released in the form of emitted photons (characteristic X-rays), and also it can be transferred to another electron and eject the electron to form Auger electrons. Due to this second ejection process, Auger electrons can only be detected from the very surface of the specimen, less than 5 nm. In this thesis, AES was also used to identify Fe catalyst particle patterns after pretreatment by JAMP 9500F Auger microprobe.

2.4.7 Raman Spectroscopy

Raman spectroscopy is a technique that is used to investigate vibrational, rotational, and other low-frequency modes in a system. A laser light is emitted

onto a specimen, interacting with phonons or other excitations leading to the energy shift of the laser photons, from which the information about phonons in the specimen can be obtained and analyzed. In this thesis, Raman spectra were collected in back-scattering geometry with a custom Raman spectrometer, equipped with a 2000 grooves/mm holographic reflection grating, 50 mm f/1.8 Nikon camera collection lens, and an Andor back-thinned charge-coupled device (CCD) detector cooled to -80°C . Excitation utilized *p*-polarized light incident at 49° relative to the substrate normal using an Argon ion laser at 514.5 nm (Coherent Innova 308).

2.4.8 Contact Angle Measurement

Contact angle measurement in this thesis was employed to determine the hydrophilicity of CNTAs and modified CNTAs. Contact angle is measured using a contact angle goniometer, FTA200 (First Ten Ångstroms). The system consists of an optical subsystem, a high resolution camera and software to capture and analyze the profile of a drop of liquid on a substrate. A dynamic mode was also applied due to the quick immersion of the pure water droplet into modified CNTAs.

2.4.9 Image-Pro[®] Plus Software

Image-Pro[®] Plus is a comprehensive image analysis software, which can be used to calculate phase percentage, count small cells, measure particle size distribution, etc.

2.5. References

- [1] Sridharan, M.; Sillassen, M.; Böttiger, J.; Chevallier, J.; Birkedal, H. *Surface&Coating Technology* **2007**, 202, 920-924.
- [2] Wei, W.; Cui, X.; Chen, W.; Ivey, D. G. *Journal of Physical Chemistry C* **2008**, 112, 15075-15083.
- [3] Hiraoka, T.; Najafabadi, A. I.; Yamada, T.; Futaba, D. N.; Yasuda, S.; Tanaike, O.; Hatori, H.; Yumura, M.; Iijima, S.; Hata, K. *Advanced Functional Materials* **2010**, 20, 422-428.
- [4] Kötz, R.; Carlen, M. *Electrochimica Acta* **2000**, 45, 2483-2498.
- [5] Reddy, A. L. M.; Shaijumon, M. M.; Gowda, S. R.; Ajayan, P. M. *Journal of Physical Chemistry C* **2010**, 114, 658-663.
- [6] Wei, W.; Cui, X.; Chen, W.; Ivey, D. G. *Journal of Power Sources* **2009**, 186, 543-550.
- [7] Cullity, B. D.; Stock, S. R. in *Elements of X-ray diffraction*, 3rd edition, (Prentice Hall, New Jersey, 2001).
- [8] Williams, D. B.; Carter, C. B. *Transmission electron microscopy: a text book for materials science*, (Springer, New York, 1996).
- [9] Goldstein, J. I.; Newbury, D. E.; Joy, D. C.; Lyman, C. E.; Echlin, P.; Lifshin, E.; Sawyer, L.; Michael, J. R. *Scanning electron microscopy and X-ray microanalysis*, 3rd edition, (Springer, New York, 2003).

Chapter 3

Growth of Millimeter-Scale Carbon Nanotube Arrays by Conventional Chemical Vapor Deposition: Effect of Catalyst Particle Interspacing*

* Material in this chapter has been published in:

Cui, X. W.; Wei, W. F.; Harrower, C.; Chen, W. X. *Carbon*, 2009, 47, 3441-3451.

3.1. Introduction

Intensive research efforts have been undertaken to synthesize millimeter-scale vertically aligned carbon nanotube arrays (CNTAs) due to their unique electrical, thermal and mechanical properties, and their great potential of usage for making composites [1, 2], field emission devices [3, 4], field effect transistors [5, 6], electrochemical and biosensors [7, 8]. The most popular method used for CNTA growth is chemical vapor deposition (CVD) because it provides great flexibility in controlling the arrangement, density and length of carbon nanotubes (CNTs) [9]. Tremendous progress has been achieved in the growth of CNTs by CVD method. For instance, Iijima et al. succeeded on growing 2.5 mm single-walled CNT (SWCNT) arrays by water-assisted CVD (WACVD) [10]. Millimeter-scale double-walled CNT (DWCNT) and multiwalled CNT (MWCNT) arrays have also been grown through WACVD [11, 12]. Water, as a weak oxidizer, is used to selectively remove catalyst-bound amorphous carbon, and to substantially increase the activity and lifetime of catalyst particles. The lifetime of catalyst particles without adding H₂O was claimed to be only several minutes in thermal CVD growth [10, 13]. However, recently, Hart et al. [14] and Zhang et al. [15] proved that conventional chemical vapor deposition (CCVD) without adding H₂O could also grow millimeter-scale MWCNT arrays with catalyst lifetime over 1 hr. More recently, Li et al. [9] reported that CNTA growth appears to involve a lengthening–thickening process in xylene-ferrocene injection CVD method.

However, the explicit mechanisms of the lifetime of catalyst particles and the growth kinetics of CNTAs in CCVD method are still not fully understood.

The physiochemical properties of CNTs are determined by their length, diameter, wall number and chirality, which are highly sensitive to catalyst particles. By controlling catalyst particle size, WACVD and CCVD techniques have been used to selectively grow SWCNT, DWCNT and other MWCNT arrays [16-21]. It is generally accepted that the diameter and wall number of CNTs could be controlled by catalyst particle size [22]. Catalyst particle density was also claimed to play a key role in CNTA growth [23, 24]. It is generally believed that high particle density is necessary for CNTs to have a vertically aligned growth mode, while low particle density leads to CNT entanglement [14, 25], although the explicit correlation hasn't been provided. Without the presence of etching agent, like water, the control of catalyst particles becomes particularly essential in CCVD to produce millimeter-scale CNTAs. It has been reported that catalyst particle size and density in CCVD could be tuned by using different pretreatment conditions [14, 23] or by adding a thin layer of Mo on Fe catalyst film [26]. Catalyst particle interspacing could also be controlled by pretreatment conditions; however, the significance of inter-particle spacing and the tuning of CNTA height, CNT diameter and wall number by inter-particle spacing have not been reported.

In this chapter, catalyst particle interspacing was found to be a more accurate parameter than particle density to quantify the characteristics of densely packed catalyst particles and to affect CNTA growth. The effect of inter-particle spacing was established and systematically studied based on the investigations on catalyst particle size, density and inter-particle spacing using field emission scanning electron microscopy (FESEM) and Auger spectroscopy, and on the growth kinetics of CNTAs using FESEM and high resolution transmission electron microscopy (HRTEM). It is anticipated that this study on the effect of inter-particle spacing may provide improved understanding and new insights on the growth mechanism of CNTAs by CCVD.

3.2. Experimental Procedure

A buffer layer of 30 nm-thick Al_2O_3 and a catalyst film of 1 nm or 3 nm-thick Fe were sputtered sequentially on Si wafers. The sputtering process, catalyst film pretreatment and MWCNT array growth by CCVD were presented in detail in Chapter 2. The catalyst films were pretreated for different periods under 200 sccm Ar and 400 sccm H_2 gas flow at 775°C . CNTA growth was conducted for various growth periods from 5 min to 2 hrs. For catalytic Fe nanoparticle investigation, fast cooling (~ 1 min) was employed to avoid further evolution of catalyst particles.

The morphology and height of MWCNT arrays were characterized by a JSM-6301FXV field-emission scanning electron microscopy (FESEM). The size, distribution and composition of fast cooled nanoparticles were characterized by FESEM and JAMP 9500F Auger microprobe. Chemistry analysis of the substrate surfaces before and after CNTA growth was carried out by X-ray photoelectron spectroscopy (XPS) using a Kratos AXIS Ultra X-ray photoelectron spectrometer. High-resolution transmission electron microscopy (HRTEM, JOEL 2010 operated at 200 kV) was also performed to measure the diameter and wall numbers of CNTs. A comprehensive image analysis software, Image-Pro[®] Plus, was used to analyze the mean particle size, density and inter-particle spacing on the quenched surface. The detailed procedures are as follows: 1) At least ten different locations were sampled by FESEM on each specimen to produce measurements statistically significant. 2) From each location, the particle density and the distribution of particle size could be acquired by Image-Pro[®] Plus. 3) The results obtained in 2) were used to calculate the mean particle size and the inter-particle spacing at the location. The calculation of inter-particle spacing was made based on the mean particle size and particle density by assuming a uniform distribution of particles. 4) Finally, the mean particle size, density, inter-particle spacing and their 95% confidence intervals of the specimen were obtained by statistically analyzing the particle data from all the detected locations on the specimen.

3.3. Results and Discussion

3.3.1. Morphology and Growth Kinetics of Vertically Aligned MWCNT Arrays

Highly dense, millimeter-long MWCNT arrays were deposited on both Fe(1nm) and Fe(3nm) catalyst films after 1 hr CNT test without any etching agents, such as water, air or plasma, as shown in Figure 3-1. Figure 3-1a is the side view of 1.1 mm long CNTAs deposited on the Fe(3nm) catalyst film, while Figure 3-1b is that of 0.9 mm long CNTAs deposited on the Fe(1nm) catalyst film. The optimum pretreatment (Ar/H₂ at 775°C) time was 60 min for Figure 3-1a and 4 min for Figure 3-1b. It should be noted that the breakdown of catalyst films could occur during the heating step, thus the control of heating rate is very important for the catalyst particle formation. Here, the heating rate was maintained at 37.5°C/min.

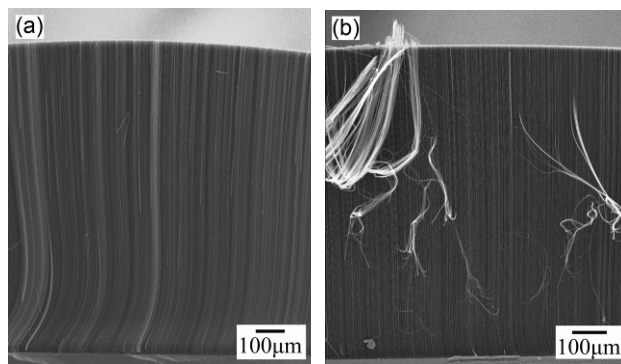


Figure 3-1. FESEM cross section images of vertically aligned CNTAs after 1 hr CNT test: (a) 1.1 mm long CNTA grown on 60 min-pretreated Fe(3nm) catalyst film; (b) 0.9 mm long CNTA grown on 4 min-pretreated Fe(1nm) catalyst film.

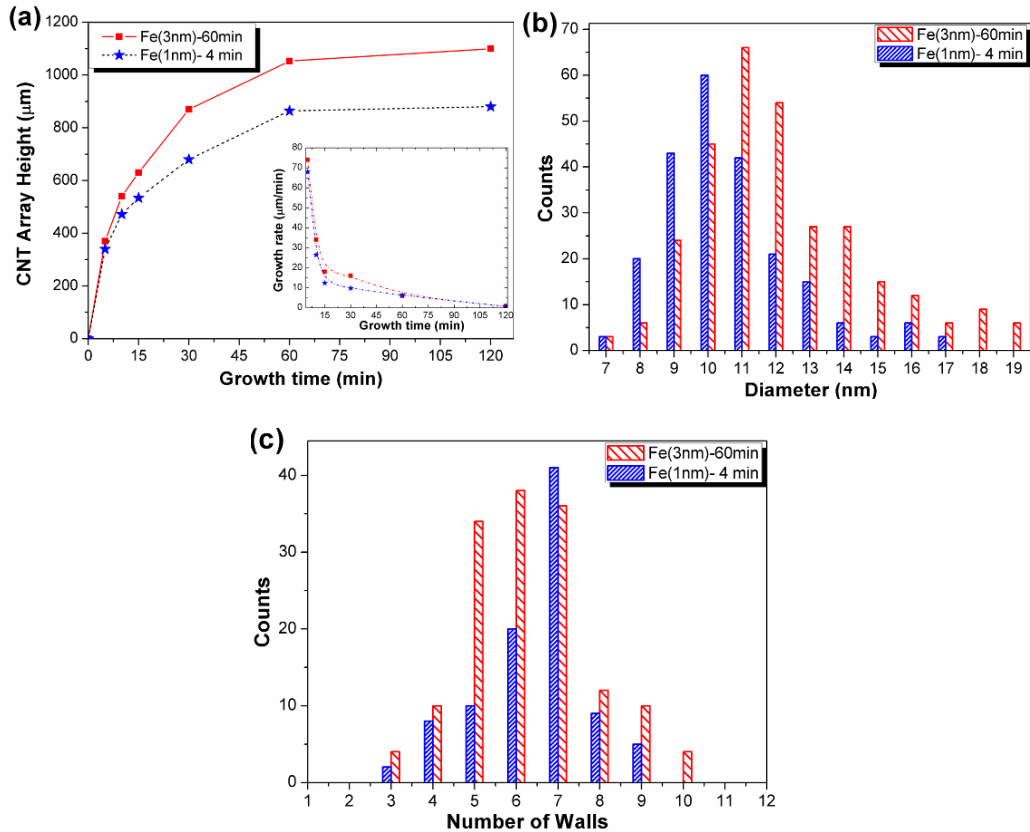


Figure 3-2. (a) Growth kinetic curves of CNTAs grown on 60 min-pretreated Fe(3nm) and 4 min-pretreated Fe(1nm) catalyst films. The inset is the corresponding growth rate vs. growth time curves for the two catalyst films. (b) The histograms of the diameter of CNTs grown on the catalyst films in (a); (c) The histograms of the wall number of CNTs grown on the catalyst films in (a).

The growth kinetics of the CNTAs formed on the Fe(3nm) and Fe(1nm) catalyst films under the corresponding optimum pretreatment conditions is shown in Figure 3-2a. Both curves show a parabolic-like trend with higher growth rate in the first 15 min. The initial growth rate was determined to be 74 μm/min and 68

$\mu\text{m}/\text{min}$ for the Fe(3nm) and Fe(1nm) catalyst films, respectively. These values are higher than those of MWCNT arrays formed by CCVD ($<15\text{-}60 \mu\text{m}/\text{min}$) in other groups [13, 15, 27]. The initial growth rate decreases dramatically and comes down to less than $5\mu\text{m}/\text{min}$ after 1hr growth as shown in the inset in Figure 3-2a. It is also noted that the lifetime of the Fe nanoparticles on both samples is considerably longer (more than 1 hr) than that reported in the literature [10, 13]. The statistic distribution of the diameter and wall number of CNTs after 30 min growth on the optimum-pretreated catalyst films is displayed in Figure 3-2b and 3-2c, respectively. It is shown that, on average, CNTs with 11.5 nm diameter and 5-7 walls were formed on 60 min-pretreated Fe(3nm) catalyst film, while CNTs with 10.3 nm diameter and 6-7 walls were formed on 4 min-pretreated Fe(1nm) catalyst film. Patole et al. [22] has reported a substantial decrease of CNT height (from 1.2 mm to 0.38mm) and an increase of wall number of CNTs (from 8 to 15) with increasing Fe catalyst film thickness from 1 nm to 3 nm. In fact, the present work shows the opposite trend. It was found that both Fe(3nm) and Fe(1nm) catalyst films could grow millimetre-long CNTAs; and CNTAs grew faster and longer on the Fe(3nm) catalyst film than those on the Fe(1nm) catalyst film under the corresponding optimum pretreatment conditions, as shown in Figure 3-2a. The diameter and wall number of CNTs deposited on both optimum-pretreated catalyst films are also comparable, as shown in Figure 3-2b and 3-2c. As CNTA growth is highly related to catalyst particles, especially in CCVD, the observations in Figure

3-2 could be understood by investigating the catalyst particles formed after different pretreatments, which is presented in the following sections.

3.3.2. Characterization of Catalyst Particles after Different Pretreatments

The catalyst particles after different pretreatments for Fe(1nm) and Fe(3nm) catalyst films were characterized to illustrate the effect of pretreatments on the catalyst particle formation and the effect of catalyst particles on the growth of CNTAs. Fast cooling pretreated catalyst films from 775°C to room temperature was performed to minimize any changes in particle size and distribution during cooling period. The particles were then examined by SEM, instead of atomic force microscopy (AFM) as used by other researchers [12, 23]. AFM has limited lateral resolution and could not give reliable particle size, shape and density [28]. Besides, Al₂O₃ buffer layer itself also shows particle-like topography after pretreatment, which may mix up with catalyst particles in the image obtained by AFM [23]. As shown in the SEM images in Figure 3-3 and 3-4, the nanoparticles and their distributions after different pretreatments on the two catalyst films can be clearly observed. The composition of the particles on the pretreated surfaces was further examined using Auger spectroscopy. As shown in Figure 3-3b, strong Fe peaks in the Auger profile were detected from the particles, while only Al and O peaks were detected from the substrate. Auger mapping was also performed.

Figure 3-3d is the Auger Fe mapping image taken on 6 min-pretreated Fe(1nm) catalyst film. Regions in red have the highest Fe signal, while regions in green or blue have intermediate or zero Fe signal, respectively. It is apparent that the pattern in Figure 3-3d is well consistent with the SEM image in Figure 3-3c. Therefore, all the nanoparticles shown in the SEM images are Fe catalyst particles.

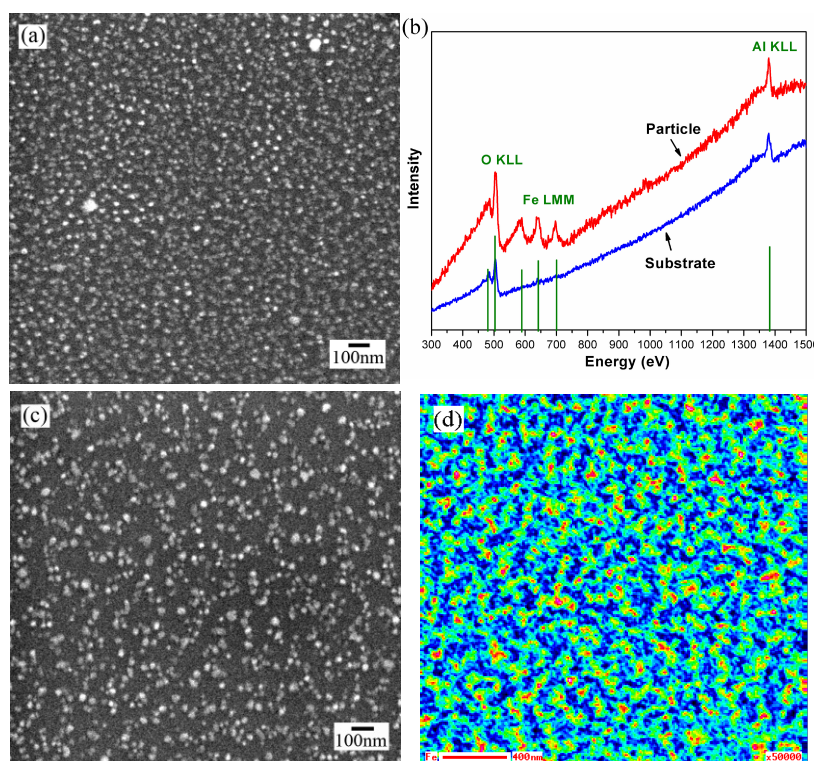


Figure 3-3. FESEM images of the Fe(1nm) catalyst film (a) after pretreatment for 4 min; (b) Auger profiles detected from the particles and substrate in (a); (c) after pretreatment for 6 min; (d) Auger mapping of the catalyst film in (c).

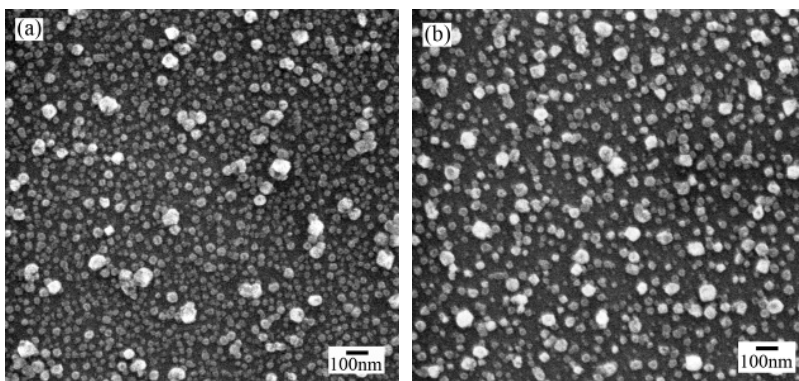


Figure 3-4. FESEM images of the Fe(3nm) catalyst film after (a) pretreatment for 60 min; (b) pretreatment for 70 min.

The Fe nanoparticle size and density observed on the SEM images were quantitatively determined using Image-Pro[®] Plus. After pretreatment for 4 min, the Fe(1nm) catalyst film broke apart to very small and densely packed Fe nanoparticles, as shown in Figure 3-3a. The mean particle density on this film was determined to be $8.23 \times 10^{10} (\pm 0.25 \times 10^{10}) / \text{cm}^2$, and the average particle size was 16.1 ± 0.2 nm. However, after pretreatment for 6 min, the small and densely packed Fe nanoparticles in Figure 3-3a coalesced to a larger particle size (24.0 ± 0.5 nm), and a much lower particle density ($3.12 \times 10^{10} (\pm 0.20 \times 10^{10}) / \text{cm}^2$) in Figure 3-3c. The coarsening of catalyst particles under over-pretreated conditions is driven by surface energy minimization, more likely through the diffusion of Fe as adatoms on the Al_2O_3 surface [29]; as a result, this coarsening process leads to an increase of average particle size and a decrease of particle density [30], which is consistent with the observation in this study. The same trend was also found for the Fe(3nm)

catalyst film. Relatively large (29.3 ± 0.7 nm) but densely packed ($4.89 \times 10^{10} (\pm 0.12 \times 10^{10}) / \text{cm}^2$) Fe nanoparticles were formed after pretreatment for 60 min as shown in Figure 3-4a; and the particle size was increased to 35.5 ± 1.0 nm and particle density was reduced to $2.83 \times 10^{10} (\pm 0.18 \times 10^{10}) / \text{cm}^2$ after pretreatment for 70 min as shown in Figure 3-4b. It should be noted that the ranges of the data determined above are 95% confidence interval of the mean. The determined particle densities are in the same order of magnitude as the CNT densities obtained by some other researchers through CCVD and WACVD processes [14, 17]. It is interesting to see that the kinetics of catalyst particle formation is slower for the thicker film under the same pretreatment environment, possibly because thicker film needs to absorb more energy to break apart. It is then suggested that the effect of Fe catalyst film thickness on CNTA growth cannot be clarified without considering the influence of pretreatment conditions. As the pretreatment condition has a great influence on the catalyst particle formation, the observations in Figure 3-2 can be attributed to the different optimum pretreatment conditions used for the two catalyst films to grow CNTAs, rather than only one pretreatment condition used by Patole et al. [22]. The catalyst particle data and the dimensions of CNTs grown from the corresponding catalyst particles for 30 min are summarized in Table 3-1.

3.3.3. Dependence of CNTA Growth on Catalyst Particle Interspacing

Table 3-1 shows that, on the catalyst film with the same thickness, catalyst particles with smaller particle size and higher particle density could grow longer CNTAs, which is consistent with the results reported by Zhang et al. [23]. However, the trend breaks down if the change of the catalyst film thickness is considered. For example, 4-min pretreated Fe(1nm) catalyst film has yielded smaller and denser catalyst particles than 60-min pretreated Fe(3nm) catalyst film, as shown in Table 3-1; however, CNTAs grew faster and longer on the latter film rather than on the former film, as shown in Figure 3-2. The same results can also be obtained if comparing 6-min pretreated Fe(1nm) catalyst film with 70-min pretreated Fe(3nm) catalyst film. It is implied that another parameter, which can also be controlled by the pretreatment conditions, is predominant in the present case. Note that, in Figure 3-4a, 60-min pretreated Fe(3nm) catalyst film has quite densely packed catalyst particles, although the value of particle density is not very high. To quantify the densely packed catalyst particles, inter-particles spacing, defined as the average distance between the perimeters of neighbouring particles, was also determined and compared with the effect of particle density.

Based on the average Fe particle size and density determined, the inter-particle spacing could be calculated. The mean inter-particle spacing was found to be small for 60 min-pretreated Fe(3nm) catalyst film and 4-min pretreated Fe(1nm)

Table 3-1. Summary of catalyst particle data and the dimensions of CNTs grown from the corresponding catalyst particles for 30 min

Fe Film Thickness on Fe/Al ₂ O ₃ /Si	Pretreatment Time (min)	Mean Particle Density ($\times 10^{10}/\text{cm}^2$)	Mean Particle Size (nm)	Mean Inter-particle Spacing (nm)	CNTA height (μm)	CNT Diameter (nm)	Wall Number
3 nm	60	4.89 \pm 0.12	29.3 \pm 0.7	15.9 \pm 1.2	930	11.5	5-7
	70	2.83 \pm 0.18	35.5 \pm 1.0	24.0 \pm 2.7	350	31.7	19-23
1 nm	4	8.23 \pm 0.25	16.1 \pm 0.2	18.8 \pm 0.7	670	10.3	6-7
	6	3.12 \pm 0.20	24.0 \pm 0.5	32.6 \pm 2.3	70	29.7	20-25

catalyst film, which was 15.9 ± 1.2 nm and 18.8 ± 0.7 nm, respectively. Futaba et al. [28] has measured the average distance between neighbouring SWCNTs to be 14 nm. This value is very comparable to the mean inter-particle spacing obtained in the above calculation. However, the average inter-particle spacing for 70-min pretreated Fe(3nm) catalyst film and 6-min pretreated Fe(1nm) catalyst film in this study was a little large, 24.0 ± 2.7 nm and 32.6 ± 2.3 nm, respectively. The catalyst particle interspacing data are also summarized in Table 3-1.

The importance of inter-particle spacing can be clearly observed by plotting the CNTA heights versus catalyst particle size, density and inter-particle spacing based on the data in Table 3-1. As shown in the inset plots (a) and (b) in Figure 3-5, although the values of catalyst particle size and density varied a lot, they did not display any meaningful correlation with CNTA height. Inter-particle spacing, on the other hand, demonstrates a strong correlation with CNTA height, that is, CNTA height decreases dramatically with increasing inter-particle spacing. It indicates that, in this investigation, the range of variation in inter-particle spacing is more significant than that in particle size and density, and thus inter-particle spacing plays a predominant role in influencing CNTA height. It should be noted that the increase of catalyst particle size is always accompanied with a decrease of particle density and an increase of inter-particle spacing for the pretreatment of the catalyst films with the same thickness. Thus, there is no difference between

high particle density and small inter-particle spacing when the thickness of the catalyst films is unchanged. However, when investigating the CNTA growth on the catalyst films with different thicknesses, high particle density is not necessarily associated with a small inter-particle spacing. The decrease of particle density was also found to yield smaller inter-particle spacing (shown in Table 3-1). As suggested by Figure 3-5, inter-particle spacing is a more accurate parameter than particle density to quantify the characteristics of densely packed catalyst particles.

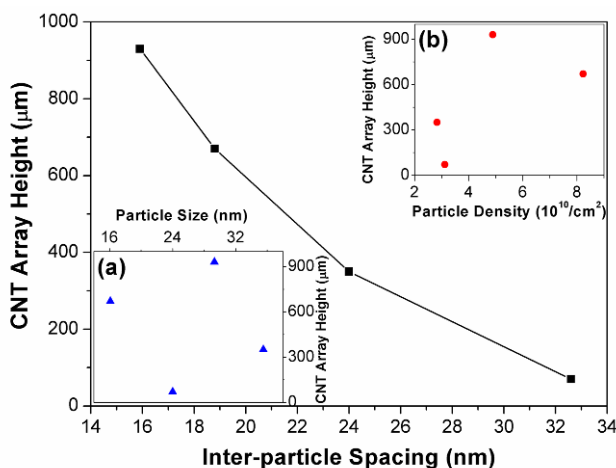


Figure 3-5. CNTA height vs. inter-particle spacing, particle size (inset (a)) and particle density (inset (b)).

In addition, inter-particle spacing was found to possibly affect the diameter and wall number of CNTs. As shown in Table 3-1, catalyst particles formed on 60-min pretreated Fe(3nm) catalyst film are larger than those on 6-min pretreated Fe(1nm)

catalyst film (29.3 nm to 24.0 nm). It is generally believed that the CNT diameter can be correlated to the catalyst particle size. Surprisingly, after a 30 min's growth, the diameter and wall number of CNTs formed on the former film are much smaller, 11.5 nm and 5-7 walls, than those of CNTs formed on the latter film, 29.7 nm and 24 walls, as shown in Table 3-1. This may be ascribed to the large difference in the inter-particle spacing between these two films (15.9 nm to 24.0 nm). More discussion of this point has been provided in the following section. Furthermore, this discussion also proves that, to affect CNTA growth, the difference in catalyst particle size in the current conditions is negligible comparing with the difference in inter-particle spacing. Thus, the effect of catalyst particle size is obscured by inter-particle spacing, which is also suggested by Figure 3-5. These results point to the importance of adjusting the pretreatment conditions and the thickness of catalyst film to acquire flexible control of catalyst particle size and interspacing.

3.3.4. CNTA Growth Mechanism Affected by Catalyst Particle Interspacing

CNTA growth has been found to exhibit two growth modes, tip growth and root growth, depending on the adhesion between catalyst and substrate [27]. Zhang et al. [31] also suggested a synchronous growth mode of CNTAs grown by cyclohexane- ferrocene injection CVD method. In the present study, several

techniques have been used to determine CNTA growth mode. In TEM observations, Fe particles were found at the tip of CNTs, as shown in Figure 3-6a. To confirm the observations by TEM, SEM and XPS analysis were also performed. Futaba et al. [28] found by SEM that catalyst particles were strongly adhered to the substrate after removal of CNTAs. Zhu et al. [32] detected very high Fe peaks by XPS after removal of CNTAs. Therefore, the root growth mode was suggested in their reports. However, SEM image in Figure 3-6b shows that, after removal of the grown CNTA, many craters (indicated by white arrows in Figure 3-6b) rather than catalyst particles can be found. XPS spectra in Figure 3-6c also demonstrate much weaker Fe peaks and stronger Al peaks on the substrate after removal of the grown CNTA than those on the as-pretreated catalyst film. Quantitative analysis of XPS spectra gives a substantial reduction in the Fe/Al atomic ratio from 5:1 on the as-pretreated catalyst film to 1:13 on the substrate after removal of the grown CNTA for Fe(3nm) catalyst films, and from 1.4:1 to 1:16 for Fe(1nm) catalyst films. The SEM and XPS analyses strongly confirm that most catalyst particles were lifted off the substrate by the grown CNTA. However, small amount of Fe left on the substrate was also detected by XPS, suggesting that the CNTA also shows a synchronous growth mode in the present study.

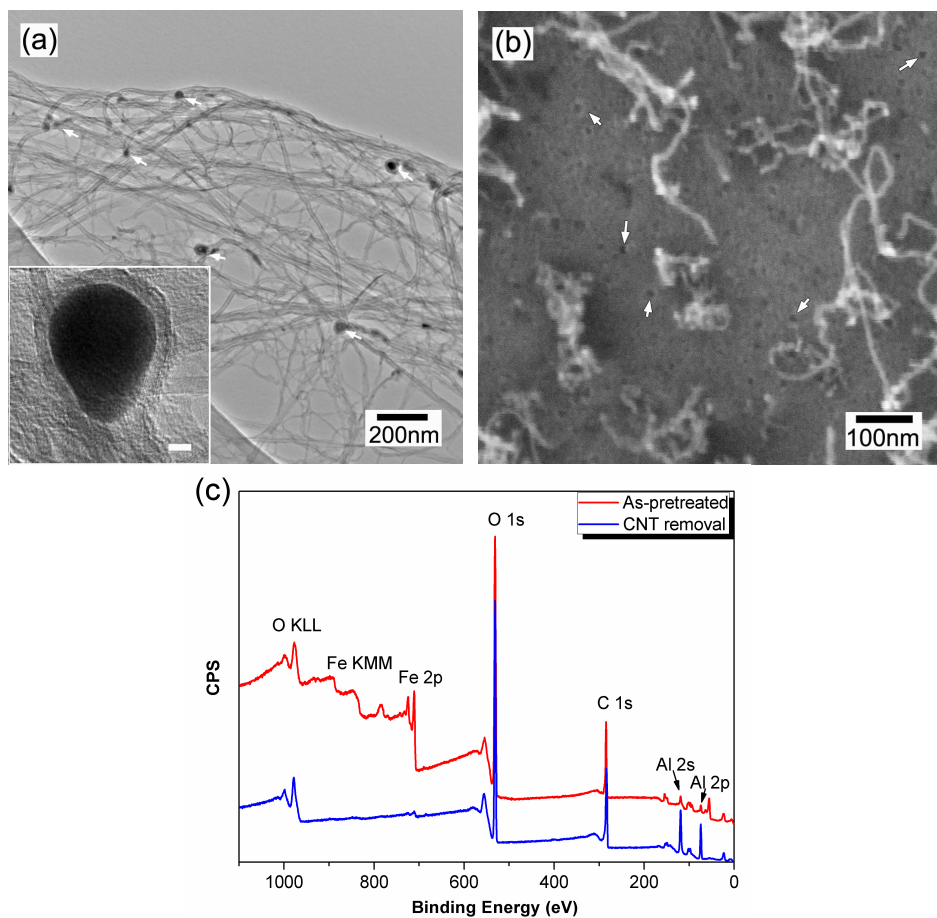


Figure 3-6. (a) TEM image of CNTs deposited for 30 min on the Fe(3nm) catalyst film after pretreatment for 60 min; the inset is a HRTEM image showing the catalyst particle at the tip of the CNT (scale bar: 5 nm); (b) FESEM image of 60 min-pretreated Fe(3nm) catalyst film after removal of the grown CNTA; (c) XPS spectra of the as-pretreated catalyst film and the substrate after removal of the grown CNTA.

High resolution surface and cross section images of CNTAs deposited on the Fe(1nm) catalyst film after 30 min CNT test are shown in Figure 3-7. The pretreatment time used for growing CNTAs in Figure 3-7a and 3-7b was 4 min,

while that for growing CNTAs in Figure 3-7c and 3-7d was 6 min. Compared with the data in Table 3-1, the CNTAs grown on the small inter-particle spacing catalyst film (Figure 3-7a and 3-7b) are much higher than those on the large inter-particle spacing catalyst film (Fig. 3-7c and 3-7d), which can be seen from the insets in Figure 3-7a (670 μm) and Figure 3-7c (70 μm), respectively. The long CNTA is densely packed with individual CNTs hardly seen on the surface in Figure 3-7a. However, the short CNTA in Figure 3-7c is sparsely packed with randomly grown CNTs visible on the surface. They are entangled together and form the net shape. By comparing Figure 3-7b with 3-7d, it is also evident that most CNTs in the long CNTA (Figure 3-7b), although appears wavy in shape, grew in the direction perpendicular to the substrate as indicated by the arrow; while most CNTs in the short CNTA (Figure 3-7d) are not well aligned to the upward direction and demonstrate strong crossover and entanglement.

Fan et al. [4] suggested that Van der Waals interaction is one of the reasons for the aligned growth of CNTs. Consequently, when inter-particle spacing is small, catalyst particles and/or CNTs are primarily confined by their neighbours to grow in the upward direction, as shown in Figure 3-7a and 3-7b. However, when inter-particle spacing is large, little confinement from their surroundings promotes relatively random growth of CNTs, as shown in Figure 3-7c and 3-7d. Once CNTs can grow in directions quite deviated from the vertical direction, less interaction

Therefore, the period of the predominant increase of CNTA height (defined as lengthening time) is short for the large inter-particle spacing catalyst films. It is proposed that inter-particle spacing affects the growth kinetics of CNTAs by affecting their lengthening time.

To further clarify how inter-particle spacing affects CNTA growth, HRTEM images of over 200 MWCNTs under each growth condition were taken to investigate the change of CNT wall number during CNTA growth. Figure 3-8 shows some typical HRTEM images of the CNTs deposited for different growing periods. Within a 5-10 min growth period, CNTs are mostly double-walled or triple-walled. The wall number increases to 5-8 walls after 30 min growth, 12-16 walls after 1hr growth, and goes up to 25-30 walls in the second hour growth. The change of CNT wall number with CNTA growth time was also summarized in Figure 3-8. The wall number at long growth periods can still be counted, although the outer walls of CNTs are not in good graphitization, because of the deposition of graphitic-like layers, as also reported by Hata et al. [31]. Figure 3-2a and Figure 3-8 demonstrate an obvious lengthening-thickening process during CNTA growth by CCVD, as observed by Li et al. using xylene-ferrocene injection CVD method [9]. Li et al. [9] claimed that in the lengthening process, catalysts are active and CNTs grow in height; while in the thickening process, CNTs stop growing in height and their diameters are increased by deposition of pyrolyzed

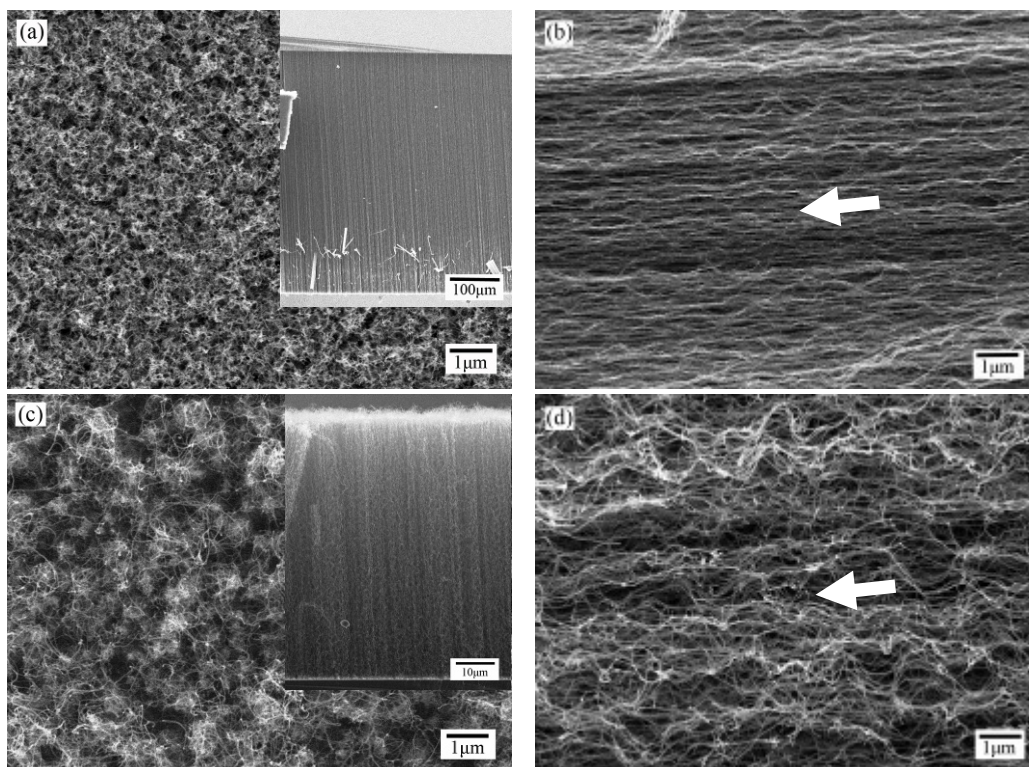


Figure 3-7. High resolution surface morphology and cross section FESEM images of CNTAs deposited for 30 min on the Fe(1nm) catalyst film after (a), (b) pretreatment for 4 min; (c), (d) pretreatment for 6 min. The insets are low magnification FESEM images of the CNTAs from the corresponding pretreated catalyst films.

will be present among the neighbouring particles and/or CNTs for maintaining the aligned growth. As a result, although individual CNTs may still grow within the CNTA, the increase of the CNTA height on the large inter-particle spacing catalyst films stops much earlier than that on the small inter-particle spacing catalyst films.

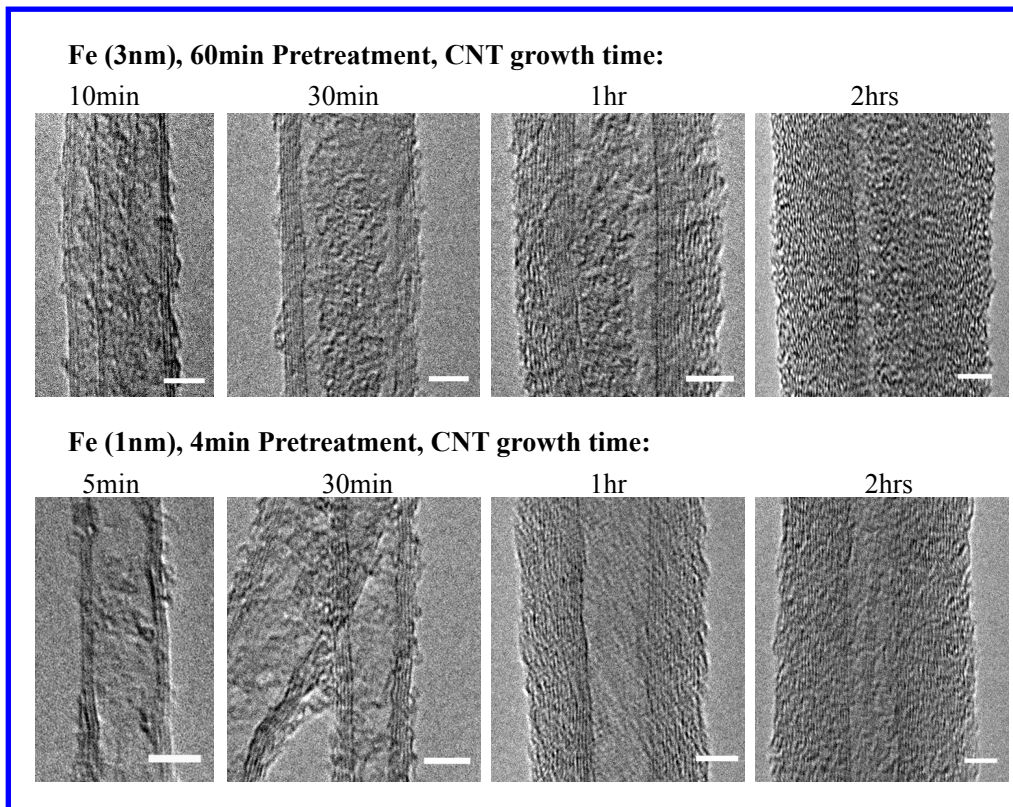
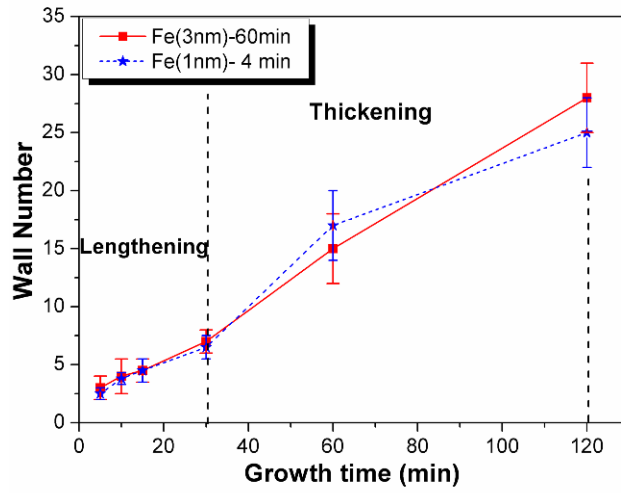


Figure 3-8. Wall number of CNTs grown on 60 min-pretreated Fe(3nm) and 4 min-pretreated Fe(1nm) catalyst films vs. CNT growth time, and HRTEM images of the corresponding CNTs (scale bar: 5 nm).

carbon. However, it is apparent from the diagram in Figure 3-8 that the lengthening process and thickening process are competitive. In the first 30 min, CNTA growth is dominated by the lengthening process and CNT wall number increases very slowly, while after 30 min, it is dominated by the thickening process and CNTAs grows a little in height. It is worth to note that CNTs grown on 4 min-pretreated Fe(1nm) catalyst film thicken more severely than those on 60 min-pretreated Fe(3nm) catalyst film in the region between 30 min and 1 hr, indicating a shorter lengthening time for CNTAs grown on the former film.

Figure 3-9 also suggests that inter-particle spacing could affect the diameter and wall number of CNTs because the thickening time was readjusted concurrently with the lengthening time. Hata et al. [33] found that SWCNTs could be thickened to multiwalled like CNTs as the pyrolytic carbon deposition from the gas phase. The epitaxial growth of graphene layers on MWCNT walls from the gas phase was also recently reported by Feng et al. [34]. The diffusion of hydrocarbon gas through the catalyst particles into the CNTA is a step necessary for pyrolytic reaction within the CNTA to produce CNT thickening. Therefore, the delayed occurrence of a predominantly increase in CNT diameter and wall number on the small inter-particle spacing catalyst film, as shown in Figure 3-9, may be due to the fact that the diffusion of hydrocarbon gas is hindered when inter-particle spacing is small. Because the effect of Van der Waals interaction is a function of

interaction distance and the diffusion of hydrocarbon gas must proceed through the gap between catalyst particles, inter-particle spacing, rather than particle density, is another parameter as catalyst particle size that could affect CNTA growth.

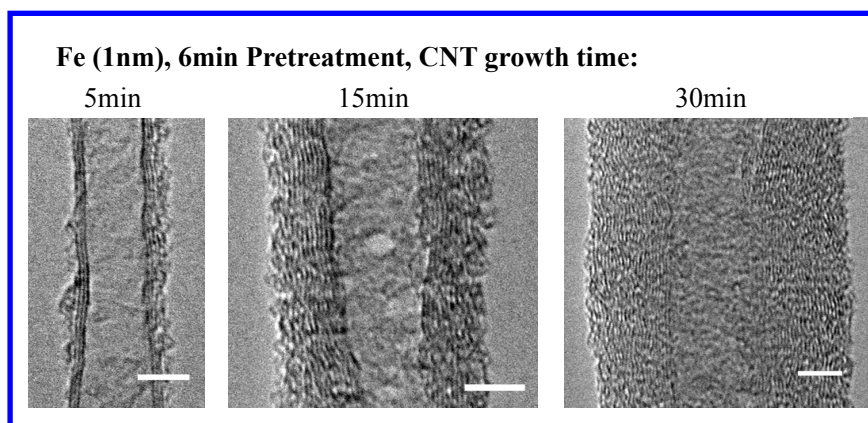
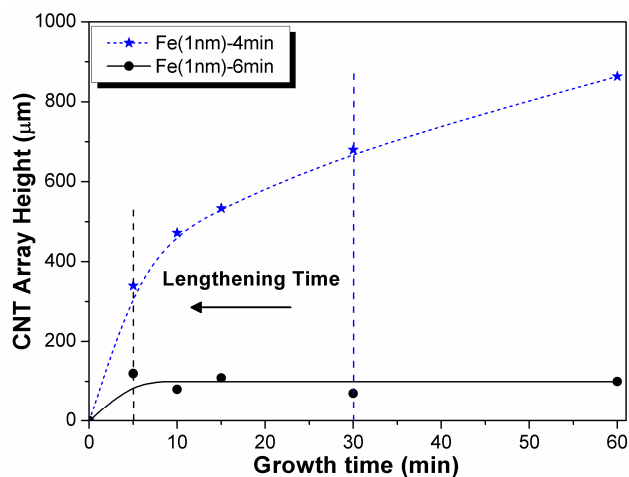


Figure 3-9. Growth kinetic curves of CNTAs grown on 4 min-pretreated and 6 min-pretreated Fe(1nm) catalyst films, and HRTEM images of the corresponding CNTs (scale bar: 5 nm).

3.4. Conclusions

Vertically aligned millimeter-scale CNTAs have been successfully deposited on both Fe(3nm)/Al₂O₃ and Fe(1nm)/Al₂O₃ catalyst films under different optimum pretreatment conditions by conventional chemical vapor deposition. By investigating the catalyst particles before CNTA growth, it has been found that inter-particle spacing is a more accurate parameter than particle density to quantify the characteristics of densely packed catalyst particles. Adjusting the pretreatment conditions and the thickness of catalyst film can produce flexible control of catalyst particle size and interspacing. In addition, inter-particle spacing was found to play a significant role in influencing CNTA height, CNT diameter and wall number in the present study. Furthermore, the growth kinetics of CNTAs grown from the two catalyst films with different pretreatment conditions shows a competitive lengthening-thickening process. Based on the studies of the growth kinetics, it has been shown that inter-particle spacing affects the CNTA height by affecting their lengthening time, and accordingly affects the diameter and wall number of CNTs because of the concurrent change in the thickening time. These results elucidate the effect of inter-particle spacing in CNTA growth and deepen our understanding of the growth mechanism of CNTAs by CCVD.

3.5. References

- [1] Jung, Y. J.; Kar, S.; Talapatra, S.; Soldano, C.; Viswanathan, G.; Li, X.; Yao, Z.; Ou, F. S.; Avadhanula, A.; Vajtai, R.; Curran, S.; Nalamasu, O.; Ajayan, P. M. *Nano Letters* **2006**, 6, 413-418.
- [2] Moniruzzaman, M.; Winey, K. I. *Macromolecules* **2006**, 39, 5194-5205.
- [3] Zhu, L.; Sun, Y.; Hess, D. W.; Wong, C. P. *Nano Letters* **2006**, 6, 243-247.
- [4] Fan, S. S.; Chapline, M. G.; Franklin, N.R.; Tomblor, T. W.; Cassell, A. M.; Dai, H. J. *Science* **1999**, 283, 512-514.
- [5] Shimada, T.; Sugai, T.; Ohno, Y.; Kishimoto, S.; Mizutani, T.; Yoshida, H.; Okazaki, T.; Shinohara, H. *Applied Physics Letters* **2004**, 84, 2412-2414.
- [6] Misewich, J. A.; Martel, R.; Avouris, P.; Tsang, J. C.; Heinze, S.; Tersoff, J. *Science* **2003**, 300, 783-786.
- [7] Lin, Y.; Lu, F.; Tu, Y.; Ren, Z. *Nano Letters* **2004**, 4, 191-195.
- [8] Yun, Y. H.; Shanov, V.; Schulz, M. J.; Dong, Z. Y.; Jaziehe, A.; Heineman, W. R.; Halsall, B. H.; Wong, D. K. Y.; Bange, A.; Tu, Y.; Subramaniamb, S. *Sensors and Actuators B* **2006**, 120, 298-304.
- [9] Li, X.; Zhang, X.; Ci, L.; Shah, R.; Wolfe, C.; Kar, S.; Talapatra, S.; Ajayan, P. M. *Nanotechnology* **2008**, 19, 455609(7).
- [10] Hata, K.; Futaba, D. N.; Mizuno, K.; Namai, T.; Yumura, M.; Iijima, S. *Science* **2004**, 306, 1362-1364.

- [11] Yamada, T.; Namai, T.; Hata, K.; Futaba, D. N.; Mizuno, K.; Fan, J.; Yudasaka, M.; Yumura, M.; Iijima, S. *Nature Nanotechnology* **2006**, 1, 131-136.
- [12] Yun, Y. H.; Shanov, V.; Tu, Y.; Subramaniam, S.; Schulz, M. J. *Journal of Physical Chemistry B* **2006**, 110, 23920-23925.
- [13] Poretzky, A. A.; Geohegan, D. B.; Jesse, S.; Ivanov, I. N.; Eres, G. *Applied Physics A* **2005**, 81, 223-240.
- [14] Hart, A. J.; Slocum, A. H. *Journal of Physical Chemistry B* **2006**, 110, 8250-8257.
- [15] Zhang, C.; Pisana, S.; Wirth, C. T.; Parvez, A.; Ducati, C.; Hofmann, S.; Robertson, J. *Diamond and Related Materials* **2008**, 17, 1447-1451.
- [16] Futaba, D. N.; Hata, K.; Yamada, T.; Mizuno, K.; Yumura, M.; Iijima, S. *Physical Review Letters* **2005**, 95, 056104 (4).
- [17] Ci, L.; Vajtai, R.; Ajayan, P. M. *Journal of Physical Chemistry C* **2007**, 111, 9077-9080.
- [18] Hafner, J. H.; Bronikowski, M. J.; Azamian, B. R.; Nikolaev, P.; Rinzler, A. G.; Colbert, D. T.; Smith, K. A.; Smalley, R. E. *Chemical Physics Letters* **1998**, 296, 195-202.
- [19] Xiong, G. Y.; Wang, D. Z.; Ren, Z. F. *Carbon* **2006**, 44, 969-973.
- [20] Yu, H.; Zhang, Q.; Luo, G.; Wei, F. *Applied Physics Letters* **2006**, 89, 223106 (3).

- [21]Gohier, A.; Ewels, C. P.; Minea, T. M.; Djouadi, M. A. *Carbon* **2008**, 46, 1331-1338.
- [22]Patole, S. P.; Alegaonkar, P. S.; Shin, H. C.; Yoo, J. B. *Journal of Physics D: Applied Physics* **2008**, 41, 155311 (6).
- [23]Zhang, H.; Cao, G.; Wang, Z.; Yang, Y.; Shi, Z.; Gu, Z. *Journal Physical Chemistry C* **2008**, 112, 4524-4530.
- [24]Zhong, G. F.; Iwasaki, T.; Kawarada, H. *Carbon* **2006**, 44, 2009-2014.
- [25]Kayastha, V. K.; Yap, Y. K.; Pan, Z.; Ivanov, I. N.; Poretzky, A. A.; Geohegan, D. B. *Applied Physics Letters* **2005**, 86, 253105(3).
- [26]Kayastha, V. K.; Wu, S.; Moscatello, J.; Yap, Y. K. *Journal of Physical Chemistry C* **2007**, 111, 10158-10161.
- [27]Wang, Y.; Luo, Z.; Li, B.; Ho, P. S.; Yao, Z.; Shi, L.; Bryan, E. N.; Nemanich, R. J. *Journal of Applied Physics* **2007**, 101, 124310(8).
- [28]Futaba, D. N.; Hata, K.; Namai, T.; Yamada, T.; Mizuno, K.; Hayamizu, Y.; Yumura, M.; Iijima, S. *Journal of Physical Chemistry B* **2006**, 110, 8035-8038.
- [29]Nessim, G. D.; Hart, A. J.; Kim, J. S.; Acquaviva, D.; Oh, J.; Morgan, C. D.; Seita, M.; Leib, J. S.; Thompson, C. V. *Nano Letters* **2008**, 8, 3587-3593.
- [30]Thompson, C. V. *Acta Metallurgica* **1988**, 36, 2929-2934.
- [31]Zhang, Q.; Zhou, W.; Qian, W.; Xiang, R.; Huang, J.; Wang, D.; Wei, F.; *Journal of Physical Chemistry C* **2007**, 111, 14638-14643.
- [32]Zhu, L.; Xiu, Y.; Hess, D. W.; Wong, C. P. *Nano Letters* **2005**, 5, 2641-2645.

[33] Yasuda, S.; Hiraoka, T.; Futaba, D. N.; Yamada, T.; Yumura, M.; Hata, K.

Nano Letters **2009**, 9, 769-773.

[34] Feng, X.; Liu, K.; Xie, X.; Zhou, R.; Zhang, L.; Li, Q.; Fan, S. S.; Jiang, K.

Journal of Physical Chemistry C **2009**, 113, 9623-9631.

Chapter 4

Growth Kinetics of Millimeter-Scale Carbon Nanotube Arrays by Chemical Vapor Deposition in the Presence and Absence of Water: Mechanisms in Lengthening and Thickening Stages*

*Material in this chapter has been published in:

Cui, X. W.; Wei, W. F.; Chen, W. X. **Carbon**, 2010, 48, 2782-2791.

Cui, X. W.; Wei, W. F.; Chen, W. X. **Materials Research Society Symposium Proceedings**, Volume 1204, Warrendale, PA, 2010, paper number: 1204-K05-01.

4.1. Introduction

Since the unique electrical, thermal and mechanical properties of carbon nanotubes (CNTs) strongly depend on their structures [1, 2], tremendous efforts have been made to produce CNTs with desirable structures. To date, the growth of CNT arrays (CNTAs) by chemical vapor deposition (CVD) methods has attracted a great attention not only because of their characteristic CNT growth features, such as selective spatial growth, large area deposition, aligned growth [3], but also because of their flexible control of CNT structures, such as CNT length [4, 5], diameter [6, 7], wall number [8, 9], chirality [10, 11] and purity [12]. In particular, synthesis of single-walled CNT (SWCNT) and multiwalled CNT (MWCNT) arrays by chemical vapor deposition (CVD) in both presence (water-assisted CVD (WACVD)) and absence (conventional CVD (CCVD)) of water has been extensively studied. Iijima et al. reported a super-growth of 2.5 mm single-walled CNT (SWCNT) arrays in 10 min by WACVD [4]. Millimeter-scale MWCNT arrays, especially double-walled CNT (DWCNT) arrays, have also grown successfully through WACVD and CCVD [7, 13-15]. In addition, a broad range of applications for SWCNTs, MWCNTs and their arrays has been explored in many areas, such as field emission devices [16, 17], electrochemical and biosensors [13, 18], supercapacitors [19], etc. To modify MWCNT properties and to extend its applications, the control of wall number is important. For instance, SWCNTs, despite of diverse properties, have shown unsatisfactory electrical and thermal

stability, which can be compromised by using DWCNTs [7]. In this sense, precise control of CNT wall number becomes particularly important because MWCNTs may possess unique properties of interest as wall number changes.

A clear understanding of the growth mechanism and growth kinetics of CNTAs would serve as a guide to the manipulation of CNT structures. The growth kinetics of SWCNT arrays by WACVD has been investigated by Hata et al. [20]. It was found that the growth of SWCNT array agrees well with the radioactive decay model, and the effect of water was proved to act as a weak oxidizer to enhance and preserve catalyst activity. Recently, the accumulation process of carbonaceous impurities resulting from the pyrolytic deposition on the CNTAs has been exclusively studied [12]. These theoretical studies of SWCNT array growth provide a key to control SWCNT length and purity. However, so far, theoretical studies of MWCNT arrays, which are also crucial for controlling MWCNT structures, especially CNT wall number, haven't been clearly elucidated.

This study was initiated to investigate and understand the growth kinetics of MWCNT arrays in WACVD and CCVD. The growth kinetics of MWCNT arrays in WACVD and CCVD were investigated by field emission scanning electron microscopy (FESEM), and the CNT diameter and wall number were investigated by high resolution transmission electron microscopy (HRTEM). It was found that

the kinetics in both methods demonstrates lengthening and thickening stages, as was found for the vapor grown carbon fibers [21]. Here, the lengthening is defined as the increase of CNTA height, while the thickening is referred to as the increase of CNT wall number. The detailed analyses of the kinetics in the lengthening stage and thickening stage are presented. The effect of water and the effect of ethylene and hydrogen gas flow rates in WACVD have also been elucidated. These findings provide an improved understanding of the growth mechanism and growth kinetics of MWCNT arrays, which may shed light on fabricating MWCNTs with controlled structures and properties.

4.2. Experimental Procedure

A buffer layer of 30 nm-thick Al_2O_3 and a catalyst film of 1 nm-thick Fe were sputtered sequentially on Si wafers. The sputtering process, catalyst film pretreatment and MWCNT array growth by CCVD and WACVD were presented in detail in Chapter 2. To investigate the effects of ethylene and hydrogen flow rates, different rates of C_2H_4 or H_2 were flowed into the system in the MWCNT array growth stage for 30 min with other parameters fixed.

The height of MWCNT arrays were characterized by a JSM-6301FXV FESEM. To obtain a statistical distribution of CNT wall number, more than 200 individual

CNTs under each growth condition were examined by HRTEM (JOEL 2010 operated at 200 kV). Raman spectra were collected in back-scattering geometry with a custom Raman spectrometer. Raman scattered light was collected normal to the sample surface where at least three positions were randomly chosen on each sample.

4.3. Results and Discussion

4.3.1. Lengthening and Thickening Process in WACVD

Figure 4-1a shows the growth kinetics of MWCNT arrays fabricated through WACVD under the conditions of 400 sccm C₂H₄, 400 sccm H₂, 200 sccm Ar and 100 sccm Ar/H₂O. The lengthening rate of the array height was found to be constant at 48 μm/min in the initial 45 min. It then gradually decreased over the subsequent 15 min, finally reaching an array height of 2.3 mm. Figures 4-1b to 4-1e display the typical HRTEM images of MWCNTs grown for different periods. Little increase of CNT wall number can be observed in the initial 45 min (Figures 4-1b and 4-1c), while the increase of CNT wall number is seen to be predominant after 45 min (Figures 4-1d and 4-1e). Figure 4-1 clearly demonstrates two distinct stages of MWCNT array growth in WACVD: the linear lengthening stage (before 45 min) and the thickening stage (after 45 min). This long linear lengthening stage has not been characterized so far, although it appeared in the growth of MWCNT

arrays by WACVD in Schulz's work [23]. It should note that the growth kinetics of MWCNT arrays in WACVD is quite different from that of SWCNT arrays. For the latter case, the lengthening rate decreased exponentially with time and no noticeable linear lengthening stage has been identified [20].

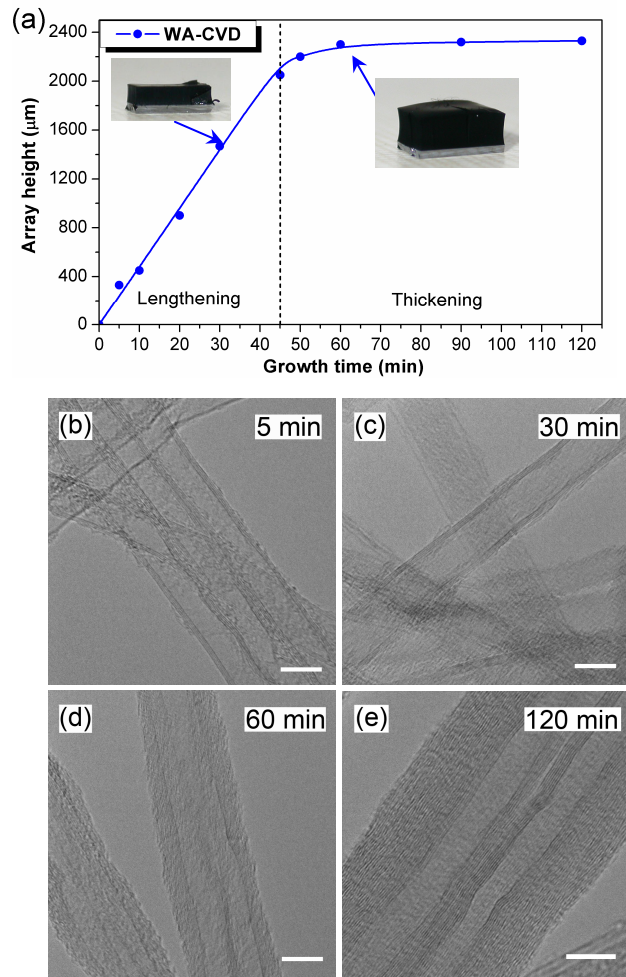


Figure 4-1. (a) The growth kinetic curve of MWCNT arrays grown by WACVD; the insets are photographs of millimeter-long MWCNT arrays in two stages (Si wafer is 500 μm thick). (b)-(e) are typical HRTEM images of MWCNTs grown by WACVD for (b) 5 min; (c) 30 min; (d) 60 min; (e) 120 min, respectively. (Scale bar in HRTEM images: 10 nm)

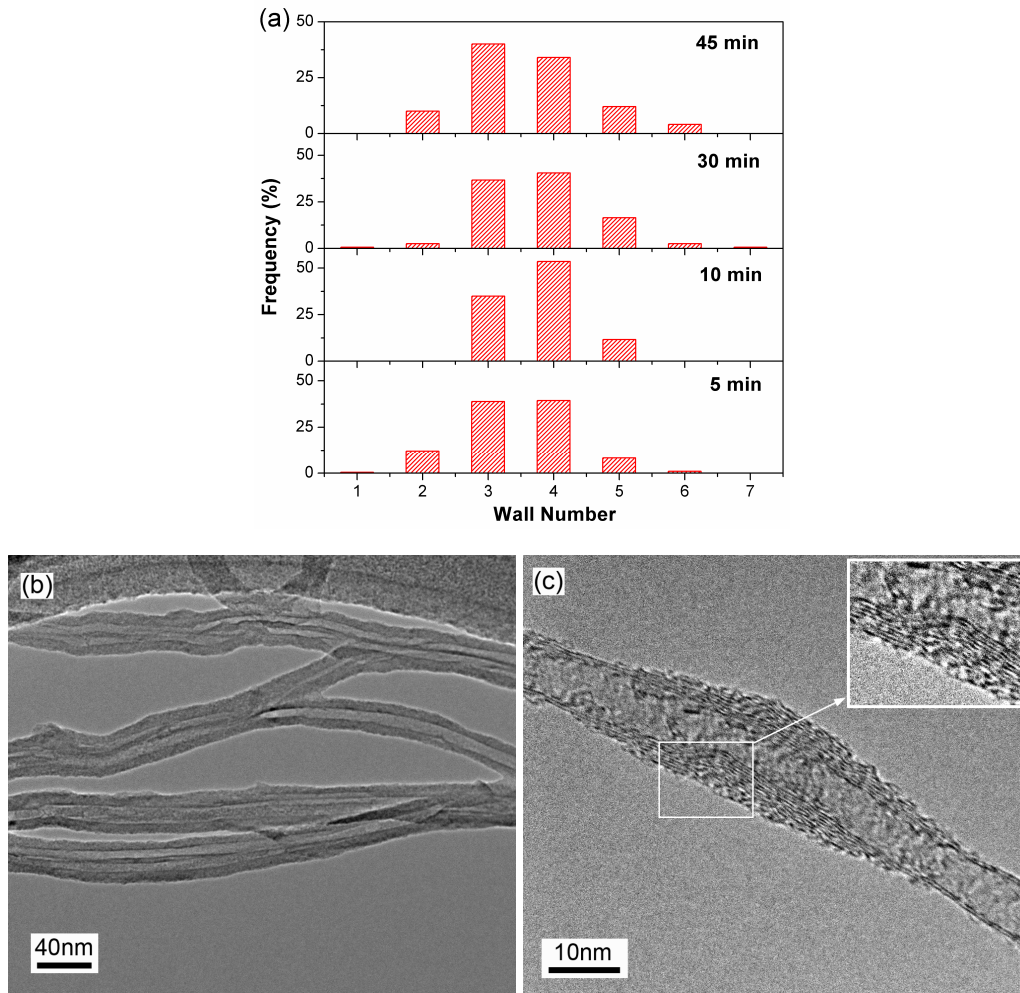


Figure 4-2. (a) A family of histograms of the wall number of MWCNTs grown for different periods, from 5 min to 45 min, by WACVD. (b) TEM image of MWCNTs grown by WACVD for 120 min showing the final stage of gas phased-induced thickening. (c) HRTEM image of a DWCNT grown by WACVD for 60 min showing the nucleation stage (conical structure) of gas phased-induced thickening.

The statistical distribution of wall number of MWCNTs grown for various periods

up to 45min by WACVD is shown in Figure 4-2a. In the lengthening stage of WACVD, CNT wall number distributes in a very narrow range with triple-walled and four-walled CNTs taking up over 80% of total MWCNTs; and the average wall number, as calculated based on the histograms, remained constant (Figure 4-3). The substantial increase of CNT wall number after 45 min was also extensively studied by HRTEM, as shown in Figures 4-1 and 4-2. Figure 4-1e and Figure 4-2b show a segment of two MWCNTs grown next to each other; thick graphitic layers were found only on the surfaces exposed to the reactive gases, while the wall number didn't increase on the unexposed surfaces. This implies that the outer walls were deposited from the gas phase, probably because the reactive gases cannot diffuse into the small interspacing between the MWCNTs. The deposition of graphitic layers on CNTs from the gas phase during CNTA growth was also reported recently in other studies [12, 24]. In addition, it was further revealed in this study that the nucleation sites of graphitic layers on CNT walls from the gas phase appear conical in morphology, as shown in Figure 4-2c. The formation and growth mechanism of conical structure on MWCNTs at high temperatures ($>1050^{\circ}\text{C}$) were elaborately investigated by Monthieux et al. [25-27]. The preferential nucleation of graphitic layers at the defects on CNT walls (also shown in Figure 4-2c) could serve as an alternative explanation of forming conical structure at the lower growth temperature (775°C). Since catalysts are not involved, this thickening process is termed as gas phase-induced

thickening in this study. It should be noted that the variation of wall number along the tube axis in Figure 4-1d demonstrates the intermediate stage of the gas phase-induced thickening process.

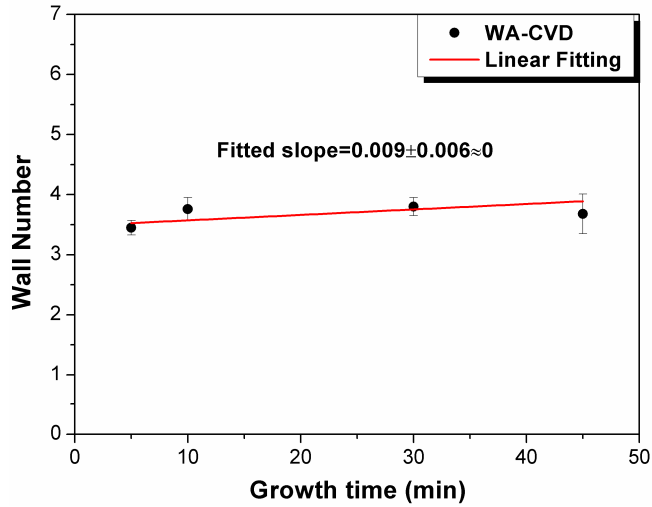


Figure 4-3. Plot of CNT wall number as a function of growth time in the initial 45 min of WACVD. The solid line is the linear fitting line with very small slope showing that the CNT wall number remained constant in the initial 45 min of WACVD.

A radioactive decay model was proposed by Hata et al. [20] to explain SWCNT array growth in WACVD, which can be expressed by

$$H(t) = \beta\tau_0(1 - e^{-t/\tau_0}) \quad (4-1)$$

where H , β and τ_0 are the height, the initial lengthening rate and the characteristic catalyst lifetime of SWCNT arrays, respectively. For MWCNT array

growth in WACVD, the entire growth kinetics shown in Figure 4-1a could not be fitted by the radioactive decay model to an acceptable agreement, because of a considerable long linear lengthening stage in the initial 45 min. However, fitting the kinetics data for the growth periods from 45 min to 120 min by the radioactive decay model with a predetermined initial lengthening rate of 48 $\mu\text{m}/\text{min}$ yielded excellent agreement ($R^2 = 0.9962$), as shown in Figure 4-4a. The fitted characteristic catalyst lifetime is 5.56 min. According to Eq. (4-1), the product of the initial lengthening rate and the characteristic lifetime when added up to the MWCNT array height at 45 min gives the theoretical maximum height, H_{max} , which is calculated to be 2317 μm and matches well with the experimentally obtained maximum height of 2330 μm . Since Eq. (4-1) quantitatively describes the deactivation kinetics for catalyst particles [28], the simulated results reveal that catalyst particles start to deactivate from 45 min. As a result, the simulation further proves that the growth kinetics of MWCNT arrays in WACVD can be divided into two stages, a lengthening stage and a thickening stage. In the lengthening stage, the deactivation of catalyst particles is negligible, while in the thickening stage the deactivation of catalyst particles is evident and follows the radioactive decay model. Interestingly, the constant lengthening rate of the array height (Figure 4-1a) and the unchanged CNT wall number (Figure 4-2a) in the lengthening stage indicate that the deposition rate of MWCNT graphitic layers from catalysts is invariable. This, in turn, supports that the catalyst activity

remains unchanged in the lengthening stage of WACVD.

To quantitatively describe the growth kinetics of MWCNT arrays in the lengthening stage of WACVD, the dimension of a MWCNT is defined in Figure 4-4b. Based on Figure 4-4b, the area (A) of graphitic walls of a MWCNT is calculated as

$$A = 2\pi n \left(r + \frac{n-1}{2} d \right) l \quad (4-2)$$

where l, r, n, d are the MWCNT length, inner radius, wall number, interspacing of graphitic walls (0.34 nm), respectively. In the case of a fixed wall number, Eq. (4-3) can be derived from Eq. (4-2) as

$$\frac{dl}{dt} = \frac{M}{2\pi n \left(r + \frac{n-1}{2} d \right)} \quad (4-3)$$

where M is the deposition rate of graphitic layers ($M = dA/dt$). M is related to catalyst activity if n is the intrinsic wall number (the wall number that is not caused by the gas phase-induced thickening). Assuming that CNTA height can be linearly correlated to the actual CNT length by a coefficient depending on the amplitude of CNT waviness, l could also be considered to be CNTA height. This assumption is reasonable especially for CNTAs that grow from catalyst patterns with very small inter-particle spacing, in which MWCNTs were observed to be

less deviated from the growth direction [22]. Therefore, Eq. (4-3) reveals that MWCNT array height increases linearly with growth time when catalyst activity and the intrinsic wall number of MWCNTs remain constant, which quantitatively reflects the situation of MWCNT array growth in the linear lengthening stage of WACVD (Figure 4-1a). This finding may point to a promising direction for harvesting MWCNTs with desirable characteristics: by choosing proper growth conditions, different linear lengthening stages corresponding to different wall number could be obtained to produce MWCNT arrays with desirable height and CNT wall number.

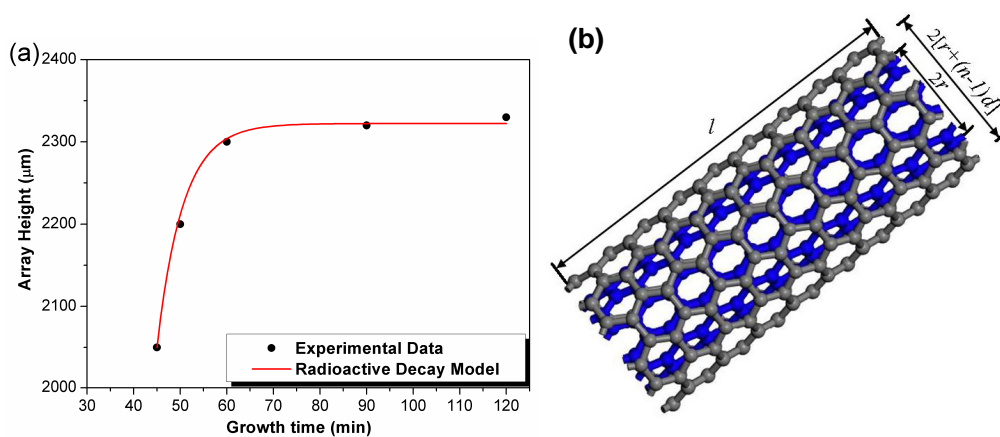


Figure 4-4. (a) The fitting of the growth kinetic data (dots) of MWCNT arrays grown after 45 min by WACVD to the radioactive decay model (solid line). (b)

The defined parameters for the dimension of a MWCNT.

It is noted that MWCNTs grown by WACVD in this investigation have a larger

inner diameter (7.1 nm) than that in Hata's work (2.8 nm) [19, 29], indicating a larger catalyst particle size for this MWCNT array growth. Smaller catalyst particles are suggested to have higher activities [30, 31]. It is consistent with the considerable difference in the initial growth rate (IGR) observed in these two studies, 207 $\mu\text{m}/\text{min}$ for the supergrowth [20] and 48 $\mu\text{m}/\text{min}$ for WACVD in this work. This clearly demonstrates the dominant effect of particle size on IGR, although the growth rate could also be affected by catalyst particle interspacing [22] and by catalyst-buffer layer interaction [32, 33]. Gohier et al. [31] also stated that larger catalyst particles have lower chemical reactivity, and hence carbon patches/embryos should be less tightly bound on the surface of the larger particles. As such, the weaker binding of carbon embryos deposited on the surface of large particles could retard the nucleation of graphitic layers on catalyst, which was reported to deactivate catalyst by preventing further absorption of carbon atoms on catalyst [24]. Therefore, the existence of a lengthening stage with unchanged catalyst activity can be expected due to the presence of larger catalyst particles, in comparing with those reported in Hata's work [19, 20].

4.3.2. Lengthening and Thickening Process in CCVD

The growth kinetics of MWCNT arrays in CCVD under the conditions of 400 sccm C_2H_4 , 400 sccm H_2 and 200 sccm Ar is shown in Figure 4-5a. Apparently,

there is no linear lengthening stage for MWCNT array growth in CCVD as that seen in WACVD. As also shown in Figure 4-5, most CNTs grown for 5 min are double-walled and triple-walled (Figure 4-5b). The CNT wall number increases up to 4-5 walls for the growth period of 15 min (Figure 4-5c), and to 6-8 walls for 30 min (Figure 4-5d). The statistical distribution of wall number of MWCNTs

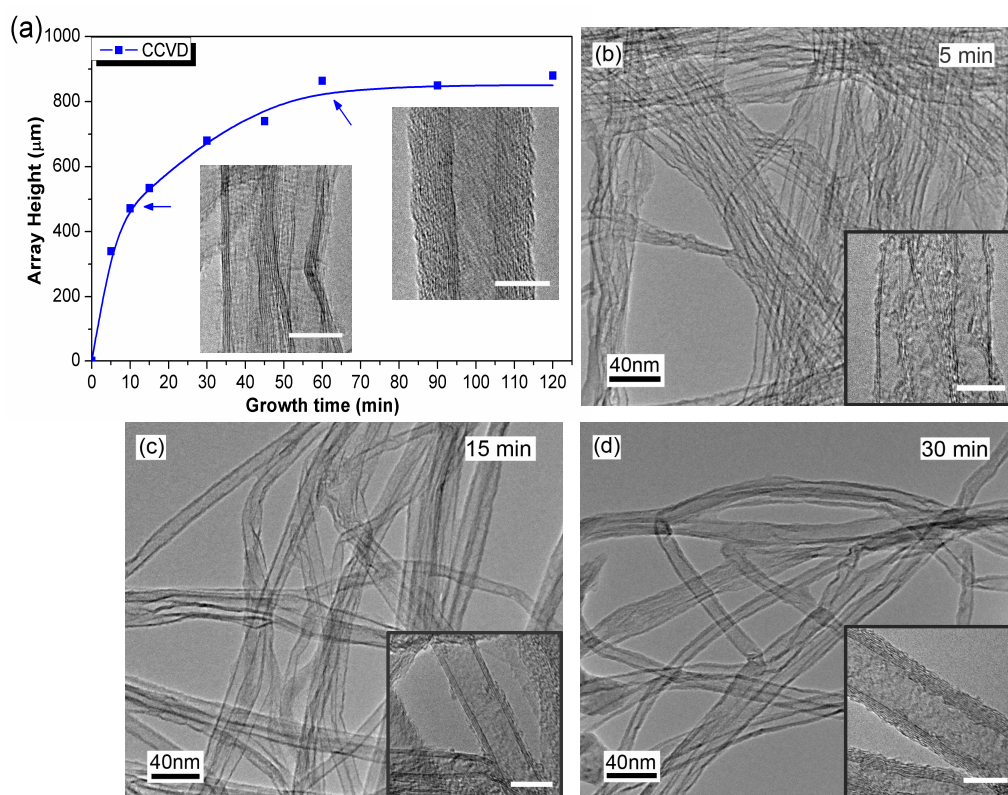


Figure 4-5. (a) The growth kinetic curve of MWCNT arrays grown by CCVD; the insets are HRTEM images of MWCNTs grown for 10 min and 60 min in CCVD. (b) and (c) are TEM images of MWCNTs grown in CCVD for 5 min, 15 min and 30 min, respectively. (Scale bar in HRTEM images: 10 nm)

grown for various periods up to 30 min by CCVD is shown in Figure 4-6. It is interesting that MWCNTs with different wall numbers could be selectively produced in CCVD simply by a control of the growth period in this stage (before 30 min). For longer growth periods, CNT wall number increases rapidly and gas phase-induced thickening becomes prominent, since similar thickening behaviour as shown in Figure 4-2b was easily observed at the growth periods after 60 min in CCVD. In addition, a few MWCNTs grown for 30 min have also been found to undergo nucleation (conical structure) for gas phase-induced thickening (Figure 4-7) indicating the onset of the gas phase-induced thickening process after 30 min in CCVD.

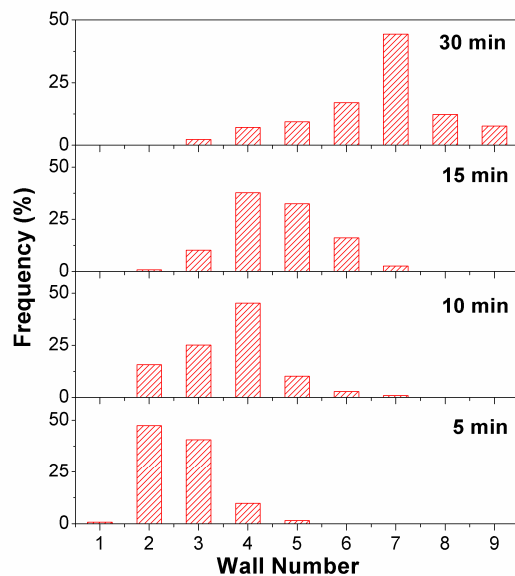


Figure 4-6. A family of histograms of the wall number of MWCNTs grown for different periods, from 5 min to 30 min, by CCVD. The thickening process in the lengthening stage of CCVD is confidently proved by this diagram.

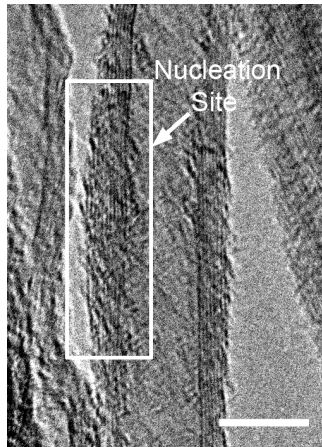


Figure 4-7. HRTEM image of a MWCNT grown for 30 min by CCVD showing the nucleation sites (conical structure) for the gas phase-induced thickening.

(Scale bar in the HRTEM image: 10 nm)

MWCNT array height was plotted as a function of CNT wall number in Figure 4-8a. It is evident that in the lengthening stage of CCVD (before 30 min), the lengthening process is predominant, and CNT wall number increases slowly. In the thickening stage of CCVD (after 30 min), the thickening process becomes dominated with little increase of MWCNT array height. Figures 4-5 and 4-8a indicate that the kinetics of MWCNT array growth in CCVD demonstrates competitive lengthening and thickening processes with the thickening process occurring in CCVD much earlier (after 5 min) than that in WACVD (after 45 min).

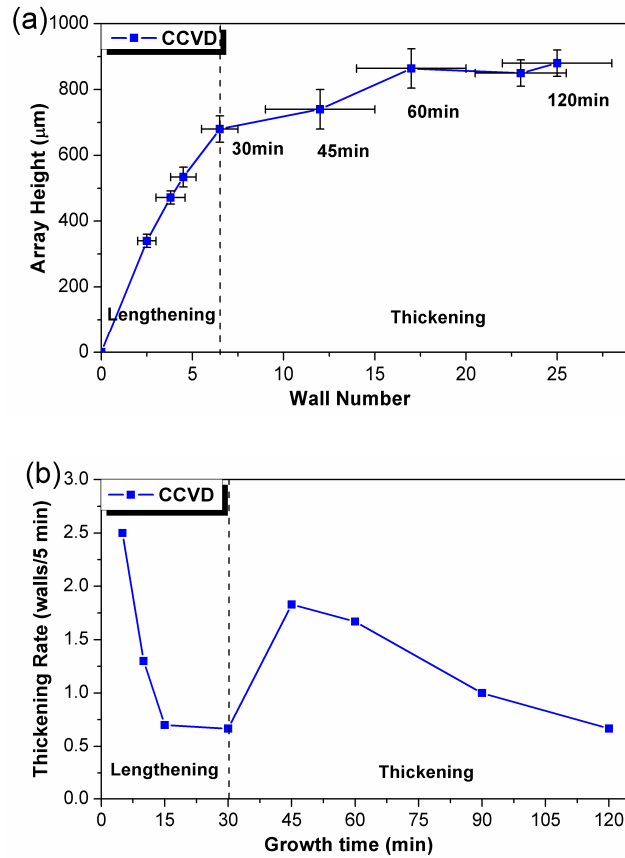


Figure 4-8. Plots of (a) MWCNT array height vs. CNT wall number; (b) MWCNT thickening rate vs. growth time, in CCVD.

To further disclose the distinct thickening behaviour in CCVD, the thickening rate is plotted as a function of growth time in Figure 4-8b. It is seen in the figure that the thickening rate decreases in the initial 30 min, quickly increases after 30 min and then decreases again. As gas phase-induced thickening becomes predominant after 30 min growth, the increase of thickening rate after 30 min indicates that the accumulation rate of graphitic layers from the gas phase increases with growth

time. This is because carbon species previously deposited act as nuclei for further carbon accumulation, which is consistent with the results reported by Hata et al. [12]. As MWCNTs grow in wall number, CNT interspacing decreases. This may restrict the flow of reaction gases into the MWCNT arrays and reduce the exposure of MWCNTs to the gas phase. Hence, the thickening rate decreases substantially after 60 min. However, the rapid decrease of the thickening rate in the lengthening stage of CCVD, as seen in Figure 4-8b, remains unclear. The nucleation of conical structure by gas phase-induced thickening was not observed in this stage from extensive TEM characterization. It means that the extension of newly nucleated graphitic layers is much faster than continuous nucleation of new graphitic layers at the same location forming the conical structure. More discussion about the distinct thickening behaviour in this stage will be presented later.

Based on the results shown in Figures 4-5 and 4-8, a simulation of CNT wall number vs. growth time was made for MWCNT arrays grown by CCVD. A sheaf of straight lines can be created in Figure 4-5a by connecting the origin to the various points of array height. According to Eq. (4-3), each straight line is characterized by a fixed M value representing the average deposition rate of graphitic layers (dA/dt) up to the growth period, and a fixed n value equal to the CNT wall number of the MWCNT arrays at the growth period. The simulation

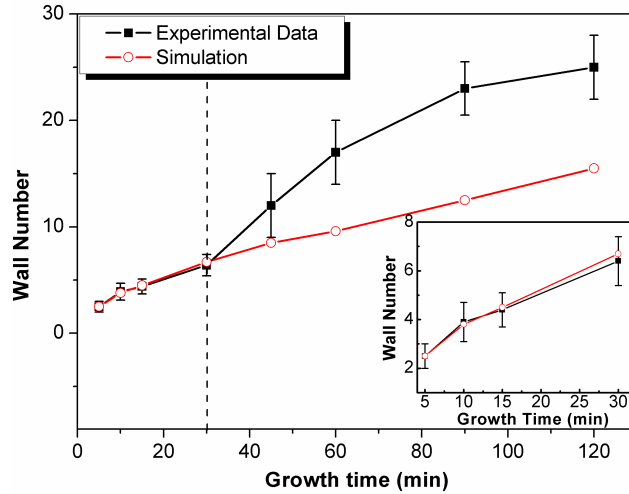


Figure 4-9. Plot of CNT wall number as a function of growth time in CCVD; the inset is the enlarged view of the fitting curve in the initial 30 min.

shown in Figure 4-9 was made through the following steps of calculation: first, the initial value of M was obtained from the average growth rate up to 5 min's growth, as shown in Figure 4-5a, and the average CNT wall number of MWCNT arrays grown for 5 min; this initial M value was then used to predict the CNT wall number corresponding to all subsequent growth periods. Figure 4-9 displays that the predicted wall numbers are in a good agreement with the experimental data obtained in the initial 30 min, but appear quite deviated after 30 min. The deviation after 30 min suggests a higher M value in this stage. The increase in M value proves that gas phase-induced thickening become predominant after 30 min, because of the direct deposition of graphitic layers on the CNT walls from the gas phase. On the other hand, M value shows little change for the growth time less than 30 min. The calculation in this stage further reveals that the

competitive nature of lengthening and thickening is solely governed by the rate of carbon deposition (constant M); and CNTA height and CNT wall number can be therefore predicted according to Eq. (4-3). This finding provides us with experimental solutions to fabricate MWCNTs with characteristic structures such as CNTA height and CNT wall number.

4.3.3. Raman Spectroscopy and Thickening Behavior in the Lengthening Stage of CCVD

Raman Spectroscopy is widely used in examining the structural changes of MWCNTs [34]. In this study, first-order Raman Spectroscopy (514.5 nm) was employed on the MWCNT arrays grown for different periods by WACVD and CCVD. The Raman spectra normalized to D peak as shown in Figures 4-10a and 4-10b demonstrate two Raman bands, G band and D band. G band, at $\sim 1570 \text{ cm}^{-1}$, is related to graphite tangential E_{2g} Raman active mode, which is due to the stretching vibrations of sp^2 -hybridized carbon. D band, $\sim 1345 \text{ cm}^{-1}$, is a breathing mode of A_{1g} symmetry, which only becomes active in the presence of disorder, such as heteroatom vacancies, grain boundaries, finite size effects or other effects [35]. Accordingly, the intensity ratio of I_G/I_D gives the information about the crystallinity of MWCNTs, which was plotted versus growth time in Figure 4-10c. The I_G/I_D ratio close to unity shown in Figure 4-10c is typical for

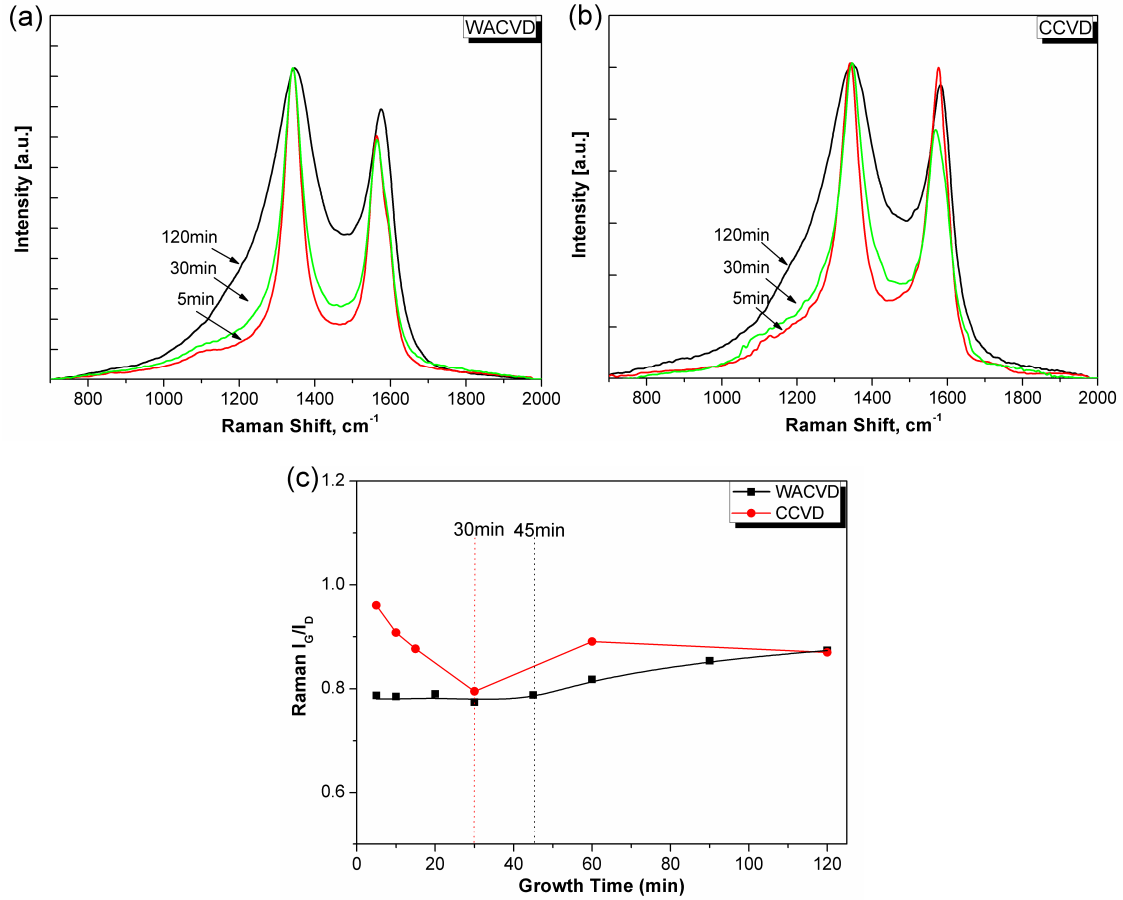


Figure 4-10. Raman spectra for MWCNT arrays grown for 5 min, 30 min and 120 min by (a) WACVD and (b) CCVD. (c) The growth time dependence of G/D ratio.

MWCNT arrays grown by other thermal CVD methods [15, 24, 36]. As also shown in Figure 4-10c, the I_G/I_D ratio displays a little variation for the MWCNT arrays grown by WACVD. The deposition of graphitic layers on SWCNTs could decrease the I_G/I_D ratio (from ~ 11 to ~ 4) [12]; however, no decrease of I_G/I_D ratio has been detected in the thickening stage of WACVD. Instead, the D peak is substantially broadened by gas phase-induced thickening, as shown in Figure

4-10a. The broadening of the D peak is related to a distribution of clusters with different orders and dimensions [37], and thus it also indicates the deterioration of the crystallinity of MWCNTs. The broadening of D peak is clearly shown for the MWCNT arrays after 30 min growth by CCVD (Figure 4-10b) suggesting that gas phase-induced thickening becomes predominant in this stage, which is consistent with HRTEM observations. Interestingly, Figure 4-10b and 4-10c also demonstrates that the I_G/I_D ratio decreases for the MWCNT arrays grown in the initial 30 min of CCVD. It is a different trend from that in WACVD. The decrease of the I_G/I_D ratio in the lengthening stage of CCVD can be attributed to the distinct thickening process observed in this stage, which will be discussed in detail in the following paragraph.

As discussed in Figure 4-8b, the extension of newly nucleated graphitic layers is much faster than continuous nucleation of new graphitic layers at the same location forming the conical structure in the lengthening stage of CCVD. Thus, the thickening rate in this stage is determined by the nucleation rate of graphitic layers. Amelinckx et al. [38] proposed that additional graphitic layers would nucleate during MWCNT growth, from the nearest active sites on catalyst or by forming graphene caps around catalyst. This is reasonable because the nucleation rate may be different from the inner walls to the outer walls. Our finding about the nucleation of graphitic layers on CNT walls also suggests their nucleation on the

surface of catalyst. It was further proposed that, once new graphitic layers are nucleated on catalyst, they could be extended either by carbon diffusion from catalyst or by carbon deposition directly from the gas phase. It should be noted that, although the thickening in the latter case is caused by carbon deposition from the gas phase, it occurs through a process involving catalyst; and therefore, this thickening process is termed as catalyst-induced thickening in this study. Furthermore, graphitic layers, even if they are nucleated at the defects on CNT walls, could have been joined with graphitic layers nucleated at and grown from catalyst; otherwise, the conical structures should be observed in this stage. The schematic diagram of catalyst-induced thickening and gas phased-induced thickening is shown in Figure 4-11.

The nucleation of graphitic layers should be slower on larger catalyst particles, as discussed in WACVD. Therefore, with increasing number of graphene caps around catalyst, catalyst particle size increases and catalyst activity decreases, both of which could reduce the nucleation rate of graphitic layers on catalyst. This explains why the thickening rate decreases with growth time in the lengthening stage of CCVD. In addition, although catalyst-induced thickening couldn't form conical structure, it still induces new defects during the extension of newly nucleated graphitic layers, which decreases the I_G/I_D ratio in the lengthening stage of CCVD. The constant I_G/I_D ratio in the lengthening stage of WACVD confirms

that no thickening process occurs in this stage, which is also consistent with HRTEM observations.

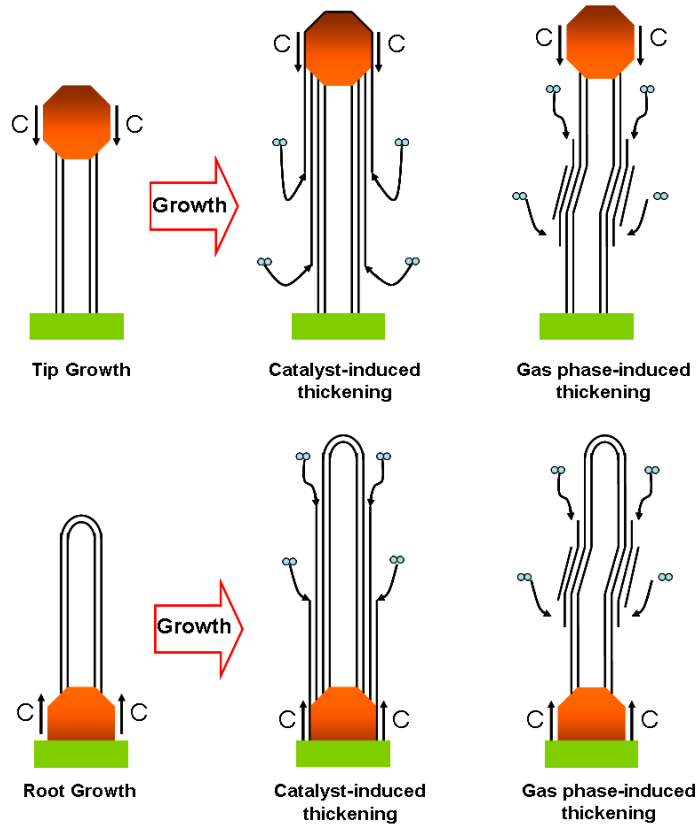


Figure 4-11. Schematic diagram of catalyst-induced and gas phase-induced thickening for both tip and root growth modes.

4.3.4. The Effect of Water

This study investigated the growth kinetics of MWCNT arrays by CVD in the presence and absence of water in the same system. The beneficial effect of adding

water in the MWCNT array growth environment is clearly presented. By comparing Figure 4-1a with Figure 4-5a, the duration of the lengthening stage in WACVD is longer (45 min) than that in CCVD (30 min); and the catalysts maintain their activity for a long period, 45 min, in WACVD. These results indicate that water preserves catalyst activity for MWCNT growth, which agrees well with the result reported before [20]. More importantly, the analyses in this study also prove that water preserves the catalyst activity by significantly inhibiting catalyst-induced and gas phase-induced thickening processes in the lengthening stage of WACVD, in addition to the general belief that water is able to burn out amorphous carbon on catalyst. This might be because water, as a weak oxidizer, increases the activation energy for graphitic layers to nucleate on catalyst or at the defects of CNT walls from the gas phase. Furthermore, adding water was proved to inhibit Ostwald ripening due to the ability of oxygen and hydroxyl species to reduce diffusion rates of catalyst atoms [39]. Our study also shows that the beneficial effect of water reported here can be achieved only when the catalyst films were pretreated in a Ar and H₂ gas mixture containing small amount of water. It implies that the modification of catalyst particle surface or catalyst pattern in the presence of water is another important factor to inhibit the thickening processes in the lengthening stage of WACVD, which requires further investigation in the future.

4.3.5. The Effects of Ethylene and Hydrogen for MWCNT Array Growth in WACVD

The effects of ethylene and hydrogen were further investigated to understand the growth mechanism and to optimize the growth conditions for MWCNT arrays in WACVD. Figure 4-12a shows the variation of CNTA heights with the ethylene flow rates spanning from 25 sccm to 400 sccm at the array growth period of 30 min. Other growth parameters were fixed as in Figure 4-1.

The CNTA height was found to increase sharply for the ethylene flow rates from 25 sccm to 100 sccm, and level off for the larger ethylene flow rates. The statistical distribution of the wall number of MWCNTs grown under different ethylene flow rates is also shown in Figure 4-12b. It is demonstrated that MWCNTs have 2-4 walls, when the ethylene flow rate is lower than 100 sccm; while the CNT wall number was increased to 3-5 walls when the ethylene flow rate is larger than 200 sccm. Low ethylene flow rate can shift the dynamic equilibrium and CNT growth process to carbon radical shortage [40, 41]; hence, MWCNT array growth is limited by the low concentration of carbon radicals in the low ethylene flow rate region (<100 sccm). In addition, carbon radicals were not consumed to increase CNT wall number in this region. Therefore, CNTA height increases fast with ethylene flow rate when it is lower than 100 sccm. However, the CNT wall number was raised by continuously increasing the C_2H_4

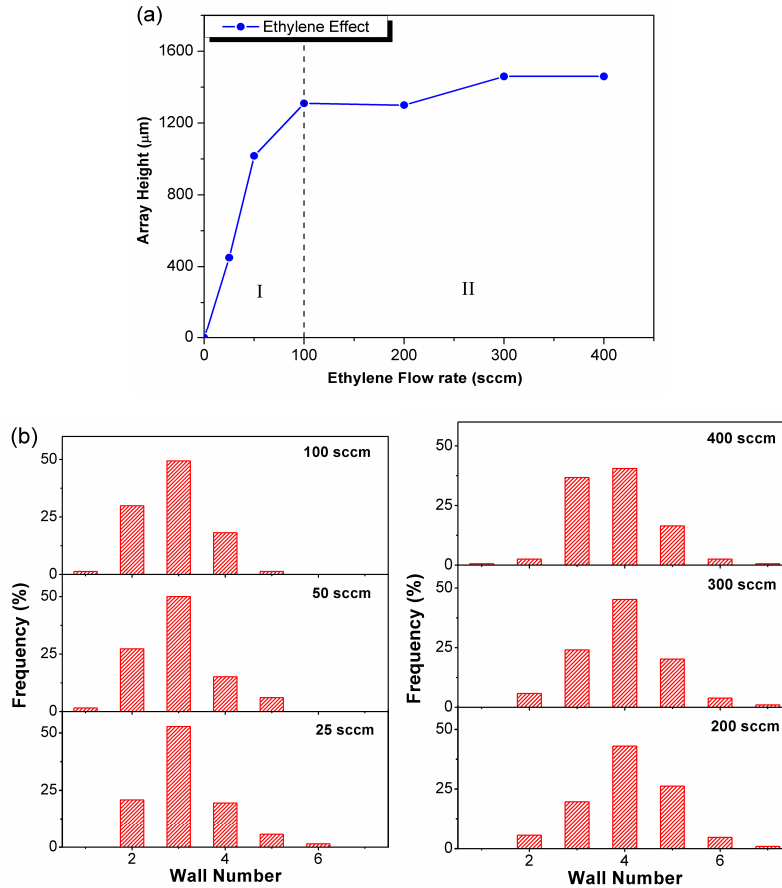


Figure 4-12. (a) MWCNT array height vs. ethylene flow rate. (b) A family of histograms of the wall number of MWCNTs grown for different ethylene flow rates, from 25 sccm to 400 sccm, by WACVD.

flow rate from 100 sccm to 200 sccm, which is consistent with the ethylene effect in CCVD reported by Zhang et al. [42]. This indicates that ethylene flow rate influences MWCNT array growth not only in the growth stage of CNTAs, but also in the nucleation stage of CNT walls. Further increase of ethylene flow rate may make the ethylene over-saturated and not be involved in the MWCNT array growth.

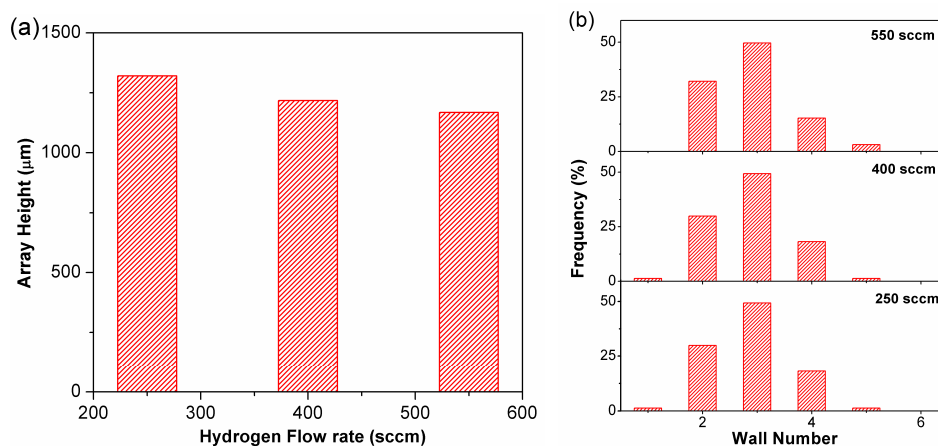


Figure 4-13. (a) MWCNT array height vs. hydrogen flow rate. (b) A family of histograms of the wall number of MWCNTs grown for different hydrogen flow rates, from 250 sccm to 550 sccm, by WACVD.

Hydrogen also has a strong effect on MWCNT array growth by etching polycyclic hydrocarbon species which tends to encapsulate catalyst surfaces [43]. In this study, the hydrogen effect was examined at the growth conditions of 100 sccm C_2H_4 , 200 sccm Ar, 100 sccm Ar/ H_2O and growth period of 30 min. Figure 4-13a shows the variation of CNTA heights with hydrogen flow rates ranging from 250 sccm to 550 sccm. The statistical distribution of CNT wall number under different hydrogen flow rates is also displayed in Figure 4-13b. Surprisingly, no significant change of CNTA height and CNT wall number was observed within this large-range variation of hydrogen flow rate. It should be noted that the change of hydrogen flow rate was only conducted in the MWCNT array growth stage, while that used to pretreat the catalyst films was maintained at 400 sccm.

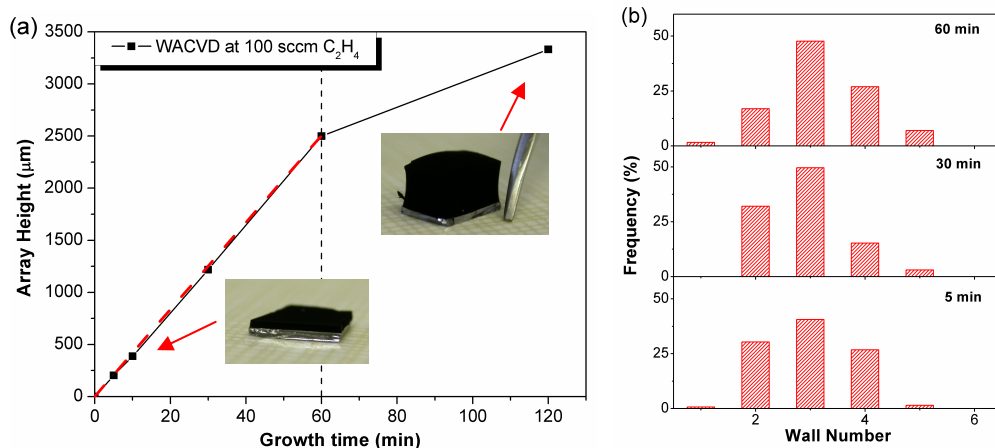


Figure 4-14. (a) The growth kinetic curve of MWCNT arrays grown by WACVD at 100 sccm C_2H_4 ; the insets are photographs of millimeter-long MWCNT arrays in two stages (Si wafer is 500 μm thick). (b) A family of histograms of the wall number of MWCNTs grown for different periods, from 5 min to 60 min, by WACVD at 100 sccm C_2H_4 .

Since the ethylene flow rate at 100 sccm is a critical point, the growth kinetics of MWCNT arrays was also performed under the conditions of 100 sccm C_2H_4 , 400 sccm H_2 , 200 sccm Ar and 100 sccm Ar/ H_2O , as shown in Figure 4-14a. This kinetic curve demonstrates a long linear lengthening stage, which is consistent with the growth kinetics curve obtained at 400 sccm C_2H_4 in Figure 4-1a. In addition, the CNT wall number in this linear lengthening stage was found to be the invariable, as shown in the histograms in Figure 4-14b, which proves that the catalyst activity remains unchanged in the linear lengthening stage of WACVD. Figure 4-1 and Figure 4-14 support the previous proposition in Section 4.3.1 that

by choosing proper growth conditions (changing ethylene flow rate in this case), different linear lengthening stages can be obtained, which guide us to produce MWCNT arrays with both selective height and controllable CNT wall number. It is also suggested that changing the H₂O level may be another route to acquire different linear lengthening stages.

The effect of ethylene can be further explored by comparing two kinetic curves in Figure 4-1a and Figure 4-14a. It is noted that the linear lengthening stage is longer for 100 sccm C₂H₄ kinetics curve in Figure 5a (60 min) than that for 400 sccm C₂H₄ kinetics curve in Figure 1a (45 min). At high ethylene flow rate, the recombination of carbon radicals becomes significant [42], which makes the catalysts start to deactivate earlier by the faster nucleation of graphitic layers on the catalyst surfaces. From this point of view, the choice of 30 min as the growth period to investigate the ethylene effect in Figure 4-12 could avoid the effect of catalyst deactivation on the CNTA height. Furthermore, the etching of polycyclic hydrocarbon species that tends to encapsulate catalyst surfaces for hydrogen gas should be negligible in the linear lengthening stage before the deactivation of catalysts. This explains the insignificant effect of hydrogen flow rate on CNTA height and CNT wall number in this study. Although two kinetic curves in Figure 4-1a and Figure 4-14a gives linear lengthening stages with two different wall numbers, the fabrication of single-walled or double-walled CNTs in the CNTA

was not achieved by changing the reaction environment. To grow single-walled or double-walled CNTs, catalyst particles and their patterns (extremely small particles with small inter-particle spacing) should be the controlling factors. It is believed that fast-heating treatment is essential to achieve these required patterns.

4.4. Conclusions

By investigating the growth kinetics of MWCNT arrays, it was found that the kinetics demonstrates lengthening and thickening stages in both WACVD and CCVD. In the lengthening stage of WACVD, CNT wall number remains constant and catalysts preserve the activity; while in the thickening stage, MWCNTs thicken substantially by the gas phase-induced thickening process and catalysts deactivate following the radioactive decay model. In CCVD, the lengthening and thickening processes were found to be competitive. Although gas phase-induced thickening also predominates in the thickening stage of CCVD, it was found that catalyst-induced thickening occurs in the lengthening stage of CCVD. Furthermore, water was proved to preserve the catalyst activity by significantly inhibiting catalyst-induced and gas phase-induced thickening processes in WACVD. In addition, in WACVD, ethylene flow rate has a great influence on MWCNT array growth not only in the growth stage of CNTAs, but also in the nucleation stage of CNT walls; while hydrogen flow rate shows insignificant

effect on MWCNT array growth in the lengthening stage of WACVD. It is believed that this study, on one hand, confirms the existence of previously proposed radioactive decay model; but more importantly, reveals the unique growth mechanism and growth kinetics of MWCNT arrays in WACVD and CCVD, which are fundamentally different from those of SWCNT arrays. These results and analyses would provide us with a theoretical guide to the manipulation of CNT structures and thus CNT properties.

4.5. References

- [1]. Hamada, N.; Sawada, S. I.; Oshiyama, A. *Physical Review Letters* **1992**, 68, 1579-1581.
- [2]. Rao, A. M.; Richter, E.; Bandow, S.; Chase, B.; Eklund, P. C.; Williams, K. A.; Fang, S.; Subbaswamy, K. R.; Menon, M.; Thess, A.; Smalley, R. E.; Dresselhaus, G.; Dresselhaus, M. S. *Science* **1997**, 275, 187-191.
- [3]. Graham, A. P.; Duesber, G. S.; Hoenlein, W.; Kreupl, F.; Liebau, M.; Martin, R.; Rajasekharan, B.; Pamler, W.; Seidel, R.; Steinhögl, W.; Unger, E. *Applied Physics A* **2005**, 80, 1141-1151.
- [4]. Hata, K.; Futaba, D. N.; Mizuno, K.; Namai, T.; Yumura, M.; Iijima, S. *Science* **2004**, 306, 1362-1364.
- [5]. Meshot, E. R.; Plata, D. L.; Tawfick, S.; Zhang, Y.; Verploegen, E. A.; Hart, A. *J. ACS Nano* **2009**, 3, 2477-2486.
- [6]. Ci, L.; Vajtai, R.; Ajayan, P. M. *Journal of Physical Chemistry C* **2007**, 111, 9077-9080.
- [7]. Yamada, T.; Namai, T.; Hata, K.; Futaba, D. N.; Mizuno, K.; Fan, J.; Yudasaka, M.; Yumura, M.; Iijima, S. *Nature Nanotechnology* **2006**, 1, 131-136.
- [8]. Patole, S. P.; Alegaonkar, P. S.; Shin, H. C.; Yoo, J. B. *Journal of Physics D: Applied Physics* **2008**, 41, 155311 (6).
- [9]. Xiong, G. Y.; Wang, D. Z.; Ren, Z. F. *Carbon* **2006**, 44, 969-973.
- [10]. Smalley, R. E.; Li, Y.; Moore, V. C.; Price, B. K.; Colorado, R.; Schmidt, H.

- K.; Hauge, R. H.; Barron, A. R.; Tour, J. M. *Journal of the American Chemical Society* **2006**, 128, 15824-15829.
- [11]. Iwasaki, T.; Robertson, J.; Kawarada, H. *Nano Letters* **2008**, 8, 886-890.
- [12]. Yasuda, S.; Hiraoka, T.; Futaba, D. N.; Yamada, T.; Yumura, M.; Hata, K. *Nano Letters* **2009**, 9, 769-773.
- [13]. Yun, Y. H.; Shanov, V.; Schulz, M. J.; Dong, Z. Y.; Jaziehe, A.; Heineman, W. R.; Halsall, B. H.; Wong, D. K. Y.; Bange, A.; Tu, Y.; Subramaniamb, S. *Sensors and Actuators B* **2006**, 120, 298-304.
- [14]. Zhang, H.; Cao, G.; Wang, Z.; Yang, Y.; Shi, Z.; Gu, Z. *Journal of Physical Chemistry C* **2008**, 112, 4524-4530.
- [15]. Hart, A. J.; Slocum, A. H. *Journal of Physical Chemistry B* **2006**, 110, 8250-8257.
- [16]. Zhu, L.; Sun, Y.; Hess, D. W.; Wong, C. P. *Nano Letters* **2006**, 6, 243-247.
- [17]. Fan, S. S.; Chapline, M. G.; Franklin, N.R.; Tomblor, T. W.; Cassell, A. M.; Dai, H. J. *Science* **1999**, 283, 512514.
- [18]. Lin, Y.; Lu, F.; Tu, Y.; Ren, Z. *Nano Letters* **2004**, 4, 191-195.
- [19]. Futaba, D. N.; Hata, K.; Yamada T.; Hiraoka T.; Hayamizu Y.; Kakudate Y.; Tanaike, O.; Hatori, H.; Yumura, M.; Iijima, S. *Nature Materials* **2006**, 5, 987-994.
- [20]. Futaba, D. N.; Hata, K.; Yamada, T.; Mizuno, K.; Yumura, M.; Iijima, S. *Physical Review Letters* **2005**, 95, 056104(4).

- [21]. Tibbetts, G. G. *Carbon* **1992**, 30, 399-406.
- [22]. Cui, X.; Wei, W.; Harrower, C.; Chen, W. *Carbon* **2009**, 47, 3441-3451.
- [23]. Yun, Y. H.; Shanov, V.; Tu, Y.; Subramaniam, S.; Schulz, M. J. *Journal of Physical Chemistry B* **2006**, 110, 23920-23925.
- [24]. Feng, X.; Liu, K.; Xie, X.; Zhou, R.; Zhang, L.; Li, Q.; Fan S.; Jiang K. *Journal of Physical Chemistry C* **2009**, 113, 9623-9631.
- [25]. Allouche, H.; Monthieux, M.; Jacobsen, R. L. *Carbon* **2003**, 41, 2897-2912.
- [26]. Allouche, H.; Monthieux, M. *Carbon* **2005**, 43, 1265-1278.
- [27]. Monthieux, M.; Allouche, H.; Jacobsen, R. L. *Carbon* **2007**, 45, 1651-1661.
- [28]. Patole, S. P.; Park, J. H.; Lee, T. Y.; Lee, J. H.; Patole, A. S.; Yoo, J. B. *Applied Physics Letters* **2008**, 93, 114101(3).
- [29]. Futaba, D. N.; Hata, K.; Namai, T.; Yamada, T.; Mizuno, K.; Hayamizu, Y.; Yumura, M.; Iijima, S. *Journal of Physical Chemistry B* **2006**, 110, 8035-8038.
- [30]. Xiang, R.; Yang, Z.; Zhang, Q.; Luo, G.; Qian, W.; Wei, F.; Kadowaki, M.; Einarsson, E.; Maruyama, S. *Journal of Physical Chemistry C* **2008**, 112, 4892-4896.
- [31]. Gohier, A.; Ewels, C. P.; Minea, T. M.; Djouadi, M. A. *Carbon* **2008**, 46, 1331-1338.
- [32]. Patole, S. P.; Yu, S. M.; Shin, D. W.; Kim, H. J.; Han, I. T.; Kwon, K. W.; Yoo, J. B. *Journal of Physics D: Applied Physics* **2010**, 43, 095304(7).
- [33]. Amama, P. B.; Pint, C. L.; Kim, S. M.; McJilton, L.; Eyink, K. G.; Stach, E.

- A.; Hauge, R. H.; Maruyama, B. *ACS Nano* **2010**, 4, 895-904.
- [34]. Ritter, U.; Scharff, P.; Siegmund, C.; Dmytrenko, O. P.; Kulish, N. P.; Prylutsky, N. L.; Belyi, N. M.; Gubanov, V. A.; Komarova, K. I.; Lizunova, S. V.; Poroshin, V. G.; Shlapatskaya, V. V.; Bernas, H. *Carbon* **2006**, 44, 2694-2700.
- [35]. Murphy, H.; Papakonstantinou, P.; Okpalugo, T. I. T. *J. Vac. Sci. Technol. B* **2006**, 24, 715-720.
- [36]. Kim, K. E.; Kim, K. J.; Jung, W. S.; Bae, S. Y.; Park, J.; Choi, J.; Choo, J. *Chemical Physics Letters* **2005**, 401, 459-464.
- [37]. Ferrari, A. C.; Roberson, J. *Physical Review B* **2000**, 61, 14095-14107.
- [38]. Amelinckx, S.; Zhang, X. B.; Bernaerts, D.; Zhang, X. F.; Ivanov, V.; Nagy, J. B. *Science* **1994**, 265, 635-639.
- [39]. Amama, P. B.; Pint, C. L.; McJiton, L.; Kim, S. M.; Stach, E. A.; Murray, P. T.; Hauge, R. H.; Maruyama, B. *Nano Letters* **2009**, 9, 44-49.
- [40]. Eres, G.; Kinkhabwala, A. A.; Cui, H.; Geohegan, D. B.; Poretzky, A. A.; Lowndes, D. H. *Journal of Physical Chemistry B* 109, **2005**, 16684-16694.
- [41]. Zhong, G.; Iwasaki, T.; Robertson, J.; Kawarada, H. *Journal of Physical Chemistry B* 111, **2007**, 1907-1910.
- [42]. Zhang, H.; Cao, G.; Wang, Z.; Yang, Y.; Shi, Z.; Gu, Z. *Journal of Physical Chemistry C* **2008**, 112, 12706-12709.
- [43]. Chakrabarti, S.; Nagasaka, T.; Yoshikawa, Y.; Pan, L.; Nakayama, Y. *Japanese Journal of Applied Physics* 45, **2006**, L720-L722.

Chapter 5

A Novel Hydrophilic Mn₃O₄/Millimeter-Long Carbon Nanotube Array Composite Electrode for Electrochemical Supercapacitors*

* Material in this chapter has been submitted to :

Cui, X. W.; Hu, F. P.; Wei, W. F.; Chen, W. X. *Carbon*, 2010, in revision.

5.1. Introduction

Individual carbon nanotubes (CNTs) possess excellent electrical, thermal and mechanical properties [1]. Thus, a single CNT or dispersed CNTs have been widely used in the areas of field emission devices [2, 3], electrochemical and biosensors [4, 5], supercapacitors [6], etc. In the same manner, the macroscopic forms of CNTs, e.g., millimeter-long carbon nanotube arrays (CNTAs), also have extraordinary properties, such as high aspect ratio [7], aligned pore structure [8], high conductivity, chemical stability [9], etc. However, millimeter-long CNTA based applications are limited, primarily due to fabrication difficulties, which can either damage the tubes or break up the configuration of the tubes within millimeter-long CNTAs [8]. Recently, Hata et al. have developed a liquid-induced collapse method to prevent the cracking of millimeter-long single-walled CNT (SWCNT) arrays [8, 10]. Other restrictions to the use of CNTAs are their hydrophobic state [11] and their highly-packed-CNT structures, which inhibit the decoration of CNTAs by the methods such as direct electrodeposition in aqueous electrolytes and sputtering.

Due to the extraordinary properties of CNTAs, millimeter-long CNTAs have been attempted to be used as supercapacitors in aqueous and organic electrolytes [12-14]. Specifically, Zhang et al. reported a capacitance of 14.1 F/g for 0.8 mm long CNTA in 7 M KOH electrolyte [15], and around 22 F/g for 1.0 mm long

CNTA in an ionic liquid electrolyte [16]. Thus, utilization of the electrical double-layer capacitance (EDLCs) of CNTA alone cannot yield sufficient performance for electrochemical supercapacitors (ESs). In order to increase energy density as well as power density, transitional metal oxides must be deposited within CNTAs to form Faradic pseudo-capacitors [17]. In addition, these kinds of thick and compact electrodes are advantageous for applications with area-limited configuration, because it could increase energy density by occupying high ratios of apparent area, weight and volume with active material. Zhang et al. has reported a potentiodynamic electrodeposition method to deposit ~100 nm diameter manganese oxide nanoflowers within CNTAs in an aqueous electrolyte [18]. However, their method is only applicable to the decoration of short CNTAs (< 35 μm). Due to the above mentioned restrictions to the use of millimeter-long CNTAs, no method has been reported to fabricate millimeter-long CNTA as an electrode with transition metal oxides well dispersed in it.

In this chapter, we successfully achieve this goal by dip-casting Mn_3O_4 nanoparticles uniformly dispersed within a 0.9 mm long CNTA scaffold. Two different Mn_3O_4 nanoparticle loadings (mass ratio of $\text{Mn}_3\text{O}_4/\text{CNTA}$) were used to prepare the composite arrays, a high Mn_3O_4 loading (84%) and a low Mn_3O_4 loading (33%). The corresponding composites will be denoted as $\text{Mn}_3\text{O}_4/\text{CNTA}(0.84)$ and $\text{Mn}_3\text{O}_4/\text{CNTA}(0.33)$, respectively. Contact angle

measurement shows that the as-prepared $\text{Mn}_3\text{O}_4/\text{CNTA}$ composites are hydrophilic, which is an essential factor for improved performance of ESs [19]. The maximum specific capacitance of the $\text{Mn}_3\text{O}_4/\text{CNTA}(0.84)$ composite electrode was found to be 143 F/g, leading to an exceptionally high area-normalized capacitance of 1.70 F/cm^2 . When normalized to the mass of the deposited Mn_3O_4 nanoparticles, the specific capacitance was estimated to be as high as 292 F/g. A high-rate capacity was also shown for Mn_3O_4 in the composite electrodes, 100 F/g in $\text{Mn}_3\text{O}_4/\text{CNTA}(0.84)$ and 181 F/g in $\text{Mn}_3\text{O}_4/\text{CNTA}(0.33)$ at a scan rate of 100 mV/s. This work not only develops a novel $\text{Mn}_3\text{O}_4/\text{CNTA}$ composite which is promising for high performance area-limited ESs, but also opens up a new route of utilizing ultra-long CNTAs.

5.2. Experimental Procedure

5.2.1. Millimeter-long Carbon Nanotube Array (CNTA) Growth

Conventional chemical vapor deposition (CCVD) was used to grow millimeter-long CNTAs. P-type Si wafers (100) coated with a buffer layer of 30 nm Al_2O_3 film and a catalyst film of 3 nm Fe by DC magnetron sputtering were used as the substrates. Catalyst film pretreatment and MWCNT array growth for CCVD were conducted in a single-zone quartz tube furnace with an inner diameter of 5 in. The tube chamber was first evacuated to ≤ 0.1 Torr. After Ar

purging for 1 hr, the furnace temperature was ramped up to 775 °C and held for 60 min under 200 sccm Ar and 400 sccm H₂ gas flow. 400 sccm C₂H₄ was then flowed into the system for 30 min. At the end of CNTA growth, the flow of H₂ and C₂H₄ was terminated and the system was purged again with Ar during furnace cooling to below 100 °C. After the CCVD process, 0.9 mm long CNTA were grown on the non-conductive substrate.

5.2.2. Composite Electrode Production

The Mn₃O₄/CNTA composite electrode was prepared as follows and schematically shown in Figure 5-1. (1) The as-grown CNTA was removed from the non-conductive substrate and completely immersed into Mn(CH₃COO)₂•4H₂O/ethanol solution for 3 min. (2) The dipped CNTA was quickly taken out and exposed to 10 drops of the same solution, 1 drop (~ 0.014 mL) every minute. (3) The dripped CNTA was dried at room temperature and atmosphere for 2 hrs, and put into a 100 °C furnace for 1 hr. (4) Then, the sample was annealed at 300 °C for 2 hrs to form a Mn₃O₄/CNTA composite. (5) A thin Au layer was sputtered to the back of the dip-casted composite, which was then attached to a double-sided conducting tape and the exposed area (other than the composite electrode) was sealed with green Mask-it (purchased from Caswell, Inc.). The weight of the as-grown CNTA and the composite were measured by the

microbalance of Accu-225D (Fisher Scientific) with a weighing precision of 10 μg . The mass loading of the Mn_3O_4 was calculated from their weight difference. 0.25 M $\text{Mn}(\text{CH}_3\text{COO})_2 \cdot 4\text{H}_2\text{O}$ /ethanol solution was used to prepare the $\text{Mn}_3\text{O}_4/\text{CNTA}(0.84)$ composite array, while 0.1 M $\text{Mn}(\text{CH}_3\text{COO})_2 \cdot 4\text{H}_2\text{O}$ /ethanol solution was used to prepare the $\text{Mn}_3\text{O}_4/\text{CNTA}(0.33)$ composite array. For comparison, as-grown CNTAs were also fabricated to the pure CNTA electrodes by removing the as-grown CNTA from the substrate and only conducting step (5).

5.2.3. Materials Characterization

The nanostructure and chemistry of as-grown CNTA and $\text{Mn}_3\text{O}_4/\text{CNTA}$ composite were characterized by JSM-6301FXV (JOEL) field emission scanning electron microscopy (FESEM), JAMP 9500F (JOEL) field emission scanning Auger microprobe (FE-SAM), and transmission electron microscopy (TEM) (JOEL 2010 equipped with a Noran ultra-thin window (UTW) X-ray detector). Chemical state analysis was carried out by X-ray photoelectron spectroscopy (XPS) using a Kratos AXIS Ultra-x-ray photoelectron spectrometer. A monochromatic Al source, operating at 210 W with a pass energy of 20 eV and a step of 0.1 eV, was utilized. Curve fitting and background subtraction were accomplished using Casa XPS Version 2.3.13 software. Energy-dispersive spectroscopy (EDS) mapping was acquired by a peltier-cooled 10 mm^2 Bruker Quantax Silicon drift detector

attached to Zeiss EVO MA 15 LaB₆ filament SEM. The contact angle measurement device used was FTA200 (First Ten Ångstroms).

5.2.4. Electrochemical Capacitive Behavior

Electrochemical capacitive behavior was investigated with a Solartron SI1287 potentiostat/galvanostat under cyclic voltammetry (CV) and galvanostatic charge-discharge modes, and with a Gamry PC4/750 potentiostat/galvanostat under potentiostatic electrochemical impedance spectroscopy (EIS) mode, in an aqueous electrolyte of 0.5 M Na₂SO₄. A three-electrode cell configuration was employed, consisting of the pure CNTA or composite electrode as the working electrode, a platinum plate as the counter electrode and a saturated calomel electrode (SCE) as the reference electrode. All potentials quoted are with respect to SCE. Cyclic voltammograms were recorded between -0.2 and 0.8V (vs. SCE) at various scan rates ranging from 2 mV/s to 200 mV/s. Galvanostatic charge-discharge was also conducted in the voltage range of -0.2 and 0.8V (vs. SCE) at various specific currents spanning from 0.5 A/g to 75 A/g. EIS measurements were conducted in constant voltagemode (0.4V vs. SCE) by sweeping frequencies from 100 kHz to 0.01 Hz at an amplitude of 5 mV.

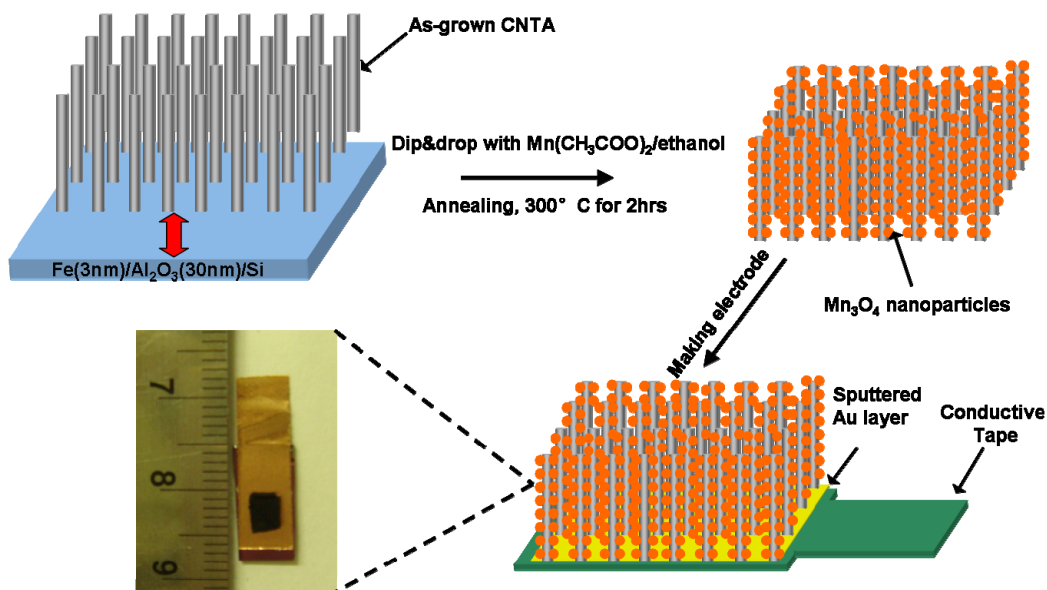


Figure 5-1. Schematic diagram of making Mn₃O₄/CNTA composite electrode. The inset image is the photograph of the composite electrode before sealed with green Mask-it.

5.3. Results and Discussion

5.3.1. Characterization of CNTA

The detailed characterization of as-grown CNTAs was presented in Chapter 3 or in our previous report [20]. The individual CNTs have an average diameter of 11.5 nm with a wall number of 5-7. The height and density of the CNTA is 0.9 mm and 0.069 g/cm³, respectively. The density of the CNTA is twice that for 1 mm long SWCNT array (0.03 g/cm³) [8]. The large differences in wall number and CNTA inner diameter dictate the deviation in CNTA density. Based on these data, it was calculated that 92.3% empty space exists in the as-grown CNTAs. The as-grown

CNTA is hydrophobic in nature with a contact angle of 138° (Figure 5-2). However, good wettability of the as-grown CNTA can be achieved with some non-aqueous liquids such as ethanol, acetone, ethylene glycol, etc, making the dissolved $\text{Mn}(\text{CH}_3\text{COO})_2$ salt permeable into the CNTA.

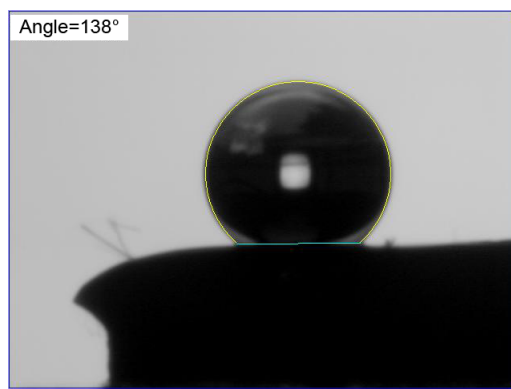


Figure 5-2. Surface wettability of as-grown CNTA with a contact angle of 138° .

5.3.2. Structural Characterization of $\text{Mn}_3\text{O}_4/\text{CNTA}$ Composite Arrays

The morphology, chemistry and crystal structure of the composites were investigated by transmission electron microscopy (TEM) and energy-dispersive spectroscopy (EDS), as shown in Figure 5-3. Figure 5-3a is a TEM image of a strip of $\text{Mn}_3\text{O}_4/\text{CNTA}(0.33)$ taken from the centre of the composite. It is clearly displayed that, after the dip-casting treatment, the CNT walls appear serrated with decorated nanoparticles. These nanoparticles are well dispersed along the CNTs. The EDS spectrum shown in Figure 5-3b gives the chemistry in the region in

Figure 5-3a. Only C, O, Mn and Cu (from Cu grid) peaks are detected suggesting that the composite is very clean and the decorated particles are manganese oxides. In order to obtain the crystal structure of the manganese oxide nanoparticles, the selected area diffraction (SAD) was conducted and the SAD pattern is shown in Figure 5-3c. It is determined that, in addition to well known CNT diffraction rings (graphitic carbon), all other diffraction rings can be assigned to the tetragonal hausmannite-Mn₃O₄ phase [space group *I41/amd* with lattice constants $a = b = 5.762\text{\AA}$ and $c = 9.470\text{\AA}$ (JCPDS 24-0734)]. It reveals that the inserted Mn(CH₃COO)₂ salts have been transferred to nanocrystalline Mn₃O₄ particles within millimeter-long CNTA during the annealing at 300°C for 2 hrs in air. A TEM micrograph of a strip of Mn₃O₄/CNTA(0.84) composite is also shown in Figure 5-3e. The high Mn₃O₄ loading in the composite exhibits a similar structure to that for the low Mn₃O₄ loading in Figure 5-3a, except that nanoparticle aggregation occurred in Mn₃O₄/CNTA(0.84) as indicated in the framed regions in Figure 5-3e. Nanoparticle aggregation in Mn₃O₄/CNTA(0.84) was also evident in Figure 5-4, which compares the bright-field and dark-field TEM images of the two composites. Furthermore, the statistical distributions of the Mn₃O₄ nanoparticle size in the two composites were acquired from the bright-field TEM images taken from 10 different locations. Mn₃O₄ nanoparticle size is distributed in a very narrow range with an average size of 6.0 nm for Mn₃O₄/CNTA(0.33) and 7.3 nm for Mn₃O₄/CNTA(0.84), as shown in Figure 5-3d and 5-3f, respectively.

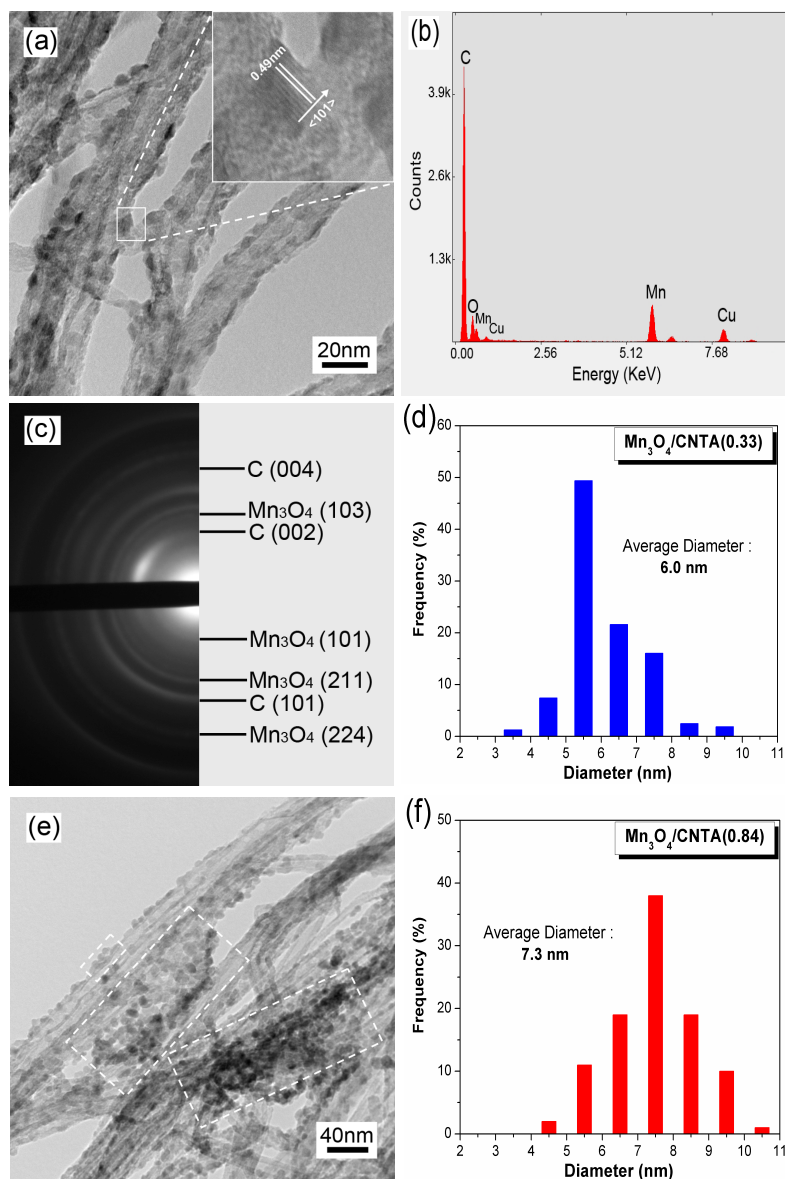


Figure 5-3. (a) TEM image of $\text{Mn}_3\text{O}_4/\text{CNTA}(0.33)$ and its inset HRTEM image of the Mn_3O_4 nanoparticle. (b) EDS and (c) SAD patterns detected from $\text{Mn}_3\text{O}_4/\text{CNTA}(0.33)$ in (a). (d) Statistical distribution of Mn_3O_4 nanoparticle size deposited within CNTA in $\text{Mn}_3\text{O}_4/\text{CNTA}(0.33)$. (e) TEM image of $\text{Mn}_3\text{O}_4/\text{CNTA}(0.84)$. (f) Statistical distribution of Mn_3O_4 nanoparticle size deposited within CNTA in $\text{Mn}_3\text{O}_4/\text{CNTA}(0.84)$.

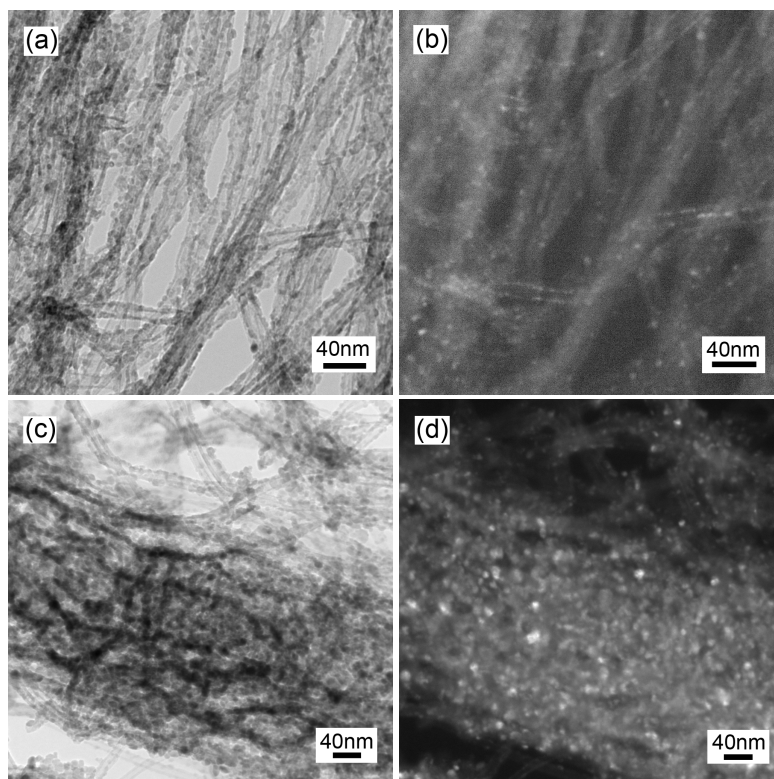


Figure 5-4. (a) Bright-field and (b) dark-field TEM images of $\text{Mn}_3\text{O}_4/\text{CNTA}(0.33)$.

(c) Bright-field and (d) dark-field TEM images of $\text{Mn}_3\text{O}_4/\text{CNTA}(0.84)$.

X-ray photoelectron spectroscopy (XPS) was also employed to study the chemical state of the deposited manganese oxide nanoparticles by analyzing the high resolution Mn 3s doublet peaks. The doublet Mn 3s peaks are caused by parallel spin coupling between electrons in the 3s and 3d orbitals. The oxidation states of Mn increases with a decrease in 3s peak splitting widths (ΔE) in an approximate linear relation [21, 22]. As shown in Figure 5-5, ΔE is 5.52 eV, which can be converted into an average oxidation valence of +2.5, suggesting that the manganese oxides are in the form of Mn_3O_4 . This is consistent with the crystal

structure obtained from the SAD pattern in Figure 5-3c.

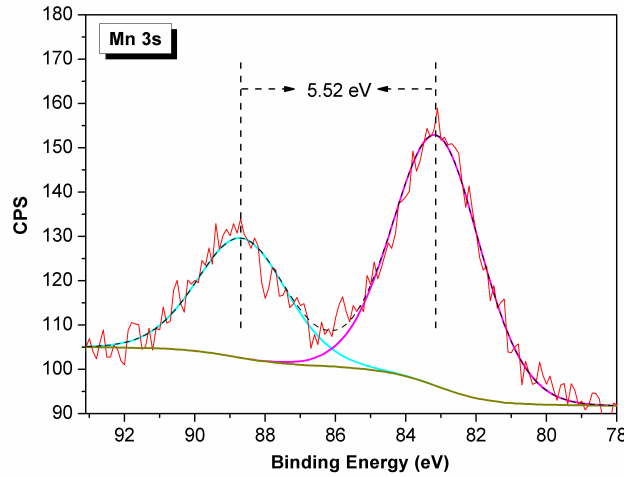


Figure 5-5. XPS Mn 3s spectrum from $\text{Mn}_3\text{O}_4/\text{CNTA}$ composite. The splitting width of the doublet peaks is indicated.

Figure 5-6 shows the surface morphology and cross section field-emission scanning electron microscopy (FESEM) micrographs of the composites after annealing at 300°C for 2 hrs. It is noted that the volume of CNTA was reduced by 7% after dipping with the ethanol solution and annealing at 300°C . This zipping effect is believed to be caused by the change of surface tension of the liquids during evaporation, which is consistent with the observation reported before [8]. The reason for small decrease in CNTA volume after annealing can be seen from Figure 5-6. The composite did not zip to the near-ideal graphitic spacing as was the case for 1 mm long SWCNT array [8], but retained the original morphology of CNTA with aligned macropores or macrochannels indicated by the arrows in Figure 5-6b

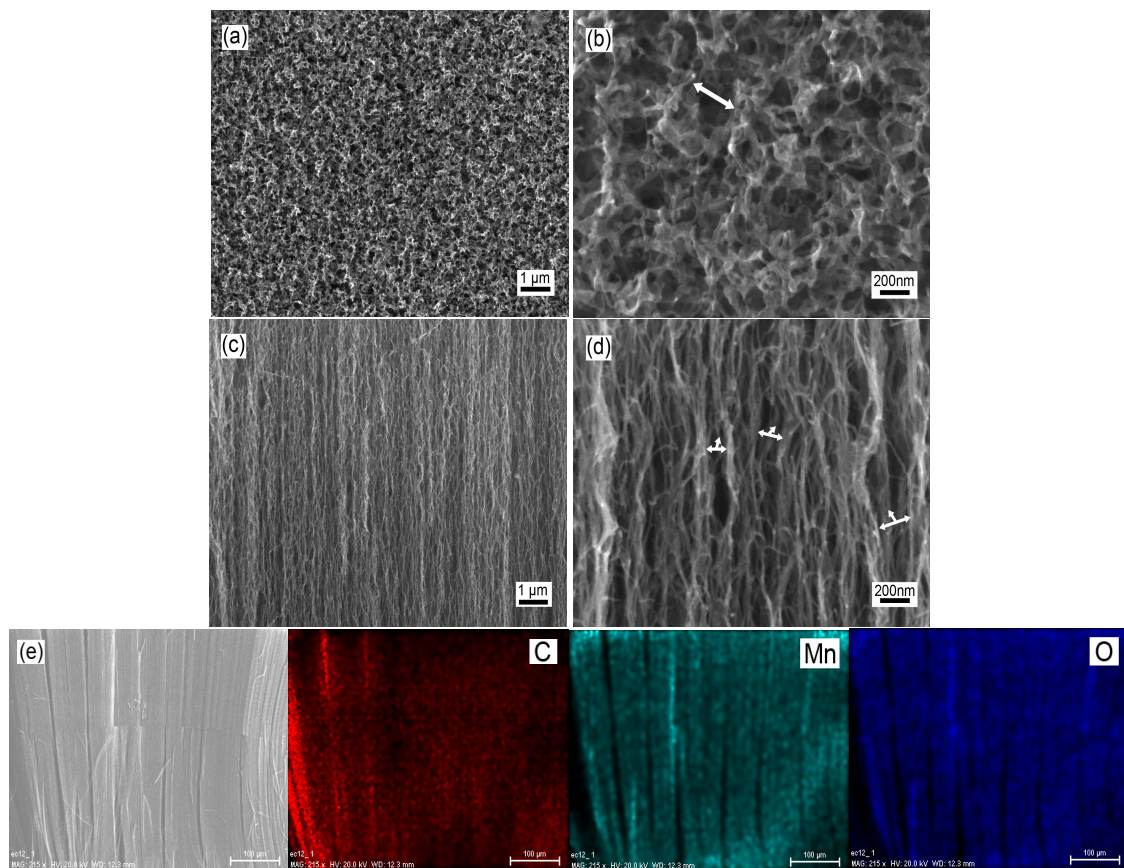


Figure 5-6. (a,b) Surface morphology and (c,d) cross section FESEM images of Mn₃O₄/CNTA composites at different magnifications.

(e) Cross-section SEM image of Mn₃O₄/CNTA composite and its corresponding EDS mapping patterns for C, Mn and O.

and 5-6d. These aligned macrochannels are advantageous in terms of the performance of ESs, which will be discussed later. Additionally, the uniformity of Mn_3O_4 nanoparticle distribution within a large range of the composites was confirmed by EDS mapping shown in Figure 5-6e. Therefore, the obtained structures were composite arrays with Mn_3O_4 nanoparticles homogeneously distributed within millimeter-long CNTA. It is worthy to note that the strategy to prepare composite arrays presented in this study can also be extended to integrate other metal oxide nanoparticles, or even metallic nanoparticles (by annealing in reducing environments), into CNTA for different applications. Combined with its own extraordinary properties, CNTA is a good support for active materials.

5.3.3. Hydrophilicity of Mn_3O_4 /CNTA Composite Arrays

Many applications involving the use of dispersed CNTs and CNTA strongly depend on their surface wettability [23]. Up to now, the most developed method used to change CNT wettability is surface functionalization [24]. However, the surface functionalization is only applicable to dispersed or entangled CNTs, as CNTA could be easily fractured and/or collapse during solution evaporation after surface functionalization. Tuning surface wettability during the process of CNTA growth is another solution [25], but the tuning range is very limited. Interestingly, in this investigation, it was found that the Mn_3O_4 nanoparticle-decorated CNTA is

completely hydrophilic, as shown in Figure 5-7a. The standing time of water droplet on the surface of the composite is less than 0.5s. Although a fair amount of Mn was introduced into the CNTA, it provides another route to change the wettability of CNTA without destroying their alignment and integrity. More importantly, this surprising change of wettability to aqueous electrolyte for millimeter-long CNTAs, not only broadens their applications, for example, in ESs, but also allows CNTAs to be treated by other methods, for instance, electrodeposition.

The very short standing time of water droplet on the surface of the array indicates that water droplet was completely inserted into the aligned hydrophilic pore or channels (indicated by the arrows in Figure 5-6b and 5-6d) within the array. Dubal et al. reported that a Mn_3O_4 thin film is hydrophilic with a contact angle of 60° [19]. Thus, the hydrophilicity of the composite array should be ascribed to the Mn_3O_4 nanoparticles which are well dispersed and decorated on CNT walls. The gap between the decorated CNTs forms the aligned hydrophilic channels. Hence, the aligned hydrophilic channels for electrolyte ion transportation, the Mn_3O_4 nanoparticles for Faradaic reactions and the good conductivity of CNTA, as schematically shown in Figure 5-7b, imply that the novel composite array could be a promising structure for high performance area-limited electrode ESs, which will be discussed in the following section.

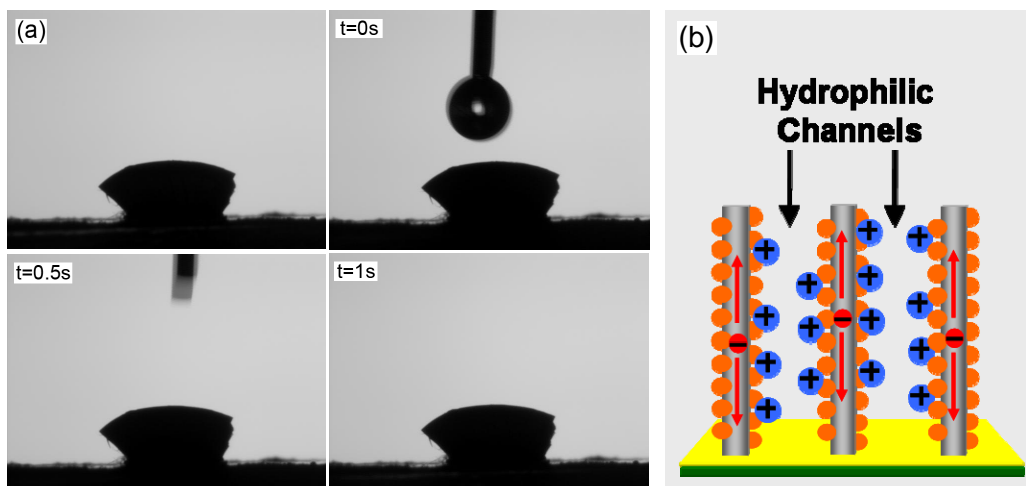


Figure 5-7. (a) Time sequence images of a water droplet dropped to the surface of Mn₃O₄/CNTA composite. (b) Schematic diagram of the inner structure of Mn₃O₄/CNTA composite showing how the composite works in ESs.

5.3.4. Electrochemical Properties of Mn₃O₄/CNTA Composite Electrodes

Electrochemical properties of the Mn₃O₄/CNTA(0.84) and Mn₃O₄/CNTA(0.33) composite electrodes are shown in Figures 5-8, 5-9 and 5-10. The cyclic voltammetry (CV) curves of the two composite electrodes in 0.5 M Na₂SO₄ electrolyte at various scan rates are shown in Figure 5-8a and 5-8b. For comparison, the CV curves at a scan rate of 50 mV/s for the two composite electrodes and the as-grown CNTA electrode were plotted in Figure 5-9a. The nearly rectangular shape of CV curves with no obvious redox peaks from -0.2 and 0.8V (vs. SCE) indicates good capacitive performance for these three electrodes. This is also confirmed by the near linear galvanostatic charge-discharging curves

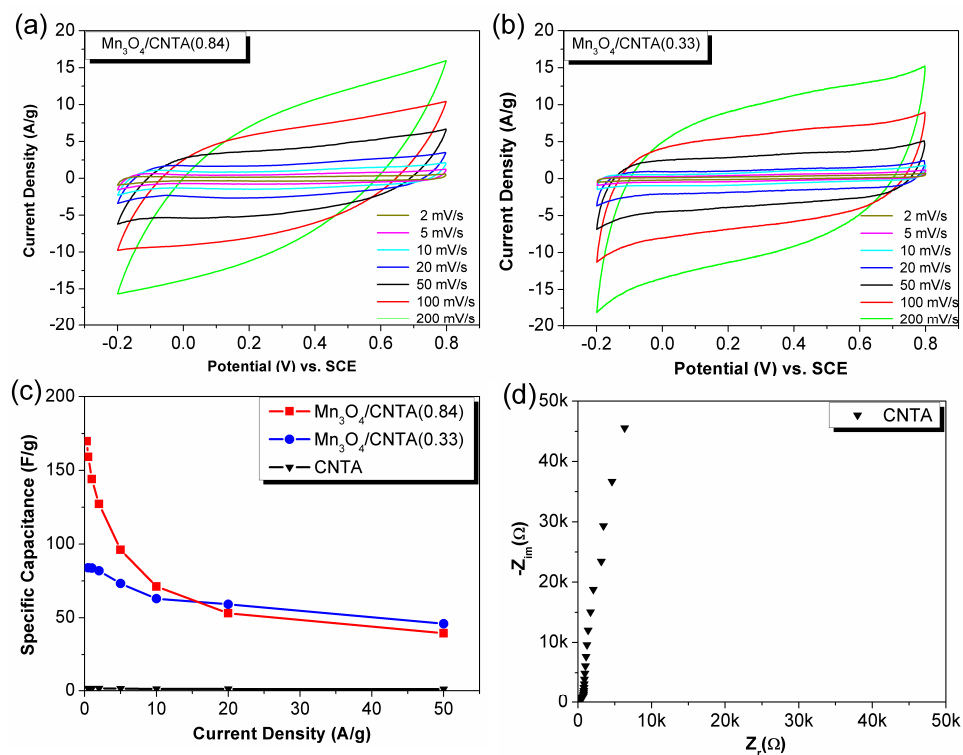


Figure 5-8. CV curves of (a) Mn₃O₄/CNTA(0.84) composite electrode and (b) Mn₃O₄/CNTA(0.84) composite electrode detected in 0.5 M Na₂SO₄ electrolyte at various scan rates spanning from 2 mV/s to 200 mV/s. (c) Specific capacitance for Mn₃O₄/CNTA composite electrodes at two different loadings and as-grown CNTA electrode calculated from galvanostatic charge-discharge curves at various current densities. (d) Nyquist plot for the as grown CNTA electrode.

at a specific current of 1A/g in Figure 5-9b. In addition, a negligible voltage (IR) drop was detected for the composite electrodes (Figure 5-9b), suggesting their low internal resistance. The specific capacitance of these three electrodes was also plotted versus various scan rates and specific currents in Figure 5-9c and 5-8c,

respectively. The comparable values measured by these two methods reflect that the specific capacitance obtained in this study is of high accuracy. The highest specific capacitance of 143 F/g was obtained for the Mn₃O₄/CNTA(0.84) composite electrode at a scan rate 2 mV/s. This value is almost one order of magnitude higher than the results reported in the literature for different heights of CNTA detected in aqueous and organic solutions [12-16]; and even higher than the activated, thin film and dispersed CNTs [26]. The specific capacitance, therefore, should be primarily from the pseudo-capacitance of the deposited Mn₃O₄ nanoparticles. This is consistent with the large difference in the CV curves and charge-discharge curves between the composite electrodes and the as-grown CNTA electrode, shown in Figure 5-9a and 5-9b. Interestingly, the area-normalized capacitance for the Mn₃O₄/CNTA(0.84) and Mn₃O₄/CNTA(0.33) composite electrodes is 1.70 F/cm² and 0.79 F/cm², respectively, which is one order of magnitude higher than that for Mn₃O₄ thin films [19] and much higher than that for MnO₂-carbon composite (usually 10-50 mF/cm² [27]). These results imply that newly developed Mn₃O₄/CNTA composite electrode is an improved area-limited electrode for ESSs. The capacitance values for these three electrodes derived from cyclic voltammetry were summarized in Table 5-1. It should also be noted that, in this investigation, the specific capacitance of the as-grown CNTA electrode is in the range of 1-2 F/g, an order of magnitude lower than those reported in the literature. One reason for the above discrepancy is that the CNTA

used in this study is very thick, 0.9 mm, and CNTA is hydrophobic with a contact of 138° (Figure 5-2); thus, the actual surface used for EDLC may be only within the outermost 100 μm . Another important reason is related to the neutral aqueous electrolyte used. The electrochemical performance of CNTA and CNTs measured in acidic H_2SO_4 or alkaline KOH electrolytes may activate the CNTA or CNTs during the cycling process.

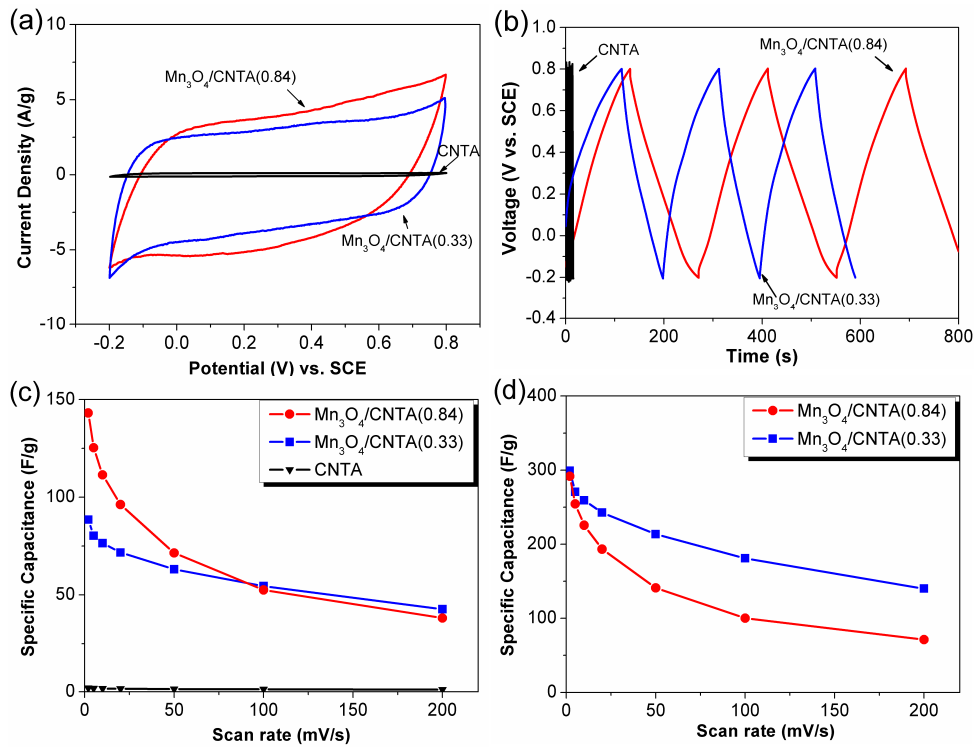


Figure 5-9. (a) CV curves of $\text{Mn}_3\text{O}_4/\text{CNTA}$ composite electrodes at two different loadings and as-grown CNTA electrode at 50 mV/s. (b) Galvanostatic charge-discharge curves of the three electrodes at 1 A/g. (c) Specific capacitance for the three electrodes calculated from CV curves at various scan rates. (d) Specific capacitance for the deposited Mn_3O_4 nanoparticles for the composite electrodes with two loadings at various scan rates.

Table 5-1. Capacitance values for Mn₃O₄/CNTA(0.84), Mn₃O₄/CNTA(0.33) composite electrodes and as-grown CNTA electrode derived from cyclic voltammetry.

	Specific Capacitance (F/g) at 2 mV/s	Mn ₃ O ₄ -Specific Capacitance ^a (F/g) at 2 mV/s	Mn ₃ O ₄ -Specific Capacitance ^a (F/g) at 100 mV/s	Area-normalized Capacitance (F/cm ²)
Mn ₃ O ₄ /CNTA(0.84)	143	292	100	1.70
Mn ₃ O ₄ /CNTA(0.33)	89	299	181	0.79
As-grown CNTA	1.84			0.012

a: the total sample capacitance is the sum of the CNTA double-layer capacitance $\times 10$ (using the comparative values in the literature) and the Mn₃O₄ pseudocapacitance.

Since the aqueous electrolyte was proved to be capable of penetrating into the $\text{Mn}_3\text{O}_4/\text{CNTA}$ composite arrays, more CNTA surfaces should be exposed to the electrolyte. To accurately determine the specific pseudo-capacitance of the deposited Mn_3O_4 , the specific capacitance of the as-grown CNTA under different scan rates obtained in this study was magnified 10 times to the comparative values in the literature. This capacitance was then subtracted from the total specific capacitance of the composite electrodes by considering the mass ratios of $\text{Mn}_3\text{O}_4:\text{CNTA}$. The calculated specific pseudo-capacitance contributed purely from the deposited Mn_3O_4 nanoparticles is presented in Figure 5-9d. It is noted that the maximum specific capacitance for the two different Mn_3O_4 -loaded electrodes is similar, 292 F/g for $\text{Mn}_3\text{O}_4/\text{CNTA}(0.84)$ and 299 F/g for $\text{Mn}_3\text{O}_4/\text{CNTA}(0.33)$, which justifies the method used to acquire the specific capacitance for the Mn_3O_4 . It also rationalizes the high energy density for the Mn_3O_4 nanoparticles. Recently, Dai et al. [28] reported a specific capacitance of 131.2 F/g and Dubal et al. [19] reported a specific capacitance of 193 F/g for Mn_3O_4 films. Most other results in the literature are lower than these two values, because it is known that Mn_3O_4 is a low-specific capacitance material compared with MnO_2 [29]. However, in this study, Figure 5-9d and Figure 5-3 indicate that Mn_3O_4 can increase its specific capacitance by decreasing the Mn_3O_4 particle size to less than 10 nm in diameter (Figure 5-3d and 5-3f), since this allows full access of the active material, Mn_3O_4 , to the aqueous electrolyte. Furthermore, at a high

scan rate of 100 mV/s, the specific capacitance of the Mn_3O_4 still remains as high as 100 F/g in $\text{Mn}_3\text{O}_4/\text{CNTA}(0.84)$ and 181 F/g in $\text{Mn}_3\text{O}_4/\text{CNTA}(0.33)$, indicating high rate capacity and high power density of the Mn_3O_4 . This property can also be attributed to the aligned hydrophilic channels and nanosized Mn_3O_4 particles. The aligned hydrophilic channels provide fast electrolyte ion diffusion into the composite array, and nanosized Mn_3O_4 particles offer short cation diffusion path for bulk Faradaic reactions. These results show that the electrochemical performance of transitional metal oxides, both in terms of capacitance and power characteristics, strongly depends on their electrode structure [27]. The importance of Mn oxide morphology, crystal structure, cation valences and defect chemistry to the specific capacitance has also been discussed in our previous reports [30-32].

Figure 5-10a shows the Nyquist plots for the two composite electrodes analyzed by electrochemical impedance spectroscopy (EIS). It reveals that the charge-transfer resistance for $\text{Mn}_3\text{O}_4/\text{CNTA}(0.84)$ is $\sim 12 \Omega$, which is much larger than that for $\text{Mn}_3\text{O}_4/\text{CNTA}(0.33)$, $\sim 1.2 \Omega$. Such a high charge-transfer resistance for $\text{Mn}_3\text{O}_4/\text{CNTA}(0.84)$ would be detrimental to rate capacity, which is consistent with the CV results shown in Figure 5-9c and 5-9d where $\text{Mn}_3\text{O}_4/\text{CNTA}(0.84)$ has inferior capacitance at high scan rates compared with $\text{Mn}_3\text{O}_4/\text{CNTA}(0.33)$. This trend can be attributed to a larger Mn_3O_4 size and nanoparticle aggregation for $\text{Mn}_3\text{O}_4/\text{CNTA}(0.84)$ observed in the TEM images in Figure 5-3e, 5-3f and Figure

5-4. In both cases, the cation diffusion path in the active material increases resulting in a decrease in rate capacity. Figure 5-10b illustrates the capacitance retention of the composite arrays versus cycle number. The slight increase in specific capacitance around 200-300 cycles suggests an activation process occurred in the initial stage of cycling, while the specific capacitance retains 77%-81% of the original value after 1000 cycles at a scan rate of 50 mV/s.

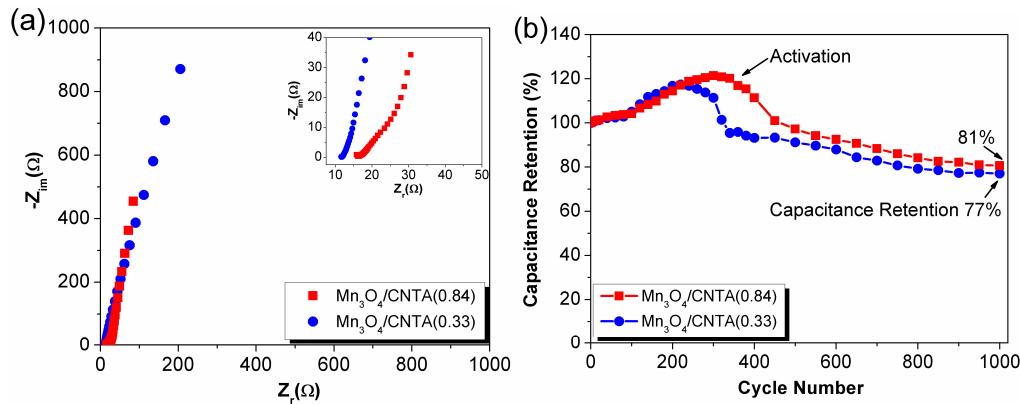


Figure 5-10. (a) Nyquist plots for $Mn_3O_4/CNTA(0.84)$ and $Mn_3O_4/CNTA(0.33)$ composite electrodes. (b) Variation of capacitance with respect to CV cycle number for $Mn_3O_4/CNTA(0.84)$ and $Mn_3O_4/CNTA(0.33)$ composite electrodes and also for the deposit Mn_3O_4 nanoparticles.

It is important to note that direct deposition of nanoparticles within CNTAs saves several procedures needed for the deposition of nanoparticles on the dispersed CNTs, such as CNT purification, filtering, mixture with binder, etc. This work may also stimulate future efforts on the fabrication of patterned 3D composite

arrays.

5.4. Conclusions

We have successfully deposited uniformly dispersed Mn_3O_4 nanoparticles within millimeter-long CNTAs by dip-casting method from non-aqueous solutions. After modification with Mn_3O_4 nanoparticles, CNTAs have been changed from hydrophobic to hydrophilic without their alignment and integrity being destroyed. The hydrophilic $\text{Mn}_3\text{O}_4/\text{CNTA}$ composite electrode presents high capacitance and long cycle life, making it very promising for ESs. Interestingly, the deposited Mn_3O_4 nanoparticles demonstrate superior specific capacitance and rate capacity because of their nanosize and the excellent nanostructured scaffold, millimeter-long CNTA. Moreover, the strategies for tuning the composite structure are versatile, e.g., manipulating the size of hydrophilic channels and using different transitional metal oxides by dip-casting or electrodeposition, which may further improve the performance of ESs. This 3D-nanoparticle decorated hierarchical porous structure is also desired for other applications, such as hydrogen storage, gas or liquid sensors, lithium ion batteries, etc. Therefore, this work not only develops a novel, nano-architected $\text{Mn}_3\text{O}_4/\text{CNTA}$ composite which is promising for high performance area-limited ESs, but also opens up a new route of utilizing ultra-long CNTAs as a support for active materials.

5.5. References

- [1]. O'Connell, M. J. in *Carbon nanotubes: properties and applications*, edited by O'Connell, M. J. (CRC Press, Boca Raton, 2006).
- [2]. Zhu, L.; Sun, Y.; Hess, D. W.; Wong, C. P. *Nano Letters* **2006**, 6, 243-247.
- [3]. Fan, S. S.; Chapline, M. G.; Franklin, N.R.; Tomblor, T. W.; Cassell, A. M.; Dai, H. J. *Science* **1999**, 283, 512-524.
- [4]. Yun, Y. H.; Shanov, V.; Schulz, M. J.; Dong, Z. Y.; Jaziehe, A.; Heineman, W. R.; Halsall, B. H.; Wong, D. K. Y.; Bange, A.; Tu, Y.; Subramaniamb, S. *Sensors and Actuators B* **2006**, 120, 298-304.
- [5]. Lin, Y.; Lu, F.; Tu, Y.; Ren, Z. *Nano Letters* **2004**, 4, 191-195.
- [6]. Kaempgen, M.; Chan, C. K.; Ma, J.; Cui, Y.; Gruner, G. *Nano Letters* **2009**, 9, 1872-1876.
- [7]. Hata, K.; Futaba, D. N.; Mizuno, K.; Namai, T.; Yumura, M.; Iijima, S. *Science* **2004**, 306, 1362-1364.
- [8]. Futaba, D. N.; Hata, K.; Yamada T.; Hiraoka T.; Hayamizu Y.; Kakudate Y.; Tanaike, O.; Hatori, H.; Yumura, M.; Iijima, S. *Nature Materials* **2006**, 5, 987-994.
- [9]. Chen, Q. L.; Xue, K. H.; Shen, W.; Tao, F. F.; Yin, S. Y.; Xu, W. *Electrochimica Acta* **2004**, 49, 4157-4161.
- [10]. Futaba, D. N.; Miyake, K.; Murata, K.; Hayamizu, Y.; Yamada, T.; Sasaki, S.; Yumura, M.; Hata, K. *Nano Letters* **2009**, 9, 3302-3307.

- [11]. Lau, K. K. S.; Bico, J.; Teo, K. B. K.; Chhowalla, M.; Amaratunga, G. A. J.; Milne, W. I.; McKinley, G. H.; Gleason, K. K. *Nano Letters* **2003**, 3, 1701-1705.
- [12]. Talapatra, S.; Kar, S.; Pal, S. K.; Vajtai, R.; Ci, L.; Victor, P.; Shaijumon, M. M.; Kaur, S.; Nalamasu, O.; Ajayan, P. M. *Nature Nanotechnology* **2006**, 1, 112-116.
- [13]. Shah, R.; Zhang, X.; Talapatra, S. *Nanotechnology* **2009**, 20, 395202(5).
- [14]. Honda, Y.; Haramoto, T.; Takeshige, M.; Shiozaki, H.; Kitamura, T.; Ishikawa, M. *Electrochemical and Solid-State Letters* **2007**, 10, A106-A110.
- [15]. Zhang, H.; Cao, G.; Yang, Y. *Nanotechnology* **2007**, 18, 195607(4).
- [16]. Zhang, H.; Cao, G.; Yang, Y.; Gu, Z. *Journal of the Electrochemical Society* **2008**, 155, K19-K22.
- [17]. Simon, P.; Gogotsi, Y. *Nature Materials* **2008**, 7, 845-854.
- [18]. Zhang, H.; Cao, G.; Wang, Z.; Yang, Y.; Shi, Z.; Gu, Z. *Nano Letters* **2008**, 8, 2664-2668.
- [19]. Dubal, D. P.; Dhawale, D. S.; Salunkhe, R. R.; Pawar, S. M.; Fulari, V. J.; Lokhande, C. D. *Journal of Alloys and Compounds* **2009**, 484, 218-221.
- [20]. Cui, X.; Wei, W.; Harrower, C.; Chen, W. *Carbon* **2009**, 47, 3441-3451.
- [21]. Toupin, M.; Brousse, T.; Bélanger, D. *Chemistry of Materials* **2002**, 14, 3946-3952.
- [22]. Wei, W.; Cui, X.; Chen, W.; Ivey, D. G. *Journal of Power Sources* **2009**, 186, 543-550.

- [23]. Zanello, L. P.; Zhao, B.; Hu, H.; Haddon, R. C. *Nano Letters* **2006**, 6, 562-567.
- [24]. Kim, Y. T.; Ito, Y.; Tadai, K.; Mitani, T. *Applied Physics Letters* **2005**, 87, 234106(3).
- [25]. Ci, L.; Vajtai, R.; Ajayan, P. M. *Journal of Physical Chemistry C* **2007**, 111, 9077-9080.
- [26]. Ko, J. M.; Kim, K. M. *Materials Chemistry and Physics* **2009**, 114, 837-841.
- [27]. Fischer, A. E.; Pettigrew, K. A.; Rolison, D. R.; Stroud, R. M.; Long, J. W. *Nano Letters* **2007**, 7, 281-286.
- [28]. Dai, Y.; Wang, K.; Xie, J. *Applied Physics Letters* **2007**, 90, 104102(3).
- [29]. Sharma, R. K.; Oh, H. S.; Shul, Y. G.; Kim, H. *Physica B: Condensed Matter* **2008**, 403, 1763-1769.
- [30]. Wei, W.; Chen, W.; Ivey, D. G. *Journal of Physical Chemistry C* **2007**, 111, 10398-10403.
- [31]. Wei, W.; Cui, X.; Chen, W.; Ivey, D. G. *Journal of Physical Chemistry C* **2008**, 112, 15075-15083.
- [32]. Wei, W.; Cui, X.; Chen, W.; Ivey, D. G. *Electrochimica Acta* **2009**, 54, 2271-2275.

Chapter 6

Anodic Pulse-Electrodeposition of MnO₂ Nanorods within Hydrophilic Vertically Aligned Carbon Nanotube Arrays for Supercapacitors

6.1. Introduction

Electrochemical capacitors, also called supercapacitors, characterized by high power density and long cycle life, have attracted great attention due to their potential applications in portable and transportation systems [1, 2]. Currently, much of the research about supercapacitors are focusing on increasing energy density while using environmentally friendly materials and lowering their fabrication cost [3-5]. Thin-film supercapacitors with thicknesses from less than 10 μm down to tens or hundreds of nanometers have shown respectable gravimetric and volumetric capacitance; while the capacitance per unit area of the device is low [6]. In contrast, thick electrodes for supercapacitors are advantageous in terms of the energy density [3] as well as the area-normalized capacitance, because in such cells the active material can fill up the space to achieve high ratios of the cells' apparent area, volume and weight. In addition, metal oxides (RuO_2 , NiO , SnO_2 , MnO_2 , etc. [7-9]) exhibit pseudo-capacitance, which is comparable to or exceeds the electric double layer capacitance (EDLC) of carbon materials (activated carbon, carbide-derived carbon, carbon nanotubes (CNTs), etc. [10-12]). Among these metal oxides, MnO_2 has been thoroughly investigated because of its high capacitance, low cost and environmentally friendly nature [13]; however, the poor electrical conductivity of MnO_2 has limited its film thicknesses to a few microns. CNTs have been added to MnO_2 films to increase the electrical conductivity; the manufacturing complexity,

however, inhibits their practical applications [6].

In addition to high surface area and high conductivity similar to dispersed CNTs, vertically-aligned CNT arrays (CNTAs) are also featured with other characteristics, e.g., controllable thickness (up to millimeter scale) and aligned pore structure [3, 14, 15]. These characteristics make CNTAs a good support of active materials (e.g. MnO_2) for supercapacitors [16, 17]. However, efficient growth of CNTAs has mostly been achieved on non-conductive substrates, and CNTAs are hydrophobic and very fragile during solution treatment and electrode processing [3]. These fabrication difficulties restrict the utilization of CNTAs. Our previous work in Chapter 5 shows that hydrophobic CNTAs become hydrophilic after dip-casting Mn_3O_4 nanoparticles within CNTAs [16]. In this chapter, we present a scalable and cost-effective way to fabricate composite electrodes using millimeter-long CNTAs. Anodic pulse-electrodeposition was also employed to deposit environmentally friendly MnO_2 nanorods within hydrophilic 0.5 mm-thick Mn_3O_4 decorated CNTAs to improve their performance for supercapacitors.

6.2. Experimental Procedure

6.2.1. Millimeter-long Carbon Nanotube Array Growth

Millimeter-long CNTAs were grown by water-assisted chemical vapor deposition

(WACVD) in the environment of 100 sccm Ar, 400 sccm H₂, 100 sccm C₂H₄ for 30 min. The detailed procedure was presented in Chapter 2 or in our previous report [18].

6.2.2 Composite Electrode Production

The CNTA-based composite electrode was fabricated following the steps as schematically shown in Figure 6-1: (1) As-grown CNTA was removed from the non-conductive substrate by pasting it onto a conductive tape and lifting the substrate from the CNTA. This avoids the possibility of the fracture of CNTAs that occasionally occurs when CNTA is removed using a razor blade. The conductive tape alone could be used as a current collector, or by attaching it to Al foil. (2) The pure CNTA electrode was exposed to 15 drops of 0.25 M Mn(CH₃COO)₂•4H₂O/ethanol solution, 1 drop (~ 0.014 mL) each minute. In the meantime, the CNTA was pressed to a height of 0.5 mm by rolling. (3) The dripped and rolled CNTA was dried at room temperature for 2 hrs, and then annealed at 100 °C for 1 hr and at 300 °C for 2 hrs to form the Mn₃O₄/CNTA composite electrode. (4) Galvanic pulse-electrodeposition was used to deposit MnO₂ nanorods within Mn₃O₄/CNTA composite electrode using 0.5 M Mn(CH₃COO)₂ and 1 M Na₂SO₄ solution, room temperature, and a stirring rate of 600 rpm. The plating current density was controlled at 15 mA/cm² and the pulse

on/off time was 2s/20s. The plating time indicated in this study is the accumulated pulse-on time at the applied current density. A sample of the MnO_2 nanorods/CNTA composite electrode is shown in the optical images in Figure 6-1.

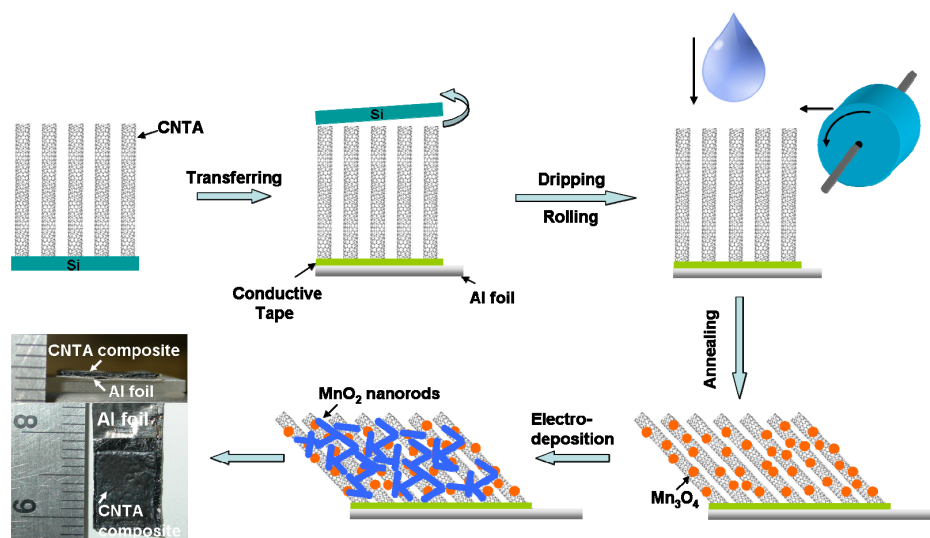


Figure 6-1. Schematic diagram of making composite electrode based on millimeter-long carbon nanotube arrays.

6.2.3. Materials Characterization and Electrochemical Measurements

The weight of the as-grown CNTA and the composite were measured on Accu-225D microbalance (Fisher Scientific) with a weight resolution of 10 μg . The mass loading of the Mn_3O_4 and MnO_2 were calculated from their weight difference before and after deposition, where a thorough drying process (dry under Ar gas for 10 hrs at 70 $^\circ\text{C}$ and under vacuum overnight) was used before weighing. The amount of CNTA and the deposited Mn oxides was controlled to be

over 1 mg. The dimensions, nanostructure and chemistry of CNTAs and MnO₂/CNTA composites were characterized by JAMP 9500F (JOEL) field emission scanning Auger microprobe (FE-SAM) and by transmission electron microscopy (TEM) (JOEL 2010 equipped with a Noran ultra-thin window (UTW) X-ray detector).

Electrochemical capacitive behavior was investigated with a Gamry PC4/750 potentiostat/galvanostat in an aqueous electrolyte of 0.5 M Na₂SO₄. A saturated calomel electrode (SCE) was used as the reference electrode and all potentials quoted are with respect to SCE. Cyclic voltammograms were recorded between -0.2 and 0.8V (vs. SCE). EIS measurements were conducted in constant voltage mode (0.4V vs. SCE) by sweeping frequencies from 100 kHz to 0.01Hz at an amplitude of 5 mV.

6.3. Results and Discussion

6.3.1. Structural Characterization

The CNTAs obtained by WACVD under the current conditions are 1.3 mm in height and consist of CNTs with 3-4 walls. WACVD extends the range of the optimum CNTA growth conditions compared with conventional CVD (CCVD, without adding water), which makes it possible for scalable production. The

density of CNTAs by WACVD was calculated to be 0.01 g/cm^3 , which is much lower than that (0.069 g/cm^3) of CNTAs obtained by CCVD. Hence, millimetre-long CNTAs by WACVD were chosen to achieve large surface area deposition of manganese oxides. The whole electrode making process is scalable and cost effective, as shown in Figure 6-1.

Figure 6-2 shows cross-section SEM images of the MnO_2/CNTA composite electrode after 20 minutes of electrodeposition. Figure 6-2a, 6-2b, and 6-2c were taken from the top, middle and bottom part of the composite, respectively, at the locations indicated in the frames in the inset image of Figure 6-2a. It is evident that nanorods were electrodeposited throughout the pressed 0.5 mm-thick CNTA scaffold, which proves the hydrophilicity of the entire CNTA after decorated with Mn_3O_4 nanoparticles [16]. Dense layers of nanorods were strongly attached to the aligned CNTs (shown within the circles) at the top and middle of the composite; while fewer nanorods were deposited at the bottom part. This is caused by diffusion control for the plating electrolyte at the bottom of the composite. The dense layer of the nanorods is also clearly demonstrated in the enlarged view in Figure 6-2d. It is important to note that active materials are difficult to deposit within the as-fabricated millimeter-scale CNTAs using other deposition methods such as sputtering or electrodeposition. The electrodeposition method that has been used for deposition on the dispersed CNTs [19] is not applicable to CNTAs

because of their fragility during sonication, acid solution treatment and drying process.

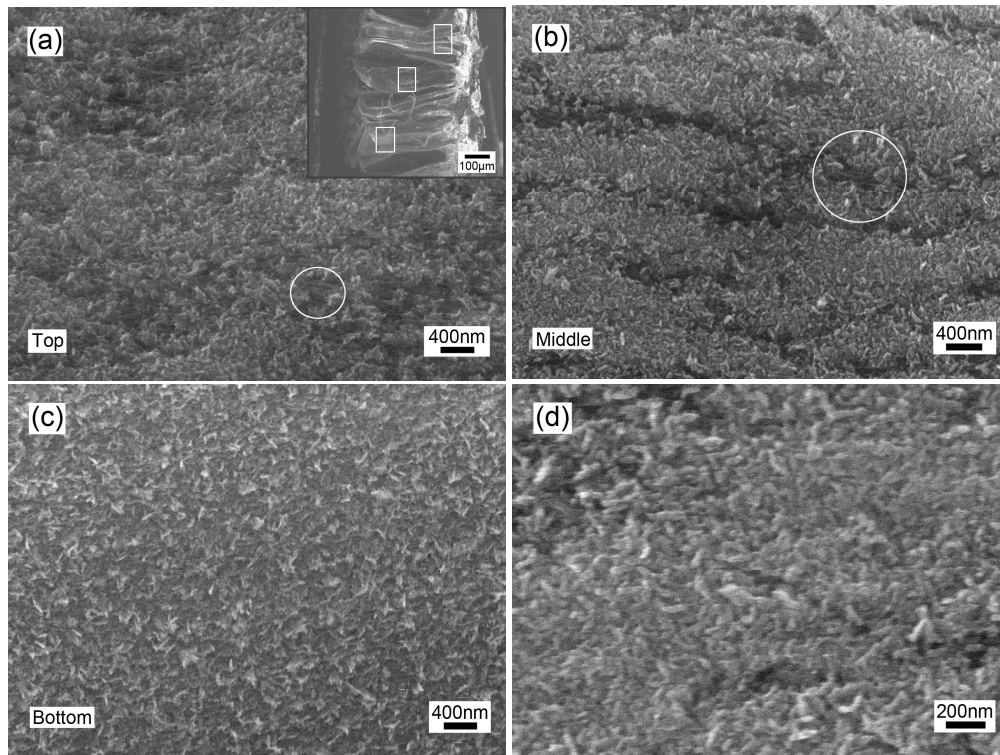


Figure 6-2. Cross-sectional SEM images taken at the top (a), middle (b), and bottom (c) part of the MnO₂ nanorods/CNTA composite; (d) a high-magnification cross-sectional SEM image. The inset image in (a) is a low-magnification SEM image showing the whole cross section of the composite.

Electrodeposited MnO₂ was further characterized by TEM. Figure 6-3a and 6-3b are bright-field and dark-field TEM images of the MnO₂/CNTA composite electrode after 20 minutes of electrodeposition. It is shown that the

electrodeposited MnO_2 crystals are attached along the CNTs and display rod-like morphology with typical rod diameters of 10 to 20 nm and rod lengths of 50 to

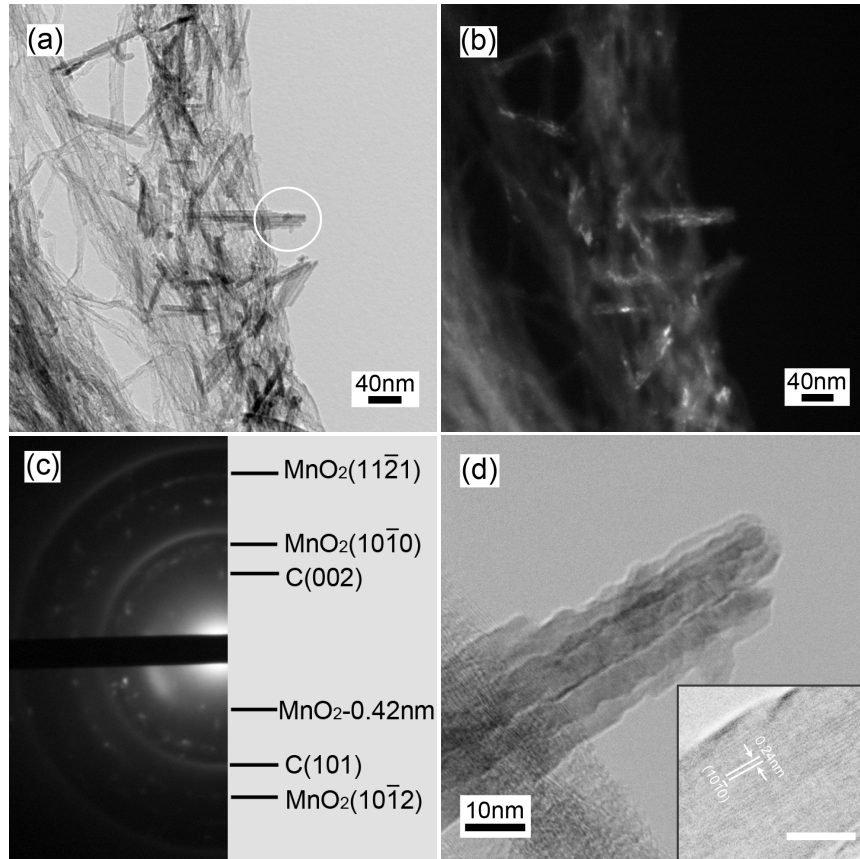


Figure 6-3. (a) Bright-field and (b) dark-field TEM images; (c) SAD pattern; (d) high-magnification TEM image with nanorod's lattice fringes in the inset image, of the MnO_2 nanorods/CNTA composite.

200 nm, consistent with SEM characterization. The selected area diffraction (SAD) pattern of MnO_2 nanorods, shown in Figure 6-3c, can be assigned to a hexagonal phase of $\epsilon\text{-MnO}_2$ (JCPDS 30-0820) with a space group of $P6_3/mmc$. The enlarged view of the $\epsilon\text{-MnO}_2$ nanorods in the circle region of Figure 6-3b is also shown in

Figure 6-3d. In addition, the lattice fringes of the nanorods with an interplanar distance of approximately 0.24 nm, shown in the inset image in Figure 6-3d, correspond to the $(10\bar{1}0)$ planes of the hexagonal ϵ - MnO_2 structure.

6.3.2 Electrochemical Properties

The electrochemical properties of MnO_2 nanorods/CNTA composite electrodes were investigated and are shown in Figure 6-4 and Table 6-1. To evaluate the performance after anodic pulse-electrodeposition of MnO_2 , three composite electrodes were tested for comparison, one Mn_3O_4 /CNTA composite electrode before electrodeposition (denoted as 0 min) and two MnO_2 /CNTA composite electrodes after 10 minutes and 20 minutes of electrodeposition (denoted as 10 min and 20 min, respectively). Figure 6-4a shows the representative CV curves of the three composite electrodes at a scan rate of 1 mV/s. It is demonstrated that the capacitance of the composite electrode increases with increasing amount of MnO_2 nanorods for 20 minutes of electrodeposition. The improvement of the gravimetric, area-normalized and volumetric capacitance values by electrodeposition is evident and the results are summarized in Table 6-1. The gravimetric capacitance values are in the range from 150 F/g to 185 F/g, which are comparable to those of MnO_2 -carbon composite reported before [4, 5, 21], and much higher than those for pure CNTA electrodes [3, 14, 15, 22]. Additionally, the area-normalized and

volumetric capacitance values are raised by a factor of 3 after 20 minutes of electrodeposition. Since CNTA itself makes a negligible contribution to the capacitance [16], increasing MnO₂ nanorods loading by electrodeposition easily increases the capacitance of the composite. To the best of our knowledge, the area-normalized capacitance of the 20 minute electrodeposited MnO₂/CNTA composite, 1.80 F/cm², is the best reported for manganese oxide composites. The gravimetric capacitance of the electrodeposited ε-MnO₂ nanorods was estimated to be around 220 F/g, as also shown in Table 6-1. This value is much higher than that (130 F/g) of anodic electrodeposited ε-MnO₂ thin films [13], revealing the significance of using CNTA as a support. Nyquist plots in Figure 6-4b further demonstrate the improved capacitance by extending plating time. It is also shown that the charge transfer resistance of all three composite electrodes is less than 20 Ω, although it increases with plating time.

It is noteworthy that WACVD-grown CNTAs used in this study have a much lower density than those obtained by CCVD. Thus, the dip-cast amount of Mn₃O₄ in this study is much lower, even though the Mn₃O₄:CNTA mass ratio is higher (1.5:1) than that reported before (0.84:1) [16]. The low loading amount of Mn₃O₄ in this study maintains its gravimetric capacitance but reduces the area-normalized and volumetric capacitance of Mn₃O₄/CNTA composite, which can be improved by further electrodeposition of MnO₂ nanorods in it.

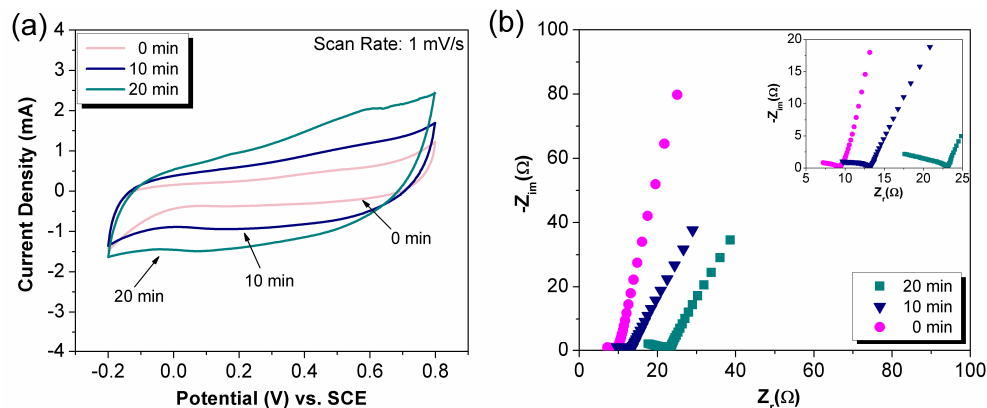


Figure 6-4. (a) CV curves and (b) EIS Nyquist plots, of three composite electrodes, a $\text{Mn}_3\text{O}_4/\text{CNTA}$ composite electrode before electrodeposition (denoted as 0 min) and two MnO_2/CNTA composite electrodes after 10 min and 20 min's electrodeposition (denoted as 10 min and 20 min, respectively).

It is also shown in Table 6-1 that the estimated capacitance for Mn_3O_4 nanoparticles (248 F/g) in this study is lower than that (299 F/g) in our previous report [16]. This is attributed to the wall number difference of CNTs in the CNTAs obtained by two different growing methods, WACVD and CCVD, as shown in Figure 6-5. Figure 6-5 clearly demonstrates that Mn_3O_4 nanoparticles distributed uniformly along individual large wall-number (7 walls) CNTs (Figure 6-5a), although the aggregation of nanoparticles was also observed at the junctions of CNTs (Figure 5-3e in Chapter 5). In contrast, fewer nanoparticles were found on individual small wall-number (3-4 walls) CNTs (frame regions in Figure 6-5b), and the nanoparticles preferentially deposited at the junctions of

Table 6-1. Improvement of the capacitance by anodic pulse-electrodeposition.

Electro-deposition Time (min)	Specific Capacitance (F/g) at 1 mV/s	Area-normalized Capacitance (F/cm ²)	Volumetric Capacitance (F/cm ³)	Specific Capacitance (F/g) of MnO _x at 1 mV/s
0	150	0.63	12.5	248 ^a (Mn ₃ O ₄)
10	179	1.27	25.4	221 ^b (ε-MnO ₂)
20	185	1.80	35.8	213 ^b (ε-MnO ₂)

a: estimated by assuming all capacitance arises from Mn₃O₄. b: calculated by the equation of $\Delta q / (\Delta V \cdot \Delta m)$, where Δq and Δm are the change of the total charge and weight before and after electrodeposition, respectively; while ΔV is the voltage window.

CNTs forming large aggregates (Figure 6-5b). The preferential aggregation of Mn_3O_4 nanoparticles on small wall-number CNTs grown by WACVD reduces their gravimetric capacitance, although this could be compensated for by increasing the Mn_3O_4 nanoparticle loading in the composite. Since the WACVD method is promising to achieve scalable production of CNTAs, rather than CCVD, precise control of CNT wall number by WACVD is an interesting direction, which has been partially discussed in Chapter 4 and may stimulate great interest in the future.

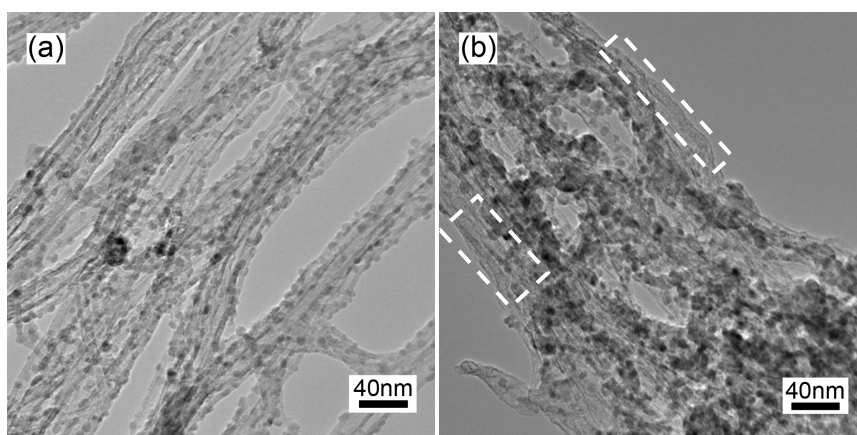


Figure 6-5. TEM images of Mn_3O_4 nanoparticles dip-casted on (a) large wall-number CNTs grown by CCVD (b) small wall-number CNTs grown by WACVD.

6.4. Conclusions

A scalable and cost-effective method was presented to fabricate composite electrodes based on millimeter-long CNTAs. The electrochemical performance of the composites was improved by anodic pulse-electrodepositing ϵ -MnO₂ nanorods within hydrophilic 0.5 mm-thick Mn₃O₄ decorated CNTAs. The maximum gravimetric capacitance was increased from 150 F/g to 185 F/g, and the area-normalized and volumetric capacitance values were raised by a factor of 3 after electrodeposition of MnO₂ nanorods. This leads to an extremely high area-normalized capacitance of 1.80 F/cm² for the MnO₂ nanorods/CNTA composite. These results may stimulate interest in using ultra-long CNTAs as three-dimensional architectures for power devices in the future.

6.5. References

- [1]. Simon, P.; Gogotsi, Y. *Nat. Mater.* **2008**, 7, 845-854.
- [2]. Kötz, R.; Carlen, M. *Electrochim. Acta* **2000**, 45, 2483-2498.
- [3]. Futaba, D. N.; Hata, K.; Yamada, T.; Hiraoka, T.; Hayamizu, Y.; Kakudate, Y.; Tanaike, O.; Hatori, H.; Yumura, M.; Iijima, S. *Nat. Mater.* **2006**, 5, 987-994.
- [4]. Fisher, A. E.; Pettigrew, K. A.; Rolison, D. R.; Stroud, R. M.; Long, J. W. *Nano Lett.* **2007**, 7, 281-286.
- [5]. Sharma, R. K.; Oh, H. S.; Shul, Y. G.; Kim, H. *J. Power Sources* **2007**, 173, 1024-1028.
- [6]. Chmiola, J.; Largeot, C.; Taberna, P. L.; Simon, P.; Gogotsi, Y. *Science* **2010**, 328, 480-483.
- [7]. Liu, X.; Pickup, P. G. *J. Power Sources* **2008**, 176, 410-416.
- [8]. Selvan, R. K.; Perelshtein, I.; Perkas, N.; Gedanken, A. *J. Phys. Chem. C* **2008**, 112, 1825-1830.
- [9]. Reddy, A. L. M.; Ramaprabhu, S. *J. Phys. Chem. C* **2007**, 111, 7727-7734.
- [10]. Shi, H. *Electrochim. Acta* **1996**, 41, 1633-1639.
- [11]. Jang, I. Y.; Muramatsu, H.; Park, K. C.; Kim, Y. J.; Endo, M. *Electrochem. Commun.* **2009**, 11, 721-723.
- [12]. Zhang, H.; Cao, G.; Yang, Y.; Gu, Z. *J. Electrochem. Soc.* **2008**, 155, K19-K22.

- [13]. Wei, W.; Cui, X.; Chen, W.; Ivey, D. G. *J. Phys. Chem. C* **2008**, 112, 15075-15083.
- [14]. Honda, Y.; Haramoto, T.; Takeshige, M.; Shiozaki, H.; Kitamura, T.; Ishikawa, M. *Electrochem. Solid-State Lett.* **2007**, 10, A106-A110.
- [15]. Shah, R.; Zhang, X.; Talapatra, S. *Nanotechnology* **2007**, 18, 195607(4).
- [16]. Cui, X.; Hu, F.; Wei, W.; Chen, W. *Carbon*, **2010**, in revision.
- [17]. Zhang, H.; Cao, G.; Wang, Z.; Yang, Y.; Shi, Z.; Gu, Z. *Nano Lett.* **2008**, 8, 2664-2668.
- [18]. Cui, X.; Wei, W.; Chen, W. *Carbon* **2010**, 48, 2782-2791.
- [19]. Nam, K. W.; Lee, C. W.; Yang, X. Q.; Cho, B. W.; Yoon, W. S.; Kim, K. B. *J. Power Sources* **2009**, 188, 323-331.
- [20]. Toupin, M.; Brousse, T.; Bélanger, D. *Chem. Mater.* **2004**, 16, 3184-3190.
- [21]. Chen, S.; Zhu, J.; Wu, X.; Han, Q.; Wang, X. *ACS Nano* **2010**, 4, 2822-2830.
- [22]. Hiraoka, T.; Najafabadi, A. I.; Yamada, T.; Futaba, D. N.; Yasuda, S.; Tanaike, O.; Hatori, H.; Yumura, M.; Ijima, S.; Hata, K. *Adv. Funct. Mater.* **2010**, 20, 422-428.

Chapter 7

General Conclusions, Contributions, and Future Work Recommendations

This chapter summarizes the novel observations and important conclusions obtained in this thesis, regarding ultra-long carbon nanotube array (CNTA) growth by conventional chemical vapor deposition (CCVD) and water-assisted CVD (WACVD) methods, as well as their applications on supercapacitors by modifying ultra-long CNTAs using dip-casting and anodic pulse-electrodeposition methods.

7.1. Growth of Ultra-long CNTAs by CCVD and WACVD

1. CNTA properties, including CNTA height, CNT diameter and wall number, are strongly dependent on the characteristics of catalyst particles it grows from. In addition to catalyst particle size, it has been found that inter-particle spacing is another important parameter that is more accurate than particle density to quantify the characteristics of densely packed catalyst particles. Adjusting the pretreatment conditions and the thickness of the catalyst film lead to flexible control of catalyst particle size and interspacing.
2. Growth kinetics of CNTAs grown from the two catalyst films (Fe-1 nm and Fe-3 nm) with different pretreatment conditions by CCVD shows that inter-particle spacing affects the CNTA height by affecting their lengthening time, and accordingly affects the diameter and wall number of CNTs because

- of the concurrent change in the thickening time.
3. The growth kinetics of multiwalled CNT (MWCNT) arrays demonstrates lengthening and thickening stages in both WACVD and CCVD methods. In the lengthening stage of WACVD, CNT wall number remains constant and catalysts preserve the activity; while in the thickening stage, MWCNTs thicken substantially by the gas phase-induced thickening process and catalysts deactivate following the radioactive decay model. In CCVD, the lengthening and thickening processes were found to be competitive. Although gas phase-induced thickening also predominates in the thickening stage of CCVD, it was found that catalyst-induced thickening occurs in the lengthening stage of CCVD.
 4. Water was shown to preserve catalyst activity by significantly inhibiting catalyst-induced and gas phase-induced thickening processes in WACVD.
 5. Ethylene flow rate has a great influence on MWCNT array growth not only in the growth stage of CNT arrays, but also in the nucleation stage of CNT walls; while hydrogen flow rate shows insignificant effects on MWCNT array growth in the lengthening stage of WACVD.

7.2. Application of Ultra-long CNTAs to Supercapacitors

1. Mn_3O_4 nanoparticles have been successfully deposited within millimetre-long CNTAs to form $\text{Mn}_3\text{O}_4/\text{CNTA}$ composite arrays through dip-casting method from non-aqueous liquids. It was shown that Mn_3O_4 nanoparticles disperse uniformly within CNTAs, which in turn changes CNTAs from hydrophobic to hydrophilic.
2. The hydrophilic $\text{Mn}_3\text{O}_4/\text{CNTA}$ composite electrode presents a high capacitance and long cycle life, making it very promising for electrochemical supercapacitors. Interestingly, the deposited Mn_3O_4 nanoparticles demonstrate superior specific capacitance and rate capacity because of their nanosize and the excellent nanostructured scaffold, millimeter-long CNTA.
3. A scalable and cost-effective method was developed to fabricate composite electrodes based on millimeter-long CNTAs. This includes the steps of transferring CNTAs onto a conductive tape, a dip-casting process to change their hydrophobicity, a rolling process to adjust CNTA height and anodic pulse-electrodeposition of active materials. The electrochemical performance was improved by anodic pulse-electrodepositing $\epsilon\text{-MnO}_2$ nanorods within hydrophilic 0.5 mm (rolled)-thick Mn_3O_4 decorated CNTAs. In particular, the area-normalized and volumetric capacitance values were raised by a factor of

3 after electrodeposition of MnO₂ nanorods. This led to an extremely high area-normalized capacitance of 1.80 F/cm² for the MnO₂ nanorods/CNTA composite.

7.3. Contributions

1. Invented a repeatable process for growing millimeter-scale CNTAs by CCVD and WACVD methods. The process of WACVD is very stable and promising for commercial production of CNTAs. (Cui, X. W.; Chen, W. X., “Fabrication of Carbon Nanotube Arrays”, US Provisional Patent Application, submitted, by Tech Edmonton.)
2. Demonstrated unique growth mechanism and growth kinetics of MWCNT arrays in WACVD and CCVD, which provides a theoretical guide to the manipulation of CNT structures, such as CNTA height, CNT wall number, CNT purity, etc.
3. Invented a method to change CNTAs from hydrophobic to hydrophilic without destroying their alignment and integrity, which is believed to open up a new route of utilizing ultra-long CNTAs. (Cui, X. W.; Chen, W. X., “Carbon Nanotube Array Composite Based Electrodes”, US Provisional Patent

Application No. USSN 61/346,361.)

4. The decoration of millimetre-long CNTAs with metal and metal oxide particles to fabricate CNTA-based composite electrodes was, for the first time, achieved in this thesis. This 3D-nanoparticle decorated hierarchical porous structure is desired for many applications, such as supercapacitors, hydrogen storage, gas or liquid sensors, lithium ion batteries, etc.

7.4. Future Work Recommendations

1. To fully uncover the relationship between catalyst patterns and CNTA properties by investigating reaction gas ratios, pretreatment conditions, etc, in order to provide theoretical and technical solutions for mass and selective growth of the desired CNTAs.
2. To investigate the underlying mechanism of the role of water in assisting ultra-long CNTA growth by carefully examining the chemistry and structure (inner and outer) of catalyst particles during catalyst particle evolution in the pretreatment stage by TEM and in the growth stage by in-situ TEM.
3. To apply an acid treatment to CNTAs immediately after the dip-casting step to

increase the defects or hydrophilic functional groups on CNT walls.

Electroless deposition method is another effective route of modification of millimeter-long CNTAs.

4. Three-dimensional cell, which are defined as “transport between electrodes remains one-dimensional at the microscopic level, while the electrodes are configured in complex geometries”, is considered to be the best configuration to demonstrate almost all the advantages of using ultra-long CNTAs. Because ultra-long CNTAs can increase energy density of the cell within the footprint area while maintain the power density of the cell. Furthermore, since CNTAs are easy to be patterned, monolithic CNTA-based cells are promising to be fabricated as high performance micro-supercapacitors.
5. The usage of ultra-long CNTA as a support for active materials is also desired and very promising to be explored in many other applications, such as hydrogen storage, gas or liquid sensors, lithium ion batteries, etc.

Appendix I

Saccharin Effects on Direct-Current Electroplating Nanocrystalline Ni-Cu Alloys*

* Material in this appendix has been published in:

Cui, X. W.; Chen, W. X. **Journal of the Electrochemical Society**, 2008, 155, K133-K139.

AI.1. Introduction

Electrodeposition of nanostructured materials has received great attention in the past several decades because of its distinct advantages in preparing thin film nanomaterials [1]: 1) a cost-effective method, comparing with other methods such as chemical vapor deposition, physical vapor deposition, etc.; 2) low fabrication temperatures, which minimize interdiffusion during deposition; 3) uniform films with controllable structure, thicknesses and compositions. Moreover, the electrodeposited nanomaterials also demonstrate distinguishable properties and have been utilized as tribological materials, corrosion resistant materials, magnetic materials, and noble metal catalysts [2-6].

Among the electrodeposited nanomaterials, electrodeposited nanocrystalline (nc) Ni-Cu alloys and their multilayers [3] have attracted growing attention because of their improved resistance to pitting corrosion [3] and their particular giant magnetoresistance properties [7]. The direct-current (dc) plating of Ni-Cu alloy coatings is normally performed at above a critical current density in order to form thick coatings with controlled compositions. However, a high and continuous current density flowing through the solution in dc plating promotes dendrite growth and rough surface formation [8]. To dc plate nc-Cu-Ni alloy coatings requires the application of even higher current densities, which could further deteriorate surface finish of the coatings and result in the formation of cracks and

pores in the deposits [9]. Ghosh et al. [10] reported that powdery deposits could be formed when current densities are over 30-40 mA/cm² in dc plating. In the last decade, many efforts have been undertaken to avoid this problem, for example, by pulse current (pc)-plating nc-Ni-Cu multilayers [3, 10, 11]. However, pc plating needs special consideration of the power supply; and it is not as efficient and cost-effective as dc plating. Up to now, no research has been reported to dc electrodeposit nc-Ni-Cu alloy coatings with a surface finish comparable to those produced by pc plating.

Organic additives are often used in electrodeposition to moderate deposit growth rates and control film quality. Most organic additives that have been attempted in dc-electroplated Ni-Cu alloy coatings were found to be complexing agents, e.g., pyrophosphate [12], glycine [13], citrate [14], etc. Saccharin, however, is another type of organic additive. Small amount of saccharin, typically 2 g/L, was found to markedly increase cathodic potential [15] and act as a leveling and grain size reduction agent in many electroplating systems including Cu-Co, Ni and Fe-Ni. [15, 16, 17]. It is believed that saccharin molecules when added in the plating solution adsorb onto the electrode surface and affect the reduction process of metal ions [17]. However, the effect of saccharin on dc Ni-Cu alloy codeposition is still unknown.

In this appendix, a reduced amount of saccharin, 0.5 g/L, was added into Green's type citrate bath [14] in order to obtain high-quality surface finish and nano-grain size Ni-Cu alloy coatings from dc plating. Saccharin effects have also been discussed in Ni-Cu alloy codeposition system.

AI.2. Experimental Procedure

Nanocrystalline Ni-Cu alloy coatings were electroplated galvanostatically by sediment codeposition (SCD) technique in which a large anode (pure Ni) was located horizontally on the top of the plating bath and the cathode (substrate to be plated) was put parallel with the anode and to the edge of 300 mL beaker. A total charge of 144 C was performed through each electrodeposition experiment by a dc power supply. Agitation was provided by a magnetic stir bar with a stirring rate of 200rpm. A water bath was set up around the system to control the temperature of solution at 30 ± 0.5 °C. The centrifugally cast HP alloy with dimensions of 10×10×2 mm was used as coating substrate. Before plating, the substrate was ground using 600-grit SiC sand papers and pretreated by degreasing and activation solutions. A very thin pure Ni layer was plated first in order to enhance the adherence of the coating to the substrate.

The basic electrolyte is similar to that previously used by Green et al. [14], where

Cu/Ni ratio is maintained as low as 1:28. The composition of basic electrolyte with sodium dodecyl sulphate (SDS) (denoted as Green bath) and with SDS and saccharin (denoted as GSS bath) is shown in Table AI-1. All the solutions were prepared from analytical reagent-grade chemicals with deionized water.

Surface morphology of the deposited coating was examined using a Hitachi H2700 scanning electron microscope (SEM). An attached Princeton Gamma-Tech (Prism IG) ultra thin window (UTW) energy dispersive spectrometer (EDS) was used to determine the composition. The phase structure was analyzed by X-ray diffraction (XRD) and also JEOL 2010 transmission electron microscope (TEM). For TEM studies, as-plated coatings were punched and thinned by jet polishing at a cell potential of 20V in a solution of 10 vol% perchloric acid and 90 vol% methanol at -30°C. Grain size distributions were processed by a comprehensive image analysis software on TEM bright field and dark field images.

A classic three-electrode cell was used. The reference electrode was a saturated calomel electrode (SCE). The steady-state polarization curves were recorded galvanostatically and corrected for ohmic drop by electrochemical impedance spectroscopy. The partial steady-state polarization curves for Ni were calculated from the deposit composition by neglecting hydrogen evolution (insignificant in the current system). Electrochemical impedance plots were recorded within a

range of 100 kHz to 0.1 Hz using Gamry PC4/750 potentiostat/galvanostat (EIS300 electrochemical impedance spectroscopy) system.

Table AI-1. Composition and operating conditions for Ni/Cu and Ni/Cu-Al plating

Composition of Green Bath	Composition of GSS Bath
Nickel sulfate ($\text{NiSO}_4 \cdot 6\text{H}_2\text{O}$): 184 g/L	Nickel sulfate ($\text{NiSO}_4 \cdot 6\text{H}_2\text{O}$): 184 g/L
Cupric sulfate ($\text{CuSO}_4 \cdot 5\text{H}_2\text{O}$): 6.24 g/L	Cupric sulfate ($\text{CuSO}_4 \cdot 5\text{H}_2\text{O}$): 6.24 g/L
Sodium citrate (NaCit_3): 76.47 g/L	Sodium citrate (NaCit_3): 76.47 g/L
Sodium dodecyl sulphate ($\text{CH}_3(\text{CH}_2)_{10}\text{CH}_2\text{OSO}_3\text{Na}$): 0.2g/L	Sodium dodecyl sulphate ($\text{CH}_3(\text{CH}_2)_{10}\text{CH}_2\text{OSO}_3\text{Na}$): 0.2g/L
	Saccharin ($\text{C}_7\text{H}_5\text{NO}_3\text{S}$): 0.5g/L
Operation conditions	
Anode: pure Ni	Temperature: 30 ± 0.5 °C
pH: ~ 4.5	Stirring rate: 200 rpm

AI.3. Results and Discussion

AI.3.1. Composition of Electroplated Ni-Cu Nanocrystalline Coatings

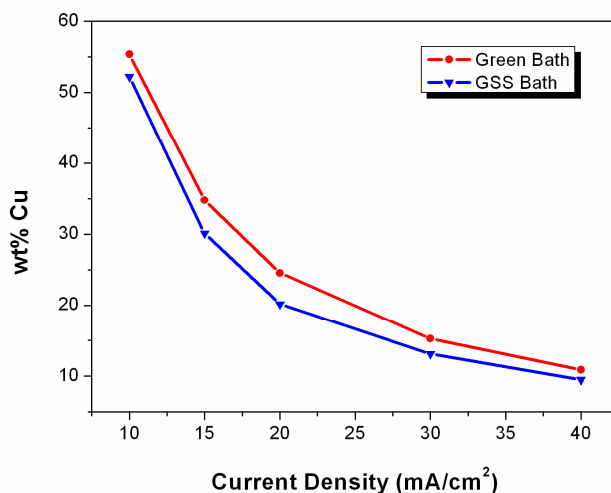


Figure AI-1. Composition of as-plated Ni-Cu alloy coatings from Green baths and GSS baths as a function of current density.

Figure AI-1 shows the dependence of Cu content in the Ni-Cu alloy coatings on the applied current densities. A wide range of Ni-Cu alloy compositions could be electroplated from Green baths and GSS baths at pH 4.5, with the lowest Cu content being around 10 wt % obtained at a current density (i) of 40 mA/cm². In contrast, Ni-Cu alloy coatings deposited from other citrate solutions couldn't reach this low Cu content at the current density of 40 mA/cm² due to higher Cu concentration or higher Cu/Ni ratio (1:10~1:4) in their baths [9, 10]. In addition,

Figure AI-1 shows that Cu reduction is suppressed by adding saccharin in the electrolyte. Since Cu reduction is under mass transfer control at these current densities, the adsorption of saccharin or other intermediate reaction products of saccharin could retard the diffusion of Cu cations onto the cathode surface, and thus restrict Cu cations reduction and Cu deposition.

AI.3.2. Characterization of Electroplated Ni-Cu Nanocrystalline Coatings

Figure AI-2 shows the surface morphology of electroplated Ni-Cu alloy coatings examined by SEM. The alloy coating (Ni-55.4 wt % Cu) obtained at $i=10$ mA/cm² from Green baths (Figure AI-2a) features a coarse nodular structure, and that (Ni-24.6 wt % Cu) produced at $i=20$ mA/cm² from Green baths (Figure AI-2b) displays fine crystalline structures. Contrarily, the alloy coatings electroplated from GSS baths, Ni-52.2 wt % Cu (Figure AI-2c) and Ni-20.2 wt % Cu (Figure AI-2d) obtained at $i = 10$ mA/cm² and $i = 20$ mA/cm², respectively, exhibit very smooth and featureless surfaces, which are comparable to those deposited by pc-plating [10]. Nodule features in the alloy coatings from GSS baths starts to appear, but to a very less degree, when the current density was increased up to 40 mA/cm² (Figure AI-2e). Cross-section backscattered images of Ni-Cu alloy coatings deposited from two different baths are also shown in Figure AI-3. Therefore, saccharin acts as a leveling agent in the dc plating of Ni-Cu alloy

coatings.

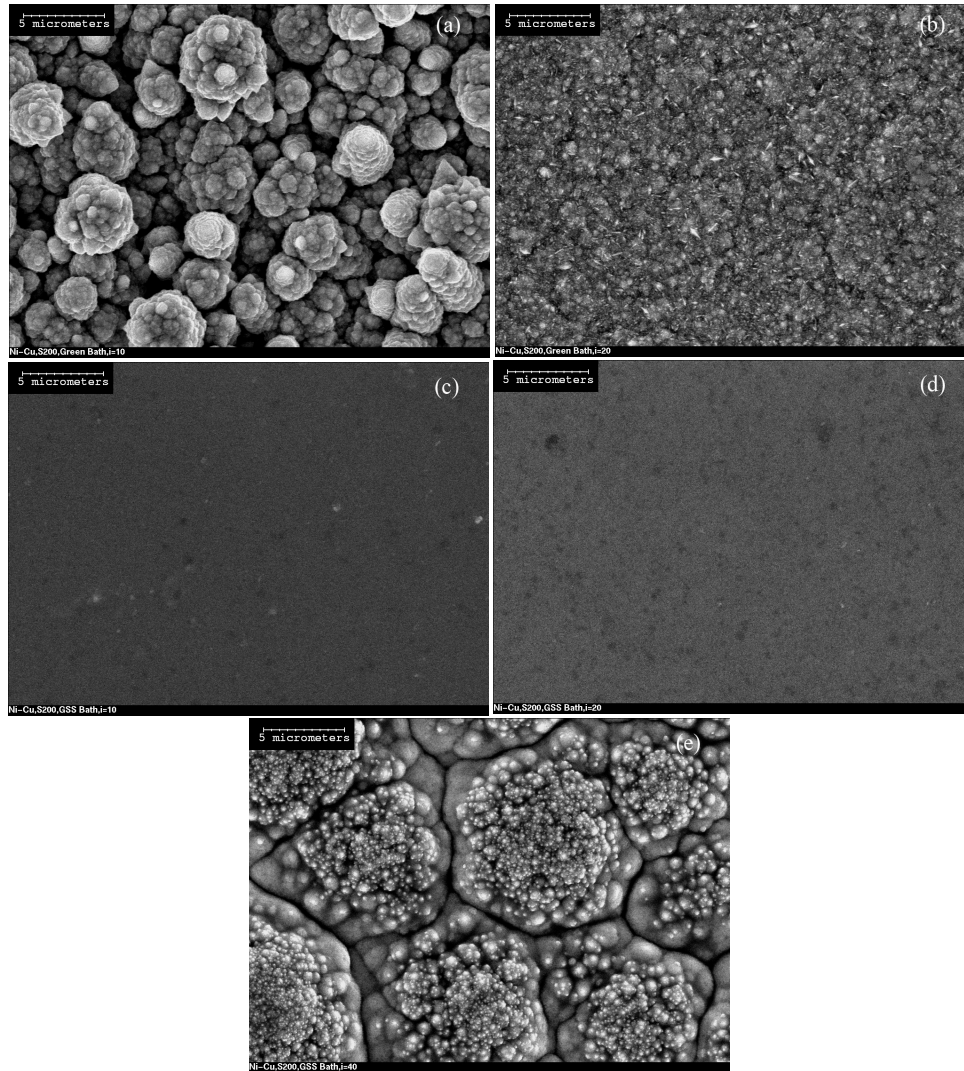


Figure AI-2. Plan-view of SEM images of as-plated Ni-Cu alloy coatings prepared from (a) Green baths, $i=10 \text{ mA/cm}^2$ (Ni-55.4 wt % Cu), (b) Green baths, $i=20 \text{ mA/cm}^2$ (Ni-24.6 wt % Cu), (c) GSS baths, $i=10 \text{ mA/cm}^2$ (Ni-52.2 wt % Cu), (d) GSS baths, $i=20 \text{ mA/cm}^2$ (Ni-20.2 wt % Cu), and (e) GSS baths, $i=40 \text{ mA/cm}^2$ (Ni-9.5 wt % Cu).

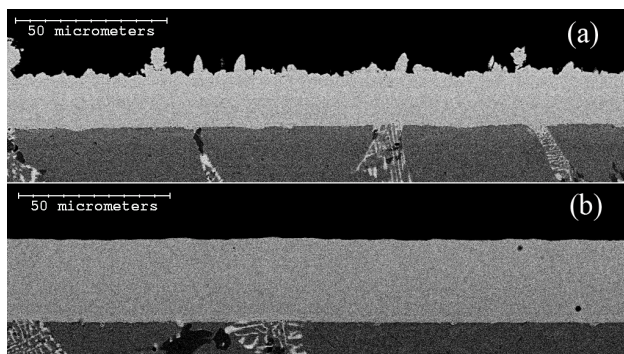


Figure AI-3. Cross-section SEM images of as-plated Ni-Cu alloy coatings prepared from (a) Green baths, $i=10 \text{ mA/cm}^2$ (Ni-55.4 wt % Cu), and (b) GSS baths, $i=10 \text{ mA/cm}^2$ (Ni-52.2 wt % Cu).

Figure AI-4 shows XRD patterns of the Ni-Cu alloy coatings deposited from Green baths and GSS baths. All peaks on the XRD patterns could be assigned to Ni-Cu solid solution, face-centered cubic (fcc) phase; no primitive tetragonal $L1_0$ -type phase was detected, which, however, was reported by Ghosh et al. [11]. By comparing the XRD patterns of the alloy coatings from Green baths (Figure AI-4a) and GSS baths (Figure AI-4b), it suggests that the addition of saccharin did not change the phase structure in the final coatings, only slightly suppressed the reduction of Cu cations.

Another characteristic shown in the XRD patterns is that the as-deposited alloy coatings are nanocrystalline as observed from the broadening of the XRD peaks. For example, it can be clearly seen from Figure AI-4 that the peaks of the alloy

coatings from Green baths are sharper than those from GSS baths. According to Sherrer's equation [18],

$$D = K\lambda / B \cos \theta \quad (\text{AI-1})$$

where D is diameter of the grain; K is a constant, and adopted as 1; B is the broadening of the line, λ is the wave-length of the X-ray, and θ is the Bragg angle. The broadening of the (111) peaks were also corrected by well annealed Ni-Cu alloy samples. Hence, the estimated grain size of the alloy coatings produced at $i = 20 \text{ mA/cm}^2$ from Green baths and GSS baths was determined based on Eq. (AI-1) to be 50 nm and 37 nm, respectively.

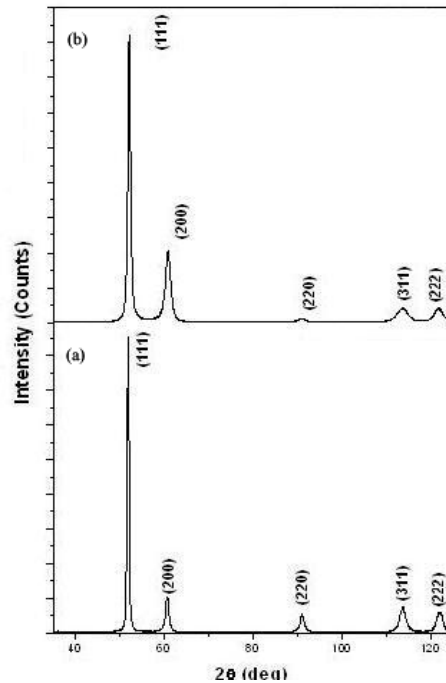


Figure AI-4. XRD patterns of as-plated Ni-Cu alloy coatings prepared at $i=20 \text{ mA/cm}^2$, from (a) Green baths (Ni-24.6 wt % Cu), and (b) GSS baths (Ni-20.2 wt % Cu).

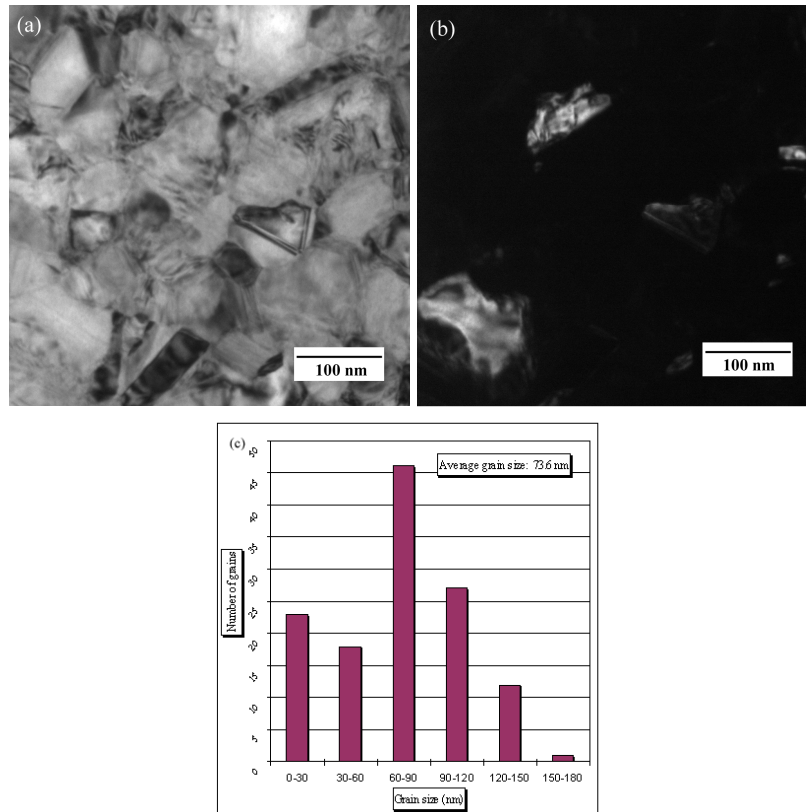


Figure AI-5. TEM images of as-plated Ni-24.6 wt % Cu coating prepared from Green baths at $i=20 \text{ mA/cm}^2$, (a) BF image, (b) DF image, and (c) distribution of grain size.

Figure AI-5 and Figure AI-6 are bright field (BF) and dark field (DF) TEM images of the as-plated Ni-Cu alloy coatings from Green baths and GSS baths produced at $i = 20 \text{ mA/cm}^2$ with the composition of Ni-24.6 wt % Cu and Ni-20.2 wt % Cu, respectively. No void or other forms of defects can be seen in the microstructure. DF images were taken by using the diffracted beams in the circled part of the diffraction rings in Figure AI-7. The statistical distributions of the grain size were acquired from BF and DF images taken from at least 10

different locations on each sample. The alloy coatings from Green baths in Figure

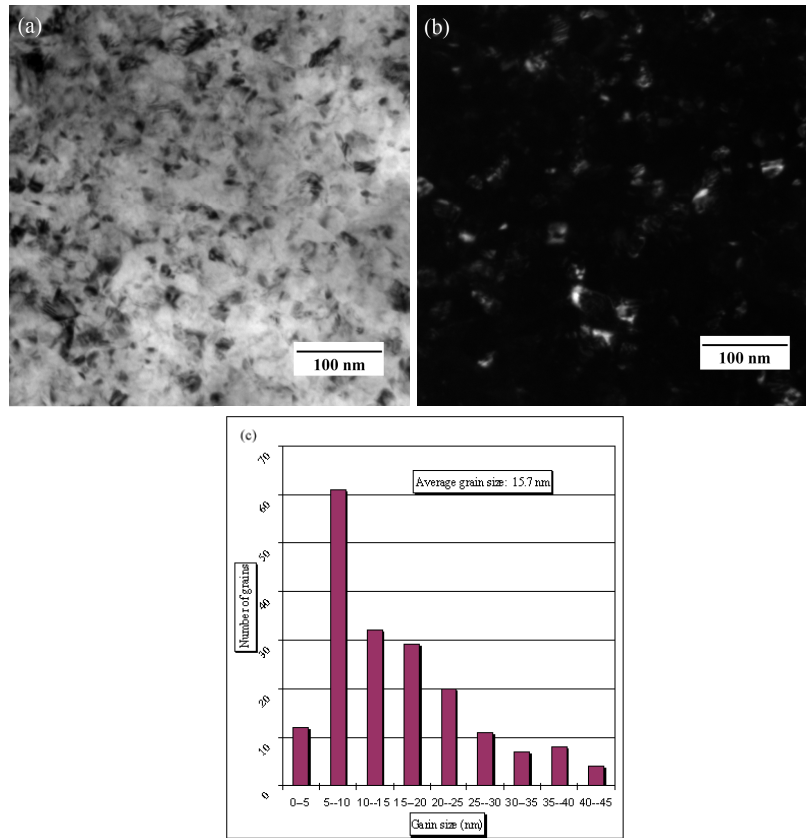


Figure AI-6. TEM images of as-plated Ni-20.2 wt % Cu coating prepared from GSS baths at $i=20 \text{ mA/cm}^2$, (a) BF image, (b) DF image, and (c) distribution of grain size.

AI-5a and AI-5b show relatively large grain size, but the grain size is still less than 100 nm. Figure AI-5c demonstrates that the grain size is in the range of 11-149 nm with an average value of 73.6 nm. This value is much higher than that of dc plated Ni-Cu alloy coatings produced at the same current density in Ghosh's work [10], which was between 10-74 nm with an average of 27.8 nm, probably

because the Cu concentration is so different for these two systems. Figures AI-6a and AI-6b show that the grain size of the alloy coatings from GSS baths is much smaller than that from Green baths. The grain size for the alloy coatings from GSS baths is in the range of 2-43 nm with an average of 15.7 nm, as shown in Figure AI-6c. This value is comparable to the grain size (12.7 nm) of the Ni-Cu alloy coatings produced by pc plating [10]. Therefore, saccharin also acts as a grain size reduction agent in the dc plating of Ni-Cu alloy coatings. Note that XRD broadening method yields less accurate grain size measurements in this system.

Electron diffraction (ED) patterns of the two alloy coatings in Figures AI-5 and AI-6 are shown in Figure AI-7. It suggests that the deposited alloy coatings from Green baths and GSS baths are both single phase fcc polycrystalline, which agrees well with the results from XRD analysis. The spotty rings in Figure AI-7a and the broader continuous rings in Figure AI-7b prove that the grain size decreases significantly by adding saccharin. However, some diffraction spots between (200) and (220) rings in Figure AI-7a and two weak rings in Figure AI-7b indicated by arrows imply the existence of the primitive tetragonal $L1_0$ -type phase in the coatings. This phase should be in a very small amount as it is below the detection limit (5 wt % or higher) of the XRD system used. This particular phase was not detected in the most of the electroplated Ni-Cu alloy coatings, except that Ghosh

et al. [11] reported a deposition of Ni-Cu alloy coatings by pc plating with a much larger amount of this $L1_0$ -type phase. Large amount of ordered nanophase increases hardness of the coating due to precipitation hardening [11], but may also impair their resistance to corrosion. In this sense, dc plated nc-Ni-Cu alloy coatings from GSS baths should be advantageous over the pc plated nc-coatings.

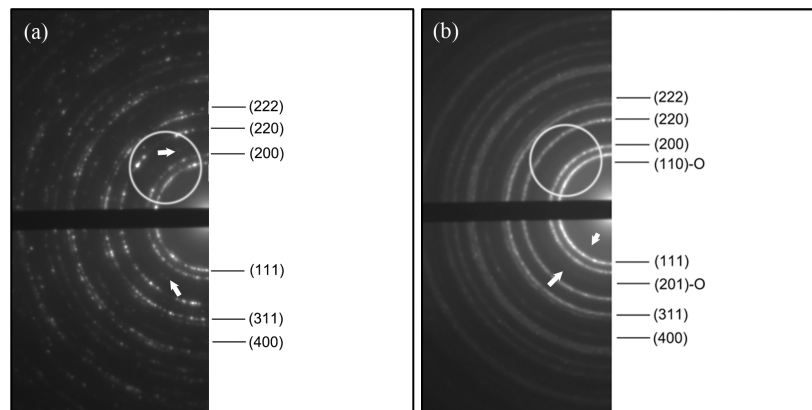


Figure AI-7. Diffraction patterns of as-plated Ni-Cu alloy coatings prepared at $i = 20 \text{ mA/cm}^2$ from (a) Green baths (Ni-24.6 wt % Cu) and (b) GSS baths (Ni-20.2 wt % Cu).

AI.3.3. Steady-state Polarization and Electrochemical Impedance Investigation

The partial steady-state polarization curves for Ni in the Ni deposition potential range (-950 to -1200 mV/SCE), corrected for ohmic drop, are shown in Figure AI-8. The addition of SDS has minor influence on Ni deposition which is

consistent with that observed in Cu-Co codeposition system [15]. The addition of saccharin or both SDS and saccharin, on the other hand, substantially shifts the polarization curves towards more negative values at high overpotentials. This shift becomes much less or disappeared at low overpotentials; e.g., no shift of overpotential was observed at $i_{total} = 20 \text{ mA/cm}^2$ when saccharin was added. All the curves in Figure AI-8 demonstrate two different behaviors (two linear stages) depending on the condition of polarization, indicating a two-step discharge of Ni^{2+} cations with intermediate adion Ni_{ad}^+ [19-22]. Also note that adding saccharin decreases Tafel slopes at low overpotentials. It reveals that the kinetics of Ni(II) reduction has also been affected by adding saccharin.

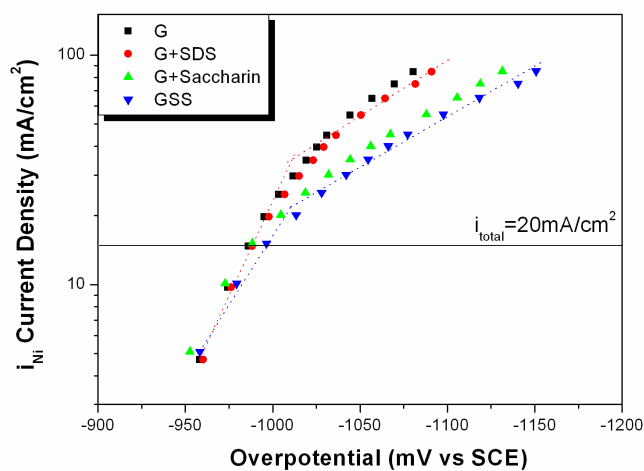


Figure AI-8. Partial steady-state polarization curves for Ni, corrected for ohmic drop, recorded in the potential range for the Ni deposition from the plating baths without additive (■), with SDS (●), saccharin (▲), and both additives (▼).

An electrochemical impedance investigation using frequencies ranging from 100 kHz to 0.1 Hz was carried out in the potential range of Ni deposition. As shown in Figure AI-9, all the Nyquist plots exhibit a high-frequency capacitive loop, which corresponds to the relaxation of the double layer capacitance, C_d . From the high-frequency capacitive loops, it is also evident that adding saccharin increases charge transfer resistance which should be caused by adsorption of saccharin or other intermediate reaction products of saccharin on the cathode surface. In addition, the solutions free of additives and those with only SDS show large low-frequency inductive loop. However, the solutions with only saccharin and with both of the additives show a much smaller low-frequency inductive loop along with a low-frequency capacitive loop.

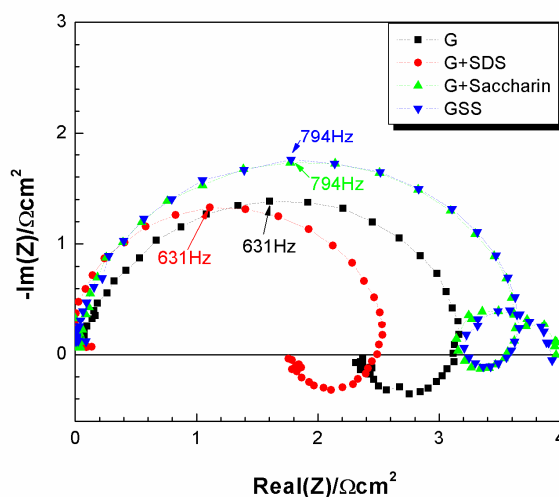


Figure AI-9. Nyquist plots recorded at a current density of 20 mA/cm^2 in the plating baths without additive (■), with SDS (●), saccharin (▲), and both additives (▼).

The low-frequency inductive loop has been ascribed to the relaxation of the electrode coverage by the adsorbed intermediate Ni_{ad}^+ [19], while the occurrence of the low-frequency capacitive loop is still controversial. The implication of EIS results has been further explored in the following discussion.

AI.3.4. Mechanism of Ni-Cu Plating as Affected by Saccharin Addition

A possible mechanism for two-step Ni deposition from a sulfate electrolyte was first proposed by Epelboin et al. [19], and further discussed by Chassaing et al. [20] with the following reactions:

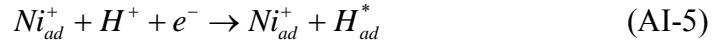


It was proposed that the intermediate adion Ni_{ad}^+ , more or less solvated and possible complexed (such as $NiOH_{ad}$), acts as both an intermediate consumed in Reaction (AI-3) and a catalyst in Reaction (AI-4).



At low pH, 1.5 to 3, Reactions (AI-5 to AI-7) have also been proposed to occur where the H_{ad}^* is strongly bonded to the cathode surface and acts as an inhibitor

for hydrogen evolution.

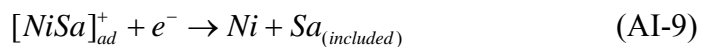


At pH values higher than 4, Watson and Walters [21] suggested that only Reactions (AI-2 to AI-4) are most likely to occur. In the present case at pH of 4.5, the observation of inductive loops on all the Nyquist plots in Figure AI-9 suggests that Reactions (AI-2 to AI-4) are most likely to occur. In addition, it is noted that there is no low-frequency capacitive loop observed for the saccharin free solutions, as shown in Figure AI-9. The variation of coverage by H_{ad}^{*} was considered to induce the low-frequency capacitive loop [20], confirming that reactions (V) to (VII) are less likely to occur at pH of 4.5.

Ghosh et al. [11] has explained grain size reduction effect of polymer molecules in Ni-Cu alloy codeposition by electrocrystallization principle. It was suggested that by increasing cathodic potential due to adsorption of polymer molecules, the number of nuclei increases; and thus the grain size is reduced by promoting grain nucleation. However, this mechanism cannot be used to explain grain size reduction caused by saccharin in the present system, because the shift of overpotential is insignificant at low current densities (in the low overpotential

stage) in Figure AI-8. However, different Tafel slopes at low overpotentials in Figure AI-8 indicate a change of Ni²⁺ reduction kinetics, which can explain the grain size reduction effect of saccharin. In Reaction (AI-4), Ni⁺_{ad} represents a self-perpetuating kink site for Ni²⁺ reduction. In the Ni-Cu alloy plating, this kink site can also be formed [22], catalyzing Ni-Cu alloy formation and promoting grain growth. Adding saccharin, however, suppresses the occurrence of catalytic reaction (AI-4); and consequently, reduces grain size by inhibiting grain growth. The suppression of Reaction (AI-4) is evidenced by a small low-frequency inductive loop on the Nyquist plots of saccharin-containing solutions. It shows that the relaxation of Ni⁺_{ad} becomes faster by adding saccharin, which reduces the adsorption of Ni⁺_{ad} to the cathode surface acting as catalytic sites for Ni²⁺ reduction. Therefore, saccharin reduces grain size by inhibiting grain growth, rather than promoting grain nucleation, in the present system.

It is hypothesized that the reduction of Ni⁺_{ad} adsorption is caused by reactions between Ni⁺_{ad} and saccharin molecules through the following steps (“Sa” stands for saccharin or other intermediate reaction products of saccharin):



Thermodynamically, [NiSa]⁺_{ad} is much more stable than Ni⁺_{ad}, similar to the role

of adding other organic additives, e.g. citrate. It is suggested that it is the formation of $[\text{NiSa}]_{\text{ad}}^+$ that suppresses the Reaction (AI-4). The proposed Reactions (AI-8) and (AI-8) are comparable to reactions (AI-5) and (AI-7), and the variation of coverage by $[\text{NiSa}]_{\text{ad}}^+$ is able to generate a low-frequency capacitive loop, similar to the action of H_{ad}^* in low pH sulfuric solutions. Thus, it is also suggested that it is the coverage of $[\text{NiSa}]_{\text{ad}}^+$ that blocks Cu cation diffusion to the cathode at low overpotential region, which restricts the deposition of Cu, as shown in Figure AI-1.

AI.4. Conclusions

Nanocrystalline Ni-Cu alloy coatings with a mirror-surface finish and dendrite-free structure have been successfully electroplated via sediment codeposition (SCD) technique. This was achieved by adding only 0.5 g/L saccharin into a plating bath previously used by Green et al. The Cu content in the Ni-Cu alloy coatings can be controlled to be as low as 10 wt % by changing current density. The grain size in the coatings was determined by X-ray diffraction and electron microscopy analysis to be 15.7 nm in average, which is very comparable to that in pc plated Ni-Cu alloy coatings. Ordered L1_0 -type Ni-Cu nano-phase was also detected but to an amount much less than that found in pc plated Ni-Cu alloy coatings.

Saccharin was proved to suppress the reduction of Cu and act as a leveling and grain size reduction agent in Ni-Cu alloy codeposition. From the steady-state polarization and electrochemical impedance analyses, it was found that saccharin reduces grain size by inhibiting grain growth, rather than promoting grain nucleation, in the present system. It is also suggested that these saccharin effects are delivered by the formation of $[\text{NiSa}]_{\text{ad}}^+$, which reduces the adsorption of Ni_{ad}^+ to inhibiting grain growth and suppresses Cu deposition.

AI.5. References

- [1]. Hodes, G. in *Electrochemistry of Nanomaterials*, edited by Hodes, G. (VCH. Wiley, Weinheim, 2001)
- [2]. Tao, S.; Li, D. Y. *Nanotechnology* **2006**, 17, 65-78.
- [3]. Ghosh, S. K.; Dey, G. K.; Dusane, R. O.; Grover, A. K. *Journal of Alloys and Compounds* **2006**, 426, 235-243.
- [4]. Kim, D.; Park, D. Y.; Yoo, B. Y.; Sumodjo, P. T. A.; Myung, N. V. *Electrochimica Acta* **2003**, 48, 819-830.
- [5]. Löffler, M. S.; Natter, H.; Hempelmann, R.; Wippermann, K. *Electrochimica Acta* **2003**, 48, 3047-3051.
- [6]. Park, D. Y.; Myung, N. V.; Schwartz, M.; Nobe, K. *Electrochimica Acta*, **2002**, 47, 2893-2900.
- [7]. Kazeminezhad, I.; Schwarzacher, W. *Journal of Solid State Electrochemistry* **2004**, 8, 187-189.
- [8]. Orliňáková, R.; Turoňová, A.; Kladeková, D.; Gálová, M.; Smith, R. M. *Journal of Applied Electrochemistry* **2006**, 36, 957-972.
- [9]. Baskaran, I.; Narayanan, T. S. N. S.; Stephen, A. *Materials Letters* **2006**, 60, 1990-1995.
- [10]. Ghosh, S. K.; Grover, A. K.; Dey, G. K.; Totlani, M. K. *Surface and Coatings Technology* **2000**, 126, 48-63.
- [11]. Ghosh, S. K.; Grover, A. K. *Journal of Materials Research* **2006**, 21, 45-61.

- [12]. Ishikawa M.; Enomoto, H. *Journal of the Metal Finishing Society Japan* **1980**, 31, 545-551.
- [13]. Mizushima, I.; Chikazawa, M.; Watanabe, T. *Journal of the Electrochemical Society* **1996**, 143, 1978-1983.
- [14]. Green, T. A.; Russel, A. E.; Roy, S. *Journal of the Electrochemical Society* **1998**, 145, 875-881.
- [15]. Chassaing, E. *Journal of the Electrochemical Society* **2001**, 148, C690-C694.
- [16]. El-Sherik, A. M.; Erb, U. *Journal of Materials Science* **1995**, 30, 5743-5749.
- [17]. Kim, S. H.; Sohn, H. J.; Joo, Y. C.; Kim, Y. W.; Yim, T. H.; Lee, H. Y.; Kang, T. *Surface and Coatings Technology* **2005**, 199, 43-48.
- [18]. Birks L. S.; Friedman, H. *Journal of Applied Physics* **1946**, 17, 687-691.
- [19]. Epelboin, I.; Jousselein M.; Wiart, R. *Journal of Electroanalytical Chemistry* **1981**, 119, 61-71.
- [20]. Chassaing, E.; Jousselein M.; Wiart, R. *Journal of Electroanalytical Chemistry* **1983**, 157, 75-88.
- [21]. Watson S. W.; Walters, R. P. *Journal of the Electrochemical Society* **1991**, 138, 3633-3637.
- [22]. Chassaing E.; Quang, K. V. U. *Journal of Applied Electrochemistry* **1987**, 17, 1267-1280.

Appendix II

Electrochemical Study of Codeposition of Al particle – Nanocrystalline Ni/Cu composite coatings*

* Materials in this appendix has been published in:

Cui, X. W.; Wei, W. F.; Liu, H. F.; Chen, W. X. **Electrochimica Acta**, 2008, 54, 415-420.

III.1. Introduction

Codeposition of metal matrix and metal/ceramic particle composites (EMMCs) that entail desirable mechanical, physicochemical and electrocatalytic properties [1-4], has acquired great improvement in recent years. Many types of EMMCs have been developed to enhance wear resistance, Ni-Al₂O₃, Ni-SiC [5, 6], corrosion resistance, Cu-Al₂O₃, Ni-Al [7, 8], and self-lubrication, Ni-PTFE [9], etc. To extend the use of EMMCs, efforts have been made in codepositing alloy matrix-particle composite coatings, e.g., brass-graphite wear resistant composites [10] and CoNi-barium ferrite magnetic composites [11]. Recent development is codeposition of particles in a nanostructured metal matrix, like Ni and Co, which is able to produce a large range of high-performance composite coatings for specific applications [12-15]. However, little effort has been made on incorporation of particles into nanocrystalline alloy matrix that may have more potential applications and exhibit better mechanical and physicochemical properties than those found in conventional materials.

Studying the effect of particles on polarization curves could yield useful information about the codeposition process of particles within metal or alloy matrix. However, there are few reports that directly compare polarization curves with and without particles. During codeposition of nonconductive particles, it is generally believed that the cathode surface area decreases due to the coverage of

nonconductive particles, and thus potential shifts to the negative region; whereas during incorporation of conductive or semiconductive particles the cathode surface area increases, hence, potential shifts to a more positive value [16]. Webb and Robertson [17] reported a negative potential shift of polarization curves when nickel was codeposited with 0.01 μm nonconductive Al_2O_3 particles. On the other hand, Watson and Walters [18] observed a positive potential shift of polarization curves when adding 1~5 μm conductive Cr particles to the Ni sulfate electrolyte, ~50 mV for 0.1 vol % and ~100 mV for 4.2 vol % particles in the solution. Watson also found a positive displacement of potential, ~130 mV, by adding 4 vol % semiconductive SiC particles (2~3 μm) into Ni sulfate electrolyte [19]. However, some exceptions were also found. Hwang and Hwang [20] have observed that particle contents up to 5 g/L in the codeposition of SiC (~3 μm) with cobalt have no effect on the polarization curve. Liu and Chen [8] showed that Al metal particle codeposition behavior in the Ni-Al system could be well fitted by the Gugliemi's model that was originally proposed for inert particle codeposition [21]. The above inconsistency can be understood by determining electrochemical behavior of Al particles in the plating electrolyte.

In our previous work, nanocrystalline Ni/Cu alloy coatings were successfully deposited by direct current (dc) from saccharin containing Ni/Cu citrate electrolyte [22]. The present work is aimed at forming nanocrystalline Ni/Cu alloy

coatings with high volume fraction of embedded Al particles via sediment codeposition (SCD) from the same electrolyte. The effect of Al particles on polarization curves has also been studied, based on which the electrochemical mechanisms involving Ni/Cu-Al codeposition were discussed.

AII.2. Experimental Procedure

Ni/Cu-Al composite coatings were electroplated galvanostatically by sediment codeposition technique. Details of experimental setup have been reported elsewhere [8, 22]. The compositions of electrolyte and plating conditions were: 184 g/L Nickel sulfate ($\text{NiSO}_4 \cdot 6\text{H}_2\text{O}$), 6.24 g/L Cupric sulfate ($\text{CuSO}_4 \cdot 5\text{H}_2\text{O}$), 76.47 g/L Sodium citrate (NaCit_3), 0.2 g/L Sodium dodecyl sulphate, 0.5 g/L saccharin, pH 4.5, magnetic stir rate 200 rpm, and temperature $30 \pm 0.5^\circ\text{C}$. Al metal particles with an average size of 3 μm were purchased from Valimet (Stockton, CA, USA). Different amounts of Al particles were added into the electrolyte and stirred for 2 hours before plating.

Potentiodynamic polarization experiments were performed using Gamry PC4/750 potentiostat/galvanostat system scanned at a low sweep rate of 1 mV/s in the Ni/Cu codeposition potential region (from -900 mV to -1150 mV). All potentials are referred to a saturated calomel electrode (SCE). Potentiodynamic polarization

experiments were conducted under the same conditions as those used in electro-codeposition. At least two repeats were performed for each experimental condition.

Surface morphology and compositions of the deposited coatings were characterized using a Hitachi H2700 scanning electron microscope (SEM) with an attached Princeton Gamma-Tech (Prism IG) ultra thin window (UTW) energy dispersive spectrometer (EDS). The alloy matrix phase structure was analyzed by a JEOL 2010 transmission electron microscope (TEM). Grain size distributions were processed by a comprehensive image analysis software, Image-Pro[®] Plus, on TEM dark field images. To determine the volume fraction of Al particles in the composite coatings, backscattered electron (BSE) cross-section images were taken at 600 \times magnification from various locations of the coating layer. Image-Pro[®] Plus was then used to obtain the volume fraction of Al particles by adjusting the threshold level of darkness.

III.3. Results and Discussion

III.3.1. Morphology and Microstructural Studies of Ni/Cu-Al Composite Coatings

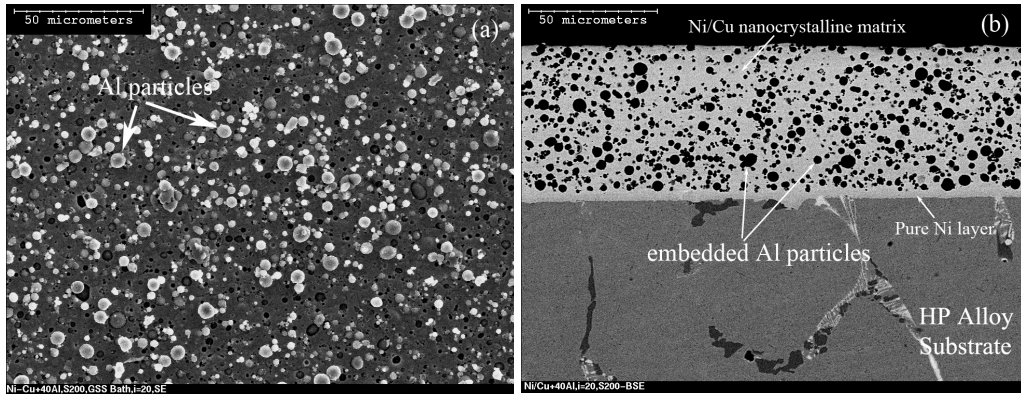


Figure AII-1. Plan view SEM image (a) and backscattered cross-section image (b) of as-plated Ni/Cu-Al particle composite coating (Ni-17 wt % Cu-8 wt % Al).

Typical surface morphology and backscattered cross-section SEM images of Ni/Cu-Al composite coatings deposited at $i=20 \text{ mA/cm}^2$ and a particle loading of 40 g/L are shown in Figure AII-1. The coating in Figure AII-1a was cleaned in ultrasonic bath for 30 min before SEM examination. Some Al particles were pulled out of the surface with holes left behind. Al particles remained attached on the surface are considered to be strongly adsorbed on the cathode surface and are to be embedded in the composite coating. Thickness of the coating is uniform across the coating layer (Figure AII-1b), which was controlled to be around 60 μm . It is also seen from Figure AII-1 that spherical Al particles are homogeneously embedded in Ni/Cu alloy matrix. Based on the composition of the alloy matrix determined by EDS and the volume fractions of Al particles from image analysis, the composition of the composite coating in Figure AII-1 was determined to be Ni-17 wt % Cu-8 wt % Al.

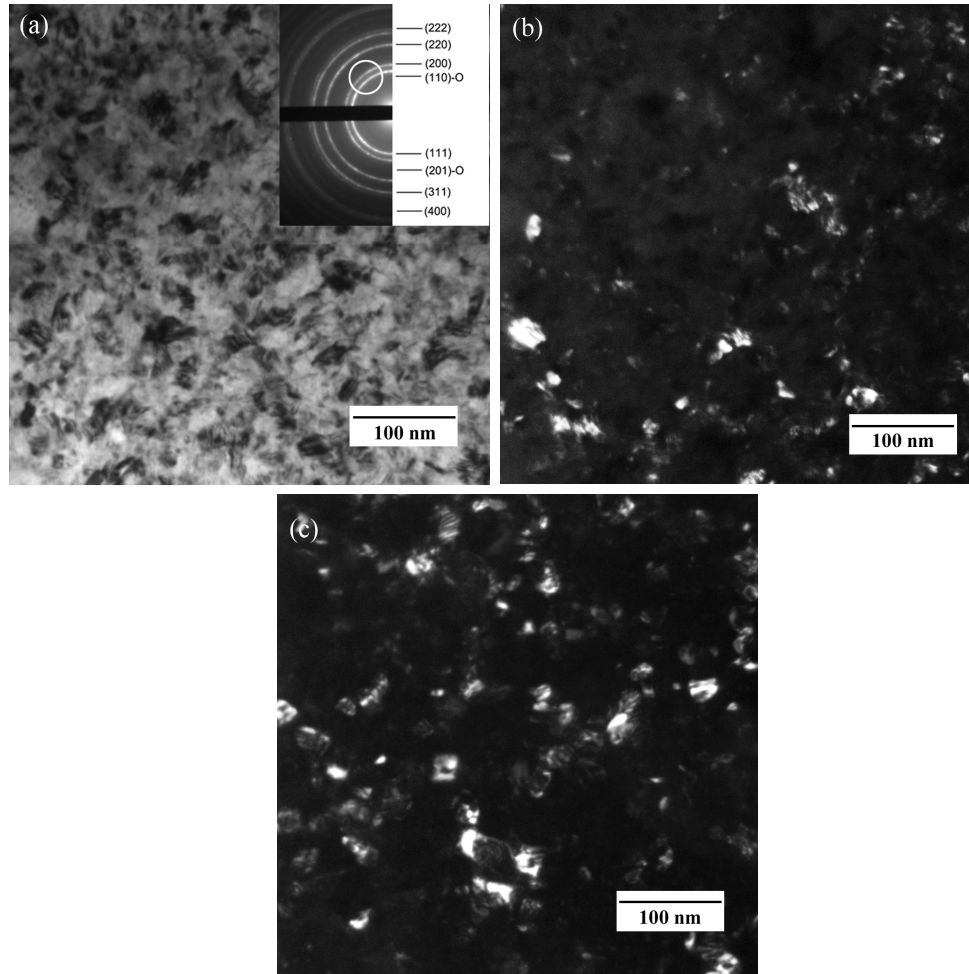


Figure AII-2. Bright-field image with its inset electron-diffraction patterns (a), and dark-field image (b) of as-plated Ni-17 wt % Cu-8 wt % Al composite coating. (c) Dark-field image of as-plated Ni-20 wt % Cu coating.

Figure AII-2a and Figure AII-2b are bright field (BF) and dark field (DF) TEM images of as-plated Ni-17 wt % Cu-8 wt % Al composite coating. No voids or void-like defects were seen in the coating microstructure. The DF image in Figure AII-2b was formed using selected electron beams from circled region on the diffraction rings shown in Figure AII-2a. The distribution of grain size obtained

from several DF images was in the range of 5-80 nm with an average value of 16 nm. In comparison, DF image of Ni-20 wt % Cu alloy coating produced at $i=20$ mA/cm² is shown in Figure AII-2c. The average grain size of the alloy coating was also determined to be 16 nm. It proves that addition of micron size Al particles has little effect on the grain size of alloy matrix, which has also been reported by Zhou et al. [23] in their study on the effect of Al particle size on electroplated Ni-Al coatings. The inserted electro diffraction (ED) patterns in Figure AII-2a show small amount of L1₀-type nano-phase in the matrix, which was also observed by Ghosh et al. [24]. Therefore, the final composite coatings were nanocrystalline Ni/Cu alloy matrix with high contents of Al particles.

AII.3.2. Potentiodynamic Polarization

Figure AII-3a shows the effect of Al metal particles on potentiodynamic polarization curves scanned within the Ni/Cu codeposition potential region (from -900 mV to -1150 mV). The scans were conducted on the fresh cathode surface (solid lines in Figure AII-3a), and on the surface plated for 30 minutes under $i=10$ mA/cm² (dash lines in Figure AII-3a). Instead of a positive potential displacement as observed in the presence of conductive (Cr) and semiconductive (SiC) particles [18, 19], all polarization curves with Al particle loadings in Figure AII-3a were shifted to more negative potentials, ~ -30 mV for 10 g/L (0.37 vol %)

and ~ -50 mV for 40 g/L (1.48 vol %) Al particles at $i=40$ mA/cm².

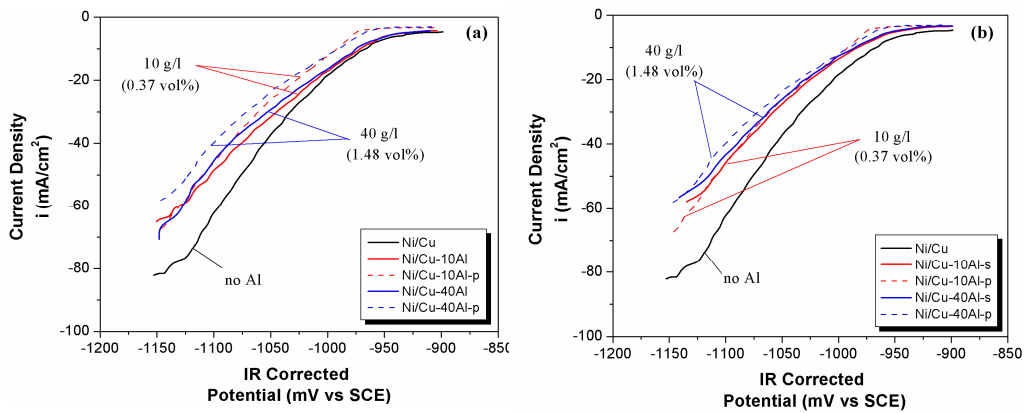


Figure AII-3. Effect of particle loading on potentiodynamic polarization scans, (a) solid lines are polarization scans start at the beginning of plating, while dashed lines are those start after 30 min plating under $i=10$ mA/cm², (b) solid lines are simulated polarization curves, while dashed lines are scans start after 30 min plating under $i=10$ mA/cm².

Negative potential displacement is a characteristic of nonconductive particles codeposition, e.g., Al₂O₃ particles in Ni [17] and Cu [25] plating. It suggests that when codeposited with Ni/Cu alloys Al metal particles show inert particle codeposition behavior. Hence, the displacement of polarization curves should be ascribed to active surface area available for Ni/Cu electrodeposition rather than the conductivity of the particles, as also discussed by Watson et al. [19]. It is believed that a thin oxide layer might be present on the surface of Al particles,

which changes surface characteristic of Al particles during codeposition. The inertial surface of Al particles decreases the active surface area, and thus shifts scans to more negative potentials.

The inertial behavior of Al particles during codeposition is also consistent with the fact that Al particles are distributed uniformly in the coating, rather than form sponge-like structure as observed during codeposition of other conductive particles [26]. This also explains why the Guglielmi's model can be used to fit the codeposition of Ni-Al particles. Note that the scans made on the fresh surface were slightly more positive than those made on the as-plated surface, Figure AII-3a. This should be a result of unsaturated coverage of Al particles on the fresh surface at the beginning of codeposition.

Simulated polarization curves with particle loadings of 10 g/L and 40 g/L are shown as solid lines in Figure AII-3b. The simulation was made based on the assumption that once Al particles attached on the cathode, all particle surface could not act as active surface for Ni/Cu codeposition. Saturated coverage values of Al particles on the surface, 21 vol % for 10 g/L and 29 vol % for 40 g/L under $i=10 \text{ mA/cm}^2$ determined by image analysis, were also used for establishing the simulated curves. The simulated curves were then compared with the actual scans performed on the surface which had been plated for 30min under $i=10 \text{ mA/cm}^2$.

It is obvious that the simulated curves fit well with the actual scans, which proves that all Al particle surface is non active for Ni/Cu codeposition.

AII.3.3. Effect of Particle Loading on Embedded Particle Content at Different Current Densities

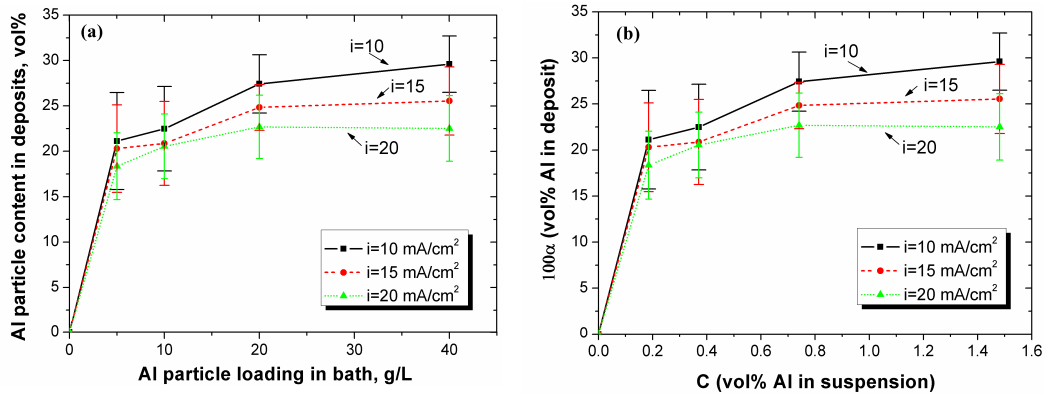


Figure AII-4. Volume percentage of embedded Al particles as a function of (a) particle loading and (b) volume percentage of particles in suspension, under different current densities. Error bar: 95% confidence.

Volume percentage of Al particles in nanocrystalline Ni/Cu alloy matrix as a function of particle loadings ranging from 5 g/L (0.18 vol %) to 40 g/L (1.48 vol %) are plotted in Figure AII-4. It can be seen that the volume percentage of Al particles in the coating increases abruptly in the initial stage and levels off after particle loading is higher than 20 g/L (0.74 vol %). This trend is highly similar to

Langmuir adsorption isotherms as observed in many inert particle codeposition systems and is the basic hypothesis of the Guglielmi's model. According to Figure AII-4, the maximum particle contents in the coatings were around 29 vol %, 25 vol % and 22 vol % at current densities of 10 mA/cm², 15 mA/cm² and 20 mA/cm², respectively. These values are a little lower than SCD Ni-Al system [8] which was between 30 and 35 vol %, but higher than CED Ni-Al system [27] which was 20 vol %.

AII.3.4. Codeposition Mechanism

The mechanism of particle electro-codeposition processes has been pursued for several decades; and several models have been developed, such as the Guglielmi's model, the Celis's model [28], the trajectory model [29] and the statistic model [30]. Nevertheless, a clear picture of the exact effect of each parameter is difficult to obtain. The mechanism for codeposition, as generally accepted, involves particle transport to the cathode surface by bath agitation and embedment in the metal by reduction of adsorbed ions [31]. The Guglielmi's model is provided by simplifying the mass transport step to loosely adsorption step, and then derived from the electrophoresis, adsorption and electrochemical processes, so some parameters, like bath agitation, bath constituents and particle type are inherently accounted for by the constants k , ν_0 in Eq. (AII-1) [31]. The above hypotheses

are also the basis of some later models, e.g., Celis's five step model [28] and Hwang and Hwang's model [20]. Deduced for inert particle codeposition, the Guglielmi's model assumes two successive adsorption steps. In the first step, particles with surrounded adsorbed ion clouds are physically and loosely adsorbed on the cathode surface. In the second step, metal ions adsorbed on particles are reduced, making particles strongly adsorbed and to be embedded in the growing coating. The validity of the Guglielmi's model has been proved in many codeposition systems under certain prescribed conditions [8, 27, 33, 34].

Since Al metal particles exhibit a codeposition behavior similar to that of inert particles and all the surface of Al particles is non active for Ni/Cu codeposition as shown in Figure AII-3, the Guglielmi's model could be adopted for the analysis of the current Ni/Cu-Al system. As the current investigation is focused on the electrochemical processes of Ni/Cu-Al plating, the flow field parameters, although important, were kept the same: stir rate 200 rpm, pH = 4.5, and temperature $30 \pm 0.5^\circ\text{C}$. Notice that the stir rate is relatively low, which would favor particle adsorption as assumed in Guglielmi's model. In addition, the Guglielmi's model should be fitted in the charge transfer region due to the use of Eq. (AII-2), so it's much confident to use current densities in the region between 10 mA/cm^2 and 20 mA/cm^2 [22].

The mathematical equations derived by Guglielmi are

$$\frac{C(1-\alpha)}{\alpha} = \frac{Wi_0}{nFd\nu_0} \cdot e^{(A-B)\eta} \cdot \left(\frac{1}{k} + C\right) \quad (\text{AII-1})$$

$$i = (1-\mathcal{G})i_0e^{A\eta} \quad (\text{AII-2})$$

when $\alpha \ll 1$ ($\mathcal{G} \ll 1$),

$$\frac{C}{\alpha} = \frac{Wi_0}{nFd\nu_0} \cdot e^{(A-B)\eta} \cdot \left(\frac{1}{k} + C\right) \quad (\text{AII-3})$$

$$i = i_0e^{A\eta} \quad (\text{AII-4})$$

where:

- α : volume percent of particles in the coating
- C : volume percent of particles in the plating bath
- M : atomic weight of deposited metal
- i_0 : exchange current density of deposited metal
- n : valence of deposited metal
- F : Faraday's constant
- d : density of deposited metal
- ν_0 : constant for particle deposition
- A and B : constant for metal deposition and particle deposition, respectively
- η and i : overpotential and current density, respectively
- k : adsorption coefficient
- \mathcal{G} : surface coverage of embedded particles

These equations relate volume fractions of embedded particles to some electrochemical parameters that can be controlled, such as C , η and i .

In many codeposition systems, the simplified Eqs. (AII-3) and (AII-4) are used with reasonable accuracy, and the data fitting process based on Eqs. (AII-3) and (AII-4) is also straightforward. However, in the present SCD Ni/Cu-Al system, α values are so high, as shown in Figure AII-4, that the term $(1 - \alpha)$ cannot be omitted. The term $(1 - \theta)$ in Eq. (AII-2), which is equal to $(1 - \alpha)$ [21], should not be neglected also in the present system. Therefore, the original Guglielmi's equations (Eqs. (AII-1) and (AII-2)) must be used to fit the data.

Substituting Eq. (AII-2) into Eq. (AII-1) yields:

$$\frac{C(1 - \alpha)^{(2-B/A)}}{\alpha} = \frac{Wi_0^{B/A}}{nFd\nu_0} \cdot i^{(1-B/A)} \cdot \left(\frac{1}{k} + C\right) \quad (\text{AII-5})$$

To fit the experimental data using Eq. (AII-5), the B/A ratio must be so pre-determined that the following two conditions must be met: First, in the $C(1 - \alpha)^{(2-B/A)}/\alpha$ vs. C plot, the selected B/A ratio must be able to group the experimental data on a sheaf of straight lines for different current densities and these lines must converge at a negative point on the abscissa where $C = -1/k$. Second, slopes of the above fitted lines at various current densities as expressed

by Eq. (AII-6) as:

$$\tan \phi = \frac{W i_0^{B/A}}{n F d v_0} \cdot i^{(1-B/A)} \quad (\text{AII-6})$$

or in the logarithm form of :

$$\log(\tan \phi) = \log \frac{W i_0^{B/A}}{n F d v_0} + \left(1 - \frac{B}{A}\right) \log i \quad (\text{AII-7})$$

should be well grouped on a straight line with its slope equal to $(1 - B/A)$ in the $\log(\tan \phi)$ vs. $\log i$ plot.

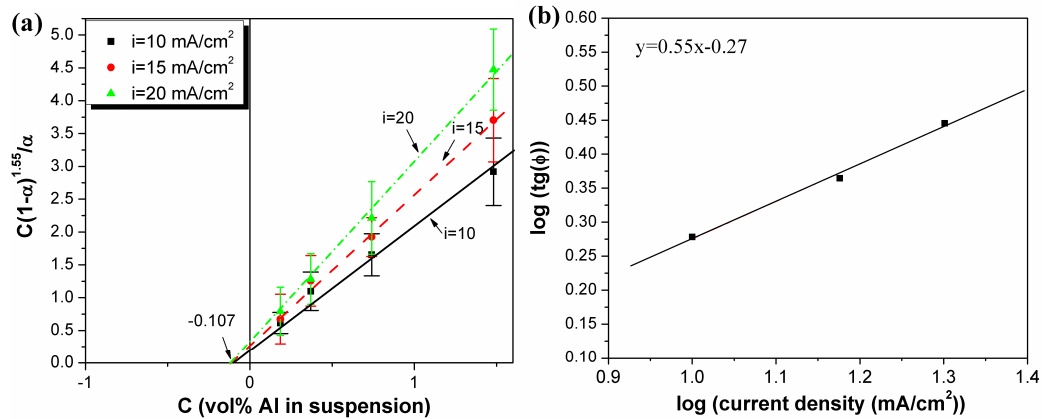


Figure AII-5. (a) $C(1-\alpha)^{1.55}/\alpha$ vs. C for Ni/Cu-Al coatings at three different current densities. Error bar: 95% confidence. (b) $\log(\tan \phi)$ vs. $\log i$ for the Ni/Cu-Al particle system.

Figure AII-5 shows the fitted results, in which B/A ratio was chosen to be 0.45. Figure AII-5a shows a sheaf of straight lines with experimental data well settled on at three different current densities and these straight lines have a common

intercept on the C axis which is found to be $1/k = 0.107$ or $k = 9.35$. In Figure AII-5b, the logarithms of the slopes of the straight lines shown in Figure AII-5a are plotted against $\log i$. The linear regression line yields a slope of 0.55 ($=1 - B/A$), which gives a B/A ratio of 0.45, a value that was pre-selected for the initial curve fitting. Therefore, the codeposition behavior of the present Ni/Cu-Al system agrees well with the Guglielmi's model under present conditions, stir rate 200 rpm, pH = 4.5 and temperature 30 ± 0.5 °C.

Although the current density used to fit the model is within a narrow range (between 10 mA/cm^2 and 20 mA/cm^2), the composition of Ni/Cu alloys can be varied from 20.2 wt % of Cu at 20 mA/cm^2 to 52.2 wt % of Cu at 10 mA/cm^2 , as reported previously [22]. In addition, the dc-electrodeposition of Ni/Cu alloys is challenged with poor surface finish as compared with electrodeposition of pure metals. A mirror-finish surface can be achieved by adding 0.5 g/L saccharin when current densities were set within 10 mA/cm^2 and 20 mA/cm^2 for the current plating system. Beyond this range, cauliflower type of surface finish would be produced even if effective agents such as saccharin were added [22]. Hence, from the point of practical applications, the current density had better be controlled below 20 mA/cm^2 , which is one of the limitations of dc-electrodepositing Ni/Cu alloys. Surface roughness effect on particle codeposition process can also be avoided when the current density is lower than 20 mA/cm^2 .

AII.4. Conclusions

Nanocrystalline Ni/Cu alloy matrix with Al metal particle composite coatings have been successfully codeposited. High Al particle content, 29 vol %, could be codeposited into nanocrystalline Ni/Cu coating matrix. Addition of Al metal particles shifted polarization curves to more negative potentials. This was attributed to the non active surface of Al particles during Ni/Cu deposition, similar to the codeposition of inert particles. Because of this similarity, parameters used in the current codeposition processes can be well fitted by the Guglielmi's model that was established for inert particle codeposition.

AII.5. References

- [1]. Napłoszek-Bilnik, I.; Budniok, A.; Łosiewicz, B.; Pająk, L.; Łągiewka, E. *Thin Solid Films* **2005**, 474, 146-153.
- [2]. Garcia, I.; Fransaer, J.; Celis, J. P. *Surface and Coatings Technology* **2001**, 148, 171-178.
- [3]. Grosjean, A.; Rezrazi, M.; Takadoun, J.; Bercot, P. *Surface and Coatings Technology* **2001**, 137, 92-96.
- [4]. Ebrahimi, F.; Bourne, G. R.; Kelly, M. S.; Matthews, T. E. *Nanostructured Materials* **1999**, 11, 343-350.
- [5]. Shao I.; Vereecken, P. M.; Chien, C. L.; Searson, P. C.; Cammarata, R. C. *Journal of Materials Research* **2002**, 17, 1412-1418.
- [6]. Stroumbouli, A.; Gyftou, P.; Pavlatou, E. A.; Spyrellis, N. *Surface and Coatings Technology* **2005**, 195, 325-332.
- [7]. Roos, J. R.; Celis, J. P.; Fransaer J.; Buelens, C. *Journal of Metals* **1990**, 42, 60-63.
- [8]. Liu, H.; Chen, W. *Surface and Coatings Technology* **2005**, 191, 341-350.
- [9]. Berçot, P.; Peña-Muñoz, E.; Pagetti, J. *Surface and Coatings Technology* **2002**, 157, 282-289.
- [10]. Ghorbani, M.; Mazaheri, M.; Khangholi, K.; Kharazi, Y. *Surface and Coatings Technology* **2001**, 148, 71-76.

- [11]. Gómez, E.; Pané, S.; Vallés, E. *Electrochemistry Communications* **2005**, 7, 1225-1231.
- [12]. Serek, A.; Budniok, A. *Journal of Alloys and Compounds* **2003**, 352, 290-295.
- [13]. Erler, F.; Jakob, C.; Romanus, H.; Spiess, L.; Wielage, B.; Lampke, T.; Steinhäuser, S. *Electrochimica Acta* **2003**, 48, 3063-3070.
- [14]. Low, C. T. J.; Wills, R. G. A.; Walsh, F. C. *Surface and Coatings Technology* **2006**, 201, 371-383.
- [15]. Gierlotka, D.; Rówiński, E.; Budniok, A.; Łągiewka, E. *Journal of Applied Electrochemistry* **1997**, 27, 1349-1354.
- [16]. Stojak, J. L.; Talbot, J. B. *Journal of Applied Electrochemistry* **2001**, 31, 559-564.
- [17]. Webb, P. R.; Robertson, N. L. *Journal of the Electrochemical Society* **1994**, 141, 669-673.
- [18]. Watson, S. W.; Walters, R. P. *Journal of the Electrochemical Society* **1991**, 138, 3633-3637.
- [19]. Watson, S. W. *Journal of the Electrochemical Society* **1993**, 140, 2235-2238.
- [20]. Hwang, B. J.; Hwang, C. S. *Journal of the Electrochemical Society* **1993**, 140, 979-984.
- [21]. Guglielmi, N. *Journal of the Electrochemical Society* **1972**, 119, 1009-1012.

- [22]. Cui, X.; Chen, W. *Journal of the Electrochemical Society* **2008**, 155, K133-K139.
- [23]. Zhou, Y.; Peng, X.; Wang, F. *Oxidation of Metals* **2005**, 64, 169-183.
- [24]. Ghosh, S. K.; Grover, A. K. *Journal of Materials Research* **2006**, 21, 45-61.
- [25]. Lozano-Morales A.; Podlaha, E. J. *Journal of the Electrochemical Society* **2004**, 151, C478-C483.
- [26]. Stankovic, V. D.; Gojo, M. *Surface and Coatings Technology* **1996**, 81, 225-232.
- [27]. Hovestad, A.; Heesen, R. J. C. H. L.; Janssen, L. J. J. *Journal of Applied Electrochemistry* **1999**, 29, 331-338.
- [28]. Celis, J. P.; Roos, J. R. *Journal of the Electrochemical Society* **1977**, 124, 1508-1511.
- [29]. Fransaer, J.; Celis, J. P.; Roos, J. R. *Journal of the Electrochemical Society* **1992**, 139, 413-425.
- [30]. Wang, D. L.; Li, J.; Dai, C. S.; Hu, X. G. *Journal of Applied Electrochemistry* **1999**, 29, 437-444.
- [31]. Hovestad, A.; Janssen, L. J. J. *Journal of Applied Electrochemistry* **1995**, 25, 519-527.
- [32]. Susan, D. F.; Misiolek, W. Z.; Marder, A. R. *Metallurgical and Materials Transactions A* **2001**, 32A, 379-390.

[33]. Wang, S. C.; Wei, W. C. J. *Materials Chemistry and Physics* **2003**, 78, 574-580.